Journal of Holography Applications in Physics
Volume 5, Special Issue, Winter 2025
© Available online at http://jhap.du.ac.ir
DOI: 10.22128/jhap.2025.001.014

Journal of Holography Applications in Physics

Conference Proceedings

International Conference on Astroparticle Physics, Gravitation and Cosmology (APGC-2025)

26-28, June 2025
Mathura, India

Committee of the APGC 2025
GLA University, Mathura
Email: apgcphy@gmail.com
Conference website: https://apgc.gla.ac.in/

Conference Proceedings of International Conference on Astroparticle Physics, Gravitation and Cosmology (APGC-2025)

Edited by
Dr. Dharm Veer Singh,
Dr. Sudhaker Upadhyay

Online ISSN: 2783-3518
Print ISSN: 2783-4778

ISBN : 978-622-5209-54-1

DOI: 10.22128/jhap.2025.001.014

Published by Journal of Holography Applications in Physics (JHAP), Damghan University Press. Tel: +98-23-35220236
Fax: +98-23-35220236

Hosting:
GLA University, Mathura, India

Organised By:
Department of Physics, GLA University, Mathura, India

Academic Partner:
Damghan University, Damghan, Iran
ARSD College, University of Delhi, New Delhi, India
KLS College, Magadh University, Gaya, India

APGC 2025

Shri Narayan Das Agrawal	Chancellor, GLA University, Mathura, India
Prof. Durg Singh Chauhan	Pro-Chancellor, GLA University, Mathura, India
Prof. Anup Kumar Gupta	Vice-Chancellor, GLA University, Mathura, India
Prof. Shailaj K. Shrivastava	Principal, KLS College, Magadh University, Gaya, India
Prof. Gyantosh Kumar Jha	Principal, ARSD College, University of Delhi, New Delhi, India
Prof. Reza Pourgholi	President, Damghan University, Damghan, Iran
Mr. Ashok Kumar Singh	Registrar, GLA University, Mathura, India
Prof. Anirudh Pradhan	Director, CCASS, GLA University, Mathura
Prof. Ashish Sharma	Dean of Academic Affairs, GLA University, Mathura, India
Prof. Kamal Sharma	Dean Research and Development, GLA University, Mathura, India
Prof. Anuj Vijay	Head, Department of Physics, GLA University, Mathura, India

APGC 2025 Scientific Advisory Board

Prof. Sushant G. Ghosh	Jamia Millia Islamia, New Delhi, India
Prof. Gopi Kant Goswami	NSUT, New Delhi, India
Prof. Rudra Prakash Malik	BHU, Varanasi, India
Prof. Ambuj Mishra	GLA University, Mathura, India
Prof. Yerlan Myrzagulov	ENU, Astana, Kazakhstan
Prof. Kairat Myrzagulov	ENU, Astana, Kazakhstan
Prof. Prasanta K. Panigrahi	SoA University, Odisha
Prof. Saibal Ray	GLA University, Mathura, India
Prof. Izzat Sakalli	EMU, North Cyprus, Turkey
Prof. Umesh Sharma	GLA University, Mathura, India
Prof. Hari Prakash Sharma	BHU, Varanasi, India
Prof. Sanjay Siwach	BHU, Varanasi, India
Prof. Vanktesh Singh	CUSB, South Bihar, India
Prof. Benoy Kumar Singh	GLA University, Mathura, India
Prof. K. P. Yogendram	IISER, Mohali, India

APGC 2025 Session Chairs

Prof. Anirudh Pradhan	CCASS, GLA University, Mathura, India
Dr. Sudhaker Upadhyay	KLS College, Magadh University, Gaya, India
Dr. Gauhar Abbas	Indian Institute of Technology, BHU, Varanasi, India
Dr. Ram Lal Awasthi	University of Delhi, New Delhi, India
Dr. Saurabh Gupta	National Institute of Technology, Calicut, India
Dr. Rohit Kumar	Vishwa Bharati University, West Bangal, India
Dr. Vijay Kumar Mishra	GLA University, Mathura, India
Dr. Raj Pal Singh	GLA University, Mathura, India

APGC 2025 Organising Committee

Dr. Dharm Veer Singh	GLA University, Mathura, India
Dr. Sudhaker Upadhyay	KLS College, Magadh University, Gaya, India
Dr. Behnam Pourhassan	Damghan University, Iran
Dr. Manish Kumar	University of Delhi, New Delhi, India
Dr. Vijay Kumar Mishra	GLA University, Mathura, India
Dr. Aradhya Shukla	GLA University, Mathura, India
Dr. Manoj Kumar Singh	GLA University, Mathura, India
Dr. Shobhit Sachan	GLA University, Mathura, India
Dr. Ashutosh Singh	GLA University, Mathura, India
Dr. Dinesh Chandra Maurya	GLA University, Mathura, India

APGC 2025 Local Organising Committee

Prof. Raj Pal Singh	GLA University, Mathura, India
Prof. Monika Goyal	GLA University, Mathura, India
Dr. Lokesh Kumar Sharma	GLA University, Mathura, India
Dr. Rashmi Singh	GLA University, Mathura, India
Dr. Saptarshi Pal	GLA University, Mathura, India
Dr. Mrinal Jauhari	GLA University, Mathura, India
Dr. Vipul Bhardwaj	GLA University, Mathura, India
Dr. Swati Singh	GLA University, Mathura, India
Dr. Sukriti	GLA University, Mathura, India

APGC 2025 Editorial Board

Table of Contents

International Conference on Astroparticle Physics, Gravitation and Cosmology (APGC-2025)
26-28 June 2025, GLA University, Mathura, India

Canonical Scalar Field with Mutually Interacting Components

Devanarayanan Rajeeb Kumar[*],
Universität Heidelberg, Grabengasse 1, 69117 Heidelberg
Jaskirat Kaur[†], S. D. Pathak[‡]
Department of Physics, Lovely Professional University,
Phagwara, 144411, Punjab, India.
Maxim Khlopov [§]
Virtual Institute of Astroparticle Physics, 75018 Paris, France
Maxim Krasnov [¶]
Institute of Physics, Southern Federal University, Rostov on Don 344090, Russia
National Research Nuclear University MEPHI, 115409 Moscow, Russia.

Abstract

In this paper, we investigate the possibility of the canonical scalar field in which the Lagrangian acts as both dark matter and dark energy. We further explore the interaction between these two components of the canonical scalar field by considering the interaction strength is linearly dependent on the rate change of their energy density, in particular, $Q = 3\alpha\dot{\rho_m}$ and $Q = 3\sigma(\dot{\rho_m} + \dot{\rho_d})$. We estimate the value of coupling strength from PLANCK-2018 observational data. The age of the universe is calculated in the spatially flat universe in the presence of interaction and without interaction which is consistent with observations for a given value of coupling parameter in the three interacting models.

1 Introduction

Several different cosmological observations, including the Supernova Ia [1,2], Baryon Acoustic Oscillation (BAO) [3,4] and Cosmic Microwave Background Radiation (CMBR) [5,6], gave that nearly 70% of the entire content of the universe constitutes of an exotic component with repulsive gravitational effect, termed as dark energy. The accelerated expansion of the universe at the present epoch, indicated by the recent Planck data can be elucidated by dark energy, which can be explained as modified matter in the energy-momentum tensor or the modified geometry in Einstein's field equations. The theory of modified energy-momentum tensor suggests two different approaches to dark energy, wherein one, dark energy density is constant, with a constant equation of date (EoS) $w_\Lambda = -1$, which is the simplest dark energy candidate, called the Cosmological constant. However, the cosmological constant problem poses a serious issue to this, as the EoS is not evolving with time. The other approach gives a more promising insight, where dark energy density is not constant but possesses an evolving equation of state, often termed as dynamical dark energy model [7–10]. Dynamical dark

[*]devanarayanan.rajeeb_kumar@stud.uni-heidelberg.de
[†]jaskiratkaur653@gmail.com
[‡]prince.pathak19@gmail.com
[§]khlopov@apc.in2p3.fr
[¶]morrowindman1@mail.ru

energy has piqued the interest of several authors and offers a way around the cosmological constant problem. Classes of scalar fields are a few of the promising candidates for the dynamic form of dark energy [11–13]. Literature [14–24] provides a detailed analysis of the cosmological behavior of scalar fields. Among the different classes of scalar fields, the simplest Lagrangian is of Quintessence, which is obtained by taking $\gamma = 1$ in the non-canonical Lagrangian of the scalar field [25–31]:

$$\mathcal{L} = X\left(\frac{X}{M^4}\right)^{\gamma-1} - V(\phi), \tag{1}$$

where M is constant with the dimension of mass, γ is a dimensionless parameter, and $X = \frac{1}{2}\dot{\phi}^2 = \frac{1}{2}(\frac{d\phi}{dt})^2$. The Friedmann–Robertson–Walker(FRW) metric given as

$$ds^2 = dt^2 - a^2(t)\left[\frac{dr^2}{1-kr^2} + r^2 d\Theta^2 + r^2\sin^2\Theta d\Phi^2\right] \tag{2}$$

where $a(t)$ is the scale factor for expansion, and k is the Gaussian curvature parameter whose values are $-1, 0, +1$ assigned for the open, flat, closed universe. For which we have the following form of the energy-momentum stress tensor

$$T^{\mu\nu} = \frac{\partial\mathcal{L}}{\partial(\partial_\mu\phi)}\partial^\nu\phi - g^{\mu\nu}\mathcal{L}. \tag{3}$$

From (3) one can obtain the energy density and pressure of the scalar field:

$$\rho_\phi = \left(\frac{\partial\mathcal{L}}{\partial X}\right)(2X) - \mathcal{L}, \tag{4a}$$

$$P_\phi = \mathcal{L}. \tag{4b}$$

Using the Lagrangian (1) in (4a) and (4b), one can obtain the following expression for pressure and energy density of a non-canonical scalar field

$$P_\phi = X\left(\frac{X}{M^4}\right)^{\gamma-1} - V(\phi), \tag{5a}$$

$$\rho_\phi = (2\gamma-1)X\left(\frac{X}{M^4}\right)^{\gamma-1} + V(\phi). \tag{5b}$$

Friedman equations without the cosmological constant Λ are

$$\frac{\dot{a}^2+k}{a^2} = \frac{1}{3m_p^2}\left((2\gamma-1)X\left(\frac{X}{M^4}\right)^{\gamma-1} + V(\phi)\right), \tag{6a}$$

$$\frac{\ddot{a}}{a} = -\frac{1}{3m_p^2}\left((\gamma+1)X\left(\frac{X}{M^4}\right)^{\gamma-1} - V(\phi)\right), \tag{6b}$$

where $m_p^2 = \frac{1}{8\pi G}$, and $c = 1$.
Equation of motion is given as:

$$\ddot{\phi} + \frac{3H\dot{\phi}}{2\gamma-1} + \left(\frac{2M^4}{\dot{\phi}^2}\right)^{\gamma-1}\left(\frac{V'(\phi)}{\gamma(2\gamma-1)}\right) = 0, \tag{7}$$

where $V'(\phi) = \frac{dV}{d\phi}$ and $H(t) = \frac{\dot{a}(t)}{a(t)}$ is the Hubble parameter.

Taking $\gamma = 1$, we obtain the energy density and pressure for spatially homogeneous Quintessence,

$$\rho_\phi = \frac{1}{2}\dot{\phi}^2 + V(\phi), \qquad p_\phi = \frac{1}{2}\dot{\phi}^2 - V(\phi). \tag{8}$$

2 Components of quintessence

The most potent and comprehensive elucidation of the current cosmological observations will require two components of the dark sector. One of them is dark matter and the other is dark energy. There is no direct or indirect laboratory evidence for the existence of these two components of quintessence. Thus, in this regard, cosmology demands evoking implausible physics multiple times to explain the current observations.

The quintessence field gives rise to two components, pressure-less dark matter with the equation of state $\omega_m = 0$ and the dark energy with the equation of state $-1 \leq \omega_{de} < -1/3$. urthermore, the cosmological constant in this case is not a true constant, but rather mimicked by the evolving dynamical dark energy, which emerges as one of the two components of the scalar field, alongside matter. One of the prodigious features of the energy-momentum tensor in (3) is that it could be interpreted as the sum of two components and one of them is dark matter and the other one is dark energy. In the [15] authors consider the non-canonical scalar field arises from string theory and show the clustered dark matter and dark energy arises from the string-inspired non-canonical scalar field. We follow the same recipe on the canonical scalar field which Lagrangian is given by (1) with $\gamma = 1$. To show this decidedly, we split the energy density and pressure of quintessence and write them in a more denotative form as

$$\rho_\phi = \rho_1 + \rho_2 \qquad P_\phi = P_1 + P_2 \tag{9}$$

If $P_1 = P_m = 0$,i.e., dust matter and this corresponds to

$$P_2 = P_d = \frac{1}{2}\dot{\phi}^2 - V(\phi). \tag{10}$$

.

And since the dynamical dark energy is mimicking the cosmological constant with the equation of state is $\omega_\Lambda = -1$,

$$\rho_2 = \rho_d = -\frac{1}{2}\dot{\phi}^2 + V(\phi). \tag{11}$$

From this we obtain the following expression for energy density and pressure for one component of the canonical scalar field said to be pressureless dust matter as

$$\rho_1 = \rho_m = \dot{\phi}^2; \quad P_1 = P_m = 0. \tag{12}$$

Expression for energy density and pressure other components of this field is

$$\rho_2 = \rho_d = -\frac{1}{2}\dot{\phi}^2 + V(\phi).; \quad P_2 = P_d = -\left(-\frac{1}{2}\dot{\phi}^2 + V(\phi)\right). \tag{13}$$

From the above splitting, we identify two distinct components. The first component exhibits the properties of pressureless matter, characterized by a pressure $P_1 = P_m = 0$ and an equation of state parameter $w_m = 0$, consistent with the behavior of cold dark matter or non-relativistic matter in the standard cosmological model. The second component, on the other hand, behaves like dark energy, with its pressure and energy density related by $P_d = -\rho_d$. This leads to an equation of state parameter $w_d = -1$, indicating that this component effectively mimics a cosmological constant. Hence, the dark energy component emerging from the splitting naturally reproduces the behavior of a Λ-like term, driving the accelerated expansion of the universe.

Under $V \longrightarrow 0$ the field ϕ evolves from some of its constant value $\phi_0 \neq 0$ while in the

In the next section, we examine the possibility of interaction between the matter and dark energy components through the transfer of energy. If the matter component ρ_m and the dark energy component ρ_d (for example, a cosmological constant ρ_Λ) are assumed to be non-interacting, their evolution is governed by separate continuity equations:

$$\dot{\rho}_m + 3H(1 + \omega_m)\rho_m = 0, \tag{14}$$

$$\dot{\rho}_d + 3H(1+\omega_d)\rho_d = 0, \tag{15}$$

where ω_m and $\omega_d = P_d/\rho_d$ denote the equation of state parameters for matter and dark energy, respectively. Solving the above equations yields the well-known scaling solutions. For pressureless matter ($\omega_m = 0$), we obtain:

$$\rho_m \propto a(t)^{-3}, \tag{16}$$

which describes the evolution of matter with the expansion of the universe. For the case where dark energy is modeled as a cosmological constant with $\omega_\Lambda = \omega_d = -1$, the energy density remains constant:

$$\rho_\Lambda = \rho_\Lambda^0. \tag{17}$$

These results are consistent with the ΛCDM model, where matter density decreases as the universe expands, while the ρ_Λ remains fixed, leading to late-time accelerated expansion.

3 Mutual interaction between the components of the canonical scalar field.

In the previous section, we investigate the possibility of dark sector components evolving from a single scalar field. Dark energy and dark matter are considered as two dominating components of the dark sector and our universe is mainly dominated by dark energy. It seems natural that the two major dominant components of the dark sector should interact. Although the interaction between components of the dark sector is not understood well. In the recent past the interacting dark energy models have been proposed by a number of authors [34–55] taking central attention of frontier researcher in cosmology. In the interacting dark energy model, one of the serious issues in the formulation of the functional form of interacting strength is because of less understanding of dark sector physics. In this section, we consider two dominating components in the universe and they possibly evolve from a single real scalar field (which itself is a potential candidate for dynamical dark energy) where the dominant components are dust matter and dark energy. These two are interacting in the sense of energy transfer between them following the local violation of the conservation of energy.

The requirement for interaction between the components arises from the need to attain a stable equilibrium state. Since the individual components are in a thermodynamic state of non-equilibrium, they achieve equilibrium through their mutual interaction.

Since during interaction conservation of energy of individual component is violated while the overall energy is conserved, thus the continuity equations (14 and 15) can be written as in the following form by considering Q as the coupling parameter of the mutual interaction between two components,

$$\dot{\rho}_d + 3H(1+\omega_d)\rho_d = -Q \tag{18}$$

$$\dot{\rho}_m + 3H(1+\omega_m)\rho_m = +Q \tag{19}$$

The functional form of the coupling parameter has some viable candidates that can be determined by satisfying the dimensionality of the continuity equations. As such, the coupling parameter has to be a function of Hubble's parameter and the energy density or a function of the time derivative of the energy density. Several authors have adopted different candidates for the functional form of the coupling parameter Q based on this motivation [34–49, 56–60]. The sign of Q, however, follows the second law of thermodynamics, wherein the transfer of energy is from the component with a higher temperature to the lower one.

Here, we propose two particular forms of the interaction term Q which are linearly proportional to the rate of change in energy density of dust matter and dark energy.

Hence:

1. $Q = \alpha\dot{\rho_m}$,
2. $Q = \sigma(\dot{\rho_m} + \dot{\rho_d})$

3.1 Interaction model I: $Q = \alpha\dot{\rho_m}$

In this interacting model the continuity equation (19) can be read as

$$\dot{\rho}_m + 3H(1+\omega_m)\rho_m = \alpha\dot{\rho_m} \tag{20}$$

with $\omega_m = 0$ as the pressure $P_m = 0$, we have the following functional form of the energy density of matter component

$$\rho_m = \rho_m^0\left(\frac{a}{a_0}\right)^{-\frac{3}{1-\alpha}} \tag{21}$$

The scaling solution of the second component of quintessence one can obtain from (21) and (18) as

$$\dot{\rho}_d + 3H(1+\omega_d)\rho_d = \alpha\frac{3H}{(1-\alpha)}\rho_m \tag{22}$$

$$\rho_d = \frac{1}{(\omega_d - \alpha - \alpha\omega_d)}\left[\alpha\rho_m^0\left(\frac{a_0}{a}\right)^{\frac{3}{1-\alpha}} + \left(\rho_d^0(\omega_d - \alpha - \alpha\omega_d) - \alpha\rho_m^0\right)\left(\frac{a_0}{a}\right)^{3(1+\omega_d)}\right]. \tag{23}$$

In the absence of interaction ($\alpha \longrightarrow 0$), and $\omega_d \sim \omega_\Lambda = -1$ energy density of components (ρ_m and ρ_λ) reduces as

$$\rho_m = \rho_m^0\left(\frac{a}{a_0}\right)^{-3}; \rho_d \sim \rho_\Lambda = \rho_\Lambda^0, \tag{24}$$

which are as expected in ΛCDM model

3.2 Interaction model II: $Q = \sigma(\dot{\rho_m} + \dot{\rho_d})$

The continuity equation (18) and (19) for two mutual components of quintessence with $\omega_\Lambda = -1$ provide

$$\dot{\rho_d} = -\frac{\sigma}{(1+\sigma)}\dot{\rho_m} \tag{25}$$

and for dust matter component

$$\frac{\dot{\rho_m}}{\rho_m} = -3(1+\sigma)\frac{\dot{a}}{a} \tag{26}$$

which give

$$\rho_m = \rho_m^0\left(\frac{a_0}{a}\right)^{3(1+\sigma)}, \tag{27}$$

and (25) with (27) gives the following scaling solution of dark energy in the interacting model-III as

$$\rho_d = \rho_d^0 + \frac{\sigma}{(1+\sigma)}\rho_m^0\left[1 - \left(\frac{a_0}{a}\right)^{3(1+\sigma)}\right]. \tag{28}$$

Here again we can see, if the coupling is zero i.e. $\sigma \to 0$, $\rho_m \sim a^{-3}$ and $\rho_d \sim$ constant again mimicking constant ΛCDM behavior.

4 Determination of Coupling term Q:

The proportionality constant in interaction term Q in three interacting models can be constrained by knowing the Hubble parameter at different redshifts. For this, let us introduce the normalized Hubble parameter $E^2(x)$ as

$$E^2(x) = \frac{H^2(x)}{H_0^2} \tag{29}$$

where $x = 1 + z = \frac{a_0}{a}$. Here in above Eq.(29) for a two-component spatially flat universe, the Friedmann equations are:

$$H^2 = \frac{8\pi G}{3}(\rho_m + \rho_d), \tag{30}$$

and

$$\frac{\ddot{a}}{a} = -\frac{4\pi G}{3}(\rho_m + \rho_d + 3(P_m + P_d)) \tag{31}$$

4.1 For $Q = \alpha\dot{\rho_m}$

For the interacting model-I $E^2(x)$ at redshift $x = 1 + z = \frac{a_0}{a}$ using Eq.(29) and (30) can be written as

$$E^2(x) = \frac{8\pi G}{3H_0^2}\left(\rho_m^0\left(\frac{a_0}{a}\right)^{\frac{3}{1-\alpha}} + \rho_d^0 - \alpha\rho_m^0\left[\left(\frac{a_0}{a}\right)^{\frac{3}{1-\alpha}} - 1\right]\right). \tag{32}$$

Let us write $\rho_c = \frac{3H_0^2}{8\pi G}$ as said to be the critical density and thus, (32) is read as in following form

$$E^2(x) = \Omega_m^0 x^{3/1-\alpha} + \Omega_d^0 - \alpha\ \Omega_m^0(x^{3/1-\alpha} - 1), \tag{33}$$

where $\Omega_m^0 = \frac{\rho_m^0}{\rho_c}$ is the matter energy density parameter and similarly $\Omega_d^0 = \frac{\rho_d^0}{\rho_c}$ is the dark energy density parameter. We define the difference of the squares of the normalized Hubble parameter $E^2(x)$ at two redshifts namely x_i and x_j as

$$E^2(x_i) - E^2(x_j) = \Delta E^2(x_i, x_j) = \Omega_m^0(1-\alpha)\left[x_i^{3/1-\alpha} - x_j^{3/1-\alpha}\right]. \tag{34}$$

We take Hubble parameter $H(z)$ at high redshift values z from [61, 62] in following table (1)

z	$H(z)$
0.88	90 ± 40
0.9	117 ± 23
1.3	168 ± 17
1.43	177 ± 18
1.75	202 ± 40

Table 1: Value of Hubble parameter $H(z)$ in Km $s^{-1}Mpc^{-1}$ at different value of redshift z [61, 62].

The concordance value from Planck CMB, BAO, etc. data analysis [63], we obtain the value of density parameter Ω_m^0 of matter and dark energy Ω_d^0 at present epoch and the current Hubble's constant H_0, as $\Omega_m^0 = 0.311$, $\Omega_d^0 = 0.689$ and $H_0 = 67.66 \pm 0.42 \approx 67.66$ Km s^{-1} Mpc^{-1}.

Thus taking the five epochs $x_1 = 1.88$, $x_2 = 1.9$, $x_3 = 2.3$, $x_4 = 2.43$ and $x_5 = 1.88$, we determine the corresponding normalized Hubble's parameters:

$$E^2(x_1) = 1.769;\;\; E^2(x_2) = 2.990;\;\; E^2(x_3) = 6.165;\;\; E^2(x_4) = 6.844;\;\; E^2(x_5) = 8.913. \tag{35}$$

The difference of the squares of the normalized Hubble parameter $\Delta E^2(x_i, x_j)$ as given (34) with Table:(1) and squared normalized Hubble parameters $E^2(x)$ given by (32) leads to ten nonlinear equations in coupling parameter α for interaction strength $Q = \alpha\dot{\rho}_m$ as follows

$$(1-\alpha)\left[(1.88)^{3/1-\alpha} - (1.9)^{3/1-\alpha}\right] = -3.926$$

$$(1-\alpha)\left[(1.88)^{3/1-\alpha} - (2.3)^{3/1-\alpha}\right] = -14.135$$

$$(1-\alpha)\left[(1.88)^{3/1-\alpha} - (2.43)^{3/1-\alpha}\right] = -16.316$$

$$(1-\alpha)\left[(1.88)^{3/1-\alpha} - (2.75)^{3/1-\alpha}\right] = -22.971$$

$$(1-\alpha)\left[(1.9)^{3/1-\alpha} - (2.3)^{3/1-\alpha}\right] = -10.209$$

$$(1-\alpha)\left[(1.9)^{3/1-\alpha} - (2.43)^{3/1-\alpha}\right] = -12.390$$

$$(1-\alpha)\left[(1.9)^{3/1-\alpha} - (2.75)^{3/1-\alpha}\right] = -19.045$$

$$(1-\alpha)\left[(2.3)^{3/1-\alpha} - (2.43)^{3/1-\alpha}\right] = -2.181$$

$$(1-\alpha)\left[(2.3)^{3/1-\alpha} - (2.75)^{3/1-\alpha}\right] = -8.836$$

$$(1-\alpha)\left[(2.43)^{3/1-\alpha} - (2.75)^{3/1-\alpha}\right] = -6.655.$$

The value of α is thus obtained numerically by solving these ten equations with the condition that Q should be small and positive. A large and negative value of Q would mean that dark energy would dominate the expansion from the outset and galaxy formation would not have been possible at the desired epochs.

Due to the non-linear nature of the system of equations, an analytical solution is not possible and we proceed to obtain the value numerically. These ten set of the numerical value of α at different redshifts given in the Table: (2) as

4.2 For $Q = \sigma(\dot{\rho_m} + \dot{\rho_d})$

We can obtain the value of σ in the same way from the normalized Hubble's parameter.Using (27) and (28) in (29), we obtain:

$$E^2(x) = \frac{8\pi G}{3H_0^2}\left(\rho_m^0\left(\frac{a_0}{a}\right)^{3(1+\sigma)} + \rho_d^0 + \frac{\sigma}{(1+\sigma)}\rho_m\left[1 - \left(\frac{a_0}{a}\right)^{3(1+\sigma)}\right]\right) \tag{36}$$

$$E^2(x) = \frac{8\pi G}{3H_0^2}\left(\frac{\sigma}{(1+\sigma)}\rho_m^0 + \rho_d^0 + \frac{\rho_m^0}{(1+\sigma)}\left(\frac{a_0}{a}\right)^{3(1+\sigma)}\right) \tag{37}$$

Using the definition of critical density and $x = 1 + z = a_0/a$

$$E^2(x) = \frac{\sigma}{(1+\sigma)}\Omega_m^0 + \Omega_d^0 + \frac{\Omega_m^0}{(1+\sigma)}x^{3(1+\sigma)} \tag{38}$$

$\Delta E^2(x_i, x_j)$	α
−1.221	0.60358
−4.396	0.296232
−5.074	0.243187
−7.144	0.158064
−3.175	0.225743
−3.853	0.172485
−5.923	0.107703
−0.678	0.00838725
−2.748	0.00838725
−2.069	0.0109265

Table 2: Value of coupling parameter α for interaction strength $Q = \alpha\dot{\rho_m}$ for ten sets of difference of squared normalized Hubble parameter given by (34).

$$\Delta E^2(x_i, x_j) = \frac{\Omega_m^0}{(1+\sigma)}\left[x_i^{3(1+\sigma)} - x_j^{3(1+\sigma)}\right] \tag{39}$$

Using the same high red-shift values, density parameters, and Hubble's constant at the same epochs as in the previous section, we obtain the set of solutions for the proportionality constant σ.

$$\frac{1}{(1+\sigma)}\left[(1.88)^{3(1+\sigma)} - (1.9)^{3(1+\sigma)}\right] = -3.926$$

$$\frac{1}{(1+\sigma)}\left[(1.88)^{3(1+\sigma)} - (2.3)^{3(1+\sigma)}\right] = -14.135$$

$$\frac{1}{(1+\sigma)}\left[(1.88)^{3/(1+\sigma)} - (2.43)^{3(1+\sigma)}\right] = -16.316$$

$$\frac{1}{(1+\sigma)}\left[(1.88)^{3(1+\sigma)} - (2.75)^{3(1+\sigma)}\right] = -22.971$$

$$\frac{1}{(1+\sigma)}\left[(1.9)^{3(1+\sigma)} - (2.3)^{3(1+\sigma)}\right] = -10.209$$

$$\frac{1}{(1+\sigma)}\left[(1.9)^{3(1+\sigma)} - (2.43)^{3(1+\sigma)}\right] = -12.390$$

$$\frac{1}{(1+\sigma)}\left[(1.9)^{3(1+\sigma)} - (2.75)^{3(1+\sigma)}\right] = -19.045$$

$$\frac{1}{(1+\sigma)}\left[(2.3)^{3(1+\sigma)} - (2.43)^{3(1+\sigma)}\right] = -2.181$$

$$\frac{1}{(1+\sigma)}\left[(2.3)^{3(1+\sigma)} - (2.75)^{3(1+\sigma)}\right] = -8.836$$

$$\frac{1}{(1+\sigma)}\left[(2.43)^{3(1+\sigma)} - (2.75)^{3(1+\sigma)}\right] = -6.655$$

The value of the proportionality constant σ is thus obtained numerically, having Q small and positive.

Using the condition that the coupling parameter must be small and positive, the smallest positive root of the set of equations near $\sigma = 0$ as the initial estimate, we obtain the values of σ from Table 3.

$\Delta E^2(x_i, x_j)$	σ
−1.221	1.52257
−4.396	0.420922
−5.074	0.321318
−7.144	0.187738
−3.175	0.291561
−3.853	0.214702
−5.923	0.120703
−0.678	−0.000160938
−2.748	0.00845819
−2.069	0.0110472

Table 3: Value of coupling parameter σ for interaction strength $Q = \sigma(\dot{\rho_m} + \dot{\rho_d})$ for ten sets of difference of squared normalized Hubble parameter given by (39).

It is observed that between the redshift epochs $z = 1.3$ and $z = 1.43$, assuming the initial estimate of $\sigma = 0$, the value of the proportionality constant σ becomes negative. This suggests a brief reversal in the direction of energy flow between the two interacting components—matter and dark energy. Specifically, energy appears to flow from matter to dark energy during this interval, indicating a slight dominance of dark energy. However, since σ remains of the order 10^{-4}, the effect is relatively small. For epochs earlier than $z = 1.3$ up to $z = 1.43$, σ remains positive, implying that energy was predominantly flowing from dark energy to matter during that period. The brief sign change of σ highlights a transitional phase in the interaction dynamics between dark energy and matter.

5 Determination of Age of Universe

We determine the age of the universe by considering two distinct phases: the non-interacting and interacting epochs.

From $z = \infty$ down to $z = 1.75$, the components of the universe (i.e. matter, dark energy and radiation) evolved independently, with no mutual interaction. During this phase, radiation contributed only a small fraction to the total energy density, with a critical density of the order $\Omega_r^0 \sim 10^{-5}$.

From $z = 1.75$ to the present epoch ($z = 0$), interactions between dark energy and dust matter begin to play a significant role, while the contribution from radiation becomes negligible. This marks the transition to the matter–dark energy dominated era, relevant for late-time cosmic evolution.

To determine the age,

$$t(z) = \int_z^\infty \frac{1}{(1+z)H(z)} dz \tag{40}$$

5.1 For $Q = \alpha\dot{\rho_m}$

During interaction, using (21),

$$H(z)^2 = \frac{8\pi G}{3}\left(\rho_m^0\left(\frac{a}{a_0}\right)^{-\frac{3}{1-\alpha}} + \rho_d^0 - \alpha\rho_m^0\left[\left(\frac{a_0}{a}\right)^{\frac{3}{1-\alpha}} - 1\right]\right) \tag{41}$$

$$H(z)^2 = H_0^2\left(\Omega_m^0(1+z)^{\frac{3}{1-\alpha}}[1-\alpha] + \Omega_d^0 + \alpha\Omega_m^0\right) \tag{42}$$

During the non-interacting epochs, taking the contribution of radiation into account as well (with the equation of state parameter $\omega_r = 1/3$), from the energy conservation relation with $\alpha = 0$,

$$H(z)^2 = H_0^2\left(\Omega_m^0(1+z)^3 + \Omega_d^0 + \Omega_r^0(1+z)^4\right) \tag{43}$$

To determine the age of the universe (AoU) by taking both interacting and non-interacting phases, we have from (40),

$$t(z) = \int_0^z \frac{1}{(1+z)H(z)}dz + \int_z^\infty \frac{1}{(1+z)H(z)}dz \tag{44}$$

Using (42) and (43),

$$t(z) = \frac{1}{H_0}\Bigg[\int_0^z \frac{1}{(1+z)\left(\Omega_m^0(1+z)^{\frac{3}{1-\alpha}}[1-\alpha] + \Omega_d^0 + \alpha\Omega_m^0\right)^{1/2}}dz + \int_z^\infty \frac{1}{(1+z)\left(\Omega_m^0(1+z)^3 + \Omega_d^0 + \Omega_r^0(1+z)^4\right)^{1/2}}dz\Bigg] \tag{45}$$

At $z = 1.75$, with $\Omega_m^0 = 0.311$, $\Omega_d^0 = 0.689$, and $\Omega_r^0 \sim 10^{-5}$,
For the values of α, the AoU is determined in terms of H_0 as :

α	AoU in terms of H_0^{-1}
0.60358	0.723212
0.296232	0.881907
0.243187	0.898824
0.158064	0.921835
0.225743	0.903926
0.172485	0.918254
0.107703	0.933457
0.000193815	0.954346
0.00838725	0.952916
0.0109265	0.952469

Table 4: Age of the Universe in terms of H_0^{-1} for the ten values of coupling parameter α.

Thus considering both the phases, interacting and non-interacting, with the corresponding values of α, the AoU is consistent with $t \sim H_0^{-1}$. The result however indicates two conclusions: The smaller the values of the proportionality constant α for the interaction term Q, the more consistent the AoU with the observed data, and these small values of α tend to occur at large red-shift epochs. The value of α is expected to be very small as well, in order for structure formation to occur. With the smallest value of the proportionality constant, $\alpha = 1.93815\times10^{-4}$, we have the AoU $t \approx 0.954346H_0^{-1} \approx 13.803$ Gyr, which is consistent with recent Planck 2018 data, 13.830 ± 0.037 Gyr.

5.2 For $Q = \sigma(\dot{\rho_m} + \dot{\rho_d})$

During interaction, using (27) and (28),

$$H(z)^2 = \frac{8\pi G}{3}\left(\rho_m^0\left(\frac{a_0}{a}\right)^{3(1+\sigma)} + \rho_d^0 + \frac{\sigma}{(1+\sigma)}\rho_m\left[1 - \left(\frac{a_0}{a}\right)^{3(1+\sigma)}\right]\right) \tag{46}$$

$$H(z)^2 = H_0^2\left(\frac{\Omega_m^0}{(1+\sigma)}\left[(1+z)^{3(1+\sigma)}+\sigma\right]+\Omega_d^0\right) \tag{47}$$

During the non-interacting epochs, with $\sigma = 0$,using (47) and (43) in (44),

$$t(z) = \frac{1}{H_0}\left[\int_0^z \frac{1}{(1+z)\left(\frac{\Omega_m^0}{(1+\sigma)}\left[(1+z)^{3(1+\sigma)}+\sigma\right]+\Omega_d^0\right)^{1/2}}dz + \int_z^\infty \frac{1}{(1+z)\left(\Omega_m^0(1+z)^3+\Omega_d^0+\Omega_r^0(1+z)^4\right)^{1/2}}dz\right] \tag{48}$$

At $z = 1.75$, with $\Omega_m^0 = 0.311$, $\Omega_d^0 = 0.689$, and $\Omega_r^0 \sim 10^{-5}$, for the values of σ, the AoU is determined in terms of H_0 as :

σ	AoU in terms of H_0^{-1}
1.52257	0.723213
0.420922	0.881907
0.321318	0.898826
0.187738	0.921836
0.291561	0.903926
0.214702	0.917170
0.120703	0.933457
−0.000160938	0.954407
0.00845819	0.952916
0.0110472	0.952469

Table 5: Age of the Universe in terms of H_0^{-1} for the ten values of coupling parameter σ.

Under both the phases, interacting and non-interacting, using the values of σ the AoU is again consistent with $t \sim H_0^{-1}$. In the results we observe a significant reversal in the proportionality constant σ for the interaction term Q, indicating a reversal in the direction of energy flow. The value of σ is however small, indicating a slight dominance of dark energy over the matter during those epochs. Taking the smallest value of the proportionality constant, $\sigma = -1.60938 \times 10^{-4}$, we have the AoU $t \approx 0.954407 H_0^{-1} \approx 13.803$ Gyr, which is again consistent with the observational data.

6 Conclusion

The energy-momentum tensor of the canonical scalar field could be considered as the sum of two components and thus the energy and pressure can be segregated into two components. Both components belong to the dark sector and one of them behave as pressure-less with non-zero energy density said to be dust-like dark matter and the second component becomes exotic said to be a mimic of cosmological constant having $P_d = -\rho_d$ with EoS $w_d \sim w_\Lambda = -1$.

We consider these two components of the dark sector to arise from a single scalar field that is mutually interacting and transfers energy between them. During the interaction, the conservation of energy is violated locally while the global conservation of energy is still intact. In the absence

of a fundamental theory of dark sector physics, we adopt the interacting coupling term purely phenomenologically, and three possible forms are given in section:(3) as $Q = \alpha\dot{\rho_m}$ and $Q = \sigma(\dot{\rho_m} + \dot{\rho_d})$. These two forms are taken as heuristically by the authors [36–38] in the interacting dark energy model. We obtain the coupling parameter numerically by using high and low-redshift $H(z)$ data with 2018-CMB PLANCK data [63]. In the model-(I) the coupling parameter $\alpha < 1$ and we obtain the age of the universe in $k = 0$ universe given in the table:(4). For $\alpha \approx 0.000193815$ we have the age of the universe as 13.803 Gyr which is consistent with observations. In the model-(II) the coupling parameter $\sigma < 1$, the age of the universe in $k = 0$ universe is given in the table:(5). For $\sigma \approx -0.000160938$ we have the age of the universe as 13.803 Gyr.

References

[1] A. G. Riess, et al.: *Astron. J.*, **116**, 1009(1998).

[2] S. Perlmutter, et al.: *Astrophys. J.*, **517**, 565(1999).

[3] C. Blake and K. Glazebrook: *Astrophys. J.*, **594**, 665(2003).

[4] H. Seo and D. J. Eisenstein, : *Astrophys. J.*, **598**, 720(2003).

[5] D. Spergel, et al.: *Astrophys. J.S.*, **148**, 175(2003).

[6] E. Komatsu, et al.: *Astrophys. J.S.*, **192**, 18(2011).

[7] M. Sami and A. Toporensky, *Mod. Phys. Lett. A*, **19**, 1509 (2004).

[8] C. Armendariz-Picon et al., *Phys. Rev. Lett.*, textbf85, 4438 (2000).

[9] J. Khoury and A. Weltman, *Phys. Rev. Lett.*, **93**, 171104 (2004).

[10] M. C. Bento et al., *Phys. Rev. D*, **66**, 043507 (2002).

[11] R. R. Caldwell, R. Dave and P. J. Steinhardt, *Phys. Rev. Lett.*, **80** (8), 1582(1998).

[12] A. R. Liddle and R. J. Scherrer, *Phys. Rev. D*, **59**, (2), 023509(1998).

[13] B. Ratra and P. J. Peebles, *Phys. Rev. D*, **37** (12), 3406(1998).

[14] T. Padmanabhan, *Phys. Rev. D*, **66**, 021301(2002).

[15] T. Padmanabhan and T. Roy Choudhury, *Phys. Rev. D*, **66** 081301(2002).

[16] J. S. Bagla, H. K. Jassal and T. Padmanabhan, *Phys. Rev. D*, **67** 063504(2003).

[17] D. Choudhury, D. Ghoshal, D. P. Jatkar and S. Panda, *Phys. Lett. B*, **544** 231(2002).

[18] G. W. Gibbons, *Phys. Lett. B*, **537** 1(2002).

[19] A. Feinstein, *Phys. Rev. D*, **66** 063511(2002).

[20] O. Sergijenko and B. Novosyadlyj, *Kinemat. Phys. Celest. Bodies*, **24** 259(2008).

[21] S K et al., *Astroparticle Physics*, **157**, 102926(2024).

[22] M.M. Verma and S. D. Pathak, *Astrophys Space Sci*, **350**, 381(2014).

[23] D. Rajeeb Kumar, S. D. Pathak, and V. K. Ojha, *CPC*, **47(5)**, 055102(2023).

[24] J. Kaur et al., *Nucl. Phys. B*, **1018**, 117010(2025)

[25] A. Diez-Tejedor and A. Feinstein, *Phys. Rev. D* **74**, 023530(2006).

[26] V. Mukhanov, A. Vikman, *JCAP* **0602**, 004(2006).

[27] S. Unnikrishnan, *Phys. Rev. D* **78**, 063007(2008).

[28] S. Unnikrishnan, V. Sahni, A. Toporensky, *JCAP* **1208**, 018(2012).

[29] S. Unnikrishnan, V. Sahni, *JCAP* **1310**, 063(2013).

[30] D. Wands, J. De-Santiago, Y. Wang, *Class. Quantum Gravity* **29**, 145017(2012). arXiv:1203.6776 [astro-ph.CO]

[31] V. Sahni, A. A. Sen, *Eur. Phys. J. C* **77**, 225(2017).

[32] E. S. Reich, *Nature*, **483**, 132(2012).

[33] R. M. Lutchyn, J. D. Sau and S. D. Sarma, *Phys. Rev. Lett.*, **105**, 077001(2010).

[34] W. Zimdahl and D. Pavon, *Phys. Lett. B*, **521**, 133(2011).

[35] A. Kundu, S. D. Pathak and V. K. Ojha, *Commun. Theor. Phys.*, **73**, 025402(2021).

[36] M. M. Verma and S. D. Pathak, *Int J Theor Phys*, **53**, 2370(2012).

[37] M. Shahalam et al., *Eur. Phys. J. C* , **75**, 395(2015).

[38] M. Shahalam et al., *Eur. Phys. J. C* , **77**, 686(2017).

[39] E. D. Valentino et al., *Phys. Rev. D* **101**, 063502(2020).

[40] W. Yang et al., *JCAP*, **09**, 019(2018).

[41] K. Akash et al.,*J. Phys.: Conf. Ser.*, **1531**, 012086(2020).

[42] V. K. Ojha, A. A. Rao and S. D. Pathak, Preprint: arXiv:2305.00277v1, https://doi.org/10.48550/arXiv.2305.00277.

[43] E. D. Valentino et al., *Phys. Dark Universe*, **30**, 100666(2020).

[44] R. Raushan and A. Singh, *Phys. Dark Universe*, **39**, 101152(2023).

[45] H. Mohseni Sadjadi and M. Alimohammadi, *Phys. Rev. D* **74**, 103007(2006).

[46] J. Väliviita, R. Maartens and E. Majerotto, *MNRAS*, **402**, 2355(2010).

[47] A. Joseph and R. Saha, *MNRAS*, **519**, 1809(2022).

[48] S. Wang and Y. Zhang, *Phys. Lett. B*, **669**, 201(2008).

[49] A. Paliathanasis, S. Pan and W. Yang, *IJMP D*, **28**, 1950161(2012).

[50] A. Bernui et al., arxiv preprint: arXiv:2301.06097v1.

[51] J . Kaur et al., *Astro. Phys.*, **157**, 102926(2024).

[52] M.B. Gavela et al., *JCAP*, **11**, 044(2010).

[53] M. Lucca, *Phys. Rev. D*, **104**, 083510(2021).

[54] M. Lucca and Deanna C. Hooper, *Phys. Rev. D*, **102**, 123502(2020).

[55] J. Kaur et al., *Universe*, **11**, 131(2025).

[56] L. P. Chimento, *Phys. Rev. D*, **81**, 043525(2010).

[57] J. H. He, B. Wang and P. Zhang, *Phys. Rev. D*, **80**, 063530(2009).

[58] B. Wang, Y. G. Gong and E. Abdalla, *Phys. Lett. B*, **624**, 141(2005).

[59] S. D. Campo, R. Herrera and D. Pavon, *Int. J. Mod. Phys. D* **20(4)**, 561(2011).

[60] K. R. Mishra et al., *Phys. Dark Universe*, **40**, 101211(2023).

[61] D. Stern et al., *JCAP*, **02**, 008(2010).

[62] J. Simon, L. Verde, and R. Jimenez, *Phys. Rev. D*, **71.12**, 123001(2005).

[63] A. Nabila et al.,*Astronomy & Astrophysics*, **641**, A6 (2020).

Angular Momentum Algebra under the framework of Generalized Uncertainty Principle

Gaurav Bhandari,[1] S. D. Pathak,[2] Manabendra Sharma,[3] and Anzhong Wang[4]

[1]*Department of Physics, Lovely Professional University, Phagwara, Punjab, 144411, India;*
E-mail: bhandarigaurav1408@gmail.com, gauravbhandari23@lpu.in.

[2]*Amity School of Applied Sciences, Amity University,*
Lucknow Campus, Lucknow, 226028, India.
Corresponding Author E-mail: sdpathak@lko.amity.edu

[3]*Centre for Theoretical Physics and Natural Philosophy,*
Nakhonsawan Studiorum for Advanced Studies,
Mahidol University, Nakhonsawan, 60130, Thailand;
E-mail: sharma.man@mahidol.ac.th.

[4]*GCAP-CASPER, Department of Physics,*
Baylor University, Waco, Texas 76798-7316, USA;
E-mail: AnzhongWang@baylor.edu

Abstract

The prediction of a minimal length scale by various quantum gravity candidates (such as string/M theory, Doubly Special Relativity, Loop Quantum Gravity, and others) has suggested modification of the Heisenberg Uncertainty Principle (HUP), resulting in the Generalized Uncertainty Principle (GUP). In this short review, we investigate the origins of the GUP and examine higher-order models, focusing on the linear plus quadratic form of the GUP. We extend the concept of minimal length to minimal angular resolution, which plays a crucial role in modifying angular momentum and its associated algebra. A comparison is made between the standard angular momentum commutator algebra and that modified by the GUP. Finally, we review its application in the hydrogen atom spectra and discuss future endeavors.

I. INTRODUCTION

General relativity (GR) is a well-established theory that has successfully explained many astrophysical phenomena and offers viable mathematical models of cosmology to determine the dynamics of the universe. At large scales gravity became predominant and thus GR serves as a viable framework at the classical level. In fact, the explanation of perihelion precession of mercury[1], deflection of light when passing through massive bodies[2], and gravitational redshift of light [3] are few epitomes of its grand success in last hundred years.

Despite its successes, particularly in describing objects like black holes, the theory appears incomplete when addressing the singularities of these objects [4–10]. GR also struggles to explain the spacetime singularity at the beginning of the universe. While the universe appears homogeneous and isotropic at large scales, minute fluctuations of order 10^{-5} are observed in CMB. These fluctuations necessitate the use of perturbative theory, where the zeroth order is the homogeneous and isotropic universe given by Friedmann-Lemaître-Robertson-Walker (FLRW) metric. In the perturbative approach, the background metric is treated classically, while the first-order correction term is quantized in linearized gravity theory [11–16].

This compels the incorporation of two fundamentally different, and yet incompatible, frameworks, quantum theory and general relativity (GR) into a coherent setting. There have been numerous attempts to develop a complete quantum theory of gravity, like String/M Theory (ST) [17–23], Loop Quantum Gravity (LQG) [24–29], and Doubly Special Relativity (DSR) [30, 31], each with its advantages and issues. One of the commonest issues amongst the quantum gravity candidates is the recovery of the lower energy regime. While these theories have made significant progress, they lack experimental evidence and yet to undergo rigorous phenomenological testing. Even if supersymmetry is observed in the Large Hadron Collider (LHC), it would only confirm the existence of an essential ingredient of string theory and would not constitute definitive evidence in favor of the theory itself [32–35]. At Planck scales, the search for a theory of quantum gravity becomes crucial, as it may address the limitations of GR. With the existence of so many approaches to QG, it is crucial to focus on extracting predictions that can be tested experimentally. Recently, many attempts have been made in this direction. However, despite some success in computing quantum gravity corrections, the extremely small Planck length and the exceedingly large Planck energy typically suppress these effects, making them difficult to observe.

In this series of endeavors, one of the simplest and potentially testable approaches to quantum gravity (QG) is the Generalized Uncertainty Principle (GUP), which incorporates the minimal length prediction of many other QG theories in the well-known Heisenberg Uncertainty Principle (HUP). According to HUP, two canonically conjugate variables position and momentum, we can achieve arbitrary precision in position measurement by giving a maximal amount of energy or when momentum is unknown. However, many QG theories predict that this arbitrary precision is not valid below the Planck length, where the classical notion of space-time no longer applies [36–52]. On considering this fact HUP can be modified by incorporating additional terms on the right-hand side of the Heisenberg uncertainty relation giving rise to GUP. Accounting for quantum fluctuations in spacetime leads to the theory of the GUP, where these fluctuations in the geometry of spacetime increase the uncertainty in measuring both position and momentum. Since the GUP modifications exist in canonically conjugate variables, most quantum gravity (QG) theories predict momentum-dependent changes to the position-momentum commutation relation. These modifications in the existing commutator brackets and the HUP affect well-known aspects of quantum mechanics, as demonstrated by [53–56]. This leads to alterations in the HUP and suggests the existence of a minimum measurable length near the Planck scale [60–62].

Studies of the GUP have revealed changes in several aspects of Quantum Mechanics (QM). For instance, the Hamiltonian describing a minimal coupling with an electromagnetic field is expected to undergo modifications, as demonstrated in [53]. This has been used to show changes in the Landau levels [53]. Additionally, the GUP is found to affect phenomena such as the Lamb shift, potential steps and barriers, which are relevant in quantum configurations like Scanning Tunnelling Microscopes [54, 55], as well as the case of a particle in a box, where the box's length becomes quantized [54–56]. Moreover, the energy levels of a simple harmonic oscillator are also altered [54]. It has been suggested that the GUP could be detected through its effects on quantum optical systems [57–59].

In this paper, we discuss GUP corrections to a significant theoretical and experimental area of quantum mechanics mainly in the line of he seminal work in [79]. Specifically, we examine how GUP leads to modifications in the angular momentum algebra. This article is organized as follows: In Sec. II, we introduce the origin of GUP and explain how to find the modified canonical variables. In Sec. III, we discuss the modifications arising from different models of GUPs to teh angular momentum algebra. Finally, in Sec. IV, we extend the

application of the modified angular momentum algebra to the hydrogen atom and observe the resulting modifications to the energy levels.

II. ORIGIN OF GENERALIZED UNCERTAINTY PRINCIPLE

Many theories of QG predict the existence of a minimal length. In string theory, it is conjectured that strings do not interact at distances smaller than their size, which is determined by their tension [63, 64]. Essentially, particles are considered as vibration of strings with fundamental lengths close to the Planck length. Various *gedanken* experiments involving black holes also suggest the existence of a minimal length. LQG inherently includes a minimal length through its discrete area and volume elements. Similarly, the DSR theory, a modification of the Special Theory of Relativity, incorporates minimal length scales and maximum measurable momentum.

The GUP represents an innovative approach in the quest for a quantum gravity theory. It involves modifications to the well-known HUP. The HUP, in its traditional form, does not accommodate the concept of a minimal length, as it allows for arbitrary values of uncertainty in position. The GUP addresses this by proposing modifications to the HUP, incorporating higher-order corrections inspired by various QG theories.

In 1995, Kempf, Mangano and Mann (KMM) proposed the generalized uncertainty relation that results in minimal measurable length [65–67] as

$$\Delta X \Delta P \geq \frac{\hbar}{2}(1 + \beta(\Delta P)^2 + \Omega), \tag{1}$$

where β is the GUP parameter and $\Omega = \beta\langle P\rangle^2$ which is a positive constant depending on the expectation value of the momentum operator. We also define $\beta = \beta_0/(M_{Pl}c)^2$ where β_0 is of the order of unity and M_{Pl} is the Planck mass. One can easily obtained the minimal observable length as $(\Delta X)^{KMM}_{min} = \hbar\sqrt{\beta}$. The above uncertainty relation is obtained in one dimension by the deformed commutator bracket

$$[X, P] = i\hbar(1 + \beta P^2). \tag{2}$$

As shown by KMM in their seminal work [65–67], the following operator equations, for X

and P can be immediately obtained from commutator algebra Eq.(2) as

$$P\phi(p) = p\phi(p), \tag{3}$$

$$X\phi(p) = i\hbar(1+\beta p^2)\partial_p\phi(p), \tag{4}$$

where X and P be symmetric operators defined on a dense domain S_∞ (Schwartz space), with respect to the scalar product

$$\langle\psi|\phi\rangle = \int_{-\infty}^{\infty} \frac{dp}{1+\beta p^2}\psi^*(p)\phi(p), \tag{5}$$

where the relation $\int_{-\infty}^{\infty} \frac{dp}{1+\beta p^2}|p\rangle\langle p| = 1$ holds, and $\langle p|p'\rangle = (1+\beta p^2)\delta(p-p')$. Given this scalar product definition, the commutation relation in Eq. (2) is exactly satisfied. Specifically, the generalized version of the HUP shown in Eq.(1) is considered to represent only the leading term in an expansion involving the small parameter $\sqrt{\beta}\Delta P$ of a higher-order GUP. Several efforts have been made to develop a complete version of the KMM GUP valid at all energy scales.

Based on the field theory on non-anticommutative superspace, Nouicer first proposed a more generalized form of GUP that broadens the validity domain of the KMM GUP. The deformed commutator bracket [68] is

$$[X, P] = i\hbar\exp\big(\beta P^2\big), \tag{6}$$

and from the Schrödinger-Robertson uncertainty relation between two operators gives

$$\Delta X\Delta P \geq \frac{\hbar}{2}\exp\big(\beta\Delta P^2\big). \tag{7}$$

In momentum space representation, this algebra is satisfied as

$$P\phi(p) = p\phi(p), \tag{8}$$

$$X\phi(p) = i\hbar\exp\big(\beta p^2\big)\partial_p\phi(p), \tag{9}$$

now using the symmetricity condition of position operator implies the modified scalar product as

$$\langle\psi|\phi\rangle = \int_{-\infty}^{\infty} \frac{dp}{\exp}(\beta p^2)\psi^*(p)\phi(p), \tag{10}$$

$$\langle p|p'\rangle = \exp\big(\beta p^2\big)\delta(p-p'). \tag{11}$$

This GUP gives the minimum uncertainty in the position as $(\Delta X)_{min}^{Nouicer} = \sqrt{\frac{e}{2}}\hbar\sqrt{\beta}$. Later this GUP was again modified to incorporate minimum uncertainty in position as well as maximum momentum as proposed by Pedram [69] as

$$[X, P] = \frac{i\hbar}{1 - \beta P^2}, \tag{12}$$

this commutator relation agrees with KMM's and Nouicer's GUP to the leading orders and contains singularity at $p^2 = 1/\beta$. This indicates that the momentum of the particle cannot exceed $\frac{1}{\sqrt{\beta}} \approx \frac{1}{\alpha}$. And, this gives the uncertainty relation as

$$\Delta X \Delta P \geq \frac{\hbar/2}{1 - \beta(\Delta P)^2}. \tag{13}$$

The position and momentum operators in the momentum representation for Pedram GUP Eq.(12) are

$$P\phi(p) = p\phi(p), \tag{14}$$

$$X\phi(p) = \frac{i\hbar}{1 - \beta p^2}\partial_p\phi(p), \tag{15}$$

and using the symmetricity condition the modified scalar product as

$$\langle\psi|\phi\rangle = \int_{-1/\sqrt{\beta}}^{1/\sqrt{\beta}} dp \exp\left(-\beta p^2\right)\psi^*(p)\phi(p), \tag{16}$$

$$\langle p|p'\rangle = \frac{\delta(p - p')}{1 - \beta p^2}. \tag{17}$$

A concise comparison of the different forms of GUPs, as discussed above, is more effectively presented in tabular form in **Table I**, along with comparative plots against the HUP shown in **Fig. 1**. We also note that the minimal length $(\Delta X)_{min}^{KMM} < (\Delta X)_{min}^{Nouicer} < (\Delta X)_{min}^{Pedram}$ shown in **Table II**.

In 2011, Ali, Das, and Vagenas proposed [55] a generalized model incorporating quadratic terms of momenta as dictated by ST and various *Gedanken experimente* in black hole physics, and linear terms suggested by DSR as in [70–76]. The GUP deformed commutator bracket is expressed as:

$$[q_i, p_j] = i\hbar\left\{\delta_{ij} - \alpha\left(p\delta_{ij} + \frac{p_i p_j}{p}\right) + \alpha^2[p^2\delta_{ij} + 3p_i p_j]\right\}, \tag{18}$$

TABLE I: Comparison of different GUP models.

GUP Model	**Deformed Commutator**	**Minimal Length Uncertainty**	**Maximal Observable Momentum**
HUP	$[X,P]=i\hbar$	✗	✗
KMM	$[X,P]=i\hbar(1+\beta P^2)$	✓	✗
Nouicer	$[X,P]=i\hbar\exp(\beta P^2)$	✓	✗
Pedram	$[X,P]=\frac{i\hbar}{1-\beta P^2}$	✓	✓

TABLE II: Minimal measurable length and maximal momenta in three GUP models.

GUP Framework	Minimal length $(\Delta X)_{min}$	Maximal momentumP_{max}
KMM	$\hbar\sqrt{\beta}$	—
Nouicer	$\hbar\sqrt{\beta}\sqrt{\frac{e}{2}}$	—
Pedram	$\frac{3\sqrt{3}}{4}\hbar\sqrt{\beta}$	$\frac{1}{\sqrt{\beta}}$

where $\alpha=\alpha_0/M_{Pl}c=\alpha_0 l_{Pl}/\hbar$, $M_{Pl}=$ Planck mass, $l_{Pl}\approx 10^{-35}m=$ Planck length, and $M_{Pl}c^2\approx 10^{19}GeV=$ Planck energy. This form of GUP gives:

$$\Delta x\geq(\Delta x)_{\min}\approx\alpha_0 l_{\mathrm{Pl}} \tag{19}$$

$$\Delta p\leq(\Delta p)_{\max}\approx\frac{M_{\mathrm{Pl}}c}{\alpha_0}. \tag{20}$$

Now we can express the modified momentum p_i in terms of low energy momentum term p_{0i}, since Eq.(18) contains quadratic momentum p_i, the latter must contain at most cubic terms of p_{0i}. So the most general form consistent with the structure is:

$$p_j=p_{0j}+ap_0p_{0j}+bp_0^2p_{0j}, \tag{21}$$

where $\alpha\sim a$, $b\sim a^2$. Now using Eq.(18)

$$[x_i,p_j]=[x_i,p_{0j}]+a([x_i,p_0]p_{0j}+p_0[x_i,p_0j])+b([x_i,p_0]p_0p_{oj}+p_0[x_i,p_0]p_{0j}+p_0^2[x_i,p_{0j}]), \tag{22}$$

the more general form of the commutator bracket of Eq.(18) incorporating linear and quadratic term is

$$[x_i,p_j]=i\hbar(\delta_{ij}+\delta_{ij}\alpha_1 p+\alpha_2\frac{p_ip_j}{p}+\beta_1\delta_{ij}p^2+\beta_2 p_ip_j), \tag{23}$$

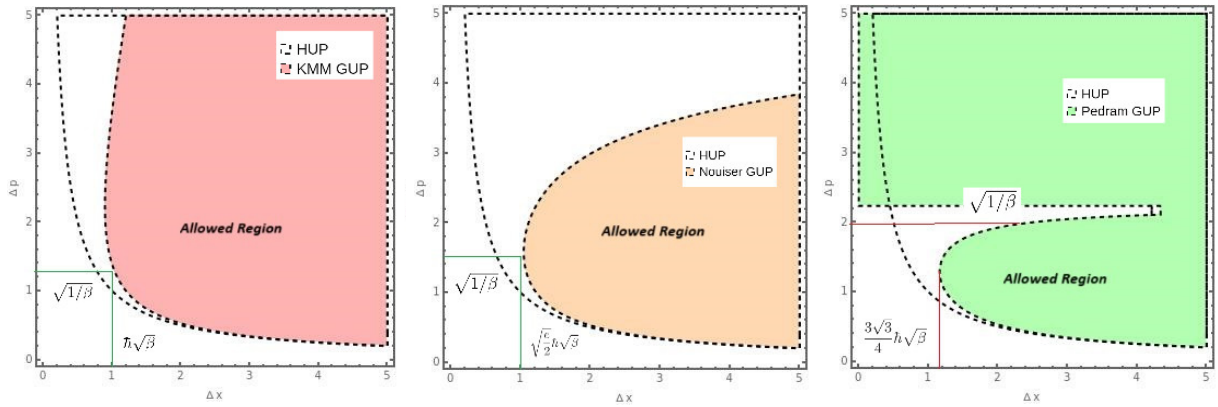

FIG. 1: In this plot, Figure (a) on the left shows a comparison between HUP and KMM GUP, where the minimal length is given by $\hbar\sqrt{\beta}$. Figure (b) represents the comparison between Nouicer GUP and HUP, which again only includes minimal length but no maximal observable momentum. The final figure compares Pedram GUP with HUP, and we observe that in this GUP, both minimal length and maximal observable momentum are present.

using Eq.(23) we obtain

$$[x_i, p^2] = [x_i, p \cdot p] = [x_i, p]p + p[x_i, p] \tag{24}$$

$$= [x_i, p_k \cdot p_k] = [x_i, p_k]p_k + p_k[x_i, p_k]$$

$$= 2i\hbar p_i \left[1 + (\alpha_1 + \alpha_2)p\right] \quad \text{using Eq.(23) to } \mathcal{O}(p), \tag{25}$$

and on comparing Eq.(24) and Eq.(25) we get,

$$[x_i, p] = i\hbar(p_i p^{-1} + (\alpha_1 + \alpha_2)p_i) \tag{26}$$

and when $\alpha_i = 0$, we obtain

$$[x_i, p] = i\hbar p_{0i} p_0^{-1}, \tag{27}$$

we know

$$p_j = P_{0j}(1 + ap_0) + \mathcal{O}(a^2) \simeq P_{0j}(1 + ap) \quad \text{[from Eq.(21)]} \tag{28}$$

which gives

$$p_0 j \simeq \frac{p_j}{1 + ap} \simeq (1 - ap)p_j, \tag{29}$$

$$p_0 = (p_{0j} p_{0j})^{\frac{1}{2}} \tag{30}$$

$$= ((1 - ap)^2 p_j p_j)^{\frac{1}{2}} = (1 - ap)p, \tag{31}$$

we also obtain

$$p_{0i}p_0^{-1}p_{0j} = (1-ap)p_i(1-ap)^{-1}p^{-1}(1-ap)p_j = (1-ap)p_ip_jp^{-1}. \tag{32}$$

and, by assuming coordinates and momenta commutes among themselves, it follows the Jacobi identity:

$$[[x_i, x_j], p_k] + [[x_j, p_k], x_i] + [[p_k, x_i], x_j] = 0. \tag{33}$$

Now using Eq.(33),we obtain

$$[x_i, p_j] = i\hbar\delta_{ij} + i\hbar a(p\delta_{ij} + p_ip_jp^{-1}) + i\hbar(2b - a^2)p_ip_j + i\hbar(b - a^2)p^2\delta_{ij}, \tag{34}$$

comparing Eq.(34) with Eq.(18) gives $a = -\alpha$ and $b = 2a^2$. We obtain the deformed momentum and position in terms of low energy-momentum terms as:

$$x_i = x_{0i}, \quad p_i = p_{0i}(1 - \alpha p_0 + 2\alpha^2 p_0^2). \tag{35}$$

We extend the idea of minimal measurable length to minimal angular resolution by choosing the angular variable and its conjugate momentum (angular momentum). We expect modifications to the well-known angular momentum algebra as a consequence of GUP.

III. MODIFIED ANGULAR MOMENTUM ALGEBRA IN THE PRESENCE OF GUP

Angular momentum in classical and quantum mechanics plays an important role in understanding many physical phenomenons and their mathematical descriptions like the trajectory of planets and planetary systems (Kepler's law), rotation of rigid bodies, the structure of atoms, and many more. In this section, we start with the classical definition of angular momentum. In classical mechanics, angular momentum measures the "amount of rotation" likewise linear momentum which measures the "amount of motion". In simple terms, for point particle, it is the cross product of position and momentum. Angular momentum also follows the law of conservation as motion is in the central field. The particle motion is restricted to the plane perpendicular to the angular momentum vector.

The classical description of the angular momentum $\vec{L}$ of a particle with mass m and linear momentum $\vec{p}$ located at position $\vec{r}$ is given by the vector cross product

$$\vec{L} = \vec{r} \times \vec{p}. \tag{36}$$

where the magnitude is given by $L = rp\sin\theta$ and θ is the angle between the vectors $\vec{r}$ and $\vec{p}$. The components in the Cartesian coordinate system are

$$L_x = yp_z - zp_y, \quad L_y = zp_x - xp_z, \quad L_z = xp_y - yp_x. \tag{37}$$

In quantum mechanics, physical quantities such as angular momentum are represented by operators acting on the wave function of a system, rather than continuous variables. The classical quantities of position and momentum are promoted to operators as we go into the quantum regime. The standard position operator $\hat{r}$ and the momentum operator $\hat{p}$ in one dimension are

$$r \equiv \hat{r} \equiv \hat{q}, \quad p \equiv \hat{p} \equiv -i\hbar\frac{d}{dq}. \tag{38}$$

To incorporate the minimal length effect, the usual position and momentum variables get modified showing a non-commutative geometry. Among the various GUP models that incorporate the minimal length effects predicted by different quantum gravity theories, we adopt in this section a generalized modification through a momentum-dependent function $\mathcal{G}(\beta p)$. The specific form of this function is model-dependent and can represent different versions of GUPs. The different forms of this function are

$$\mathcal{G}(\beta p) = \begin{cases} 1 + \beta p^2, \\ \exp(\beta p^2), \\ \frac{1}{1-\beta p^2}, \\ \delta_{ij} - \alpha\left(p\delta_{ij} + \frac{p_i p_j}{p}\right) + \alpha^2\left(p^2\delta_{ij} + 3p_i p_j\right), \end{cases} \tag{39}$$

In this section, we study how the effects of the minimal measurable length, where the modified commutator relation between position and momentum alters the standard quantum mechanics of angular momentum and its commutator relations. The modified commutator relation incorporate the minimal measurable length is given by

$$[q_i, p_i] = i\hbar\mathcal{G}(\beta p). \tag{40}$$

In the low-energy limit, where quantum gravitational effects can be neglected, we take $\beta \to 0$, which leads to $\mathcal{G}(\beta p) \approx 1$, thereby recovering standard quantum mechanics. Specifically, we focus on a more generalized form of GUP, incorporating the linear as well as the quadratic corrections. We choose the coordinates to remain invariant, and only the momentum variable is modified [77–79] as follows:

$$q_i = q_{0,i} \quad p_i = p_{0,i}[1 - k_1 p_0 + (k_2 + k_1^2)p_0^2]]. \tag{41}$$

The modified commutator relation capturing the linear and quadratic momentum dependence form of GUP is given as

$$[q_i, p_j] = i\hbar\left\{\delta_{ij} - \gamma k_1\left(p\delta_{ij} + \frac{p_i p_j}{p}\right) + \gamma^2[k_2 p^2\delta_{ij} + (2k_2 + k_1^2)p_i p_j]\right\} \tag{42}$$

where γ is related to the scales at which the quantum-gravitational effect became relevant, and is defined as the inverse of the Planck momentum $\gamma = \frac{\gamma_0}{M_{Pl}c}$ with $\gamma_0 \sim 1$, the dimensionless parameters k_1 and k_2 are introduced to explicitly distinguish the contributions arising from the linear and quadratic terms in the GUP framework. In the one dimensional case, setting $k_1 = 0$ and $k_2 = \frac{1}{3}$ reproduces the well-known Kempf-Mangano-Mann (KMM) form of the GUP, as presented in Eq. (2). The motivation for choosing this type of GUP, which includes multiple free parameters, lies in the flexibility it provides. By adjusting these parameters, we can explore and analyze various forms of the GUP. The GUP between position and momentum introduces a minimal measurable length. Similarly, if we apply GUP to angular momentum algebra, it leads to the concept of a minimal measurable angle. We expect GUP in the angular variables and their canonical angular momentum. To see this, we use the GUP-modified commutator relation of Eq.(40), which changes the commutator relation between the components of angular momentum as

$$\begin{aligned}
[L_i, L_j] &= \epsilon_{imn}\epsilon_{jrs}[q_m p_n, q_r p_s] \\
&= \epsilon_{imn}\epsilon_{jrs}\{q_m[p_n, q_r]p_s + q_r[q_m, p_s]p_n\} \\
&= i\hbar\epsilon_{imn}\epsilon_{jrs}\{q_r p_n\mathcal{G}(\beta p) - q_m p_s\mathcal{G}(\beta p)\} \\
&= i\hbar(\epsilon_{mni}\epsilon_{mjr}q_r p_n - \epsilon_{nim}\epsilon_{nsj}q_m p_s)\mathcal{G}(\beta p) \\
&= i\hbar\epsilon_{ijk}L_k\mathcal{G}(\beta p),
\end{aligned} \tag{43}$$

for the form of GUP incorporating the linear as well as quadratic dependence of Eq.(18) is

written as

$$
\begin{aligned}
[L_i, L_j] &= \epsilon_{imn}\epsilon_{jrs}[q_m p_n, q_r p_s] \\
&= \epsilon_{imn}\epsilon_{jrs}\{q_m[p_n, q_r]p_s + q_r[q_m, p_s]p_n\} \\
&= i\hbar\epsilon_{imn}\epsilon_{jrs}\left\{q_r p_n\left[\delta_{ms} - \gamma k_1\left(p\delta_{ms} + \frac{p_m p_s}{p}\right) + \gamma^2[k_2 p^2\delta_{ij} + (2k_2 + k_1^2)p_m p_s]\right]\right. \\
&\quad \left. - q_m p_s\left[\delta_{nr} - \gamma k_1\left(p\delta_{nr} + \frac{p_n p_r}{p}\right) + \gamma^2[k_2 p^2\delta_{nr} + (2k_2 + k_1^2)p_n p_r]\right]\right\} \\
&= i\hbar(\epsilon_{mni}\epsilon_{mjr}q_r p_n - \epsilon_{nim}\epsilon_{nsj}q_m p_s)(1 - k_1\gamma p + k_2\gamma^2 p^2) \\
&= i\hbar\epsilon_{ijk}L_k(1 - k_1\gamma p + k_2\gamma^2 p^2),
\end{aligned}
\tag{44}
$$

this results in the usual commutator bracket being modified with additional translational momentum terms. We also observe that angular momentum is now not only the generator of rotation but also of translation. As the GUP parameters $\gamma = 0$, we recover the original commutator algebra. The effects of GUP directly influence the angular momentum term by adding extra terms. We can expand the modified angular momentum in terms of the generators of rotation and translation through various form of GUPs, respectively, as

$$
\left\{\ L_k = L_{0,k}\mathcal{G}(\beta p)\ \right\} \quad \Rightarrow \quad
\begin{cases}
\mathcal{G}(\beta p) = 1 + \beta p^2, \\
\mathcal{G}(\beta p) = \exp\big(\beta p^2\big), \\
\mathcal{G}(\beta p) = \dfrac{1}{1 - \beta p^2}, \\
\mathcal{G}(\beta p) = \delta_{ij} - \alpha\left(p\delta_{ij} + \dfrac{p_i p_j}{p}\right) + \alpha^2[p^2\delta_{ij} + 3p_i p_j].
\end{cases}
$$

Additionally, one can verify that the Jacobi identity, an important property of the Lie algebra of angular momentum operators, using Eq.(43) as

$$
[L_i,[L_j,L_k]]+[L_j,[L_k,L_i]]+[L_k,[L_i,L_j]] = i\hbar\{\epsilon_{ijk}[L_i,L_i]+\epsilon_{ijk}[L_j,L_j]+\epsilon_{ijk}[L_k,L_k]\}\mathcal{G}(\beta p) = 0,
\tag{45}
$$

it means in the presence of GUP the Jacobi relation remains same. Furthermore, the eigenstates L^2 and L_z can be simultaneously defined when we consider the GUP modifications. This can be expressed as

$$
[L^2, L_j] = [L_i^2, L_j] + [L_j^2, L_j] + [L_k^2, L_j] = 0.
\tag{46}
$$

If we consider the commutator relation between the components of angular momentum and linear momentum, we obtain

$$\begin{aligned}[L_i, p_m] &= \epsilon_{ijk}[q_j p_k, p_m] = \epsilon_{ijk}[q_j, p_m]p_k \\ &= i\hbar\epsilon_{ijk}p_k\mathcal{G}(\beta p) \\ &= i\hbar\epsilon_{imk}p_k\mathcal{G}(\beta p),\end{aligned} \tag{47}$$

for the case of linear + quadratic form of GUP, we get

$$\begin{aligned}[L_i, p_m] &= \epsilon_{ijk}[q_j p_k, p_m] = \epsilon_{ijk}[q_j, p_m]p_k \\ &= i\hbar\epsilon_{ijk}p_k\left\{\delta_{jm} - \gamma k_1\left(p\delta_{jm} + \frac{p_j p_m}{p}\right) + \gamma^2[k_2 p^2\delta_{jm} + (2k_2 + k_1^2)p_j p_m]\right\} \\ &= i\hbar\epsilon_{imk}p_k(1 - \gamma k_1 p + k_2\gamma^2 p^2),\end{aligned} \tag{48}$$

we observe that the relation is modified by an extra term involving $\vec{p}$. The original results remain unchanged if we neglect the quantum gravitational parameters. From the above results, we can easily show that

$$\begin{aligned}[L_i, p^2] &= [L_i, p_i^2 + p_j^2 + p_k^2] = p_i[L_j, p_i] + [L_j, p_i]p_i + p_j[L_k, p_j] + [L_k, p_j]p_j \\ &= i\hbar\mathcal{G}(\beta p)[\epsilon_{jim}p_i p_m + \epsilon_{jim}p_m p_i + \epsilon_{kjn}p_j p_n + \epsilon_{kjn}p_n p_j] \\ &= 0,\end{aligned} \tag{49}$$

by the property of $\epsilon_{ijk}p_j p_k + \epsilon_{ijk}p_k p_j = 0$, and utilizing Eq.(42). The eigenstate of the component L_z commutes with p and p^2 following the standard QM theory. Consequently, we can define the simultaneous eigenstates for L^2, L_z, and p. Despite deformation of the commutator algebra induced by the GUP, the fundamental structure of quantum mechanics remains preserved. This indicates that while the algebraic relations are modified, the underlying symmetry structure, such as the form of the angular momentum algebra, remains formally intact when appropriate deformed variables are used. In this framework, it is not the representation that breaks but rather the generators and variables that get modified, leading to a consistent deformation of the algebra without altering its core Lie structure.

A. Ladder operators in the presence of Linear + quadratic form of GUP

In this subsection, we calculate the effects of the GUP-deformed algebra on the ladder operators. Using the standard procedure, it will follow the same structure as in the standard

theory, but the quantum numbers l and m are now not integers and include correction terms. As mentioned above, we can consider the simultaneous eigenstates of p, L_z, and L^2 as

$$L^2|pl'm\rangle = l'\hbar^2|pl'm\rangle, \quad L_z|pl'm\rangle = m\hbar|pl'm\rangle,$$

where l' denotes the eigenvalue of the deformed angular momentum. Using the Eq.(43), the component of angular momentum and ladder operator does not commute and gives

$$[L_z, L_\pm] = [L_z, L_x] \pm i[L_z, L_y] = \hbar(iL_y \pm L_x)(1 - \gamma k_1 p + k_2\gamma^2 p^2) = \pm\hbar L_\pm(1 - \zeta), \tag{50}$$

where ζ is the GUP corrected factor, $\zeta = k_1\gamma p - k_2\gamma^2 p^2$. The ladder operator commutes with the magnitude of angular momentum as

$$[L^2, L_\pm] = [L^2, L_x] \pm i[L^2, L_y] = 0, \tag{51}$$

this structure is consistent with the standard QM . With the help of GUP-modified commutator relation Eq.(43), we also obtain

$$[L_+, L_-] = [L_x + iL_y, L_x - iL_y] = -2i[L_x, L_y] = 2\hbar L_z(1 - \zeta). \tag{52}$$

It satisfies,

$$L_\pm L_\mp = L^2 - L_z^2 \pm \hbar L_z(1 - \zeta). \tag{53}$$

Now, using Eq.(50), Eq.(54) became:

$$L_z L_\pm|pl'm\rangle = L_\pm[L_z \pm (1 - \zeta)]|pl'm\rangle = \hbar[m \pm (1 - \zeta)]L_\pm|pl'm\rangle \tag{54}$$

and using Eq.(51), we get

$$L^2 L_\pm|pl'm\rangle = L_\pm L^2|pl'm\rangle = l'\hbar^2 L_\pm|pl'm\rangle, \tag{55}$$

and the norm of the state $L_\pm|pl'm\rangle$ is obtained as

$$||L_\pm|pl'm\rangle||^2 = \langle pl'm|L_\mp L_\pm|pl'm\rangle = \hbar^2[l' - m\{m \pm (1 - \gamma k_1 p + k_2\gamma^2 p^2)\}] \geq 0. \tag{56}$$

If we consider L^2 and L_z only, we obtain

$$||L_\pm|l'm\rangle||^2 = \langle l'm|L_\mp L_\pm|l'm\rangle = \hbar^2[l' - m\{m \pm (1 - \langle\zeta\rangle)\}] \geq 0, \tag{57}$$

the GUP modification appears as $\langle\zeta\rangle$, which is the expectation value of the corrections. The term $1 - \langle\zeta\rangle$ is a positive quantity. We also note from the eigenvalues of L^2 and L_z in Eq.

(53) that $\langle L^2\rangle \geq \langle L_z^2\rangle$, which requires $l' \geq m^2$. This implies that there is an upper and lower bound on m, denoted as m_+ and m_-, respectively. Additionally, from Eq. (57), we obtain

$$L_\pm|pl'm_\pm\rangle = 0 \implies l' = m_\pm[m_\pm \pm (1-\zeta)] \tag{58}$$

we can get $m_\pm$ from any starting value of m by multiplying u and v to L_+ and L_- respectively where $u, v \in \mathbb{N}$ as

$$m_+ = m + u(1-\zeta), \quad m_- = m - v(1-\zeta) \tag{59}$$

and on combining the above two relations, we achieve,

$$m_+ = m_- + (u+v)(1-\zeta) = m_- + n(1-\zeta) \tag{60}$$

where $n \in \mathbb{N}$. On taking the above equation and Eq.(58), one can obtain

$$m_+ = \frac{n}{2}(1-\zeta) = l(1-\zeta), \quad m_- = -\frac{n}{2}(1-\zeta) = -l(1-\zeta), \tag{61}$$

and also we get

$$l' = l(l+1)(1-\zeta)^2. \tag{62}$$

We noticed that usually, the magnetic quantum number m might not be an integer because the difference between two consecutive eigenvalues of L_z, m_1 and m_2 the difference is $(1-\zeta)$. Thus, we redefined it as

$$m \to m(1-\zeta) \tag{63}$$

Now, the new GUP-modified magnetic quantum number m has integer upper and lower bounds as

$$-l \leq m \leq l. \tag{64}$$

Next, the eigenvalues of L^2 and L_z for any given state are

$$L^2|plm\rangle = \hbar^2 l(l+1)(1-\zeta)^2|plm\rangle, \quad L_z|plm\rangle = \hbar(1-\zeta)|plm\rangle. \tag{65}$$

To show that the eigenvalues of L^2 and L_z are compatible with the uncertainty relation in Eq. (43), we first note that the expectation values of L_x and L_y in an eigenstate of L^2 and L_z are zero:

$$\langle L_x\rangle = \langle L_y\rangle = 0. \tag{66}$$

The variances of these components are given by:

$$(\Delta L_x)^2 = \langle L_x^2\rangle, \quad (\Delta L_y)^2 = \langle L_y^2\rangle. \tag{67}$$

Now, for the right-hand side of Eq. (65), the uncertainty relation between L_x and L_y is:

$$\Delta L_x \Delta L_y \geq \frac{|\langle [L_x, L_y] \rangle|}{2} = \frac{\hbar}{2}|\langle L_z \rangle (1 - \langle \zeta \rangle)| = \frac{\hbar^2}{2}|m|(1 - \langle \zeta \rangle)^2, \tag{68}$$

where we used the commutator $[L_x, L_y] = i\hbar L_z$ and the GUP correction factor $(1 - \langle \zeta \rangle)$. By the equivalence between L_x and L_y in an eigenstate of L_z, we insert Eq. (68) into the left-hand side of Eq. (65), yielding:

$$\langle L^2 \rangle = \hbar^2 l(l+1)(1 - \langle \zeta \rangle)^2 = \langle L_x^2 \rangle + \langle L_y^2 \rangle + \langle L_z^2 \rangle \geq \hbar^2 (m^2 + |m|)(1 - \langle \zeta \rangle)^2, \tag{69}$$

where the equality holds when $m = \pm l$. We observe that $\langle L_z^2 \rangle$ is bounded by $\langle L^2 \rangle$ due to the uncertainty in the other components, similar to standard quantum mechanics. Now, we will apply the results of the modified angular momentum and ladder operators to a physical system and examine how GUP modifications affect those systems [80–84].

IV. APPLICATION: MODIFIED HYDROGEN ATOM

From the sections above, we now know that by introducing a minimal angular resolution, the angular momentum algebra has changed significantly. To observe these effects, we can apply these corrections to different quantum systems. As we also know, angular momentum algebra plays an important role in understanding atomic systems. In this section, we study the modified energy levels and spectrum of hydrogen atoms based on the GUP-modified angular momentum algebra. We incorporate the effects of GUP directly into the Hamiltonian of the system.

The usual Hamiltonian for hydrogen atom for a central force with the potential energy $U(r) = \frac{e^2}{r}$ is given as

$$\mathcal{H}\psi(\vec{r}) = \left[\frac{p_r^2}{2m} + \frac{L^2}{2mr^2} - \frac{e^2}{r}\right]\psi(\vec{r}), \tag{70}$$

we have the radial momentum term p_r and the square of angular momentum which consists of both radial and angular parts. However, we include the GUP effects in terms of expected values *i.e.* $\langle \zeta \rangle = k_1 \gamma \langle p \rangle - k_2 \gamma \langle p^2 \rangle$ as

$$L^2|lm\rangle = \hbar^2 l(l+1)(1 - \langle \zeta \rangle)^2 |lm\rangle, \quad L_z|lm\rangle = \hbar m(1 - \langle \zeta \rangle)|lm\rangle, \quad \vec{p}|lm\rangle = \vec{p_0}(1 - \langle \zeta \rangle)|lm\rangle. \tag{71}$$

In this context, $\langle \zeta \rangle$ represents the average value of the GUP corrections. It is crucial to assume expectation values for observable physical quantities when considering Planck-scale

corrections. From Eq. (71), we observe that $\vec{L}$ is proportional to $\vec{L}_0$, and both L_i and L^2 commute with the Hamiltonian $\mathcal{H}$. Using this result, the GUP-modified radial part of the Schrödinger equation becomes

$$\left[\frac{p_{0,r}^2}{2m}(1-\langle\zeta\rangle)^2+\frac{\hbar^2 l(l+1)}{2mr^2}(1-\langle\zeta\rangle)^2-\frac{e^2}{r}\right]y_l(r)=Ey_l(r). \tag{72}$$

where E is the energy eigenvalue. The above Eq. (72) consists of two parts one is the unperturbed part without the GUP modification, expressed in terms of the unmodified momentum and angular momentum, and other is the perturbative part that includes the corrections. It can be written as:

$$\left[\frac{p_{0,r}^2}{2m}+\frac{\hbar^2 l(l+1)}{2mr^2}-\frac{e^2}{r}\right]y_l(r)+\left[\frac{p_{0,r}^2}{2m}+\frac{\hbar^2 l(l+1)}{2mr^2}\right]\{\langle\zeta\rangle^2-2\langle\zeta\rangle\}y_l(r)=Ey_l(r). \tag{73}$$

Here, the first term represents the low-energy part of the Hamiltonian without GUP corrections. Now on choosing the variables like,

$$\chi=\sqrt{\frac{-2mE}{\hbar^2}},\quad a=\frac{\hbar^2}{me^2},\quad \nu=\frac{1}{a\chi},\quad z=\frac{2\chi r}{1-\langle\zeta\rangle},\quad y_l(r)=z^{(l+1)}e^{-\frac{z}{2}}v(z) \tag{74}$$

and substituting these variables in Eq.(72) gives

$$\left[z\frac{d^2}{dz^2}+(2l+2-z)\frac{d}{dz}+\left(\frac{\nu}{1-\langle\zeta\rangle}-l-1\right)\right]=0. \tag{75}$$

On taking $\gamma=0$ the above equation changes to the well-known Laguerre equation. With the given condition as

$$n'=\frac{\nu}{1-\langle\zeta\rangle}-l-1\in\mathbb{N}. \tag{76}$$

On solving the Eq.(75) we obtain the associated Laguerre polynomial

$$L_{n'}^{(2l+1)}(z)=\sum_{i=0}^{n'}\frac{(-1)^i(n'+2l+1)!\,z^i}{(n'-i)!\,(2l+1+i)!\,i!}. \tag{77}$$

Then, the solution for the Schrodinger equation (72) for the radial part is

$$y_l(r)=z^{(l+1)}e^{-\frac{z}{2}}\sum_{i=0}^{n'}\frac{(-1)^i(n'+2l+1)!\,z^i}{(n'-i)!\,(2l+1+i)!\,i!}, \tag{78}$$

and the modified principal quantum number is

$$n=\nu=\frac{e^2}{\hbar}\sqrt{\frac{m}{-2E}}=(n'+l+1)(1-\langle\zeta\rangle)=n_0(1-\langle\zeta\rangle), \tag{79}$$

where n_0 is the principal quantum number. The GUP-deformed expression of the energy level of the hydrogen atom is

$$\begin{aligned} E_n &= -\frac{2\pi e^4}{h^2}\frac{m}{[(n'+l+1)(1-\langle\zeta\rangle)]^2} \\ &= -\frac{e^4}{h^2c^2}\frac{mc^2}{n^2} \\ &\approx E_n^{(0)}[1+2k_1\gamma\langle p_0\rangle+\gamma^2(3k_1^2\langle p_0\rangle^2-2k_2\langle p_0^2\rangle)], \end{aligned} \tag{80}$$

$E_n^{(0)}$ represents the energy for the corresponding energy level in the standard theory. With GUP corrections, the energy for the hydrogen atom now includes additional terms involving the expectation values of p_0 and p_0^2 in a $|n_0lm\rangle$ eigenstate. If we consider no GUP effects by setting $\gamma = 0$, we recover the original energy level expression. In standard QM, the energy emitted or absorbed during a transition between two energy levels is given by the energy difference between the two states. Thus, it is straightforward to determine the frequency and wavelength of the emitted or absorbed lines through the wavelength and differrence in energy level relation. It is also well known that the energy of the hydrogen atom is inversely proportional to the square of the principal quantum number. From this, we can also calculate the wavelength of the emitted photon when the atom transitions from energy level E_i to E_f as:

$$\frac{1}{\lambda} = \frac{|E_i - E_f|}{hc} = R_\infty \left| \frac{1}{n_{0,f}^2(1-\langle\zeta_f\rangle)^2} - \frac{1}{n_{0,i}^2(1-\langle\zeta_i\rangle)^2} \right|, \tag{81}$$

where R_∞ is the Rydberg constant. Equation (81) shows that the GUP-modified spectrum not only depends on the principal quantum number but also includes corrections involving the expectation values of the electron's momentum, as well as its angular momentum quantum numbers.

V. CONCLUSION

Quantum mechanics, as is well known, is based on the Heisenberg uncertainty relation. Many quantum gravity theories predict the need for modifications that incorporate the concept of a minimal length. With the development of various quantum gravity theories, identifying a distinct signature of quantum gravity remains a significant challenge, making experimental testing crucial for measuring Planck scale effects in low-energy quantum

systems.

In this review, we study the effects of the GUP on angular momentum algebra and how it modifies systems where angular momentum is required. We begin by reviewing the origin of the GUP and the higher-order GUP introduced by Nouicer and Pedram in Sec. II. We also discuss the deformed commutator bracket proposed by Ali, Das, and Vagenas, along with the derivation of the deformed canonical variables.

In this paper, we consider a momentum-dependent functional term, $\mathcal{G}(\beta p)$, which captures both minimal length corrections and higher-order modifications to the uncertainty principle. The function $\mathcal{G}(\beta p)$ is model-dependent and thus accommodates various formulations of the Generalized Uncertainty Principle (GUP). We focus specifically on the deformed commutator bracket containing linear and quadratic momentum terms and explore its implications for the angular momentum algebra. Our analysis reveals that the GUP-modified position–momentum commutation relation leads to corrections in the angular momentum algebra, introducing an additional term that reflects the GUP-induced deformation. A comparison between the standard angular momentum algebra and its GUP-deformed counterpart is presented in Table III.

In Sec. IV, we carry out the application of these modifications and examine how they affect the energy levels and energy spectrum of the hydrogen atom. We observe that the principal quantum number changes due to the modification, with additional terms representing the average values of p and p^2, which affect the energy levels of the hydrogen atom. We also note that the energy spectrum now includes corrections that account for the expected values of the electron's momentum and angular momentum quantum number.

Since higher-order GUPs will also follow the same algebra with additional higher-order terms, we expect the algebra to remain consistent for these higher-order GUPs also. With these modifications to the angular momentum algebra, new avenues for phenomenological testing and theories are opened, which can potentially be tested in the future in contexts such as the Zeeman effect, Stark effect, simple harmonic oscillator (SHO), and others. This modification to the angular momentum algebra provides an opportunity to tighten the upper bound of the GUP parameter as studied in [85] by considering systems with angular momentum like Hydrogen atom in our case. We leave this for our future endeavors.

TABLE III: Comparison of Standard Angular Momentum Algebra and GUP-Modified Algebra

Aspect	**Standard Angular Momentum**	**GUP-Modified Algebra**
Commutator Relations	$[L_i, L_j] = i\hbar\epsilon_{ijk}L_k$	$[L_i, L_j] = i\hbar\epsilon_{ijk}L_k(1 - k_1\gamma p + k_2\gamma^2 p^2)$
Jacobi Identity	$[L_i,[L_j,L_k]]+[L_j,[L_k,L_i]]+[L_k,[L_i,L_j]] = 0$	$[L_i,[L_j,L_k]]+[L_j,[L_k,L_i]]+[L_k,[L_i,L_j]] = 0$
Commutators with L^2	$[L^2, L_j] = 0$	$[L^2, L_j] = 0$
Commutators with Momentum	$[L_i, p_j] = i\hbar\epsilon_{ijk}p_k$	$[L_i, p_j] = i\hbar\epsilon_{ijk}p_k(1-\gamma k_1 p+ k_2\gamma^2 p^2)$
Commutators with p^2	$[L_i, p^2] = 0$	$[L_i, p^2] = 0$
Eigenstates of L^2 and L_z	Can be simultaneously defined	Can still be defined simultaneously
Commutator with L_z	$[L_z, L_\pm] = \pm\hbar L_\pm$	$[L_z, L_\pm] = \pm\hbar L_\pm(1 - \zeta)$
Norm of the State	$\|\|L_\pm\|l, m\rangle\|\|^2 \geq 0$	$\|\|L_\pm\|p, l', m\rangle\|\|^2 \geq 0$ with GUP corrections
Quantum Numbers	Integer values for l and m	Integer values but with bounds on m due to GUP

Authors' Contributions

Gaurav Bhandari: Writing - review & editing, Writing - original draft, Visualization, Resources, Formal analysis. S.D. Pathak: Validation, Supervision, Formal analysis, Conceptualization. Manabendra Sharma: Writing - review & editing, Validation, Supervision, Investigation, Formal analysis, Conceptualization. Anzhong Wang: Validation,Formal anal-

ysis.

Data Availability

The manuscript has no associated data or the data will not be deposited.

Conflicts of Interest

The authors declare that there is no conflict of interest.

Ethical Considerations

The authors have diligently addressed ethical concerns, such as informed consent, plagiarism, data fabrication, misconduct, falsification, double publication, redundancy, submission, and other related matters.

Funding

This research did not receive any grant from funding agencies in the public, commercial, or non-profit sectors.

Acknowledgment

Authors would like to thank Iran Science Elites Federation, Tehran, Iran.

---

[1] N. C. Rana, "An investigation of the motions of the node and perihelion of Mercury", *A & A*, **181**, 195(1987)

[2] Genov *et al.*, "Mimicking celestial mechanics in metamaterials", *Nat. Phys.*, **5**, 687(2009). DOI: 10.1038/nphys1338

[3] R. Wojtak, S. H. Hansen, J. Hjorth, "Gravitational redshift of galaxies in clusters as predicted by general relativity", *Nature*, **477**, 567(2011). DOI: 10.1038/nature10445

[4] J. D. Bekenstein, "Black holes and entropy", *Phys. Rev. D*, **7**, 2333 (1973). DOI: 10.1103/PhysRevD.7.2333

[5] S. W. Hawking, "Black hole explosions?", *Nature*, **248**, 30 (1974). DOI: 10.1038/248030a0

[6] S. W. Hawking, "Black holes and thermodynamics", *Phys. Rev. D*, **13**, 191 (1976). DOI: 10.1103/PhysRevD.13.191

[7] S. Chandrasekhar and K. S. Thorne, "The mathematical theory of black holes", *Am. J. Phys.*, **53**, 1013 (1985). DOI: 10.1119/1.13992

[8] J. Kormendy and D. Richstone, "Inward Bound—The Search For Supermassive Black Holes In Galactic Nuclei", *Ann. Rev. Astron. Astrophys.*, **33(1)**, 581 (1995). DOI: 10.1146/annurev.aa.33.090195.003053

[9] S. W. Hawking, "Particle Creation by Black Holes", *Commun. Math. Phys.*, **43**, 199 (1975) [Erratum-ibid. 46, 206 (1976)]. DOI: 10.1007/BF02345020

[10] W. G. Unruh, "Sonic analog of black holes and the effects of high frequencies on black hole evaporation", *Phys. Rev. D*, **51**, 2827 (1995). DOI: 10.1103/PhysRevD.51.2827

[11] A.H. Guth, S.Y. Pi, "Fluctuations in the new inflationary universe", *Phys. Rev. Lett.*, **49**, 1110(1982). DOI: 10.1103/PhysRevLett.49.1110

[12] A.D. Linde, "A new inflationary universe scenario: a possible solution of the horizon, flatness, homogeneity, isotropy and primordial monopole problems", *Phys. Lett. B*, **108**, 389(1982). DOI: 10.1016/0370-2693(82)91219-9

[13] J.M. Bardeen, P.J. Steinhardt, M.S. Turner, "Spontaneous creation of almost scale-free density perturbations in an inflationary universe", *Phys. Rev. D*, **28**, 679(1983). DOI: 10.1103/PhysRevD.28.679

[14] A. Ashtekar and M. Bojowald, "Quantum geometry and the Schwarzschild singularity", *Classical and Quantum Gravity*, **23**, 391 (2005). DOI: 10.1088/0264-9381/23/2/008

[15] A. Singh, H. K. Jassal and M. Sharma, "Perturbations in tachyon dark energy and their effect on matter clustering", *J. Cosmol. Astropart. Phys.*, **2020**, 8 (2020). DOI: 10.1088/1475-7516/2020/05/008

[16] A. Ashtekar, "Loop quantum cosmology: an overview", *Gen. Relativ. Gravit.*, **41**, 707(2009). DOI: 10.1007/s10714-009-0763-4

[17] G. Veneziano, "A stringy nature needs just two constants", *Europhys. Lett.*, **2**, 199 (1986). DOI: 10.1209/0295-5075/2/3/006

[18] E. Witten, "Reflections on the fate of spacetime", *Phys. Today*, **49**, 24 (1996). DOI: 10.1063/1.881493

[19] F. Scardigli, "Generalized uncertainty principle in quantum gravity from micro-black hole gedanken experiment", *Phys. Lett. B*, **452**, 39(1999). DOI: 10.1016/S0370-2693(99)00167-7

[20] D. J. Gross, P. F. Mende, "String theory beyond the Planck scale", *Nucl. Phys. B.*, **303**, 407(1988). DOI: 10.1016/0550-3213(88)90390-2

[21] D. Amati, M. Ciafaloni, G. Veneziano, "Can spacetime be probed below the string size?", *Phys. Lett. B*, **216**, 41 (1989). DOI: 10.1016/0370-2693(89)91366-X

[22] T. Yoneya, "On the interpretation of minimal of minimal length in string theories", *Modern Physics Letters A*, **4**, 16 (1989). DOI: 10.1142/S0217732389001817

[23] C. A. Mead, "String theory, supersymmetry, unification, and all that", *Rev. Mod. Phys.*, **71**, S112 (1999). DOI: 10.1103/RevModPhys.71.S112

[24] M. Sharma, T. Zhu and A Wang, "Background dynamics of pre-inflationary scenario in Brans-Dicke loop quantum cosmology", *Commun. Theor. Phys.*, **71**, 1205 (2019). DOI:10.1088/0253-6102/71/10/1205

[25] L.J. Garay, "Quantum gravity and minimum length", *Int. J. Mod. Phys.*, **10**, 145 (1995). DOI: 10.1142/S0217751X95000085

[26] A. Ashtekar, S. Fairhurst and J.L. Willis, "Quantum gravity, shadow states and quantum mechanics", *Classical and Quantum Gravity*, **20**, 1031 (2003). DOI: 10.1088/0264-9381/20/6/302

[27] G.M. Hossain, V. Husain and S.S. Seahra, "Background-independent quantization and the uncertainty principle", *Class. Quantum Grav.*, **27**, 165013 (2010). DOI: 10.1088/0264-9381/27/16/165013

[28] C. Rovelli, "Strings, loops and others: a critical survey of the present approaches to quantum gravity", *arXiv preprint gr-qc/9803024*, (1998). DOI: 10.48550/arXiv.gr-qc/9803024

[29] M. Sharma, T. Zhu, A. Wang, "Background dynamics of pre-inflationary scenario in Brans-Dicke loop quantum cosmology", *Commun. Theor. Phys.*, **71**, 1205(2019). DOI: 10.1088/0253-6102/71/10/1205

[30] Giovanni Amelino-Camelia, "Doubly-special relativity: Facts, myths and some key open issues", *Symmetry*,**2**, 230(2010). DOI: 10.3390/sym2010230

[31] S. Ghosh, "Lagrangian for doubly special relativity particle and the role of noncommutativity", *Phys. Rev. D*, **74**,084019 (2006). DOI: 10.1103/PhysRevD.74.084019

[32] D. Amati, M. Ciafaloni and G. Veneziano, "Classical and Quantum Gravity Effects from Planckian Energy Superstring Collisions", *Int. J. Mod. Phys. A*, **3**, 1615 (1988). DOI: 10.1142/S0217751X88000710

[33] D. Amati, M. Ciafaloni and G. Veneziano, "Superstring Collisions at Planckian Energies", *Phys. Lett. B*, **197**, 81 (1987). DOI: 10.1016/0370-2693(87)90346-7

[34] D. Amati, M. Ciafaloni and G. Veneziano,"Higher Order Gravitational Deflection And Soft Bremsstrahlung In Planckian Energy Superstring Collisions", *Nucl. Phys. B*, **347**, 550 (1990). DOI: 10.1016/0550-3213(90)90375-N

[35] G. M. Hossain, V. Husain and S. S. Seahra, "Background independent quantization and the uncertainty principle", *Class. Quant. Grav.*, **27**, 165013 (2010) arXiv:1003.2207[gr-qc]. DOI: 10.1088/0264-9381/27/16/165013

[36] A. Tawfik and A. Diab, "Review on Generalized Uncertainty Principle", *Reports on Progress in Physics*, **78**, 12 (2015). DOI: 10.1088/0034-4885/78/12/126001

[37] S. Hossenfelder, "Minimal length scale scenarios for quantum gravity", *Living Rev. Rel.*, **16**, 2 (2013). DOI: 10.12942/lrr-2013-2

[38] A. Peres and N. Rosen, "Quantum Limitations on the Measurement of Gravitational Fields", *Phys. Rev.*, **118**, 335 (1960). DOI: 10.1103/PhysRev.118.335

[39] H. S. Snyder, "Quantized space-time", *Phys. Rev.*, **71**, 38 (1947). DOI: 10.1103/PhysRev.71.38

[40] C. N. Yang, "On quantized space-time", *Phys. Rev.*, **72**, 874 (1947). DOI: 10.1103/PhysRev.72.874

[41] E. P. Wigner, "Relativistic Invariance and Quantum Phenomena", *Rev. Mod. Phys.*, **29**, 255 (1957). DOI: 10.1103/RevModPhys.29.255

[42] H. Salecker and E. P. Wigner, "Quantum limitations of the measurement of space-time distances", *Phys. Rev.*, **109**, 571 (1958). DOI: 10.1103/PhysRev.109.571

[43] C. A. Mead, "Possible Connection Between Gravitation and Fundamental Length", *Phys. Rev. D* , **135**, B849 (1964). DOI: 10.1103/PhysRev.135.B849

[44] C. A. Mead, "Observable Consequences of Fundamental-Length Hypotheses", *Phys. Rev.*, **143**, 990 (1966). DOI: 10.1103/PhysRev.143.990

[45] S. Majid and H. Ruegg, "Bicrossproduct structure of kappa Poincare group and noncommutative geometry", *Phys. Lett. B*, **334**, 348 (1994). DOI: 10.1016/0370-2693(94)90699-8

[46] A. Kempf, "Uncertainty relation in quantum mechanics with quantum group symmetry", *J.*

Math. Phys., **35**, 4483 (1994). DOI: 10.1063/1.530798

[47] A. Kempf, "Quantum field theory with nonzero minimal uncertainties in positions and momenta", *Preprint DAMTP/94-33*, (1994). DOI: 10.1063/1.531814

[48] G. Bhandari *et al.*, "GUP deformed background dynamics of phantom field", *General Relativity and Gravitation*, **56**, 139 (2024). DOI: 10.1007/s10714-024-03324-7

[49] G. Bhandari *et al.*, "Generalized uncertainty principle distorted quintessence dynamics", *Annals of Physics*, **473**, 169895 (2025). DOI: 10.1016/j.aop.2024.169895

[50] G. Bhandari *et al.*, "Quantum Corrected Brans-Dicke Cosmology", *Int. J. Geom. Methods Mod. Phys.*, **22**, 2550137 (2025). DOI: 10.1142/S0219887825501373

[51] G. Bhandari *et al.*, "Quantum Gravity Corrections to Hawking Radiation via GUP", *The European Physical Journal Plus*, **140**, 663 (2025). DOI: 10.1140/epjp/s13360-025-06608-2

[52] G. Bhandari, S. D. Pathak and V. K. Ojha, "RGUP corrections to scalar and fermionic fields", *The European Physical Journal Plus*, **140**, 1 (2025). DOI: 10.1140/epjp/s13360-025-06581-w

[53] S.Das and E.C.Vagenas, "Phenomenological implications of the generalized uncertainty principle", *Canadian Journal of Physics*, **87**, 233(2009). DOI: 10.1139/P08-105

[54] A.F.Ali, S.Das, and E.C.Vagenas, "A proposal for testing quantum gravity in the lab", *Phys.Rev.D*, **84**, 44013(2011). DOI: 10.1103/PhysRevD.84.044013

[55] A.F.Ali, S.Das, and E.C.Vagenas, "Discreteness of space from the generalized uncertainty principle", *Phys. Lett. B*, **678**, 497(2009). DOI: 10.1016/j.physletb.2009.06.061

[56] S. Deb, S. Das, E. C. Vagenas, "Discreteness of space from GUP in a weak gravitational field", *Physics Letters B*, **755**, 17 (2016). DOI: 0.1016/j.physletb.2016.01.059

[57] I.Pikovski *et al.*, "Probing Planck-scale physics with quantum optics", Nature Physics, **8**, 393(2012). DOI: 10.1038/nphys2262

[58] G. Bhandari *et al.*, "Generalized Uncertainty Principle and the Zeeman Effect: Relativistic Corrections Unveiled", *Nuclear Physics B*, **1012**, 116817 (2025). DOI: 10.1016/j.nuclphysb.2025.116817

[59] G. Bhandari and S. D. Pathak, "Stark Energy Shifts due to Quantum Gravity in RGUP Algebra", *Nuclear Physics B*, **1018**, 117019 (2025). DOI: 10.1016/j.nuclphysb.2025.117019

[60] M. Maggiore, "A generalized uncertainty principle in quantum gravity", *Phys. Lett. B*, **304**, 65(1993). DOI: 10.1016/0370-2693(93)91401-8

[61] F.Scardigli, "Generalized uncertainty principle in quantum gravity from micro-black hole

gedanken experiment", *Phys. Lett. B*, **452**, 39(1999). DOI: 10.1016/S0370-2693(99)00167-7

[62] A. Kempf, G. Mangano, and R.B.Mann, "Hilbert space representation of the minimal length uncertainty relation", *Phys. Rev. D*, **52**, 1108(1995). DOI: 10.1103/PhysRevD.52.1108

[63] E. Witten, "String theory dynamics in various dimensions", *Nuclear Physics B*, **443**, 1(1995). DOI: 10.1016/0550-3213(95)00158-O

[64] C. Bachas, "The short distance structure of open string theory" arXiv preprint hep-th/9907023 (1999). DOI: 10.48550/arXiv.hep-th/9907023

[65] A. Kempf,"Non-point like particles in harmonic oscillators", *J. Phys. A: Math. Gen.*, **30**, 2093 (1997). DOI: 10.1088/0305-4470/30/6/030

[66] A. Kempf, G. Mangano, R.B. Mann, "Hilbert space representation of the minimal length uncertainty relation" *Phys. Rev. D*, **52**, 1108 (1995). DOI: 10.1103/PhysRevD.52.1108

[67] A. Kempf, G. Mangano, "Minimal length uncertainty relation and ultraviolet regularization", *Phys. Rev. D*, **55**, 7909 (1997). DOI: 10.1103/PhysRevD.55.7909

[68] K. Nouicer,"Quantum-corrected black hole thermodynamics to all orders in the Planck length", *Phys. Lett. B* **646**, 63 (2007). DOI: 10.1016/j.physletb.2006.12.072

[69] P. Pedram, "A Higher Order GUP with Minimal Length Uncertainty and Maximal Momentum ",*Phys. Lett. B* 714, 317 (2012). DOI: 10.1016/j.physletb.2012.10.059

[70] L. J. Garay, "Quantum gravity and minimum length", *Int. J. Mod. Phys. A*, **10**, 145 (1995). DOI: 10.1142/S0217751X95000085

[71] K. Nozari and B. Fazlpour, "Generalized uncertainty principle, modified dispersion relations and early universe thermodynamics", *Gen. Relat. Gravit.*, **38**, 1661 (2006). DOI: 10.1007/s10714-006-0331-0

[72] R. J. Adler and D. I. Santiago, "On gravity and the uncertainty principle", *Mod. Phys. Lett. A*, **14**, 1371 (1999). DOI: 10.1142/S0217732399001462

[73] S. Hossenfelder, "Interpretation of quantum field theories with a minimal length scale", *Phys. Rev. D*, **73**, 105013 (2006). DOI: 10.1103/PhysRevD.73.105013

[74] I. Dadic, L. Jonke and S. Meljanac, "Harmonic oscillator with minimal length uncertainty relations and ladder operators", *Phys. Rev. D*, **67**, 087701, (2003). DOI: 10.1103/PhysRevD.67.087701

[75] C. Quesne and V. M. Tkachuk, "Dirac oscillator with nonzero minimal uncertainty in position", *J. Phys. A*, **38**, 1747 (2005). DOI: 10.1088/0305-4470/38/8/011

[76] C. Quesne and V. M. Tkachuk, "Lorentz-covariant deformed algebra with minimal length and application to the 1+1-dimensional Dirac oscillator", *J. Phys. A*, **39**, 109090 (2006). DOI: 10.1088/0305-4470/39/34/021

[77] A. Farag, S. Das, E.C.Vagenas, "The generalized uncertainty principle and quantum gravity phenomenology", *In The Twelfth Marcel Grossmann Meeting: On Recent Developments in Theoretical and Experimental General Relativity, Astrophysics and Relativistic Field Theories (In 3 Volumes)*, 2407 (2012). DOI: 10.1142/9789814374552_0492

[78] P. Bosso, and Saurya Das. "Generalized ladder operators for the perturbed harmonic oscillator." *Annals of Physics*, **396**, 254 (2018). DOI: 10.17586/2220-8054-2022-13-3-299-307

[79] P. Bosso, S. Das, "Generalized uncertainty principle and angular momentum", *Annals of Physics*, **383**, 416 (2017). DOI: 10.1016/j.aop.2017.06.003

[80] F. Brau, "Minimal length uncertainty relation and hydrogen atom", *J. Phys. A*, **32**, 7691 (1999). DOI 10.1088/0305-4470/32/44/308

[81] S. Benczik, L. N. Chang, D. Minic and T. Takeuchi, "The Hydrogen atom with minimal length", *Phys. Rev. A*, **72**, 012104 (2005). DOI: 10.1103/PhysRevA.72.012104

[82] M. M. Stetsko and V. M. Tkachuk, "Perturbation hydrogen-atom spectrum in deformed space with minimal length", *Phys. Rev. A*, **74**, 012101 (2006). DOI: 10.1103/PhysRevA.74.012101

[83] M. M. Stetsko, "Corrections to the ns-levels of hydrogen atom in deformed space with minimal length", *Phys. Rev. A*, **74**, 062105 (2006). DOI: 10.48550/arXiv.1706.04430

[84] M. M. Stetsko and V. M. Tkachuk, "Orbital magnetic moment of the electron in the hydrogen atom in a deformed space with minimal length", *Phys. Lett. A*, **372**, 5126 (2008). DOI: 10.1016/j.physleta.2008.06.002

[85] S. Das, E. C. Vagenas, "Universality of quantum gravity corrections", *Physical review letters*, **101**, 221301(2008). DOI: 10.1103/PhysRevLett.101.221301

Emerging Technologies for Future Gravitational Wave Detectors

V. Kumar*

Department of Physics, Institute of Applied Science and Humanities, GLA University, Mathura 281406, India and Institute of Physics, Academia Sinica, Taipei-11529, Taiwan

M. K. Singh†

Department of Physics, Institute of Applied Science and Humanities, GLA University, Mathura 281406, India

Gravitational wave (GW) astronomy has fundamentally transformed our understanding of the Universe by enabling direct observation of some of its most violent and relativistic phenomena, such as the inspiral and merger of compact objects including binary black holes and neutron stars. Unlike electromagnetic radiation, which interacts strongly with intervening matter and is therefore susceptible to absorption, scattering, and dispersion, GWs propagate through spacetime with minimal interaction, preserving their waveform signatures from source to detector. This uncorrupted transmission permits unparalleled investigation into the regime of strong-field general relativity, the equation of state of ultra-dense nuclear matter, and the physics governing the early Universe. Pioneering detections by ground-based interferometers such as Laser Interferometer Gravitational-Wave Observatory (LIGO), Virgo, and KAGRA have established GW astronomy as a central pillar of modern observational astrophysics. Nevertheless, the current generation of detectors remains limited by a variety of fundamental and technical noise sources including quantum shot noise, thermal Brownian motion in optical coatings, seismic disturbances, and suspension-related thermal fluctuations that restrict their low-frequency sensitivity and horizon reach. To overcome these barriers, next-generation observatories such as LIGO-India, the Einstein Telescope (ET), and the Cosmic Explorer (CE) are being designed with transformative technological upgrades: cryogenically cooled test masses to suppress thermal noise, ultra-high-finesse optical cavities to enhance signal amplification, extended interferometer arm lengths to increase strain sensitivity, and quantum-enhanced metrology such as frequency-dependent squeezing to mitigate quantum noise. This review provides a comprehensive assessment of these emergent detector architectures, focusing on critical technological frontiers including ultra-stable high-power laser systems, low-mechanical-loss dielectric mirror coatings, multi-stage seismic isolation platforms, low-noise suspension systems, and ultra-high vacuum infrastructures. Importantly, the next era of gravitational-wave astronomy holds profound implications beyond compact object astrophysics. Enhanced detection capabilities may illuminate the dynamics of the early Universe, potentially revealing imprints of inflationary physics, cosmic strings,

or primordial black holes. Moreover, GWs offer a unique avenue for probing the elusive dark sector: the gravitational influence of dark matter on binary dynamics, and the possible imprint of dark energy on cosmic expansion, could manifest in the waveform population statistics or cosmological distance ladder derived from standard sirens. As such, the technological and scientific evolution of GW detection is poised not only to expand the boundaries of multi-messenger astronomy but also to confront some of the deepest unresolved questions in fundamental physics and cosmology.

* vivekcrs68@gmail.com
† singhmanoj59@gmail.com

I. INTRODUCTION

In the dynamic fabric of the cosmos, a multitude of astrophysical phenomena unfolds continuously stellar births and deaths, compact object mergers, black hole collisions, and supernova explosions. These cataclysmic events generate transient perturbations in spacetime curvature, propagating outward as GW ripples predicted by Einsteins General Theory of Relativity in 1916. These waves, conceptualized as transverse spacetime distortions, travel at the speed of light and transport energy in the form of gravitational radiation. Despite this theoretical framework, Einstein himself remained doubtful about their empirical observability, given the extremely small strain amplitudes involved [1]. This skepticism prevailed for decades until a pivotal observational breakthrough in 1974: the discovery of the Hulse-Taylor binary pulsar. The measured orbital decay of the system was found to be in precise agreement with the predictions of GW energy emission, thereby offering the first compelling indirect evidence of gravitational radiation. The field underwent a dramatic transformation in 2015 with the inaugural direct detection of GWs by the LIGO, arising from the merger of two stellar-mass black holes located approximately 1.3 billion light-years from Earth [2]. This landmark event not only confirmed a century-old prediction but also inaugurated gravitational-wave astronomy as a novel observational window into the strong-field, nonlinear regime of general relativity. The subsequent 2017 detection of a binary neutron star merger by the joint LIGOVirgo collaboration marked the first multi-messenger astrophysical observation, correlating GW emission with gamma-ray bursts and electromagnetic afterglows. This event revealed the nucleosynthetic origins of heavy r-process elements such as gold and platinum, and firmly established the astrophysical relevance of GW observatories in tracing cosmic chemical evolution and relativistic dynamics. Among ongoing expansions of the global GW detector network, LIGO-India represents a transformative project. As a joint initiative between the LIGO Scientific Collaboration and Indian research institutions, LIGO-India is designed to host a full-scale Advanced LIGO interferometer, thereby adding a crucial new baseline to the international network. The strategic geographic separation will significantly enhance triangulation capabilities for source localization, improve sky coverage, and enable rapid electromagnetic follow-up, particularly in multi-messenger campaigns [3]. Moreover, LIGO-India is expected to improve the detection horizon for compact binary coalescences and enable more precise estimation of source parameters. This paper critically examines the advanced technologies driving the evolution of GW detectors, with a focus on their capacity to probe astrophysical and cosmological phenomena with increasing fidelity. Among these technologies are cryogenically cooled test masses to suppress thermal noise, ultra-low-loss dielec-

tric mirror coatings to minimize Brownian motion, and next-generation seismic isolation systems that decouple the detector from terrestrial vibrations. These innovations collectively expand the accessible parameter space for GW detection, particularly in the low-frequency regime crucial for probing heavier binary systems and intermediate-mass black holes. Gravitational-wave strain amplitudes are extraordinarily small on the order of $h \sim 10^{-21}$ corresponding to changes in distance smaller than a thousandth the diameter of a proton over interferometer arms several kilometers long. The detection of such minute displacements demands extreme optical and mechanical stability, high-fidelity metrology, and meticulous noise suppression. The operational frequency band for ground-based interferometers spans from ∼10 Hz to 5 kHz, over which different noise mechanisms dominate: seismic and Newtonian gravitational noise below 30 Hz, thermal noise from mirror coatings and suspensions in the intermediate band (30300 Hz), and quantum shot noise at higher frequencies ($>$ 300 Hz). Achieving broadband sensitivity therefore requires the coordinated application of multiple noise mitigation strategies: multi-stage active-passive suspension systems, cryogenic cooling of optics, and quantum optics techniques such as squeezed vacuum injection to reduce shot noise. Beyond their utility in astrophysics, GW observatories also offer unprecedented potential in probing fundamental physics. For instance, precise measurements of GW propagation over cosmological distances provide independent constraints on the Hubble constant and may serve as novel probes of the expansion history of the Universe. Deviations from general relativity in GW waveform phase evolution can offer hints of modified gravity or exotic compact objects. Moreover, GW could provide insights into the nature of dark energy by constraining the equation-of-state parameter w through standard sirens compact binary coalescences with electromagnetic counterparts that act as cosmic distance markers. Furthermore, the search for dark matter candidates through GW signals has gained increasing traction. Certain models predict GW signatures from dark matter-induced phenomena such as black hole superradiance, axion clouds, or primordial black hole (PBH) mergers. The stochastic gravitational-wave background arising from the incoherent superposition of unresolved sources may carry imprints of early-Universe physics, including phase transitions, cosmic strings, or inflationary reheating, all of which are sensitive to dark sector dynamics. Future observatories such as the ET and the Laser Interferometer Space Antenna (LISA) will extend sensitivity to new frequency bands, enabling detection of millihertz and nanohertz GWs from supermassive black hole binaries and relic gravitational backgrounds. The inclusion of LIGO-India within this global architecture is projected to improve sky localization by an order of magnitude, enhance polarization recovery, and substantially expand the redshift range for which GWs can be observed. This synergy of precision instrumentation and global scientific collabora-

tion will be instrumental in unveiling the hidden components of the Universe from the interior of neutron stars and formation pathways of black holes to the elusive nature of dark matter and dark energy.

II. SOURCES OF GRAVITATIONAL WAVES

GW are typically generated by non-axisymmetric acceleration of massive bodies, leading to time-varying quadrupole moments. The spiraling motion of compact astrophysical objects induces stretching and compression of the spacetime metric, resulting in the emission of detectable GWs. The primary classes of astrophysical GW sources span a wide range of masses, frequencies, and durations [3]. An overview of such sources is summarized in Table I, while strain profiles and waveform models are briefly discussed thereafter.

1. **Binary black hole merger:** The inspiral and coalescence of two black holes in a binary system emit strong GWs, with increasing amplitude and frequency as the system evolves toward merger [2–5]. A fraction of the total mass is radiated as gravitational energy, resulting in a final black hole whose mass is less than the sum of its progenitors. This source class produced the first direct GW detection in 2015 (GW150914) by LIGO, originating from a merger approximately 1.3 billion light-years away.

2. **Binary neutron star merger:** When two massive stars undergo supernova explosions, the remnants may form a neutron star binary. Gravitational radiation from the system leads to orbital decay over millions of years. As the neutron stars inspiral, they emit GWs with increasing frequency, culminating in a merger that may also produce electromagnetic counterparts such as kilonovae and gamma-ray bursts [6, 7]. The landmark event GW170817 in 2017 was the first multi-messenger detection involving GWs and EM radiation.

3. **Black hole neutron star merger:** A hybrid compact binary consisting of a neutron star and a black hole can emit GWs during its inspiral and coalescence phase. Tidal disruption of the neutron star near merger can lead to accompanying EM emission, contingent upon the mass ratio and spin alignment. Events such as GW200105 and GW200115 [4, 6–8] have provided observational evidence for this source class.

4. **Core collapse supernovae:** The gravitational collapse of a massive star's core (once nuclear fusion ceases) can result in a rapidly changing mass quadrupole, producing burst-like

GWs. However, the exact waveform morphology is model-dependent and sensitive to internal dynamics such as rotation, turbulence, and neutrino transport [9]. The end states may be neutron stars or black holes.

5. **Spinning neutron star (Pulsar):** Asymmetries or deformations on rapidly rotating neutron stars can produce continuous GW signals. The observed rotational frequency of PSR J17482446ad, the fastest known pulsar, is 716 Hz [10]. The GW amplitude depends on the ellipticity and internal structure of the neutron star.

6. **Primordial gravitational waves:** Quantum fluctuations in the early Universe during the inflationary epoch may have seeded a stochastic GW background. These GWs probe energy scales inaccessible to particle accelerators and could imprint B-mode polarization patterns in the Cosmic Microwave Background (CMB). They originate as early as 10^{-34} seconds post-Big Bang and provide a unique probe of high-energy physics [11, 12].

7. **Supermassive black hole binaries:** Resulting from galactic mergers, these binaries emit low-frequency GWs (nHz range) detectable via Pulsar Timing Arrays (PTAs). PTAs measure perturbations in the arrival times of radio pulses from millisecond pulsars, using them as ultra-stable cosmic clocks [13, 14]. These sources are inaccessible to ground-based interferometers due to their long periods.

8. **Stochastic GW background:** The incoherent superposition of unresolved sources both astrophysical (e.g., binary mergers) and cosmological (e.g., inflation, cosmic strings) forms a stochastic background. While not individually resolvable, this background contributes to the overall gravitational radiation energy density and encodes early-Universe physics.

Waveform Modeling Approaches for Compact Binary Coalescences

The modeling and interpretation of GW signals from astrophysical sources rely fundamentally on accurate theoretical waveform templates. These templates are essential for both detection and inference in matched filtering, Bayesian parameter estimation, and tests of general relativity. In the context of compact binary coalescences (CBCs) which include binary black holes (BBHs), binary neutron stars (BNSs), and neutron starblack hole (NSBH) systems the binary dynamics spans a

wide range of physical regimes, from weak-field inspiral to strong-field merger and ringdown. Consequently, multiple waveform modeling frameworks have been developed, each tailored to capture specific aspects of the coalescence process with varying degrees of approximation and computational cost. These include post-Newtonian approximations, effective-one-body models, phenomenological IMR models, and numerical relativity surrogates, among others.

- **Post-Newtonian (PN) Approximations:** The post-Newtonian formalism provides a perturbative expansion of the Einstein field equations in the regime of weak gravitational fields and slow motion, typically expressed in powers of the small parameter v/c, where v is the orbital velocity and c is the speed of light. PN approximations are analytically tractable and valid during the early inspiral phase, where radiation-reaction effects are moderate and the orbital separation is large. The formalism yields expressions for the orbital dynamics, gravitational waveform phase evolution, and energy flux. PN waveforms have historically been central to GW astrophysics, providing both analytic insight and a computational foundation for early inspiral templates. However, their validity diminishes in the strong-field regime near merger, where relativistic effects dominate and higher-order corrections become increasingly significant [15].

- **Effective-One-Body (EOB) Formalism:** The EOB approach offers a unified framework that bridges the inspiral, merger, and ringdown phases. Initially formulated as a resummation of PN dynamics, the EOB model maps the two-body problem onto an effective single-body system moving in a deformed Schwarzschild (or Kerr) spacetime. The conservative dynamics are described by an effective Hamiltonian, while the radiation-reaction force is constructed from PN-calibrated fluxes and waveform amplitudes. Crucially, EOB models are augmented by calibrations against full numerical relativity (NR) simulations, enabling high-fidelity modeling of the late inspiral and merger. Recent extensions of the EOB formalism incorporate spin effects, tidal interactions in neutron stars, and even eccentricity, making it a flexible and physically grounded tool for parameter estimation in GW astronomy [16, 17].

- **Phenomenological Models (e.g., IMRPhenom) and Numerical Relativity Surrogates (NRSur):** To complement the EOB framework, phenomenological models such as the IMRPhenom family have been developed. These models construct full inspiralmerg-erringdown (IMR) waveforms by stitching together analytical and numerical inputs using functional forms fitted across a wide parameter space. IMRPhenom waveforms are typically

represented in the frequency domain and are computationally efficient, making them well-suited for large-scale data analysis in LIGOVirgoKAGRA pipelines [18, 19]. More recently, Numerical Relativity Surrogates (NRSur) have emerged as a powerful alternative. These models employ reduced-order modeling techniques and machine learning tools to interpolate between precomputed NR waveforms. Given a dense training set, surrogates can reproduce the complex features of full NR waveforms with minimal computational cost. NRSur models offer exceptional accuracy for waveform morphology and are increasingly used in parameter estimation studies involving high signal-to-noise ratio (SNR) events [19, 20].

Collectively, these modeling strategies form the theoretical backbone of GW astronomy. The continuous refinement and validation of waveform models are essential not only for precise source characterization but also for fundamental physics applications, including tests of general relativity in the strong-field regime, constraints on the neutron star equation of state, and cosmological inference using standard sirens.

III. PRINCIPLES OF GRAVITATIONAL WAVE DETECTION

Detecting GW presents a formidable experimental challenge due to the extremely small distortions they induce in spacetime geometry. These distortions correspond to differential displacements on the order of 10^{-18} to 10^{-21} meters, necessitating the use of exquisitely sensitive interferometric techniques. Ground-based detectors such as LIGO and Virgo utilize laser interferometry based on the Michelson configuration to measure these minuscule variations in proper length. In this setup, a highly coherent and stabilized laser beam is directed toward a beam splitter, which divides the light into two orthogonal paths of equal length. These beams propagate along the interferometer arms, reflect off suspended high-reflectivity test masses (mirrors), and return to recombine at the beam splitter. The superposition of the returning beams forms an interference pattern at the photodetector. In the absence of a GW, and when both arms are of equal optical path length, the interference is destructive, resulting in a dark fringe at the output port. When a GW passes through the detector, it perturbs spacetime such that one arm is lengthened while the other is shortened an effect governed by the waves polarization and direction of incidence. This creates a time-varying phase shift between the two arms, altering the interference pattern. The result is a measurable modulation in the output light intensity, which encodes the GW's amplitude and frequency content. The strain h is defined as the fractional change in arm length,

TABLE I. Summary of typical GW sources, strain levels, frequency bands and detection methods.

Source Type	**Strain (h)**	**Frequency Band**	**Detection Method**	**References**
Binary Black Hole (BBH)	10^{-21} to 10^{-22}	∼101,000 Hz	Ground-based interferometers (LIGO, Virgo)	[2, 21]
Binary Neutron Star (BNS)	10^{-22} to 10^{-23}	∼101,000 Hz	Ground-based interferometers	[22]
NSBH Merger	$\sim 10^{-22}$	∼101,000 Hz	Ground-based interferometers	[23]
Core-collapse Supernovae	$\lesssim 10^{-23}$	∼101,000 Hz (burst)	Ground-based interferometers (burst searches)	[23]
Spinning Neutron Star	$\lesssim 10^{-26}$	∼101,000 Hz (continuous)	Continuous wave analysis	[24]
Primordial GWs	$\sim 10^{-18}$	$\sim 10^{-6}$ 1 Hz	CMB polarization, PTA, LISA	[25]
SMBH Binaries	10^{-15} to 10^{-17}	$\sim 10^{-9}$ 10^{-7} Hz	Pulsar Timing Arrays (PTA)	[26, 27]
Stochastic Background	—	Broad (nHz to kHz)	Cross-correlation analysis	[28, 29]

IV. PRINCIPLES OF GRAVITATIONAL WAVE DETECTION

Detecting GW presents a formidable experimental challenge due to the extremely small distortions they induce in spacetime geometry. These distortions correspond to differential displacements

on the order of 10^{-18} to 10^{-21} meters, necessitating the use of exquisitely sensitive interferometric techniques. Ground-based detectors such as LIGO and Virgo utilize laser interferometry based on the Michelson configuration to measure these minuscule variations in proper length. In this setup, a highly coherent and stabilized laser beam is directed toward a beam splitter, which divides the light into two orthogonal paths of equal length. These beams propagate along the interferometer arms, reflect off suspended high-reflectivity test masses (mirrors), and return to recombine at the beam splitter. The superposition of the returning beams forms an interference pattern at the photodetector. In the absence of a GW, and when both arms are of equal optical path length, the interference is destructive, resulting in a dark fringe at the output port. When a GW passes through the detector, it perturbs spacetime such that one arm is lengthened while the other is shortened an effect governed by the waves polarization and direction of incidence. This creates a time-varying phase shift between the two arms, altering the interference pattern. The result is a measurable modulation in the output light intensity, which encodes the GW's amplitude and frequency content. The strain h is defined as the fractional change in arm length,

$$h = \frac{\Delta L}{L}, \tag{1}$$

where L is the unperturbed arm length (4 km in the case of LIGO), and ΔL is the differential displacement caused by the GW. The typical GW-induced strain observed at Earth is on the order of $h \sim 10^{-21}$, corresponding to sub-femtometer displacements.

Figure 1 (adapted from [30]) illustrates the schematic of a Michelson interferometer as used in GW observatories. The change in phase difference between the two returning beams due to GW-induced path length variation is detected as light intensity fluctuations at the photodiode. The interferometric response can be expressed more formally as a time-domain detector response function:

$$h(t) = \frac{\Delta L(t)}{L}, \tag{2}$$

where $\Delta L(t)$ is the differential time-varying path length due to the passing GW. In the frequency domain, the response is further characterized by a transfer function $H(f)$, which relates the input strain to the output voltage signal via:

$$\tilde{V}(f) = H(f) \cdot \tilde{h}(f), \tag{3}$$

where $\tilde{V}(f)$ and $\tilde{h}(f)$ are the Fourier transforms of the voltage signal and GW strain, respectively. The form of $H(f)$ is determined by the interferometer's optical configuration, suspension dynamics, and control systems.

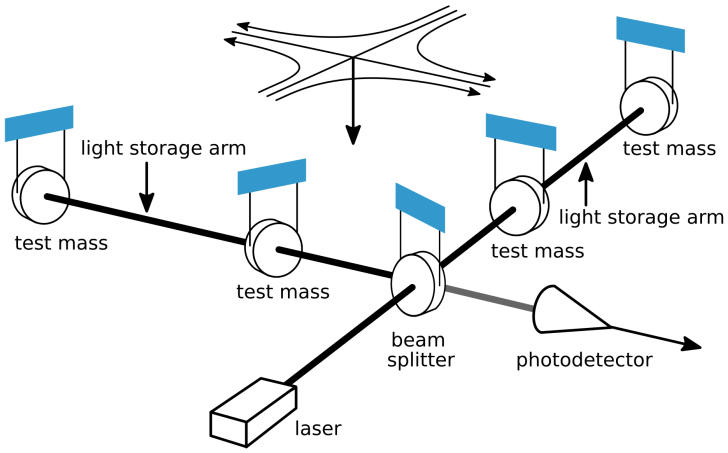

FIG. 1. Schematic diagram of Michelson interferometer [30].

As shown in Figure 3, the total noise spectrum of a GW detector is composed of various contributions, including quantum noise (shot noise and radiation pressure), thermal noise (from coatings and suspensions), seismic noise, and Newtonian noise. These components dominate at different frequency ranges and impose characteristic limits on the detectors bandwidth and sensitivity. The detection of GWs relies on precise measurement of phase shifts induced by space-time perturbations in kilometer-scale interferometers. The sensitivity to these distortions is bounded by fundamental and technical noise sources, which have been systematically reduced through advanced technologies in laser stabilization, optical coatings, suspension systems, and signal processing.

V. GLOBAL LANDSCAPE OF GRAVITATIONAL WAVE OBSERVATORIES

As of 2025, the international GW detector network comprises a mix of advanced operational facilities and several cutting-edge observatories under development. The twin Advanced LIGO detectors in Hanford and Livingston, USA [2, 4, 33], are currently engaged in their fourth observing run (O4), having undergone incremental upgrades that enable near-weekly detections. Virgo in Italy [22, 34–36] is completing its Virgo+ upgrade phase and is expected to rejoin the network during O4. KAGRA in Japan [37–39] the first large-scale cryogenic and subterranean GW observatory is steadily improving its sensitivity and angular resolution. Meanwhile, LIGO-India

[40], currently under construction in Maharashtra, is designed to replicate the Advanced LIGO architecture and is projected to begin operation by 2030, significantly enhancing the global networks source localization capabilities. The next-generation ET [41, 42], featuring a triangular underground configuration with cryogenic mirrors and extended baselines, aims to lower the low-frequency noise floor and expand sensitivity to previously undetectable signals. Concurrently, the LISA [43, 44], a space-based interferometer developed by ESA and NASA, is set to operate in the millihertz frequency band. By targeting sources such as supermassive black hole binaries, extreme mass-ratio inspirals, and relic radiation from the early Universe, LISA will enable a complementary observational regime inaccessible from ground-based platforms.

A. Sensitivity Evolution and Noise Budget

The evolution of strain sensitivity in LIGO interferometers from O1 to the projected O5 is depicted in Figure 2 [45]. Each sensitivity curve represents the amplitude spectral density (ASD) of strain noise across the frequency domain (10 Hz to several kHz). O1 (brown) achieved a BNS horizon distance of approximately 80 Mpc. Subsequent runs O2 (blue) and O3 (green and orange for Livingston and Hanford, respectively) extended this range to 100130 Mpc. The ongoing O4 run (gray) demonstrates further noise suppression, supporting BNS detections out to 160190 Mpc through techniques such as squeezed-light injection, enhanced laser power, and improved seismic isolation. The upcoming O5 run (magenta) corresponds to the aLIGO+ upgrade and is projected to exceed a 330 Mpc BNS range. In this configuration, broadband signal recycling and frequency-dependent squeezing will be implemented to optimize performance across the detection band. Notably, the most responsive frequency range ($\sim$100300 Hz) reflects the optimal balance between quantum noise, coating thermal noise, and seismic isolation facilitated by FabryProt arm cavities, thermal compensation systems, and feedback control loops.

B. Cryogenics vs. Room-Temperature Technologies

A key limitation in current detectors is the thermal noise introduced by dielectric mirror coatings. As illustrated in Figure 3 [46], quantum shot noise dominates the high-frequency regime, whereas Brownian motion within the mirror coatings becomes significant at mid-frequencies. At frequencies below $\sim$20 Hz, suspension thermal noise and Newtonian gravity gradient noise begin to

dominate. Cryogenic technologies as implemented in KAGRA and planned for ET directly address thermal noise by lowering the operating temperature of the test masses, thereby reducing Brownian motion. In contrast, room-temperature interferometers like LIGO and Virgo rely on material optimization and active thermal compensation. While cryogenics imposes stringent requirements on vibration isolation, optical absorption, and heat extraction, it remains a promising pathway to sub-Hz sensitivities in next-generation observatories.

C. Global Collaborative Infrastructure

Figure 5 presents the geographic distribution of global GW observatories [3, 30, 37, 40]. These facilities are deeply integrated into a cooperative network that enables joint observation runs, cross-calibration of data, and rapid localization of GW sources. The next sections provide detailed institutional and technical profiles of each major observatory.

1. LIGO

The LIGO operates two large-scale interferometric detectors located in Hanford, Washington and Livingston, Louisiana. Its foundational mission is the detection of minuscule distortions in spacetime caused by passing GW, utilizing ultra-sensitive laser interferometry. LIGO was the first observatory to successfully detect GW, thereby inaugurating an era of observational gravitational-wave astronomy. The interferometric configuration of LIGO is based on a Michelson interferometer with 4-km-long perpendicular arms housed in ultra-high vacuum beam tubes. Laser beams are split and directed down these arms, where they are reflected multiple times by highly reflective test mass mirrors suspended in multi-stage isolation systems to suppress seismic noise. The use of Fabry-Perot arm cavities increases the effective optical path, enhancing sensitivity. When a GW passes through the detector, it induces a differential length change in the two arms, modulating the interference pattern observed at the photodetector, as illustrated in Figure 1. LIGO made the first direct GW detection in September 2015, known as GW150914, resulting from a binary black hole merger located about 1.3 billion light-years away [2, 4]. Subsequent detections, including GW151226, GW170104, and GW170814 [34], have substantially enriched our understanding of black hole populations and their merger rates. The advent of Advanced LIGO increased sensitivity by an order of magnitude, allowing detection of events at greater distances [22]. A landmark event,

GW170817, marked the first detection of a binary neutron star merger accompanied by electromagnetic counterparts, thereby establishing the field of multi-messenger astronomy. It provided key insights into r-process nucleosynthesis responsible for the formation of heavy elements like gold and platinum. Recent detections include GW190521, potentially the first observation of an intermediate-mass black hole merger. Future upgrades under the Advanced LIGO+ program aim to further improve sensitivity and event rates, enabling detection of fainter signals and enhancing source localization through participation in the global network with Virgo, KAGRA, and the upcoming LIGO-India [4, 22, 34].

Computational Infrastructure: LIGO relies on a robust data analysis ecosystem, including the LIGO Data Grid (LDG) and dedicated clusters for real-time processing. The LSC (LIGO Scientific Collaboration) pipeline incorporates matched filtering, machine learning classifiers, and parameter estimation codes (e.g., LALInference).

2. **Virgo**

Located near Pisa, Italy, Virgo is a European GW interferometer with 3-km arms. Virgo complements LIGO in the global network and contributes significantly to source triangulation and sky localization. Like LIGO, Virgo employs laser interferometry (Figure6) is taken from article [3], with suspended mirrors in vacuum arms and Fabry-Perot cavities. Virgo played a pivotal role in improving localization of GW170814 and GW170817 [3, 22, 35], facilitating the identification of electromagnetic counterparts. The Virgo-LIGO collaboration has enabled improved accuracy in source characterization, contributing data on component masses and spin parameters of binary black hole mergers. Advanced Virgo and its successor Virgo+ have enhanced the detector's sensitivity through improvements in mirror coatings, laser power, and thermal compensation. The ongoing upgrade campaign aims to extend Virgos reach toward weaker, more distant sources, and broaden its science case to include continuous waves and stochastic backgrounds [36].

3. **KAGRA**

KAGRA, located underground in Japans Kamioka mine, is the first large-scale GW detector to operate with cryogenically cooled mirrors and in a subterranean setting. These design choices reduce thermal and seismic noise, enhancing sensitivity in low-frequency bands. Using a Fabry-

Perot-Michelson interferometer configuration with 3-km arms, KAGRA combines experience from LIGO and Virgo with innovations such as sapphire mirrors cooled to 20 K [37]. It began science operations during the O3 observation run and continues to improve its sensitivity. Figure 7 illustrates its layout it taken from article [37]. Noise sources identified in the O3GK run include shot noise, laser frequency noise, acoustic coupling, and angle-to-length conversion. Planned upgrades include beam dump installations, improved angular control systems, and mitigation of scattered light [38, 48]. Its participation enhances global detection and localization accuracy.

4. LIGO-India

LIGO-India is a collaborative project between Indian science agencies and the LIGO Laboratory (Caltech and MIT) to establish a third LIGO-class interferometer in India. The observatory, under construction in Maharashtra, will have 4-km-long arms and replicate the Advanced LIGO design [40]. The location was chosen for its low seismicity, which enhances detector stability and data quality. LIGO-India is expected to join the network in the early 2030s, significantly improving angular resolution and sky coverage. It will also foster domestic research infrastructure in optics, lasers, and gravitational physics, while enabling greater participation in multi-messenger science.

5. Next-Generation Detectors

Future detectors like the ET indicated in Figure 8 and LISA indicated in Figure 9 are set to expand GW observations into new frequency regimes. The ET will be a triangular underground facility with 10-km arms, targeting sensitivity improvements by a factor of 10 over current detectors, particularly below 10 Hz. It will probe early inspirals and the stochastic background with high fidelity. Current site characterization efforts in the Euregio Meuse-Rhine region focus on seismic isolation and environmental noise [41, 42]. LISA will consist of three spacecraft orbiting the Sun in a heliocentric triangle with 2.5 million km arms. Sensitive to millihertz GWs, LISA will detect signals from supermassive black hole mergers, extreme mass ratio inspirals, and possibly primordial sources [43, 44]. The mission, recently confirmed by ESA for Cosmic Vision L3, builds on technologies validated by LISA Pathfinder.

Each observatory contributes uniquely to the global network, improving detection confidence,

TABLE II. Comparison of major GW detectors, highlighting their arm lengths, design features, operational status, and references.

Detector	**Location**	**Arm Length**	**Key Features**	**Status (2025)**	**References**
LIGO	US (Hanford, Livingston)	4 km	Advanced interferometry; 125 W laser; squeezed light; fused silica mirrors; quadruple suspensions; LDG support	Operational (O4)	[22, 34]
Virgo	Italy	3 km	Super-polished silica mirrors with dielectric coatings; 50 W laser; thermal compensation system; Virgo+ optics; coating R&D	Upgrading (O4)	[35, 36]
KAGRA	Japan	3 km	Cryogenic sapphire mirrors; underground facility to reduce seismic and anthropic noise; laser power under development	Operational (O4)	[37]
LIGO-India	India	4 km	Located in a seismic quiet zone; national R&D initiatives; replication of LIGO instrumentation	Under Construction (2030)	[40]
ET	Europe	10 km	Triangular topology; underground installation; cryogenics; next-generation design sensitivity	In design phase	[41]
LISA	Space	2.5 million km	Millihertz frequency band; heliocentric orbit; space-based laser interferometry between free-floating test masses	In design phase (2035)	[43]

sky localization, and the ability to pursue multi-messenger astrophysics across diverse source classes and frequencies and is summeried in table II.

VI. TECHNOLOGICAL ENHANCEMENTS AND SENSITIVITY IMPROVEMENTS

A. Signal Amplification Techniques

To detect the minuscule spacetime strain caused by GW typically on the order of 10^{-21} modern interferometric detectors rely on advanced signal amplification and noise-reduction strategies. These technologies extend the effective optical path length, increase circulating power, and enhance signal-to-noise ratio (SNR), thereby allowing for the detection of weaker and more distant astrophysical events. Three cornerstone methods that enable such enhancements are the implementation of FabryProt arm cavities, power recycling, and signal recycling. Together, these define the resonant optical topology of detectors such as Advanced LIGO and Virgo.

1. FabryProt Cavity

In contemporary GW detectors, the arms of the Michelson interferometer are embedded with high-finesse FabryProt cavities to augment the phase shift induced by passing GW. Each arm contains two highly reflective mirrors separated by a distance L, forming a resonant cavity that allows the laser field to circulate multiple times before recombining at the beam splitter. This increases the effective interaction time between the laser light and the differential arm-length variation caused by GWs [49, 50]. The phase difference $\Delta\phi$ induced by a GW of strain amplitude h over arm length L is given by:

$$\Delta\phi = \frac{4\pi h L}{\lambda},$$

where λ is the laser wavelength. The FabryProt configuration effectively increases L to an optical path length NL, where N is the average number of bounces inside the cavity. At resonance, constructive interference causes the intra-cavity field to build up significantly, while destructive interference suppresses back-reflection into the laser source. The finesse $\mathcal{F}$ of the cavity quantifies its sharpness of resonance:

$$\mathcal{F} = \frac{\pi\sqrt{R}}{1-R},$$

where R is the reflectivity of the mirrors. A higher finesse leads to greater optical build-up and narrower linewidths, selectively enhancing sensitivity in desired frequency bands while suppressing off-resonant noise components [51]. FabryProt cavities are dynamically tunable via piezoelectric actuators or electro-optic modulators, enabling real-time control of resonance conditions. This tunability is also crucial for maintaining cavity locking via feedback control systems. Figure 11 illustrates the FabryProt cavity taken from [52] architecture employed in GW interferometers.

2. **Power Recycling**

The Michelson interferometer, when operated at a dark fringe (destructive interference at the output port), reflects most of the input laser power back toward the source. To reclaim this unused optical power and enhance the interferometers efficiency, a partially transmitting Power Recycling Mirror (PRM) is placed between the laser and beam splitter, forming the Power Recycling Cavity (PRC) [53]. The retro-reflected light is constructively interfered with incoming laser light inside the PRC, resulting in significant enhancement of intra-cavity optical power. In Advanced LIGO, this leads to circulating powers in excess of 700 kW. Higher power improves the SNR for phase fluctuations induced by GWs. To suppress associated thermal noise especially coating Brownian noise and thermoelastic damping optical beam spot sizes on the test masses were increased. This required careful optimization of the PRM curvature and PRC geometry to preserve cavity stability and mode matching under high-power operation [50, 51, 54]. A schematic of power recycling implementation is shown in Figure 7.

3. **Signal Recycling**

Signal recycling is a complementary resonant technique that enhances detector sensitivity to specific frequency bands of GW signals. A partially reflective Signal Recycling Mirror (SRM) is placed at the output (anti-symmetric) port of the interferometer, forming the Signal Recycling Cavity (SRC) with the arm cavities [50, 53–56]. By tuning the position and reflectivity of the SRM, the detector response can be shaped: broadband for general-purpose detection or narrow-band to enhance sensitivity around selected frequencies (e.g., BNS inspirals or specific ringdown modes). This flexibility enables the detector to trade bandwidth for peak sensitivity, depending on the astrophysical targets. The SRC effectively modifies the interferometers optical transfer func-

tion. When tuned appropriately, it causes constructive interference of the GW sidebands within the cavity, thereby enhancing the response to particular signal frequencies before photodetection. Figure 7 presents the schematic layout of signal recycling implementation.

4. Quantum Noise and Standard Quantum Limit (SQL)

In the absence of classical noise sources, interferometers are ultimately limited by quantum fluctuations of light. These manifest as shot noise (photon counting uncertainty) at high frequencies and radiation pressure noise at low frequencies. The Standard Quantum Limit (SQL) for strain sensitivity is given by $S_h^{SQL}(f) = \frac{8\hbar}{mL^2\omega^2}$, where $\hbar$ is the reduced Planck constant, m is the test mass, L is the interferometer arm length, and $\omega = 2\pi f$ is the angular frequency. Advanced detectors employ quantum squeezing to surpass the SQL by injecting non-classical light with reduced uncertainty in one quadrature. Frequency-dependent squeezing, implemented via filter cavities, allows shot noise reduction at high frequencies while avoiding radiation pressure noise amplification at low frequencies. These techniques represent a new frontier in quantum-limited metrology.

B. Sensitivity Enhancement Methods

1. Seismic Isolation

Seismic and anthropogenic ground vibrations impose a significant low-frequency noise floor in terrestrial interferometric GW detectors such as LIGO and Virgo. This seismic noise is particularly detrimental in the frequency range below ∼10 Hz, where direct coupling to test masses can mask astrophysical signals. To suppress these perturbations, advanced seismic isolation systems have been developed that combine both passive and active strategies [56]. Passive isolation employs mechanical filters such as multistage pendulums and geometric anti-spring systems, which act as mechanical low-pass filters attenuating ground motion above their resonance frequencies. Active isolation, on the other hand, utilizes vibration sensors (e.g., geophones, accelerometers) coupled with feedback control systems to apply real-time counteracting forces via actuators. This hybrid approach has enabled modern observatories to achieve displacement noise suppression exceeding 10 orders of magnitude at frequencies around 1 Hz. In particular, the test masses are suspended by quadruple pendulum systems in LIGO and Virgo, where each stage is carefully engineered

to damp specific mechanical modes. Additional isolation platforms such as LIGOs Hydraulic External Pre-Isolator (HEPI) and Internal Seismic Isolation (ISI) systems further decouple the optics from ground motion. These implementations have been critical in achieving long-duration stable operations, improving low-frequency sensitivity, and enhancing detector duty cycles for observing transient GW signals.

2. Mirror Coating

Highly reflective test-mass mirrors are core optical elements in GW interferometers, and their coating properties critically govern detector sensitivity. These mirrors, located at the interferometer arm ends, must exhibit ultra-high reflectivity (greater than 99.99%) with extremely low optical absorption and mechanical dissipation. The optical and mechanical characteristics of the mirror coatings thus directly impact the strain sensitivity, thermal noise floor, and quantum noise coupling of the detector across its frequency band.

1. Reflectivity and Coating Structure

Dielectric Bragg mirrors comprising alternating layers of high and low refractive index materials are used to achieve the required reflectivity. In Advanced LIGO and KAGRA, the standard materials are SiO_2 (silica, low-index) and Ta_2O_5 (tantala, high-index). Doping Ta_2O_5 with TiO_2 modifies its internal structure and reduces its mechanical loss by up to 25%, forming $Ti:Ta_2O_5$ [57, 58]. Amorphous silicon (a-Si) is a promising alternative high-index material due to its high refractive index ($\sim$3.5) and substantially lower mechanical loss compared to tantala. Its use can reduce the number of bilayers needed to achieve the same reflectivity, thereby decreasing coating thermal noise [59, 64]. However, its optical absorption is significantly higher at 1064 nm, which restricts its use in current detectors. This can be mitigated through annealing or by shifting operation to 1550 nm [59]. Silicon nitride (SiN_x), particularly in high-tensile-stress stoichiometries, offers tunable optical properties, excellent environmental stability, and very low mechanical loss angles (on the order of 10^{-5}). With optical absorption below 1 ppm at 1550 nm, it represents a promising candidate for use in cryogenic detectors such as LIGO Voyager and the ET [60]. Crystalline coatings based on epitaxially grown GaAs/AlGaAs or GaP/AlGaP multilayers exhibit exceptionally low mechanical loss angles (below 10^{-5}) and optical absorption below 1 ppm. These materials

offer an order of magnitude improvement in coating thermal noise relative to amorphous systems. However, current technological challenges in substrate bonding and limited wafer sizes constrain their widespread deployment and summerized in Table III [61, 62].

TABLE III. Representative coating materials considered for GW detectors, including mechanical and optical characteristics.

Material	**Refractive Index (1064 nm)**	$\phi_{\mathbf{mech}}$ (Room T)	**Optical Absorption (ppm)**	**Applicable Wavelength**	**References**
SiO_2	∼1.45	$\sim 2 \times 10^{-4}$	< 0.5	1064/1550 nm	[57, 58]
Ta_2O_5	∼2.1	$\sim 4 \times 10^{-4}$	< 1	1064 nm	[64]
Ti:Ta_2O_5	∼2.1	$\sim 3 \times 10^{-4}$	< 1	1064 nm	[64]
a-Si	∼3.4	$< 1 \times 10^{-4}$	1001000 (room T)	1550 nm	[59]
SiN_x	2.02.3	1×10^{-5}	< 1	1550 nm (cryogenic)	[60]
GaAs/AlGaAs	∼3.4	$< 5 \times 10^{-5}$	< 1	1550 nm (cryogenic)	[61, 62]

2. Thermal Noise and Advanced Stack Design

Thermal (Brownian) noise in the mirror coatings represents one of the dominant fundamental noise sources in the mid-frequency range (30300 Hz), which encompasses most binary inspiral signals. According to the fluctuationdissipation theorem, the power spectral density of displacement thermal noise due to the coatings scales with the mechanical loss angle:

$$S_x^{\text{thermal}}(f) \propto \frac{k_B T}{\pi^2 f} \cdot \phi_{\text{mech}}$$

Thus, reducing ϕ_{mech} in coating materials is essential for minimizing thermal noise in interferometric GWdetectors. The current industry standard employs alternating bilayers of SiO_2 and Ti-doped Ta_2O_5 [64]. Advanced coating architectures now explore composite multilayers composed of materials with complementary optical and mechanical properties. For instance, high-refractive-index but relatively high-loss materials such as amorphous silicon (a-Si) can be buried beneath low-loss outer layers like SiO_2 or SiN_x, effectively mitigating

thermal noise while maintaining high optical reflectivity. Recent advances in ion-beam sputtering have enabled the production of silicon nitride (SiN_x) coatings with mechanical loss angles as low as $(1.0 \pm 0.1) \times 10^{-4}$ and optical absorption levels of only a few ppm at 1064 nm, following thermal annealing above 900 °C [60]. These coatings have demonstrated a thermal noise reduction of approximately 25% relative to the baseline coatings used in Advanced LIGO. Crystalline multilayer coatings while still under active research exhibit mechanical loss angles an order of magnitude lower than those of amorphous counterparts. If scalable to large, curved mirror substrates, such coatings may become a breakthrough technology for third-generation cryogenic interferometers [61, 62].

VII. USE OF ARTIFICIAL INTELLIGENCE IN GRAVITATIONAL WAVE DETECTION

Artificial Intelligence (AI), particularly through machine learning (ML) and deep learning (DL) architectures, is emerging as a transformative paradigm in the field of GW data analysis. Traditional techniques, notably matched filtering, remain central to signal detection pipelines and are underpinned by optimal signal processing theory in the presence of Gaussian noise. However, these methods become computationally prohibitive when applied to high-dimensional parameter spaces and are sensitive to deviations from stationary, Gaussian noise conditions frequently encountered in real detector data. In contrast, AI-based algorithms have demonstrated remarkable potential in automating and accelerating various stages of the GW analysis workflow including real-time detection, glitch classification, non-Gaussian noise mitigation, and rapid parameter estimation while maintaining competitive accuracy relative to classical methods. A particularly successful implementation has been the use of convolutional neural networks (CNNs), which are well-suited for learning spatial and temporal features from structured data such as spectrograms and strain time series. George and Huerta [66] first demonstrated that CNNs trained on numerically generated GW templates could reliably detect black hole merger signals embedded in realistic noise, achieving sensitivity comparable to matched filtering at significantly reduced computational cost. Gabbard et al. [67] extended this approach to raw time-domain LIGO data, producing highly accurate binary classification models capable of real-time detection. In addition to classification tasks, unsupervised architectures such as autoencoders have been effectively employed for signal denoising and anomaly detection. These models learn a compressed latent representation of clean

GW signals and are capable of isolating and reconstructing them from corrupted input by filtering out transient noise artifacts (glitches). This approach has proven valuable for enhancing data quality in non-stationary environments, where traditional whitening and veto methods underperform.

Generative adversarial networks (GANs), which involve adversarial training between a generator and a discriminator network, have been employed to synthetically reconstruct gravitational waveforms [68]. By learning the statistical distribution of both background noise and signal morphologies, GANs can interpolate between templates, enabling more generalizable waveform recovery. Recurrent neural networks (RNNs), particularly those incorporating long short-term memory (LSTM) cells, are adept at modeling temporal dependencies in sequential data. These architectures have been applied to transient signal detection, yielding superior performance in scenarios where signals evolve non-linearly over time, such as precessing binaries or eccentric inspirals. More recently, inference frameworks such as normalizing flows and neural posterior estimation (NPE) have been proposed for accelerated Bayesian parameter estimation. These techniques construct surrogate posteriors for physical parameters such as component masses, spins, inclination angles, and sky localization while retaining accuracy comparable to computationally intensive methods like Markov Chain Monte Carlo (MCMC) and nested sampling [69–71]. The ability to evaluate posterior distributions in real time is particularly relevant for next-generation detectors (e.g., the ET and LISA), which are expected to produce higher event rates and lower-latency requirements. Despite their promise, AI-based GW detection frameworks also face important challenges. One notable issue is the risk of false positives, where spurious signals (e.g., glitches or instrumental artifacts) are misclassified as genuine astrophysical events. This is especially problematic in unmodeled burst searches or low-SNR regimes. Overfitting is another concern models trained on limited or non-representative datasets may fail to generalize to unseen noise environments or rare signal classes. Furthermore, most deep learning methods operate as black boxes, limiting interpretability and raising caution in mission-critical pipelines where uncertainty quantification is essential.

To mitigate these limitations, recent efforts focus on:

- Training on augmented datasets with realistic noise simulations (e.g., glitch injections, domain adaptation).
- Incorporating uncertainty estimates via Bayesian neural networks or dropout-based approximations.

- Hybridizing ML models with physical priors or constraints from numerical relativity and analytical waveform models.

As the sensitivity and bandwidth of detectors improve, and as multi-messenger astronomy demands rapid response capabilities, AI will become increasingly indispensable in both low-latency trigger generation and large-scale data post-processing. The integration of AI with traditional techniques, under rigorous validation, is poised to redefine data handling in next-generation GW observatories.

VIII. CONCLUSION

The direct detection of GW has ushered in a new era in experimental astrophysics and fundamental physics, offering access to phenomena that were previously inaccessible through electromagnetic observations. Events such as binary black hole mergers, neutron star coalescences, and core-collapse supernovae have been firmly established as powerful GW sources, providing empirical insights into strong-field general relativity, nuclear matter at supra-nuclear densities, and the astrophysical environments of compact objects. The continued enhancement of detector sensitivity driven by innovations in optical coatings, seismic isolation, cryogenic suspensions, and quantum-enhanced metrology has allowed facilities such as LIGO, Virgo, and KAGRA to probe deeper into the cosmos, detecting fainter and more distant events with higher fidelity. Of particular importance are the advances in mirror coating technologies, where reducing thermal noise, minimizing optical absorption, and maximizing reflectivity are critical to achieving the quantum-limited performance of current and future detectors. These improvements, coupled with refined interferometric techniques and high-power laser stabilization, are instrumental in expanding the accessible frequency bandwidth and increasing the signal-to-noise ratio for a broader class of GW sources. The upcoming LIGO-India observatory, in conjunction with the existing global network, is poised to significantly enhance sky localization accuracy, event triangulation, and duty cycle coverage. Beyond confirming binary coalescence signals, LIGO-India is expected to play a pivotal role in the detection of continuous GWs from rapidly rotating neutron stars, the stochastic background from unresolved astrophysical sources, and potentially primordial GWs originating from inflationary physics. Furthermore, artificial intelligence has emerged as an indispensable asset in modern GW astronomy. Machine learning models ranging from convolutional and recurrent neural networks to normalizing flows and generative frameworks are not only improving real-time

detection and noise classification but are revolutionizing parameter inference by offering faster and scalable alternatives to traditional Bayesian methods. As the data complexity and event rates increase with third-generation observatories such as the ET and CE, the integration of AI-based pipelines will become essential for extracting maximal scientific value. Looking ahead, a number of open challenges and exciting frontiers remain. The detection of a cosmological stochastic GW background would offer profound insights into early-Universe dynamics, including possible signatures of cosmic inflation, phase transitions, and topological defects. Meanwhile, the development of next-generation detectors such as space-based interferometers (e.g., LISA) and atom interferometry or quantum sensor platforms promises to extend the observable GW spectrum into both ultra-low and high-frequency regimes, filling the gaps left by terrestrial interferometers. In conclusion, the field of GW detection is rapidly evolving into a multidisciplinary domain that synthesizes precision engineering, computational science, data-intensive AI methods, and fundamental theoretical physics. These ongoing advancements are not only transforming our understanding of compact objects and cosmic evolution but are also enabling a new class of experiments that probe the fundamental structure of spacetime itself. The coming decades promise unprecedented discoveries that will further entrench GW astronomy as a cornerstone of multi-messenger astrophysics and cosmology.

AUTHORS' CONTRIBUTIONS

All authors have the same contribution.

DATA AVAILABILITY

The manuscript has no associated data or the data will not be deposited.

CONFLICTS OF INTEREST

The authors declare that there is no conflict of interest.

ETHICAL CONSIDERATIONS

The authors have diligently addressed ethical concerns, such as informed consent, plagiarism, data fabrication, misconduct, falsification, double publication, redundancy, submission, and other related matters.

FUNDING

This research did not receive any grant from funding agencies in the public, commercial, or non-profit sectors.

ACKNOWLEDGMENT

Authors are thankful to research team member for their fruitful discussion under matters included in this manuscripts.

---

[1] A. Einstein, Die Grundlage der allgemeinen Relativittstheorie, Ann. Phys. **354** 769 (1916). (In German). DOI: 10.1002/andp.19163540702

[2] B. P. Abbott et al., Observation of gravitational waves from a binary black hole merger, Phys. Rev. Lett. **116** 061102 (2016). DOI: 10.1103/PhysRevLett.116.061102

[3] N. Arnaud et al., The Global Control of the Virgo experiment, Nucl. Instr. and Meth. Phys. Research Sect. A **550** 1 (2005). DOI: 10.1016/j.nima.2005.03.173

[4] B. P. Abbott et al., GW151226: Observation of gravitational waves from a 22-solar-mass binary black hole coalescence, Phys. Rev. Lett. **116** 241103 (2016). DOI: 10.1103/PhysRevLett.116.241103

[5] R. Abbott et al., GW190521: A Binary Black Hole Merger with a Total Mass of 150 $M_{\odot}$, Phys. Rev. Lett. **125** 101102 (2020). DOI: 10.1103/PhysRevLett.125.101102

[6] E. Pian, Mergers of Binary Neutron Star Systems: A Multimessenger Revolution, Front. Astron. Space Sci. **7** (2020). DOI: 10.3389/fspas.2020.609460

[7] B. P. Abbott et al., An upper limit on the stochastic gravitational-wave background of cosmological origin, Nature **460** 990 (2009). DOI: 10.1038/nature08278

[8] M. R. Izquierdo et al., Large Eddy Simulations of Magnetized Mergers of Black Holes and Neutron Stars, Phys. Rev. D (2024). DOI: arXiv:2403.09770v1

[9] A. Burrows and D. Vartanyan, Core-Collapse Supernova Explosion Theory, Nature **589** 29 (2021). DOI: 10.1038/s41586-020-03059-w

[10] R. Prix, Gravitational Waves from Spinning Neutron Stars, In: Becker, W. (eds) Neutron Stars and Pulsars. Astrophysics and Space Science Library, Springer, Berlin, Heidelberg. **357** 651 (2009). DOI: 10.1007/978-3-540-76965-1_24

[11] D. Wang, Primordial Gravitational Waves 2024, Cosmology and Nongalactic Astrophysics (2024). DOI: arXiv:2407.02714

[12] Y. H. Yu and S. Wang, Primordial Gravitational Waves Assisted by Cosmological Scalar Perturbations, Eur. Phys. J. C, **84** 555 (2024). DOI: 10.1140/epjc/s10052-024-12937-w

[13] J. Antoniadis et al., The second data release from the European Pulsar Timing Array I. The dataset and timing analysis, (2023). DOI: arXiv:2306.16224

[14] M. Charisi et al., Efficient Large-Scale, Targeted Gravitational-Wave Probes of Supermassive Black-Hole Binaries, Phys. Rev. Lett. **132** 061401 (2024). DOI: 10.1103/PhysRevLett.132.061401

[15] L. Blanchet, Gravitational radiation from post-Newtonian sources and inspiralling compact binaries, Living Rev. Relativity **17** 2 (2014). DOI: 10.12942/lrr-2014-2

[16] A. Buonanno and T. Damour, Effective one-body approach to general relativistic two-body dynamics, Phys. Rev. D **59** 084006 (1999). DOI: 10.1103/PhysRevD.59.084006

[17] S. Bernuzzi, Neutron star merger remnants, Gen. Relativ. Gravit. **52** 108 (2020). DOI: 10.1007/s10714-020-02752-5

[18] S. Khan et al., Frequency-domain gravitational waves from nonprecessing black-hole binaries. II. A phenomenological model for the advanced detector era, Phys. Rev. D **93** 044007 (2016). DOI: 10.1103/PhysRevD.93.044007

[19] J. Blackman et al., Fast and Accurate Prediction of Numerical Relativity Waveforms from Binary Black Hole Coalescences Using Surrogate Models, Phys. Rev. Lett. **115** 121102 (2015). DOI: 10.1103/PhysRevLett.115.121102

[20] S. E. Field et al., Fast prediction and evaluation of gravitational waveforms using surrogate models, Phys. Rev. X **4** 031006 (2014). DOI: 10.1103/PhysRevX.4.031006

[21] Max Planck Institute for Gravitational Physics, The First Binary Black Hole Merger Observed by LIGO, (2016). [CrossRef].

[22] B. P. Abbott et al., GW170817: Observation of Gravitational Waves from a Binary Neutron Star Inspiral, Phys. Rev. Lett. **119** 161101 (2017). DOI: 10.1103/PhysRevLett.119.161101

[23] A. Mezzacappa et al., Core collapse supernova gravitational wave emission for progenitors of 9.6, 15, and 25 $M_{\odot}$, Phys. Rev. D **107**(4) 043008 (2023). DOI: 10.1103/PhysRevD.107.043008

[24] N. Lu et al., Inferring neutron star properties with continuous gravitational waves, Mon. Not. R. Astron. Soc. **521**(2) 2103 (2023). DOI: 10.1093/mnras/stad390

[25] S. Ray et al., Gravitational wave: generation and detection techniques, (2023). DOI: arXiv:2312.17291

[26] K. Schutz and Chung-Pei Ma, Constraints on individual supermassive black hole binaries from pulsar timing array limits on continuous gravitational waves, Mon. Not. R. Astron. Soc. **459**(2), 1737 (2016). DOI: 10.1093/mnras/stw768

[27] L. Z. Kelley et al., The gravitational wave background from massive black hole binaries in Illustris: spectral features and time to detection with pulsar timing arrays, Mon. Not. R. Astron. Soc. **471**, 4508 (2017). DOI: 10.1093/mnras/stx1638

[28] J. D. Romano and N. J. Cornish et al., Detection methods for stochastic gravitational-wave backgrounds: a unified treatment, Living Rev Relativ. **20**(2) (2017). DOI: 10.1007/s41114-017-0004-1

[29] N. van Remortel et al., Stochastic gravitational wave background: Methods and implications, Progress in Particle and Nuclear Physics **128** 104003 (2023). DOI: 10.1016/j.ppnp.2022.104003

[30] LIGO collaboration : [LIGO Website]

[31] B. P. Abbott et al. LIGO: The Laser Interferometer Gravitational Wave Observatory, Rep. Prog. Phys. **72** 076901 (2009). DOI: 10.1088/0034-4885/72/7/076901

[32] W. A. Edelstein et al., Limits to the measurement of displacement in an interferometric gravitational radiation detector, J. Phys. E Sci. Instrum., **11**(7) 710 (1978). DOI: 10.1088/0022-3735/11/7/030

[33] A. Abramovici et al., LIGO: The Laser Interferometer Gravitational Wave Observatory, Science **256** 5055 (1992). DOI: 10.1126/science.256.5055.325

[34] R. Abbott et al., GW190814: Gravitational Waves from the Coalescence of a 23 Solar Mass Black Hole with a 2.6 Solar Mass Compact Object, Astrophy. Journal Lett. **896** (2020). DOI: 10.3847/2041-8213/ab960f

[35] J. Abadie et al. (LIGO Scientific Collaboration, Virgo Collaboration), Search for Gravitational Waves from Low Mass Compact Binary Coalescence in LIGO's Sixth Science Run and Virgo's Science Runs 2 and 3, Phys. Rev. D **85** 082002 (2012). DOI: 10.1103/PhysRevD.85.082002

[36] J. Abadie et al. (LIGO Scientific Collaboration, Virgo Collaboration), All-sky search for gravitational-wave bursts in the second joint LIGO-Virgo run, Phys. Rev. D. **85** 122007 (2012). DOI: 10.1103/PhysRevD.85.122007

[37] Y. Michimura et al. Mirror actuation design for the interferometer control of the KAGRA gravitational wave telescope, Class. Quantum Grav. **34** 225001 (2017). DOI: 10.1088/1361-6382/aa90e3

[38] H. Abe et al., Performance of the KAGRA detector during the first joint observation with GEO 600 (O3GK), Prog. Theor. Exp. Phys. **2023**(10) 10A101 (2023). DOI: 10.1093/ptep/ptac093

[39] T. Akutsu et al., The status of KAGRA underground cryogenic gravitational wave telescope, Journal of Physics Conference Series, **1342**(1) 012014 (2020). DOI: 10.1088/1742-6596/1342/1/012014

[40] LIGO-India collaboration: [LIGO-India Website].

[41] A. Abac et al., The Science of the Einstein Telescope (2025). DOI: arXiv:2503.12263v1

[42] Einstein Telescope: [Einstein Telescope Website].

[43] P. A. Seoane et al., Astrophysics with the Laser Interferometer Space Antenna, Living Rev. Relativ. **26** 2 (2023). DOI: 10.1007/s41114-022-00041-y

[44] LISA Collaboration: [LISA Website].

[45] R. Abbott et al., Search for Gravitational Waves Associated with Gamma-Ray Bursts Detected by Fermi and Swift During the LIGO-Virgo Run O3b, Astrophy. Journal **928**(2) 186 (2022). DOI: 10.3847/1538-4357/ac532b

[46] J. G. Rollins, E. Hall, C. Wipf and L. McCuller, pygwinc: gravitational wave interferometer noise calculator Astrophysics Source Code Library Record ascl:2007.020 (2020). [Astrophysics Source Code Library], [pygwinc on LIGO GitLab].

[47] J. Baird and M. Barsuglia, Fine-Tuning the Optical Design of the Advanced Virgo+ Gravitational-Wave Detector Using Binary-Neutron Star Signals, Galaxies **8**(4) 86 (2020). DOI: 10.3390/galaxies8040086

[48] B. P. Abbott, et al., Prospects for Observing and Localizing Gravitational-Wave Transients with Advanced LIGO, Advanced Virgo and KAGRA, Living Rev. Relativ. **21** 3 (2018). DOI: 10.1007/s41114-020-00026-9

[49] L. M. A. Lobo, C. Moreno and G. G. Torales, Simulation of Fabry-Perot cavities in a Michelson interferometer, Proc. SPIE 7499, Seventh Symposium Optics in Industry, 74990W (2009). DOI: 10.1117/12.851133

[50] M. A. Arain and G. Mueller, Design of the Advanced LIGO recycling cavities, Optics Express, **16**(14), 10018 (2008). DOI: 10.1364/OE.16.010018

[51] J. Belfi and F. Marin, Sensitivity below the standard quantum limit in gravitational wave detectors with Michelson-Fabry-Perot readout, Phys. Rev. D **77** 122002 (2008). DOI: 10.1103/PhysRevD.77.122002

[52] R. X. Adhikari et al., A cryogenic silicon interferometer for gravitational-wave detection, Class. Quantum Grav. **37** 165003 (2020). DOI: 10.1088/1361-6382/ab9143

[53] F. Matichard et al., Seismic isolation of Advanced LIGO: Review of strategy, instrumentation and performance, Class. Quantum Grav. **32** 185003 (2015). DOI: 10.1088/0264-9381/32/18/185003

[54] I. Nardecchia, Detecting Gravitational Waves with Advanced Virgo, Galaxies, **10**(1), 28 (2022). DOI: 10.3390/galaxies10010028

[55] J. Aasi, et al., Advanced LIGO, Class. Quantum Grav. **32** 7 074001 (2015). DOI: 10.1088/0264-9381/32/7/074001

[56] S. Reid and I. W. Martin, Development of Mirror Coatings for Gravitational Wave Detectors, Coatings, **6**(4) 61 (2016). DOI: 10.3390/coatings6040061

[57] J. Steinlechner, Development of mirror coatings for gravitational- wave detectors, Phil. Trans. R. Soc. A **376** 20170282 (2018). DOI: 10.1098/rsta.2017.0282

[58] M. Molina-Ruiz et al., Hydrogen-Induced Ultralow Optical Absorption and Mechanical Loss in Amorphous Silicon for Gravitational-Wave Detectors, Phys. Rev. Lett. **131** 256902 (2023). DOI: 10.1103/PhysRevLett.131.256902

[59] J. Steinlechner et al., Thermal noise reduction and absorption improvements in amorphous silicon optical coatings, Class. Quantum Grav. **37** 205008 (2020). DOI: 10.1103/PhysRevD.91.042001

[60] G. D. Cole et al., Tenfold reduction of Brownian noise in high-reflectivity optical coatings, Nature Photonics **7** 644 (2013). DOI: 10.1038/nphoton.2013.174

[61] G. D. Cole et al., High-performance near- and mid-infrared crystalline coatings, Optica **3** 647 (2016). DOI: 10.1038/nphoton.2013.174

[62] G. D. Cole et al., Substrate-transferred GaAs/AlGaAs crystalline coatings for gravitational-wave detectors, Appl. Phys. Lett. **122** 110502 (2023). DOI: 10.1364/OPTICA.3.000647

[63] S. A. Webster et al., Thermal-noise limited optical cavity, Phys. Rev. A **77** 033847 (2008). DOI: 10.1103/PhysRevA.77.033847

[64] G. M Harry et al., Titania-doped tantala/silica coatings for gravitational-wave detection, Class. Quantum Grav. **24**(2) 405 (2007). DOI: 10.1088/0264-9381/24/2/008

[65] M. Fazio et al. Low thermal noise mirror coatings utilising titanium dioxide and germanium dioxide mixtures (2025). DOI: arXiv:2502.07679

[66] D. George and E. A. Huerta, Deep learning for real-time gravitational wave detection and parameter estimation: Results with Advanced LIGO data, Phys. Lett. B **778** 64 (2018). DOI: 10.1016/j.physletb.2017.12.053

[67] H. Gabbard et al., Matching matched filtering with deep networks for gravitational-wave astronomy, Phys. Rev. Lett. **120** 141103 (2018). DOI: 10.1103/PhysRevLett.120.141103

[68] Z. Que et al., Accelerating Recurrent Neural Networks for Gravitational Wave Experiments (2021). DOI: arXiv:2106.14089v1

[69] S. R. Green et al., Complete parameter inference for GW sources using deep learning, Phys. Rev. D **102** 104057 (2020). DOI: 10.1103/PhysRevD.102.104057

[70] M. Dax et al., Real-Time Gravitational Wave Science with Neural Posterior Estimation", Phys. Rev. Lett. **127** 241103 (2021). DOI: 10.1103/PhysRevLett.127.241103

[71] G. Venugopalan et al., Global optimization of multilayer dielectric coatings for precision measurements, Optics Express **32** 7 11751 (2024). DOI: 10.1364/OE.513807

0.48

(a)b

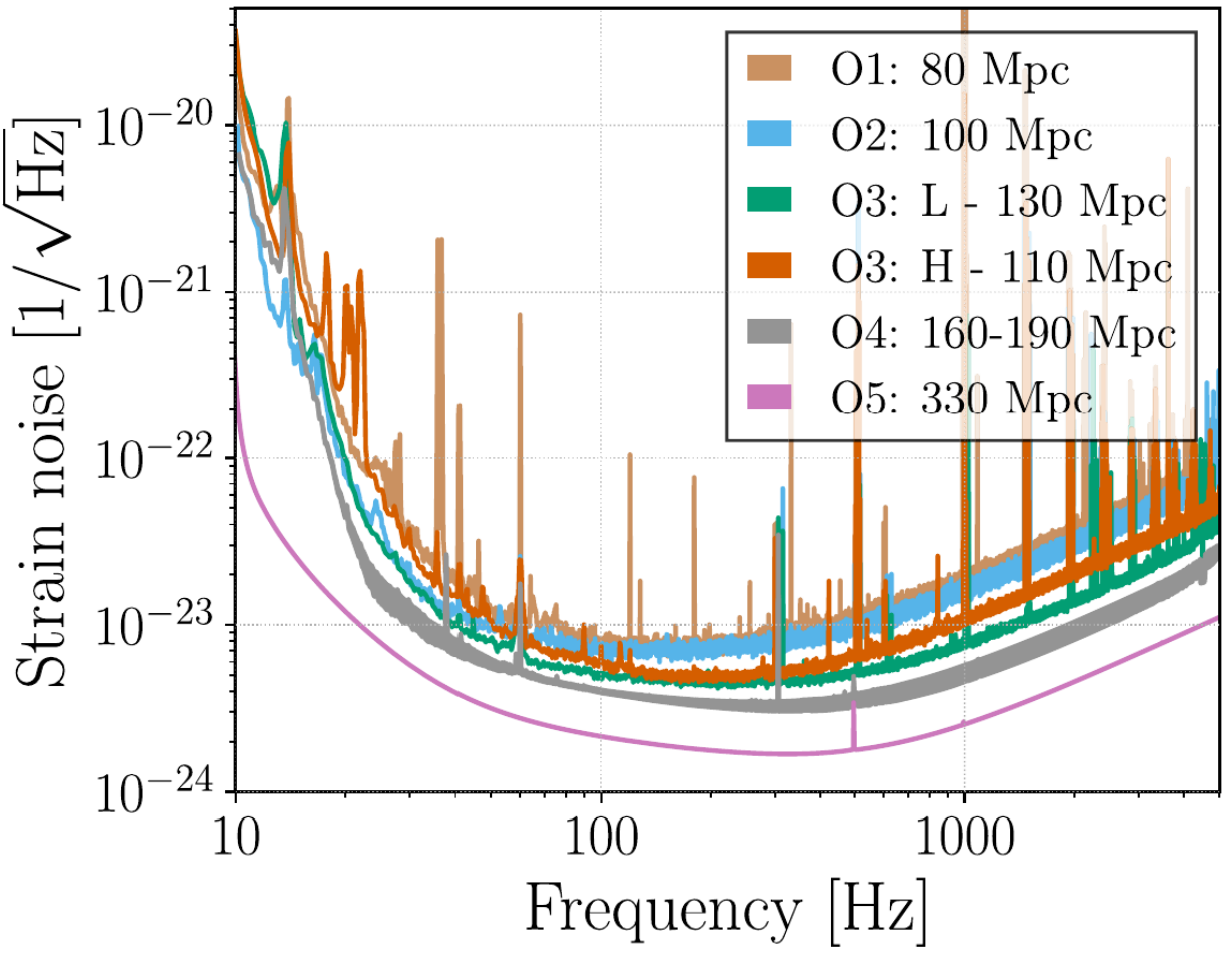

FIG. 2.

0.46

(a)b

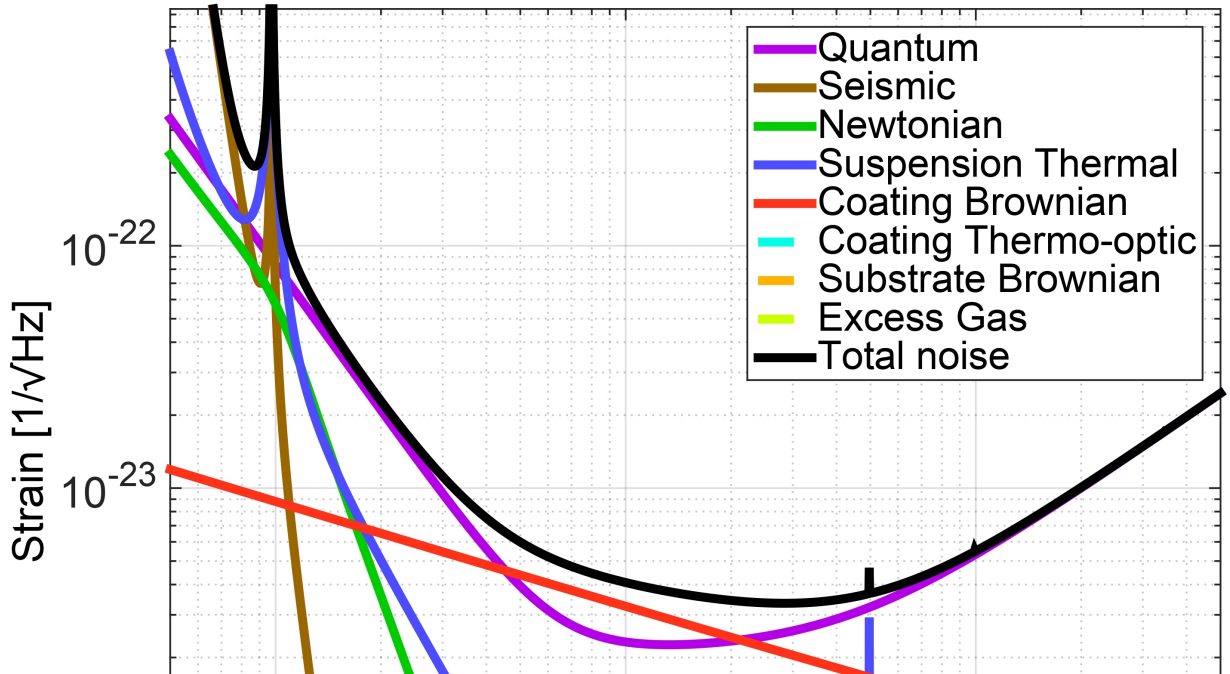

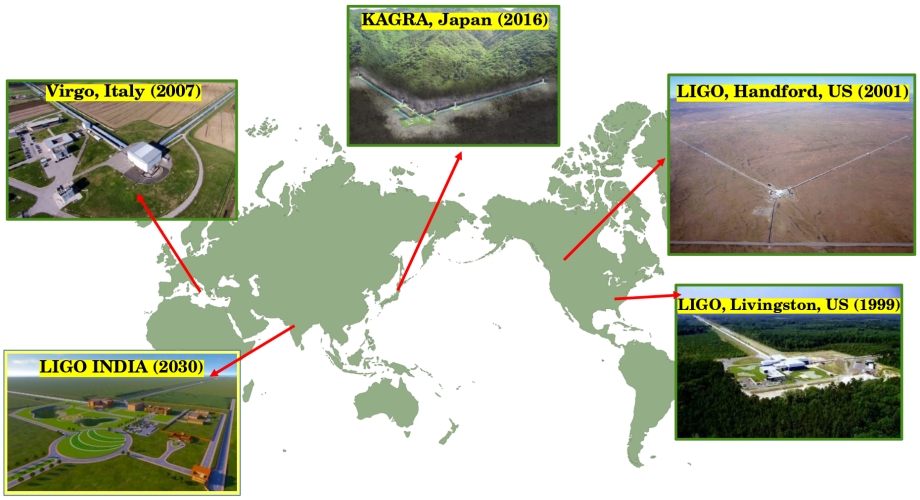

FIG. 5. Schematic map indicating the global locations of gravitational-wave observatories.

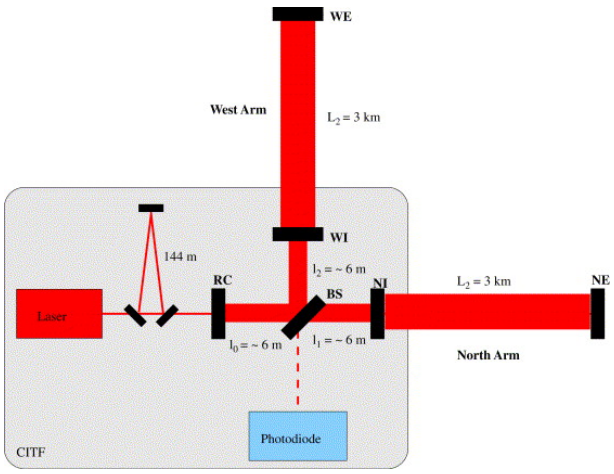

FIG. 6. Schematic diagram of Virgo experimental setup [3].

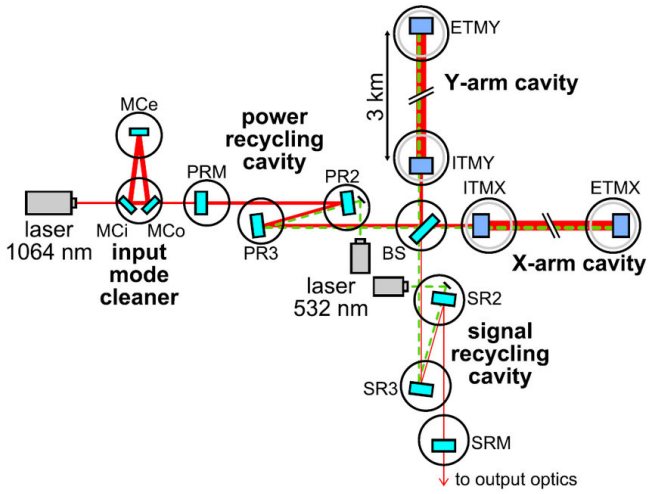

FIG. 7. Schematic diagram of KAGRA experimental setup [37].

0.49

(a)b

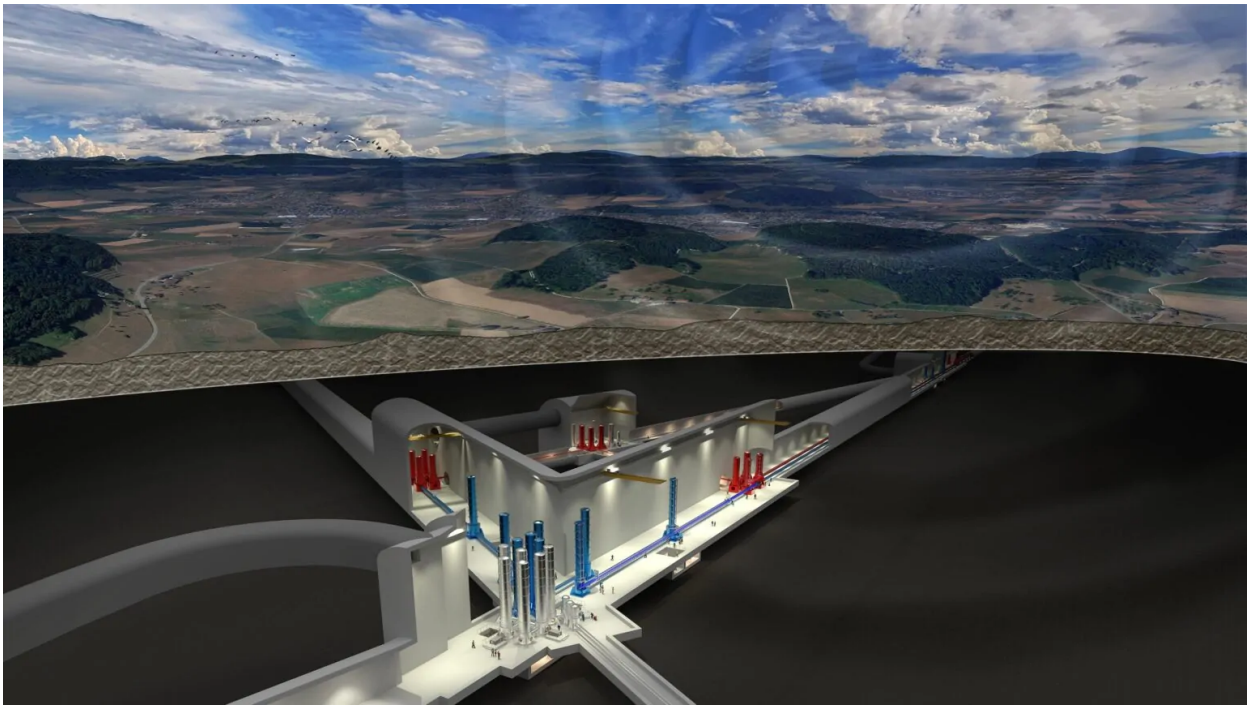

FIG. 8.

0.49

(a)b

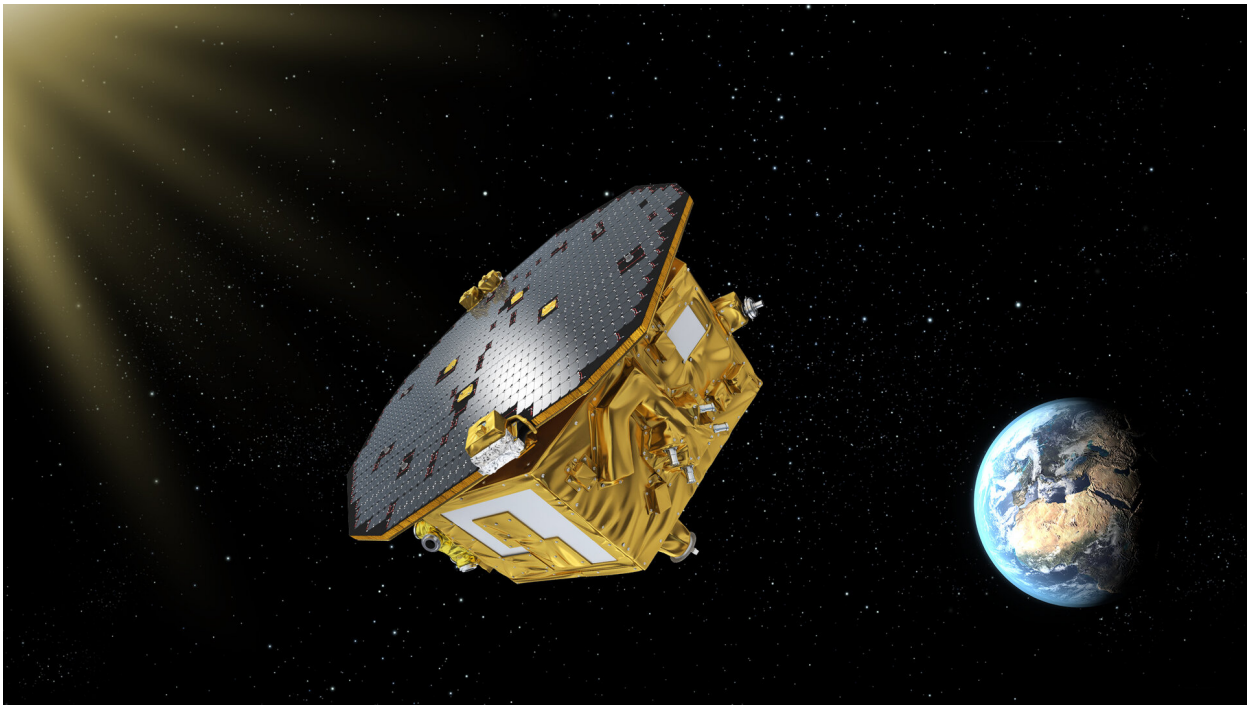

FIG. 9.

FIG. 10. (a) Schematic diagram of Einstein Telescope [41] (b) Schematic diagram of LISA [43]

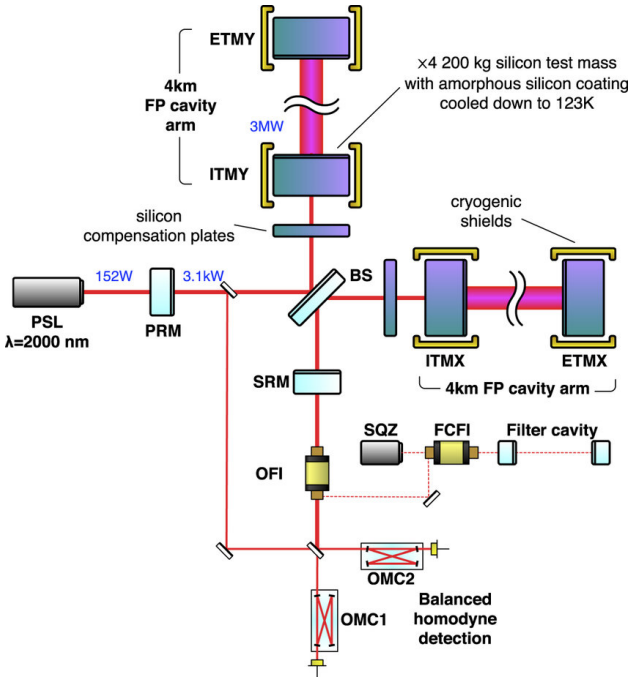

FIG. 11. Schematic of a FabryProt cavity embedded in one arm of a Michelson interferometer. The multiple reflections effectively increase the interaction length between light and spacetime strain [52].

Zero-Energy Tachyons in Curved Spacetime: Quantum and Gravitational Aspects of Superluminal Motion

Vivek Kumar Srivastava,[1] Alok Kumar Verma,[2] Garima Vaish,[3] Neha Bhatnagar,[4] and Sudhaker Upadhyay[5,*]

[1]*Department of Physics, Prof. Rajendra Singh (Rajju Bhaiya) Institute of Physical Sciences for Study and Research, Veer Bahadur Singh Purvanchal University, Jaunpur, 222001, Uttar Pradesh, India*

[2]*Department of Physics, Prof. Rajendra Singh (Rajju Bhaiya) Institute of Physical Sciences for Study and Research, Veer Bahadur Singh Purvanchal University, Jaunpur, 222001, Uttar Pradesh, India;*

[3]*Department of Physics, University of Allahabad, Prayagraj, 211002, Uttar Pradesh, India;*

[4]*School of Basic and Applied Sciences, JSPM University, Pune, 412207, Maharashtra, India;*

[5]*Department of Physics, K. L. S. College, Magadh University, Nawada, 805110, Bihar, India*

Abstract

The pioneering research of superluminal particles revealed notable advancements in special and general theory of relativity. It prompts the meticulous perusal of tachyons quantum mechanically. The analysis of zero energy tachyon and their interaction with the tardyons has been scrutinized using the Klein-Gordan equation. This interaction involves the momentary interaction of psychons and tardyons. The concept of superposition of superluminal waves is introduced, which expounds the happening of an event in the realm of subluminal frame. It provides a new avenue for the causality in a superluminal frame of reference. Approaching towards the application, the existence of mind waves has been proposed, which correspond to individual cause and effect relationships with superluminal and subluminal physics. It explains the phenomenon involved in the occurrence of an event from the consciousness of our mind in physical reality.

*Electronic address: sudhakerupadhyay@gmail.com

I. INTRODUCTION

Elementary particles can be trilaterally categorised owing to their relative motion [1]. The two groups of the particles with speed less and equal to the speed of light, subluminal and luminal respectively, have been empirically substantiated [2–13] while the third one, with a speed greater than the speed of light, has not been much explored. The study of motion of a particle or system of particles always governed by their relative motion. Non-relativistic motion of the particles is governed by the Galilean transformation. While the relativistic motion is governed by the Lorentz transformation relations. Several attempts for theoretical affirmation of superluminal particles, tachyons, have been done [14–25]. Recently, we have generalised the transformation relations for subluminal and superluminal particles to remove the ambiguity that arose earlier for tachyons [26]. It resolved the delusion about highest approachable speed based on classical and quantum formulation for faster than light particles. Albeit, existence of superluminal particles could not be found experimentally, but based on the theoretical developments, significant advancements in transdisciplinary areas have been reported [11, 27–45]. Occasionally, the existence of tachyons was questioned due to violation of the causality principle, but this was eventually settled using the different thought experiments based on the subluminal and superluminal frame of reference [46–49]. This complexity was also addressed by the authors in their earlier work [50].

In Section II, origin of the particles with superluminal velocity and transition from subluminal to superluminal physics have been discussed using gamma factor. The value of gamma factor with respect to speed renders infinity for speed approaching to speed of light and zero for infinite speed. This manifests the zero energy of particle approaching infinite velocity. These superluminal particles of zero energy are known as psychons.

The study of field associated with subluminal particles (tardyons) and psychons, its characteristic, and interaction between them have been studied comprehensively in Section III. The analyses of wave function corresponding to different states in superluminal field have been carried out by superluminal and subluminal operators. Investigation of state vector Ψ for psychon in superluminal frame is performed by using the Klein-Gordan equation for free energy tachyon. This equation reduces in the form of Helmholtz equation corresponding to frequency $\omega = 0$. The solution for this equation comes up with an idea of momentary interaction with tardyons. It signifies the point like time for an interaction, which provides

imaginary scalar potential (U) and real vector potential ($\mathbf{A}$). The one to one momentary interaction of psychon and tardyon cause a change in momentum of psychon from ($\mathbf{p}$) to ($\mathbf{p} - \mathbf{A}$). This interaction provides the total Lagrangian $\mathcal{L}$ as the sum of Lagrangian of psychon ($\mathcal{L}_p$) and Lagrangian of dendron ($\mathcal{L}_d$). On solving the action of aggregate state of psychonic and tardyonic system, Euler-Lagrange equation modified the Helmholtz equation in the form of non-homogeneous second ordered partial differential equation for psychon. The solution of this equation provides the wave function of psychon after the momentary interaction of psychon and tardyon. The resultant wave function of an event associated with the combined effect of waves associated with psychon and tardyon is discussed following the lock and key model. The characteristic of resultant waves quantum state follows the similar pattern as proposed by Penrose [51] in the role of gravity.

In Section IV, interaction has been correlated with the study of causality to validate the causality in superluminal frame of reference. Based on this correlation, we also discuss the causes which affects the happening of an event and effect as an resultant in the realist situation. In order to make a parallel application based understanding, a psychological model based on mind and brain has been discussed. The mind-brain identity theory of Place and Smart has been discussed [52, 53], which was discarded by Putnam [54]. Mind and brain are considered to be different, both by nature and characteristics. Mind is immaterialistic while brain is materialistic. The nerve units of brain world are said to be dendrons and mental units of mind world are psychons. Accordingly, brain and mind are treated as the subluminal and superluminal frame of reference. Although the relationship between the mind and tachyons has been discussed by a few authors [37, 38, 55, 56], no work has been done on how tachyons and the fundamental ideas of consciousness connect the states of mind and brain. In this analysis, the concept of consciousness developed by Penrose was examined and compared. Consciousness is attributed to quantum computations in microtubules by the Orchestrated Objective Reduction (Orch OR) theory, which governs wavefunction collapse through a gravitational objective reduction mechanism [57–59]. The characteristic of the obtained wave function along with the interaction coupling constant (μ) are used to explain the cause and effect phenomena associated with the brain. The role of consciousness in strengthening the interaction between mind and brain has been analyzed which decides the potential to manage and produce a major impact on an event in the physical world. Finally, in Section V, we articulate our concluding remarks.

II. CONCEPT OF TACHYONS AND ZERO ENERGY TACHYONS

In the theory of special relativity, transformation gamma factor is indispensable and conclusive one, given by

$$\gamma = \frac{1}{\sqrt{1 - \frac{v^2}{c^2}}}, \tag{1}$$

where $v < c$. This factor governs the relative motion of the particle or system of particles. Theory of faster-than-light particles, tachyons, pave a way forward towards the transition from Einstein's physics to the world of superluminal physics. This transition is originated from the Lorentz factor. Bilaniuk *et.al.* [14] proposed the existence of such particles with imaginary rest mass based on the Lorentz factor, Eq. (1). Further on, some other researchers claimed the gamma factor in the form of

$$\Gamma = \frac{1}{\sqrt{\frac{V^2}{c^2} - 1}}, \tag{2}$$

where $V > c$. The generalised gamma factor which is valid for all ranges of the velocities as follow [26]

$$\Gamma_G = \frac{1}{\sqrt{1 - \frac{v^2}{c^2}}} \frac{1}{\sqrt{1 - \frac{V^2}{c^2}}} \frac{v + iV}{\sqrt{v^2 + V^2}}. \tag{3}$$

The generalised gamma factor (Γ_G) can be used to deduce the transformation factor for tardyons and tachyons both, in the form of Eq. (1) & (2), respectively. The variation of the generalised gamma factor with respect to the frame velocity signifies that within the limit of the speed of light, gamma factor approaches infinity as frame velocity gets closer to the speed of light. Beyond this limit, as frame velocity exceeds to speed of light, gamma factor approaches to zero for infinite velocity from infinity. The variation of gamma factor also evinces that for the subluminal case acceleration is required for increase in velocity whereas, in superluminal case acceleration is required to decrease the velocity from infinity to the speed of light (c). Thus, beyond c, particles may behave as self-emitting energy source. For an infinite velocity, gamma variation apprises zero energy of the superluminal particles. This zero energy tachyon (ZET) at infinite velocity is termed as the psychon [37, 38, 55, 56]. The theoretical development of superluminal particles in both classical and quantum realm is based on the gamma factor. In conformity with the classical approaches, it signalizes the simultaneous existence of subluminal and superluminal frame of reference.

III. INTERACTION OF ZERO ENERGY TACHYONS AND TARDYONS

The distinct possible subluminal and superluminal states are being collectively spelled out to understand the process of interactions between them. This interaction world results an output stage whose final efficacy is in the subluminal frame of reference. In the perpetuity of this work, we have consider the superluminal operator $\hat{O}$ and subluminal operator $\hat{o}$. These operators act over a particular state in superluminal frame, defined by a wavefunction ψ as follows

$$\hat{O}\psi = E\psi, \tag{4}$$

and

$$\hat{o}\psi = e\psi. \tag{5}$$

This operation results the set of eigen values and corresponding eigen vectors. $E_i's$ and $e_i's$ are the eigen values with the eigen vectors $\psi_i's$. The combination of eigen vectors produces a new basis state vector which follows both the completeness and orthonormality conditions, results the combined output state as Ψ, defined as

$$\Psi = A_1\psi_1 + A_2\psi_2 + ... + A_n\psi_n. \tag{6}$$

The state vector Ψ represents a particular tachyonic state in superluminal frame of reference. The Klein-Gordon equation for a free tachyon having imaginary mass M over a particular state in superluminal frame is given by [15, 25, 60, 61]

$$(-M^2)\psi(\mathbf{r}, t) = 0. \tag{7}$$

where, $\equiv \dfrac{\partial^2}{\partial t^2} - \dfrac{\partial^2}{\partial x^2} - \dfrac{\partial^2}{\partial y^2} - \dfrac{\partial^2}{\partial z^2}$ and $\psi(\mathbf{r}, t) = \psi(\mathbf{r})\psi(t)$, on separating the time dependence of ψ. The solution of Eq. (7) is given by

$$\psi = e^{i\omega t}\psi(\mathbf{r}), \tag{8}$$

where $\psi(\mathbf{r})$ satisfies the following conditions

$$(\nabla^2 + k^2)\psi(\mathbf{r}) = 0 \quad \text{and} \quad \omega^2 = k^2 - M^2, \tag{9}$$

in which $\nabla^2 \equiv \dfrac{\partial^2}{\partial x^2} + \dfrac{\partial^2}{\partial y^2} + \dfrac{\partial^2}{\partial z^2}$. In the superluminal frame, energy get vanishes for infinite velocity of the particle with momentum Mc. The interaction of such superluminal

particles with an ordinary subluminal particles cause the transfer of momentum without any alteration in energy. The zero-energy solution of Eq. (7) corresponds to frequency $\omega = 0$ and $k^2 = M^2$ and satisfies the Helmholtz equation, given by

$$(\nabla^2 + M^2)\psi_0(\mathbf{r}) = 0. \tag{10}$$

Thus one may represent the field as in the form of

$$\Psi_0(\mathbf{r}, t) = e^{iMt}\psi_0(\mathbf{r}), \tag{11}$$

and four-vector A as $A^\mu = (U, \mathbf{A})$ can be represented as

$$U = \frac{\partial \Psi_0}{\partial t} = iM\Psi_0 \quad \text{and} \quad \mathbf{A} = -\nabla\Psi_0, \tag{12}$$

the scalar potential (U) is purely imaginary whereas the vector potential $(\mathbf{A})$ is real. The interaction of psychons, which obey Eq. (10), with tardyons, which follows the Schrödinger equation, an electromagnetic potential will be associated with the solution of the Helmholtz equation. On considering the interaction of psychon with tardyon, Schrödinger equation for non-relativistic tardyon interacting with electromagnetic scalar potential (U) and vector potential $(\mathbf{A})$ [37, 38, 55] will be

$$i\frac{\partial \psi}{\partial t} = \Big[\frac{1}{2m}(-i\nabla - \mu\mathbf{A})^2 + \mu U + V(\mathbf{r})\Big]\psi, \tag{13}$$

where μ is the coupling constant. As it has been discussed above that the interaction is momentary, momentum of psychon $(\mathbf{p})$ changes to the momentum $(\mathbf{p} - \mathbf{A})$ for tardyon after the interaction. It stipulates that the Schrödinger equation of system at the time other than interaction satisfies the following equation

$$i\frac{\partial \psi}{\partial t} = \Big[-\frac{1}{2m}\nabla^2 + V(\mathbf{r})\Big]\psi. \tag{14}$$

The Lagrangian density $\mathcal{L}_p$ for free tachyon field governed by the Klein-Gordan equation, Eq. (7) is given as

$$\mathcal{L}_p = \frac{1}{2}\Big[\Big(\frac{\partial \psi}{\partial t}\Big)^2 - (\nabla\psi)^2 + M^2\psi^2\Big]. \tag{15}$$

Correspondingly, Lagrangian density $\mathcal{L}_d$ for a real scalar field ϕ with mass (m) of tardyon is

$$\mathcal{L}_d = \frac{1}{2}\Big[\Big(\frac{\partial \phi}{\partial t}\Big)^2 - (\nabla\phi)^2 - m^2\phi^2\Big]. \tag{16}$$

The total Lagrangian of the system L of this inter-field interaction, with the Lagrangian density ($\mathcal{L}_{interaction} = \mu\phi\psi$) for a bilinear interaction, when the free energy tachyons will interact with the tardyons is

$$L = \int_{vol.} \left\{ \frac{1}{2} \left[\left(\frac{\partial \psi}{\partial t} \right)^2 - (\nabla\psi)^2 + M^2\psi^2 + \left(\frac{\partial \phi}{\partial t} \right)^2 - (\nabla\phi)^2 - m^2\phi^2 \right] + \mu\phi\psi \right\} d^3\mathbf{r}. \tag{17}$$

This interaction between free energy tachyons and tardyons is feasible in the context of momentary inter-field scalar interactions. This inter-field scalar momentary interaction must satisfy the condition of stability as

$$\mu^2 < m^2 M^2. \tag{18}$$

The action integral of the system of particle and field together is

$$S = \int_{t_1}^{t_2} L\, dt = \int_{t_1}^{t_2} dt \int_{vol.} \mathcal{L}\, d^3\mathbf{r} \tag{19}$$

$$= \int_{t_1}^{t_2} dt \int_{vol.} \left\{ \frac{1}{2} \left[\left(\frac{\partial \psi}{\partial t} \right)^2 - (\nabla\psi)^2 + M^2\psi^2 + \left(\frac{\partial \phi}{\partial t} \right)^2 - (\nabla\phi)^2 - m^2\phi^2 \right] - \mu\phi\psi \right\} d^3\mathbf{r}. \tag{20}$$

It results the wave function Φ, which represents the final output characteristics associated with the combined field effect of the wavefunction ψ and ϕ associated with psychons and tardyons, respectively. In a similar vein, Nobel laureate Penrose proposed the lump of the superposition of entangled quantum state in context of gravitational field [51].

IV. CORRELATION OF INTERACTION WITH CAUSALITY AND ITS APPLICATIONS

The theory of faster-than-light particles is reinforced by the most contestable concept of the principle of causality. The causality principle explicates the chronological pattern of cause and effect. In the inceptive stage of the theory of superluminal particles, causality principle was one of the most debatable subject matters. A possible intermediate elucidation is proposed on the basis of thought experiment with subluminal and superluminal frame of reference by Srivastava *et al.* [50]. This explanation for the non-violation of causality principle is different from the other's thought experiment descriptions by exploring it in the frame of reference. Based on this study cause and effect have been correlated with an

interaction between zero energy tachyon and tardyons. The combined state of superluminal and subluminal operators over the wavefunction ψ results the cause of an event, given by Eq. (6), in the superluminal frame of reference. This state is responsible for the production of an effect, defined as Φ, for any physical event under the influence of present state of the subluminal frame ϕ, which is the result of previously defined effect. Ergo, final state wavefunction Φ which is a resultant effect of a possible event. The wavefunction Φ is the function of both $\phi's$ and $\psi's$ *i.e.,* $\Phi \equiv \Phi(\psi_j, \phi_k)$, in the subluminal frame of reference. This final state wave function explains the cause and effect responsible for happening of an event.

The numerous interdisciplinary and application-based works with tachyons drive us to argue for a correlation of tachyons and tardyons with the mind and brain, respectively. The correlation proposed by Hari [37, 38, 55, 56] circumscribed only with the mind and tachyon. In the perpetuity of this work, first we analyze the concept of mind and brain and perceive their distinctions. Subsequently, a parallel model as a psychological application has been developed to correlate it with subluminal and superluminal physics.

The mind-brain identity theory emerged in the middle of the 20th century, following the early claims that mind and brain were the same. This identity theory asserts that the mental state of mind is same as the physical state of brain, as well as both mind and brain follow the same processes [52, 53]. Putnam proposed a strong disagreement for the mind-brain identity theory [54]. The proposed analysis adheres the disagreement with mind-brain identity theory. It is proposed that the brain in an organ of mind containing billions of neurons. All the collective observable activities or effects from different regions of brain spell out the upcoming phenomenon. It governs by the present and previous state of mind. Brain is supposed to be purely materialistic. Dendrons are nerve unit of brain world. Different possible states and processes of the brain are observed in the frame of brain world. Being a physical entity, it can be analyzed physically in real world. This materialistic behavior of brain emphases its nature as a subluminal frame of reference. The subluminal nature of brain world allows to espouse the non-relativistic classical and quantum theories for brain. Progressing towards theory of mind, it is purported that unlike the brain, mind is not a materialistic unit. It lies the concept to make change between the states and processes of brain. It is a non-physical entity and have its influence over the brain. The mental units of mind world are ZETs, which is defined as the psychons [38, 55]. Due to these characteristics, mind is treated as superluminal frame of reference. The thought processing happens in the

mental world which produces an observable effects. The different observed possible states of brain in subluminal frame is controlled by the mind operator of superluminal frame of reference. It ensures the development of psychons as per the relativistic quantum field theory in superluminal frame of reference.

The proposed superluminal and subluminal operators operated over the particular state of mind, whose wavefunction ψ is associated with the superluminal field is given by Eqs. (4) & (5). These operations results the eigen vectors, whoes combination result the different causes of an event, defined by Eq. (6). The interaction of mind waves with brain entities adheres to the same methodology and criteria as the interaction of tachyons and tardyons follows. This interaction results the psychonic wave associated with the mind and tardyonic or dendronic wave associated with the brain, respectively. It represents the state of mind, encompassing emotions, thoughts, perceptions, memories, *etc.* Penrose [57, 58] suggested that consciousness depends in some way on processes of the general nature of quantum computations occurring in the brain, these being terminated by some form of objective reduction (OR) theory. The Orchestrated Objective Reduction (Orch OR) theory, proposed by Penrose and Hameroff, postulates that consciousness emerges from quantum computations in neuronal microtubules, where tubulin conformations exist in superposition. These states are orchestrated by neurophysiological processes and undergo objective reduction via a gravitational threshold mechanism, as formulated by Penrose's quantum gravity hypothesis [59].

Consciousness is the awareness and interconnectedness between a particular state of mind and a state of brain. A higher level of consciousness through perception and interpretation, results in the strengthening of the coupling coefficient μ, which has the potential to alter and impact over the physical reality. Now, the combined effect of psychons and dendrons in brain is having the parallel effective outcomes in the subluminal frame of reference under the influence of wave associate with both subluminal and superluminal particles. This combined effect results the happening of an event as an effect in realist environment under the influence of causes both from the subluminal and superluminal frame as per the cause of the causality principle. The resulting wave obtained after an interaction following the frequency matching condition along with the lock and key rule represents the pattern of an energetic wave for an event that is going to happen, gets associated with the collective pattern of different mind waves and waves of the pre-happened effect observed in the brain. This study might have the

possibilities for its further exploration as subatomic processes in the brain (perhaps within neurons or even dendrites) could be influenced by quantum effects, potentially allowing for superluminal correlations or non-local interactions.

V. CONCLUSION

In this work, a theoretical model of tachyons and tardyons interconnection has been developed using the Klein-Gordan equation. This equation reduces in the form of Helmholtz equation for zero energy tachyons. Tachyons with zero energy and infinite speed are defined as psychons by the variation of the Lorentz factor. Solution of this equation provides the wave corresponding to momentary interaction of tardyon and psychon. Psychons transfer momentum without changing their energy when they come into contact with tardyons. Lagrangian density obtained by the interaction of psychons and dendrons will provide a base for the determination of stress-momentum tensor and its associated applications. After having its association with the tardyonic wave by obeying the lock and key model, final characteristics of an event represented as the effect, defined by Φ in the subluminal frame of reference. The wavefunction corresponding to the final state contains an additional coupling factor μ which determines the strength of an interaction. This interaction in superluminal and subluminal frames plays an encouraging role to develop a model in parallel universe of mind and brain as an application. Based on which, a theoretical model of mind-brain interconnection is developed using the concept of mind units, referred to as psychons and brain units, referred to as dendrons. The concept of psychons and dendrons also discarded the mind-brain identity theory. A novel interpretation of the cause and effect phenomenon is offered in conjunction with the superluminal and subluminal frames of mind and brain, respectively. Causes are associated with the different states of mind in superluminal frame, designated as Ψ. The interaction exhibits the cumulative state of the brain describing the forthcoming effect. Consciousness through perception and interpretation is the manifestation of this interaction which play crucial role in the strengthening of the coupling coefficient. It leads to present a strong connection between happening of an event and consciousness. The perpetuity of this study will create a new dimension of fundamental physics as it lies at the intersection of several advanced fields of study, including quantum mechanics, theory of relativity, neuroscience, and communication technologies.

Data Availability

The manuscript has no associated data or the data will not be deposited.

Conflicts of Interest

The authors declare that there is no conflict of interest.

Ethical Considerations

The authors have diligently addressed ethical concerns, such as informed consent, plagiarism, data fabrication, misconduct, falsification, double publication, redundancy, submission, and other related matters.

Funding

This research did not receive any grant from funding agencies in the public, commercial, or non-profit sectors.

---

[1] J R Fanchi. Tachyon Behavior Due to Mass-State Transitions at Scattering Vertices. *Physics (College. Park. Md).*, 4(1):217–228, 2022.

[2] A Einstein. On the electrodynamics of moving bodies. *Ann. Phys.*, 17(10):891–921, 1905.

[3] R Weinstock. New approach to special relativity. *Am. J. Phys.*, 33(8):640–645, 1965.

[4] N M Gibbins. Simple derivation of the Lorentz transformation. *Math. Gaz.*, 12(178):474–475, 1925.

[5] A R Lee and T M Kalotas. Lorentz transformations from the first postulate. *Am. J. Phys.*, 43(5):434–437, 1975.

[6] L Szego. The Lorentz transformation: a simple derivation. *Eur. J. Phys.*, 10(2):158–159, 1989.

[7] J M Lévy. A simple derivation of the Lorentz transformation and of the accompanying velocity and acceleration changes. *Am. J. Phys.*, 75(7):615–618, 2007.

[8] Andrea Pelissetto and Massimo Testa. Getting the Lorentz transformations without requiring an invariant speed. *Am. J. Phys.*, 83(4):338–340, 2015.

[9] C Jozsef. The Equations of Lorentz Transformation. *J. Mod. Phys.*, 7(9):952–963, 2016.

[10] S Klinaku. The general Galilean transformation. *Phys. Essays*, 30(3):243–245, sep 2017.

[11] A Issifu and F A Brito. The (De)confinement transition in tachyonic matter at finite temperature. *Adv. High Energy Phys.*, 2019:1–9, 2019.

[12] H Guo. A new paradox and the reconciliation of Lorentz and Galilean transformations. *Synthese*, 199(3-4):8113–8142, dec 2021.

[13] Jianzhong Zhao. Lorentz Transformation Derived from Relativity of Time. *J. Mod. Phys.*, 13(6):851–857, 2022.

[14] O M P Bilaniuk, V K Deshpande, and E C G Sudarshan. Meta relativity. *Am. J. Phys.*, 30(10):718–723, 1962.

[15] G Feinberg. Possibility of Faster-Than-Light Particles. *Phys. Rev*, 159(5):1089–1105, 1967.

[16] R Goldoni. Faster-than-light inertial frames and tadpoles I. *Nuov. Cim. A*, 14A(3):501–526, 1973.

[17] R Goldoni. Faster-than-light inertial frames and tadpoles II. *Nuov. Cim. A*, 14(3):527–547, 1973.

[18] M Camenzind. Relativity and free tachyons. *Gen. Relativ. Gravit*, 1(1):41–62, 1970.

[19] A Rachman and R Dutheil. On a Lorentz Transformation Related to the Dynamics of Tachyons. - I. *Lett. nuovo Cim.*, 8(10):611–617, 1973.

[20] H C Corben. Tachyon Matter and Complex Physical Variables. *Nuov. Cim. A*, 29(3):415–426, 1975.

[21] R S Vieira. An Introduction to the Theory of Tachyons. *Rev. Bras. Ensino Fis.*, 34(3):1–17, dec 2012.

[22] J M Hill and B J Cox. Einstein's special relativity beyond the speed of light. *Proc. R. Soc. A*, 468(2148):4174–4192, dec 2012.

[23] T Chang. Neutrinos as Superluminal Particles. *J. Mod. Phys.*, 04(12):6–11, 2013.

[24] J X Madarász and G Székely. The existence of superluminal particles is consistent with relativistic dynamics. *J. Appl. Log.*, 12(4):477–500, dec 2014.

[25] V K Srivastava, A K Verma, G Vaish, and S Upadhyay. A review on extended special and general theory of relativity for superluminal particles and their cosmological applications.

Zeitschrift für Naturforsch. A, 80(2):1–58, 2025.

[26] V K Srivastava, A K Verma, and G Vaish. Generalised transformation relations for superluminal particles in (3 + 1) dimensional system. *Indian J Phys*, 99(4):1415–1426, 2025.

[27] A Sen. Time and tachyon. *Int. J. Mod. Phys. A*, 18(26):4869–4888, 2003.

[28] V Gorini, A Kamenshchik, U Moschella, and V Pasquier. Tachyons, scalar fields, and cosmology. *Phys. Rev. D*, 69(12):1–16, 2004.

[29] B Wong. Existence of Tachyons and their Detection. *RRJoPHY*, 8(2):23–26, 2019.

[30] A A Antonov. Physical Reality and Essence of Imaginary Numbers in Astrophysics: Dark Matter, Dark Energy, Dark Space. *Nat. sci.*, 10(01):11–30, 2018.

[31] T Musha. Hypercomputation and Negative Entropy. *Trans Eng Comput Sci*, 1(2):1–11, 2020.

[32] A Issifu, J C M Rocha, and F A Brito. Confinement of Fermions in Tachyon Matter at Finite Temperature. *Adv. High Energy Phys.*, 2021:1–22, 2021.

[33] T E Lee, U Alvarez-Rodriguez, X H Cheng, L Lamata, and E Solano. Tachyon physics with trapped ions. *Phys. Rev. A*, 92(3):1–6, 2015.

[34] A Sen and B Zwiebach. Tachyon condensation in string field theory. *J. High Energy Phys.*, 2000(3):1–10, 2000.

[35] A Sen. Field theory of tachyon matter. *Mod. Phys. Lett. A*, 17(27):1797–1804, 2002.

[36] G Nimtz. Superluminal speed of information? *Nature*, 429(40):1–1, 2004.

[37] S D Hari. Eccles's psychons could be zero-energy tachyons. *NeuroQuantology*, 6(2):152–160, 2008.

[38] S D Hari. Mind and tachyons: How tachyon changes quantum potential and brain creates mind. *NeuroQuantology*, 9(2):255–270, 2011.

[39] Z B Todorovic. Theory of tachyonic nature of neutrino. *Fund. J. Mod. Phys.*, 6(1-2):17–47, 2013.

[40] A A Antonov. Physical Reality of Complex Numbers is Proved by Research of Resonance. *Gen. Math. Notes*, 31(2):34–53, 2015.

[41] D O Oriekhov and L S Levitov. Plasmon resonances and tachyon ghost modes in highly conducting sheets. *Phys. Rev. B*, 101(24):1–6, 2020.

[42] L Nanni. Theoretical Investigation of Subluminal Particles Endowed with Imaginary Mass. *Particles*, 4(2):325–332, 2021.

[43] K P Mooley, A T Deller, O Gottlieb, E Nakar, G Hallinan, S Bourke, D. A Frail, A Horesh,

A Corsi, and K Hotokezaka. Superluminal motion of a relativistic jet in the neutron-star merger GW170817. *Nature*, 561:355–359, 2018.

[44] K Hotokezaka, E Nakar, O Gottlieb, S Nissanke, K Masuda, G Hallinan, K P Mooley, and A T Deller. A Hubble constant measurement from superluminal motion of the jet in GW170817. *Nat. Astron.*, 3:940–944, 2019.

[45] R Duggan, H Moussa, Y Ra'di, D L Sounas, and A Alù. Stability bounds on superluminal propagation in active structures. *Nat. Commun.*, 13(1):1–10, 2022.

[46] R G Newton. Causality Effects of Particles That Travel Faster Than Light. *Phys. Rev*, 162(5):1274, 1967.

[47] O M P Bilaniuk and E C G Sudarshan. Causality and space like signal. *Nature*, 223(5204):386–387, 1969.

[48] D J Thouless. Causality and Tachyons. *Nature*, 224:506, 1969.

[49] P Caldirola and E Recami. *Causality and tachyons in relativity.* D. Reidel Publishing Company, Boston, 1980.

[50] V. K. Srivastava, A. K. Verma, and G. Vaish. Different Aspects of Faster Than Light Particles and Its Impact in Physical Reality. In R. K. Shukla, editor, *Challenges Oppor. Sci. A Multidiscip. Perspect.*, chapter 12, pages 141–155. Aryabhat Publication House, Lucknow, first edition, 2023.

[51] R Penrose. On gravity's role in quantum state reduction. *Gen. Relativ. Gravit*, 28(5):581–600, 1996.

[52] U T Place. Is consciousness a brain process? *Br. J. Psychol.*, 47(1):44–50, 1956.

[53] J J C Smart. Sensations and Brain Processes. *Philos. Rev.*, 68(2):141–156, 1959.

[54] H Putnam. *Minds and machines.* New York University Press, New York, 1960.

[55] S D Hari. Mind and tachyons: Quantum interactive dualism - Libet's causal anomalies. *NeuroQuantology*, 12(2):247–261, 2014.

[56] S D Hari. Mind and tachyons: Six-dimensional special relativity-tachyons may inform us about our future. *NeuroQuantology*, 14(1):94–105, 2016.

[57] R Penrose. *The Emperor's new mind: concerning computers, minds and the laws of physics.* Oxford University Press, 1989.

[58] R Penrose. *Shadows of the mind: an approach to the missing science of consciousness.* Oxford University Press, 1994.

[59] S Hameroff and R Penrose. Consciousness in the universe: A review of the 'Orch OR' theory. *Phys. Life Rev.*, 11(1):39–78, 2014.

[60] F F Lopez-Ruiz, J Guerrero, and V Aldaya. Proper scalar product for tachyon representations in configuration space. *Phys. Rev. D*, 102(12):1–6, 2020.

[61] J Paczos, K Debski, S Cedrowski, S Charzynski, K Turzynski, A Ekert, and A Dragan. Covariant quantum field theory of tachyons. *Phys. Rev. D*, 110(1):1–7, 2024.

International Conference on Astroparticle Physics, Gravitation and Cosmology (APGC-2025)
26-28 June 2025, GLA University, Mathura, India

Return of the technicolours

Gauhar Abbas[1,*]

[1]*Department of Physics, IIT, BHU, Varanasi*[†]

Abstract

We discuss that conventional Technicolour dynamics can be revitalized within the Dark Technicolour paradigm by invoking the Extended Most Attractive Channel hypothesis. In this framework, Standard Model fermions acquire masses via multifermion chiral condensates arising from new strong dynamics. The model incorporates three confining gauge sectors, Technicolour, Dark Technicolour, and an intermediate QCD-like sector, linked through extended gauge symmetries. The Extended Most Attractive Channel hypothesis reveals a hierarchical structure of condensates, where channels with higher net chirality become increasingly attractive. At low energies, the Dark Technicolour paradigm naturally reduces to the Froggatt–Nielsen or Standard Hierarchical Vacuum Expectation Value model, governed by residual discrete symmetries, offering a compelling resolution to the Standard Model Flavor Problem.

Based on the talk given in APGC-2025.

[†] This review is especially written for PhD students and early-stage postdoctoral fellows, aiming to provide a clear and accessible concise introduction to the dark-technicolour models.

*Electronic address: gauhar.phy@iitbhu.ac.in

I. INTRODUCTION

At the most fundamental level, our Universe is profoundly symmetric. This fact is an evidence of symmetries our Universe was born with. This elemental disposition is manifested even in the classical realm. One can observe this in the astounding patterns found throughout in nature, for example, in flowers, plants, and birds as shown in figure 1. At first glance, these patterns apparently appear highly symmetrical. However, a closer examination reveals that symmetries are subtly broken, leading to a deeper complexity beneath the surface.

Some of the symmetries of our Universe are now well understood. For instance, the visible ordinary matter, which comprises of approximately 5% of the Universe, is governed by the symmetry group $\mathrm{SU(3)_c \times SU(2)_L \times U(1)_Y}$ of the Standard Model (SM) of Particle Physics. The SM is the most successful quantum theory capable of describing the known constituents and interactions of our Universe. The truly remarkable fact is that the SM reveals an amazing and subtle pattern of symmetry even at a superficial level. For example, there are three fermionic families and three leptonic families. However, an intriguing observation is the numerical relation:

$$\begin{aligned} \text{Number of fermions} &= \text{Number of gauge bosons} \\ &= \text{Number of symmetry generators of the SM} = 12. \end{aligned} \tag{1}$$

There may still exist fundamental symmetries of the Universe that are unknown to us. This possibility is underscored by the fact that the SM symmetry group $\mathrm{SU(3)_c \times SU(2)_L \times U(1)_Y}$ accounts for only about 5% of total content of the Universe. The remaining content consists of dark-matter, which constitutes of approximately 27%, and dark energy, which makes up the rest.

This raises a compelling question: if

$$5\% \text{ of the Universe} \in \mathrm{SU(3)_c \times SU(2)_L \times U(1)_Y}, \tag{2}$$

then perhaps

$$27\% \text{ of the Universe} \in \text{a larger symmetry group, such as } \mathrm{SU(N) \times SU(N) \times \cdots \times U(1) \times \cdots \times U(1)}. \tag{3}$$

This perspective suggests, as depicted in figure 2, that dark matter may be governed by an extended or hidden gauge structure, hinting at a richer symmetry landscape beyond the SM (BSM).

A central question in modern physics is: where does the mass of the Universe's constituents come from? For ordinary visible matter, the answer lies in the Higgs mechanism. However, the introduction of the Higgs field into the SM is somewhat ad hoc and leads to several unresolved theoretical issues.

To understand this, recall that the electroweak symmetry group $\mathrm{SU(2)_L \times U(1)_Y}$ is spontaneously broken to the electromagnetic subgroup $\mathrm{U(1)_{EM}}$ by the vacuum expectation value (VEV) of the Higgs field. This symmetry-breaking process, known as the Higgs mechanism, is encoded in the SM Lagrangian:

$$\mathcal{L}_{\mathrm{SM}} = \mathcal{L}_{\mathrm{gauge,fermions}} + \mathcal{L}_{\mathrm{Higgs,gauge,fermions}}. \tag{4}$$

The first term, involving gauge fields and fermions, is highly symmetric and remains stable under quantum corrections. In contrast, the second term, which includes the Higgs field responsible for generating the masses of fermions and gauge bosons, is extremely sensitive to quantum corrections, making it one of the most theoretically fragile components of the SM.

This sensitivity becomes clear when we examine the form of the Higgs potential:

$$V(\varphi) = -\mu^2 \varphi^\dagger \varphi + \lambda (\varphi^\dagger \varphi)^2. \tag{5}$$

The spontaneous symmetry breaking (SSB) is triggered by the negative mass-squared term $(-\mu^2)$. However, the stability of the negative mass-squared term is marred by large quantum corrections:

$$\Delta\mu^2 \sim \Delta m_h^2 \sim \Lambda^2, \tag{6}$$

where Λ is the cut-off scale of the SM. This defines the well-known hierarchy problem: what stabilizes the Higgs boson mass near the electroweak scale in the presence of quadratically divergent corrections?

Over the past several decades, a significant effort has been devoted to constructing "Super Beautiful and Incredible" (SUBI) theories that elegantly solve the hierarchy problem. These frameworks predicted new physics near the electroweak scale. However, despite extensive searches at the LHC up to several TeV, no such new particles have been found.

In essence, the LHC has revealed only two critical facts:

1. The Higgs boson exists, with a measured mass of 125.20 GeV.

2. A hierarchy exists between the Higgs mass and the scale of any potential new physics.

These observations may signal a necessary shift in our theoretical perspective. Perhaps the hierarchy is not a problem to be solved, but rather a fundamental feature of nature to be understood. It may be time to reassess whether the hierarchy problem should remain the central guiding principle for BSM model building. Instead, future directions may be better motivated by observational imperatives such as the nature of dark matter, the origin of the matter–antimatter asymmetry, and the flavour structure of the SM.

A pressing and meaningful question then emerges: can the stability of the Higgs mass be achieved naturally within a framework that also accounts for these profound mysteries? Can we have a "Sweet and Inteligent" (SWEETI) theory capable of explaining, for example, the flavour structure of the SM (the so-called flavour problem) [1, 2], and at the same time stabilizing the Higgs mass with a hierarchical spectrum? From this point forward, we remain focused on addressing this question.

We begin by defining the flavour problem of the SM. Interestingly, the flavour structure of the SM is tightly linked to the Higgs field and is encoded in the Yukawa Lagrangian:

$$-\mathcal{L}_{\text{Yukawa}} \;=\; y^{u}_{ij}\bar{\psi}^{q}_{L_i}\tilde{\varphi}\psi^{u}_{R_j} + y^{d}_{ij}\bar{\psi}^{q}_{L_i}\varphi\psi^{d}_{R_j} + y^{\ell}_{ij}\bar{\psi}^{\ell}_{L_i}\varphi\psi^{\ell}_{R_j} + \text{H.c.}.$$

where L and R denote left- and right-handed charged-fermion fields, respectively.

This structure fails to explain the observed hierarchical mass spectrum of the charged fermions, as illustrated in Figure 3, as well as the hierarchy in quark mixing. Furthermore, the SM lacks a mechanism to generate neutrino masses and mixing. A genuine solution to the flavour problem must not only account for the origin of neutrino masses and oscillations but also correctly predict their mass ordering and mixing structure.

We now turn to a theoretical framework called the dark-technicolour (DTC) paradigm, which provides a compelling mechanism for achieving electroweak symmetry breaking dynamically, while also reproducing the observed Higgs boson mass. Remarkably, the DTC paradigm revives conventional technicolour (TC) theories—models that were largely set aside in the early 1980s due to their tension with electroweak precision data and difficulties in generating realistic fermion masses. In this work, we show that the DTC approach can overcome these issues, offering a viable and consistent extension of the Standard Model. Before introducing the details of the DTC paradigm, we briefly review the original TC idea and its major theoretical challenges.

II. TECHNICOLOUR

Let us consider a single fermion doublet transforming under the gauge symmetry group $SU(3)_c \times SU(2)_L \times U(1)_Y \times SU(N_{\rm TC})$ as follows [3, 4]:

$$T_q \equiv \begin{pmatrix} T \\ B \end{pmatrix}_L : (1, 2, 0, N_{\rm TC}), \tag{7}$$

$$T_R : (1, 1, +\tfrac{1}{2}, N_{\rm TC}), \qquad B_R : (1, 1, -\tfrac{1}{2}, N_{\rm TC}), \tag{8}$$

where T and B carry electric charges of $+\frac{1}{2}$ and $-\frac{1}{2}$, respectively.

Moreover, if we switch off the electroweak gauge interactions, the model exhibits a global chiral symmetry given by $SU(2)_L \times SU(2)_R$. This symmetry acts on the left- and right-handed technifermions. The strong dynamics associated with $SU(N_{\rm TC})$ leads to the formation of a chiral condensate, $\langle \bar{T}T \rangle \neq 0$, which spontaneously breaks the global symmetry down to its diagonal subgroup, $SU(2)_{L+R}$. This symmetry breaking pattern is analogous to the chiral symmetry breaking in QCD, and it gives rise to three Goldstone bosons that become the longitudinal components of the $W^{\pm}$ and Z bosons when electroweak interactions are restored.

We define the effective scalar and pseudoscalar fields associated with the technifermion bilinears as

$$\sigma \equiv \bar{T}T, \qquad \Pi^i \equiv i\bar{T}\tau^i\gamma_5 T,$$

where τ^i $(i = 1, 2, 3)$ are the Pauli matrices acting in isospin space. The scalar field σ corresponds to the chiral condensate responsible for the SSB, while the Π^i represent the associated pseudo-Nambu–Goldstone bosons (technipions). The strength of the SSB is characterized by the vacuum expectation value of the scalar field, given by

$$\langle \sigma \rangle_0 = v = 246\text{GeV}, \tag{9}$$

which is identified with the electroweak scale.

Now, let us turn on the electroweak interactions. In this context, the effective scalar and pseudoscalar fields can be organized into a complex scalar doublet φ transforming under $SU(2)_L \times U(1)_Y$ as follows:

$$\varphi = \begin{pmatrix} \Pi_1 + i\Pi_2 \\ \sigma + i\Pi_3 \end{pmatrix}. \tag{10}$$

This composite field φ plays the role of the Higgs doublet in the effective theory. The VEV of the scalar component,

$$\langle\sigma\rangle_0 = v = 246\text{GeV}, \tag{11}$$

spontaneously breaks the electroweak symmetry $SU(2)_L \times U(1)_Y$ down to the electromagnetic subgroup $U(1)_{\text{EM}}$. The three pseudoscalar components $\Pi_{1,2,3}$ become the longitudinal components of the $W^{\pm}$ and Z bosons, giving them mass via the Higgs mechanism. For more details see Ref. [5].

A. Fermion masses

In conventional TC models, it is typically assumed that the gauge symmetries of both the SM and the TC sector are embedded within a larger extended TC (ETC) gauge group. The masses of SM fermions are then generated through interactions mediated by the ETC gauge bosons and is given by [6]:

$$m_f \propto \frac{\Lambda_{\text{TC}}^3}{\Lambda_{\text{ETC}}^2}, \tag{12}$$

where Λ_{TC} is the TC confinement scale and Λ_{ETC} is the scale of the ETC interactions. However, flavour-changing neutral current (FCNC) constraints impose a severe lower bound on the ETC scale, typically requiring [6]:

$$\Lambda_{\text{ETC}} \gtrsim 10^6 \text{ GeV}. \tag{13}$$

This large separation between the TC and ETC scales leads to an extreme suppression of fermion masses, making it difficult to realistically reproduce the observed SM fermion mass spectrum.

B. Higgs mass

The lightest scalar in QCD, the σ meson, can be estimated using the relation [7]:

$$m_\sigma \approx 2m_{\text{dyn}}, \tag{14}$$

where m_{dyn} is the non-perturbatively generated dynamical mass. The mass of the σ meson turns out to be $m_\sigma \approx 500$ MeV where $m_{\text{dyn}} \approx \Lambda_{\text{QCD}} \approx 250$ MeV is assumed. This prediction is consistent with the experimental observation [8].

By analogy, the mass of a composite Higgs boson in a QCD-like TC theory can be estimated, and is given by [9]:

$$m_{\mathrm{H}} \approx 2M_{\mathrm{dyn,TC}}. \tag{15}$$

Even if we take the dynamical TC scale to be $M_{\mathrm{dyn,TC}} \approx 100$ GeV, roughly matching the electroweak scale, the resulting prediction for the Higgs mass is approximately 200 GeV. This is substantially higher than the experimentally observed Higgs mass of 125 GeV, as reported by the ATLAS and CMS collaborations [10, 11]. Consequently, QCD-like TC theories encounter a significant problem, as they tend to predict a Higgs boson that is too heavy, in clear conflict with experimental value of the Higgs mass.

C. Electroweak constraint

The dynamics of TC theories are strongly constrained by electroweak precision observables, particularly the oblique parameters S and T [12, 13]. Among these, the S parameter is especially sensitive to the particle content and spectrum of TC models. The current values, as reported by the Particle Data Group, are [8]:

$$S = -0.04 \pm 0.10, \quad T = 0.01 \pm 0.12. \tag{16}$$

These tight bounds pose a significant challenge to QCD-like TC theories, which tend to generate large positive contributions to the S parameter.

Furthermore, constraints on the vector (V) and axial-vector (A) resonances in QCD-like theories have been derived. According to Refs. [14, 15], the following bounds apply at 95 % confidence level:

$$M_A \geq M_V \geq 2 \text{ TeV}. \tag{17}$$

These limits further restrict the viable parameter space for conventional TC scenarios, motivating the search for alternative frameworks or mechanisms that can soften their contributions to the oblique parameters.

III. RETURN OF THE TECHNICOLOUR

One of the key reasons for the failure of conventional TC theories lies in the issue of hierarchy. For instance, a large hierarchy is required between the TC scale and the extended

TC (ETC) scale in order to suppress FCNCs. However, this suppression also leads to an extreme reduction in the generated fermion masses, rendering them unrealistic. This leads to us to itroduce the DTC paradigm.

A. Dark-technicolour paradigm

We now turn our attention to the DTC paradigm [16], which provides a unified framework wherein both the Standard Hierarchical Vacuum-Expectations Model (SHVM) [17–19] and the Froggatt–Nielsen (FN) mechanism [20] based on the $\mathcal{Z}_{\rm N} \times \mathcal{Z}_{\rm M}$ flavour symmetry [21–24], naturally emerge at low energies [25]. Originally proposed in [16], the DTC paradigm is based on the following key assumptions:

1. The fundamental symmetry group is given by

$$\mathcal{G} \equiv {\rm SU(N_{TC})} \times {\rm SU(N_{DTC})} \times {\rm SU(N_D)}, \tag{18}$$

   which consists of QCD-like gauge symmetries, and D represents the dark-QCD (DQCD) dynamics.

2. All fermion masses and mixings, including those of neutrinos, are generated dynamically via multi-fermion condensates. At low energies, these condensates behave as hierarchical VEVs, effectively reproducing the SHVM and addressing the flavour structure of the Standard Model.

3. The DTC framework incorporates the EMAC hypothesis, which solves the flavour problem of the SM.

The TC sector consists of TC fermions transforming under the full gauge group $\mathrm{SU}(3)_c \times \mathrm{SU}(2)_L \times \mathrm{U}(1)_Y \times \mathcal{G}$ as follows:

$$T \equiv \begin{pmatrix} T \\ B \end{pmatrix}_L : (1,2,0,{\rm N_{TC}},1,1),\ {\rm T^i_R} : (1,1,1,{\rm N_{TC}},1,1), {\rm B^i_R} : (1,1,-1,{\rm N_{TC}},1,1), \tag{19}$$

where $i = 1,2,3,\ldots,$ and the electric charges are $Q_T = +\frac{1}{2}$ and $Q_B = -\frac{1}{2}$. For collider studies, we focus on a minimal TC sector with a single fermion doublet, i.e., two flavours.

The DTC-sector, transforming under $\mathcal{G}$, includes the following Dirac fermions:

$$D^i \equiv C^i_{L,R} : (1,1,1,1,{\rm N_{DTC}},1),\ {\rm S^i_{L,R}} : (1,1,-1,1,{\rm N_{DTC}},1), \tag{20}$$

where $i = 1, 2, 3, \ldots$, and the electric charges are $Q_C = +\frac{1}{2}$ and $Q_S = -\frac{1}{2}$.

Lastly, the DQCD sector, governed by $\mathcal{G}$, features fermions transforming as:

$$\begin{aligned} F_{L,R} \equiv\ & U^i_{L,R} : (3, 1, \frac{4}{3}, 1, 1, \mathrm{N_D}), \mathrm{D^i_{L,R}} : (3, 1, -\frac{2}{3}, 1, 1, \mathrm{N_D}), \\ & N^i_{L,R} : (1, 1, 0, 1, 1, \mathrm{N_D}),\ \mathrm{E^i_{L,R}} : (1, 1, -2, 1, 1, \mathrm{N_D}), \end{aligned} \tag{21}$$

with $i = 1, 2, 3, \ldots$. These fields are vector-like under the Standard Model gauge symmetries.

We assume that the TC fermions, left-handed SM fermions, and F_R fermions are unified under an ETC symmetry, while an Extended DTC (EDTC) symmetry similarly unifies the DTC fermions, right-handed SM fermions, and F_L fermions. The SU(N_D) gauge group, corresponding to the DQCD sector, serves as a bridge between the TC and DTC dynamics. This connection naturally suppresses mixing between the two sectors by a factor of $1/\Lambda$, where Λ is the confinement scale of DQCD.

In the DTC framework, the full symmetry group $\mathcal{G}$ gives rise to three global axial symmetries that are classically conserved but quantum mechanically anomalous: $\mathrm{U(1)^{TC}_A}$, $\mathrm{U(1)^{DTC}_A}$, and $\mathrm{U(1)^{D}_A}$. These $\mathrm{U(1)_A}$ symmetries can be broken by non-perturbative effects such as instantons, which are a characteristic feature of strongly coupled gauge theories. The instanton background leads to the formation of effective multi-fermion interactions—specifically, $2K$-fermion operators—that develop nonzero VEVs [26]. As a result, the original continuous symmetry is broken down to a discrete subgroup:

$$\mathrm{U(1)_A} \to \mathcal{Z}_{\mathrm{2K}}, \tag{22}$$

where K is the number of massless fermion flavours transforming under the fundamental representation of the corresponding SU(N) gauge group. This residual discrete symmetry plays an important role in determining the low-energy structure and the spectrum of the theory, as first discussed in [26].

Consequently, the DTC framework generically leads to a residual discrete flavour symmetry of the form:

$$\mathcal{Z}_N \times \mathcal{Z}_M \times \mathcal{Z}_P \tag{23}$$

where $\mathrm{N} = 2\mathrm{K_{TC}}$, $\mathrm{M} = 2\mathrm{K_{DTC}}$, and $\mathrm{P} = 2\mathrm{K_D}$. These discrete symmetries correspond to conserved axial charges modulo $2K$, as originally noted in [26].

B. The extended most attractive channel hypothesis

Aoki and Bando (AB), in a series of seminal papers [27–29], demonstrated that multifermion states of the form $(\bar{\psi}_L\psi_R)^n$, composed of $2n$ fermions, exhibit an increasingly attractive interaction as the number of fermion pairs n increases. This enhanced attraction arises from the underlying spin and chiral structure of the system and can be systematically characterized in terms of these features [29]. Before turning to the experimental constraints relevant to the DTC paradigm, we briefly summarize the key principles of this framework.

As a concrete illustration, consider a two-fermion system in a non-Abelian gauge theory, as studied in [27–29]. If the interaction between the fermions is mediated by a single gauge boson exchange, the effective potential is given by:

$$V = g^2, F(i_1, i_2; i_1', i_2'), \langle \lambda^a(1), \lambda^a(2) \rangle, \tag{24}$$

where $\lambda^a(n)$ are the generators of the SU(N) gauge group acting on the nth fermion, and g denotes the gauge coupling constant. The indices $i_n^{(\prime)}$ encapsulate all non-colour degrees of freedom, such as momentum, spin, and chirality.

In the "most attractive channel" (MAC) hypothesis [30], the interaction factor F is assumed to be universal for fermions residing in different representations of the gauge group SU(N). Within this framework, condensation is allowed only in the $\psi_L\psi_L$ or $\bar{\psi}_L\psi_R$ channels. Consequently, the factor F plays a relatively trivial role in determining the dynamics of condensation under the MAC assumption.

In the EMAC hypothesis [27–29], the interaction factor F acquires a nontrivial dependence on the chirality of the participating fermions, specifically through the number and configuration of fermions involved in a given chiral condensate. AB argue that, due to the attractive nature of the potential in Eq. (24), a chiral condensate forms at a dynamical scale μ, which is determined by the condition:

$$V\left(g^2(\mu^2)\right) \sim 1, \tag{25}$$

where the running gauge coupling is given by:

$$g^2(\mu^2) = \frac{1}{\beta_0 \log(\mu^2/\Lambda^2)}. \tag{26}$$

Solving this condition yields the condensation scale:

$$\mu^2 \sim \Lambda^2 \exp\left(-\frac{F\langle\lambda\lambda\rangle}{\beta_0}\right). \tag{27}$$

This expression reveals that even small differences in chiral structure, encoded in the factor F, are exponentially magnified in the formation of condensates. As a result, channels with more favorable chiral configurations dominate dynamically. However, since the exact structure of F is not fully known, a complete quantitative description of the hierarchy among competing chiral channels remains an open question.

In the case of a two-fermion system, the EMAC hypothesis identifies $\bar{\psi}_R\psi_L$ and $\psi_L\psi_L$ as the most attractive channels in the spin-zero sector, consistent with the traditional MAC hypothesis. For spin-one, colour-singlet states, the configuration with highest chiral attraction is $\bar{\psi}_L\psi_L$. Further technical details and derivations can be found in Refs. [27–29].

In general, an n-body colour-singlet, spin-zero multifermion condensate of the form $(\bar{\psi}_R\psi_L)^{n/2}$, possessing maximal chirality for even n, can be characterized by its average energy as follows [27–29]:

$$\bar{E}(n) = \frac{1}{n}E(\bar{\psi}_R^{n/2}\psi_L^{n/2}) \lesssim V_E^{LL}\frac{N^2-1}{N} - V_M^{LL}\frac{N-1}{N}(n+3N+1), \tag{28}$$

where V_E^{LL} and V_M^{LL} denote the electric and magnetic components of the two-body Hamiltonian, respectively.

The above expression shows that $\bar{E}(n)$ decreases linearly with n, indicating that multifermion systems become increasingly attractive as the number of fermions grows. Consequently, a natural hierarchy emerges among the multifermion chiral condensates, following the pattern:

$$\langle\bar{\psi}_R\psi_L\rangle \ll \langle\bar{\psi}_R\bar{\psi}_R\psi_L\psi_L\rangle \ll \langle\bar{\psi}_R\bar{\psi}_R\bar{\psi}_R\psi_L\psi_L\psi_L\rangle \ll \cdots . \tag{29}$$

This series terminates at $n_{\max}$, which is bounded by the number of distinct fermion species available in the theory [27–29].

The interaction factor F exhibits a proportional dependence on the net chirality $\Delta\chi$ of the multifermion operator:

$$F \propto \Delta\chi, \tag{30}$$

where $\Delta\chi$ denotes the total chirality carried by the condensate. This leads to a parametrization of the hierarchical structure of chiral multifermion condensates as [29]:

$$\langle(\bar{\psi}_R\psi_L)^n\rangle \sim \left(\Lambda\exp(k\Delta\chi)\right)^{3n}, \tag{31}$$

with k being a constant characterizing the chirality dependence, and Λ representing the confinement scale of the non-Abelian gauge dynamics.

C. Effective low energy limits of the DTC paradigm

At low energies, the DTC paradigm can be effectively mapped onto either the SHVM or the FN mechanism based on the discrete symmetry $\mathcal{Z}_{\rm N} \times \mathcal{Z}_{\rm M}$, as illustrated in Figure 4. In this section, we examine how these low-energy effective descriptions emerge from the fundamental dynamics governing the DTC framework.

The chiral condensates in a QCD-like theory, following the hierarchical structure described in Eq. (31), are given by [31]:

$$\begin{aligned}
\langle \bar{T}T \rangle_{\Lambda_{\rm ETC}} &\approx -\frac{N_{\rm TC}}{4\pi^2} \left[\Lambda_{\rm TC} \exp(k_{\rm TC}\Delta\chi_{\rm TC})\right]^3 , \\
\langle \bar{D}D \rangle_{\Lambda_{\rm EDTC}} &\approx -\frac{N_{\rm DTC}}{4\pi^2} \left[\Lambda_{\rm DTC} \exp(k_{\rm DTC}\Delta\chi_{\rm DTC})\right]^3 , \\
\langle \bar{F}F \rangle_{\Lambda_{\rm GUT}} &\approx -\frac{N_{\rm D}}{4\pi^2} \left[\Lambda \exp(k_{\rm D}\Delta\chi_{\rm D})\right]^3 .
\end{aligned} \tag{32}$$

Figure 5 schematically illustrates the interactions responsible for charged fermion mass generation. The upper panel shows the generic interaction vertices among SM, TC, DQCD, and DTC fermions. The lower panel depicts the resulting mass-generation mechanism: the chiral condensate $\langle\varphi\rangle$ acts analogously to the Higgs VEV, while the DTC-induced multifermion condensates are denoted by $\langle\chi_r\rangle$.

Using Eq. (32), the mass matrices for the up-type quarks, down-type quarks, and charged leptons can be expressed as:

$$\mathcal{M}_{,,\ell} = y^f_{ij} \left(\frac{N_{\rm D}^{n_i/2}\, N_{\rm TC}}{4\pi^2}\right) \frac{\Lambda^3_{\rm TC}}{\Lambda^2_{\rm ETC}} \exp(6k_{\rm TC}) \frac{1}{\Lambda} \left(\frac{N_{\rm DTC}}{4\pi^2}\right)^{n_i} \frac{\Lambda^{n_i+1}_{\rm DTC}}{\Lambda^{n_i}_{\rm EDTC}} \left[\exp(3n_i k_{\rm DTC})\right]^{n_i/2} , \tag{33}$$

where we assume the TC chiral condensate is of the form $\langle \bar{T}_R T_L \rangle$, corresponding to $\Delta\chi_{\rm TC} = 2$. Furthermore, we take the ETC and EDTC couplings to be $g_{\rm ETC} = g_{\rm EDTC} \sim \mathcal{O}(1 - 4\pi)$, and assume $k_{\rm TC} > 0$. The quantity $n_i = 2, 4, 6, \ldots, 2n$ denotes the number of fermions involved in the multifermion DTC chiral condensate, which plays the role of the effective VEV $\langle\chi_r\rangle$ [16]. The scales $\Lambda_{\rm TC}$, $\Lambda_{\rm DTC}$, and Λ correspond to the confinement scales of the TC, DTC, and DQCD sectors, respectively.

At low energies, the theory reduces to the following effective Lagrangian:

$$\mathcal{L} = \frac{1}{\Lambda}\left[y^u_{ij}\bar{\psi}^q_{L_i}\tilde{\varphi}\psi^u_{R_i}\chi_r + y^d_{ij}\bar{\psi}^q_{L_i}\varphi\psi^d_{R_i}\chi_r + y^\ell_{ij}\bar{\psi}^\ell_{L_i}\varphi\psi^\ell_{R_i}\chi_r\right] + \text{H.c.}, \tag{34}$$

i and j show family indices, ψ^q_L, ψ^ℓ_L are the quark and leptonic doublets, $\psi^u_R, \psi^d_R, \psi^\ell_R$ denote the right-handed up, down-type quarks and leptons, φ and $\tilde{\varphi} = -i\sigma_2\varphi^*$ are the SM Higgs field, and its conjugate, where σ_2 denote the second Pauli matrix.

Moreover, the gauge-singlet scalar fields χ_r transform trivially under the Standard Model gauge group $\mathrm{SU(3)_c \times SU(2)_L \times U(1)_Y}$ as:

$$\chi_r : (1, 1, 0), \tag{35}$$

where $r = 1 - 6$.

The Lagrangian in Eq. 34, in fact, the effective Lagrangian of the SHVM, obtained by imposing a discrete flavour symmetry of the form

$$\mathcal{Z}_\mathrm{N} \times \mathcal{Z}_\mathrm{M} \times \mathcal{Z}_\mathrm{P}, \tag{36}$$

as discussed in Refs. [16–19], and given by,

$$\begin{aligned}
\mathcal{L}_f \;=\; & \frac{1}{\Lambda}\Big[y^u_{11}\bar{\psi}^q_{L_1}\tilde{\varphi}\psi^u_{R_1}\chi_1 + y^u_{13}\bar{\psi}^q_{L_1}\tilde{\varphi}\psi^u_{R_3}\chi_5 + y^u_{22}\bar{\psi}^q_{L_2}\tilde{\varphi}\psi^u_{R_2}\chi_2 + y^u_{23}\bar{\psi}^q_{L_2}\tilde{\varphi}\psi^u_{R_3}\chi^\dagger_2 + y^u_{33}\bar{\psi}^q_{L_3}\tilde{\varphi}\psi^u_{R_3}\chi_3 \\
& + y^d_{11}\bar{\psi}^q_{L_1}\varphi\psi^d_{R_1}\chi_1 + y^d_{12}\bar{\psi}^q_{L_1}\varphi\psi^d_{R_2}\chi_4 + y^d_{22}\bar{\psi}^q_{L_2}\varphi\psi^d_{R_2}\chi_5 + y^d_{33}\bar{\psi}^q_{L_3}\varphi\psi^d_{R_3}\chi_6 \\
& + y^\ell_{11}\bar{\psi}^\ell_{L_1}\varphi\psi^\ell_{R_1}\chi_1 + y^\ell_{12}\bar{\psi}^\ell_{L_1}\varphi\psi^\ell_{R_2}\chi_4 + y^\ell_{13}\bar{\psi}^\ell_{L_1}\varphi\psi^\ell_{R_3}\chi_5 + y^\ell_{22}\bar{\psi}^\ell_{L_2}\varphi\psi^\ell_{R_2}\chi_5 + y^\ell_{23}\bar{\psi}^\ell_{L_2}\varphi\psi^\ell_{R_3}\chi^\dagger_2 \\
& + y^\ell_{33}\bar{\psi}^\ell_{L_3}\varphi\psi^\ell_{R_3}\chi_2 + \mathrm{H.c.}\Big].
\end{aligned} \tag{37}$$

The gauge singlet fields χ_r acquire the VEVs $\langle\chi_r\rangle$ after the SSB of the $\mathcal{Z}_\mathrm{N} \times \mathcal{Z}_\mathrm{M} \times \mathcal{Z}_\mathrm{P}$ flavour symmetry. The mass matrices of charged fermions are now given by [17],

$$\begin{aligned}
&= \frac{v}{\sqrt{2}}\begin{pmatrix} y^u_{11}\epsilon_1 & 0 & y^u_{13}\epsilon_5 \\ 0 & y^u_{22}\epsilon_2 & y^u_{23}\epsilon_2 \\ 0 & 0 & y^u_{33}\epsilon_3 \end{pmatrix}, = \frac{v}{\sqrt{2}}\begin{pmatrix} y^d_{11}\epsilon_1 & y^d_{12}\epsilon_4 & 0 \\ 0 & y^d_{22}\epsilon_5 & 0 \\ 0 & 0 & y^d_{33}\epsilon_6 \end{pmatrix}, _\ell = \frac{v}{\sqrt{2}}\begin{pmatrix} y^\ell_{11}\epsilon_1 & y^\ell_{12}\epsilon_4 & y^\ell_{13}\epsilon_5 \\ 0 & y^\ell_{22}\epsilon_5 & y^\ell_{23}\epsilon_2 \\ 0 & 0 & y^\ell_{33}\epsilon_2 \end{pmatrix},
\end{aligned} \tag{38}$$

where $\epsilon_r = \dfrac{\langle\chi_r\rangle}{\Lambda}$ and $\epsilon_r < 1$.

The masses of charged fermions can be written as,

$$\begin{aligned}
m_t \;&=\; |y^u_{33}|\,\epsilon_3 v/\sqrt{2},\; m_c = \;|y^u_{22}\epsilon_2|\,v/\sqrt{2},\; m_u = |y^u_{11}|\,\epsilon_1 v/\sqrt{2}, \\
m_b \;&\approx\; |y^d_{33}|\epsilon_6 v/\sqrt{2}, m_s \approx \;\left|y^d_{22}\right|\epsilon_5 v/\sqrt{2}, m_d \approx \left|y^d_{11}\right|\;\epsilon_1 v/\sqrt{2}, \\
m_\tau \;&\approx\; |y^\ell_{33}|\epsilon_2 v/\sqrt{2},\; m_\mu \approx \;|y^\ell_{22}|\epsilon_5 v/\sqrt{2},\; m_e = |y^\ell_{11}|\,\epsilon_1 v/\sqrt{2}.
\end{aligned} \tag{39}$$

The quark mixing angles are given by,

$$\sin\theta_{12} \;\simeq\; \left|\frac{y^d_{12}}{y^d_{22}}\right|\frac{\epsilon_4}{\epsilon_5},\; \sin\theta_{23} \simeq \left|\frac{y^u_{23}}{y^u_{33}}\right|\frac{\epsilon_2}{\epsilon_3}, \sin\theta_{13} \simeq \left|\frac{y^u_{13}}{y^u_{33}}\right|\frac{\epsilon_5}{\epsilon_3}. \tag{40}$$

To generate neutrino masses, we assume that the ETC and EDTC symmetries are unified within a grand unified theory (GUT). This unification gives rise to effective dimension-6 operators, as presented in equation 42, from which the neutrino mass terms emerge. The corresponding interactions are depicted in the upper part of Figure 6, where GUT gauge bosons mediate interactions between the F_L and F_R fermions. The chiral condensate $\langle \bar{F}_L F_R \rangle$, illustrated as a circular blob, plays a role analogous to a scalar VEV, denoted by $\langle \chi_7 \rangle$. The lower part of Figure 6 schematically represents the effective formation of the neutrino mass term.

The neutrino mass matrix is recovered as,

$$= y^{\nu}_{ij} \mathrm{N_D}^{(n_i+2)/2} \frac{\mathrm{N_{TC}}}{4\pi^2} \frac{\Lambda^3_{\mathrm{TC}}}{\Lambda^2_{\mathrm{ETC}}} \exp(6k_{\mathrm{TC}}) \frac{1}{\Lambda} \left[\frac{\mathrm{N_{DTC}}}{4\pi^2}\right]^{n_i} \frac{\Lambda^{n_i+1}_{\mathrm{DTC}}}{\Lambda^{n_i}_{\mathrm{EDTC}}} \left[\exp(n_i k_{\mathrm{DTC}})\right]^{n_i/2} \frac{1}{\Lambda} \frac{\mathrm{N_D}}{4\pi^2} \frac{\Lambda^3}{\Lambda^2_{\mathrm{GUT}}} \exp(6k_{\mathrm{D}}) \quad (41)$$

The interactions illustrated in Figure 6 lead, at low energies, to the following effective Lagrangian:

$$-\mathcal{L}^{\nu}_{\mathrm{Yukawa}} \;=\; y^{\nu}_{ij}\, \bar{\psi}^{\ell}_{L_i}\, \tilde{\varphi}\, \nu_{f_R} \left[\frac{\chi_r \chi_7 \,(\text{or } \chi_r \chi_7^{\dagger})}{\Lambda^2}\right] + \mathrm{H.c.}. \quad (42)$$

The above Lagrangian, after imposing the $\mathcal{Z}_{\mathrm{N}} \times \mathcal{Z}_{\mathrm{M}} \times \mathcal{Z}_{\mathrm{P}}$ flavour symmetry, becomes [16–19],

$$\begin{aligned} \mathcal{L}_{\nu} \;=\; \frac{1}{\Lambda^2}\Big[& y^{\nu}_{11} \bar{\psi}^{\ell}_{L_1} \tilde{\varphi} \psi^{\nu}_{R_1} \chi_1^{\dagger} \chi_7^{\dagger} + y^{\nu}_{12} \bar{\psi}^{\ell}_{L_1} \tilde{\varphi} \psi^{\nu}_{R_2} \chi_4^{\dagger} \chi_7 + y^{\nu}_{13} \bar{\psi}^{\ell}_{L_1} \tilde{\varphi} \psi^{\nu}_{R_3} \chi_4^{\dagger} \chi_7 + y^{\nu}_{22} \bar{\psi}^{\ell}_{L_2} \tilde{\varphi} \psi^{\nu}_{R_2} \chi_4 \chi_7 \\ & + y^{\nu}_{23} \bar{\psi}^{\ell}_{L_2} \tilde{\varphi} \psi^{\nu}_{R_3} \chi_4 \chi_7 + y^{\nu}_{32} \bar{\psi}^{\ell}_{L_3} \tilde{\varphi} \psi^{\nu}_{R_2} \chi_5 \chi_7 + y^{\nu}_{33} \bar{\psi}^{\ell}_{L_3} \tilde{\varphi} \psi^{\nu}_{R_3} \chi_5 \chi_7 + \mathrm{H.c.}\Big], \end{aligned} \quad (43)$$

and Eq. 41 reduces to the following Dirac neutrino mass matrix:

$$= \frac{v}{\sqrt{2}} \begin{pmatrix} y^{\nu}_{11}\epsilon_1\epsilon_7 & y^{\nu}_{12}\epsilon_4\epsilon_7 & y^{\nu}_{13}\epsilon_4\epsilon_7 \\ 0 & y^{\nu}_{22}\epsilon_4\epsilon_7 & y^{\nu}_{23}\epsilon_4\epsilon_7 \\ 0 & y^{\nu}_{32}\epsilon_5\epsilon_7 & y^{\nu}_{33}\epsilon_5\epsilon_7 \end{pmatrix}, \quad (44)$$

where $\epsilon_7 = \frac{\langle \chi_7 \rangle}{\Lambda} < 1$.

Assuming all couplings are of order one, we arrive at the following remarkable predictions for the leptonic mixing angles:

$$\sin\theta^{\ell}_{12} \;\simeq\; \left| -\frac{y^{\nu}_{12}}{y^{\nu}_{22}} + \frac{y^{\ell}_{12}\,\epsilon_4}{y^{\ell}_{22}\,\epsilon_5} + \frac{y^{\ell *}_{23} y^{\nu}_{13}\,\epsilon_4}{y^{\ell}_{33} y^{\nu}_{33}\,\epsilon_5} \right| \geq \left| -\frac{y^{\nu}_{12}}{y^{\nu}_{22}} \right| - \left| \frac{y^{\ell}_{12}}{y^{\ell}_{22}} + \frac{y^{\ell *}_{23} y^{\nu}_{13}}{y^{\ell}_{33} y^{\nu}_{33}} \right| \frac{\epsilon_4}{\epsilon_5} \approx 1 - 2\sin\theta_{12}, \quad (45)$$

$$\sin\theta^{\ell}_{23} \;\simeq\; \left| \frac{y^{\ell}_{23}}{y^{\ell}_{33}} - \frac{y^{\nu}_{23}\,\epsilon_4}{y^{\nu}_{33}\,\epsilon_5} \right| \geq \left| \frac{y^{\ell}_{23}}{y^{\ell}_{33}} \right| - \left| \frac{y^{\nu}_{23}}{y^{\nu}_{33}} \right| \frac{\epsilon_4}{\epsilon_5} \approx 1 - \sin\theta_{12}, \quad (46)$$

$$\sin\theta^{\ell}_{13} \;\simeq\; \left| -\frac{y^{\nu}_{13}\,\epsilon_4}{y^{\nu}_{33}\,\epsilon_5} + \frac{y^{\ell}_{13}\,\epsilon_5}{y^{\ell}_{33}\,\epsilon_2} \right| \geq \left| \frac{y^{\nu}_{13}}{y^{\nu}_{33}} \right| \frac{\epsilon_4}{\epsilon_5} - \left| \frac{y^{\ell}_{13}}{y^{\ell}_{33}} \right| \frac{\epsilon_5}{\epsilon_2} \approx \sin\theta_{12} - \frac{m_s}{m_c}, \quad (47)$$

where $m_s/m_c = \epsilon_5/\epsilon_2$. Thus, we conclude that the leptonic mixing angles are predicted in the SHVM framework in terms of the Cabibbo angle and the mass ratio of the strange to charm quark.

This leads to highly precise predictions for the leptonic mixing angles [18]:

$$\begin{aligned} \sin\theta_{12}^{\ell} &= 0.55 \pm 0.00134, \\ \sin\theta_{23}^{\ell} &= 0.775 \pm 0.00067, \\ \sin\theta_{13}^{\ell} &\in [0.1413,\ 0.1509], \end{aligned} \tag{48}$$

which may be tested in future neutrino oscillation experiments such as DUNE, Hyper-Kamiokande, and JUNO [32].

D. Reproducing the Higgs mass

Scaling up two-flavor QCD suggests the lightest scalar singlet lies in the range 1.0 TeV $\lesssim M_{\rm H,TC} \lesssim$ 1.4 TeV, heavier than the observed Higgs mass [33]. Foadi, Frandsen, and Sannino (FFS) showed that TC dynamics can still yield a 125 GeV Higgs once SM top-quark radiative corrections are included, which lower the TC Higgs mass toward the experimental value [10, 11]. The corrected mass is given by [33]

$$M_{\rm H}^2 = M_{\rm H,TC}^2 - 12\,\kappa^2 r_t^2 m_t^2, \tag{49}$$

with $r_t = 1$ for an SM-like top Yukawa and $\kappa = \mathcal{O}(1)$. For technifermions in the fundamental representation of $SU(N_{\rm TC})$, FFS showed that the above mass range is naturally realized with a single technidoublet. We therefore adopt $\Lambda_{\rm TC} = M_{\rm H,TC} = 1$ TeV as our benchmark.

E. S-parameter

For our TC model we take $\Lambda_{\rm TC} = 10^3$ GeV and $f = F_{\Pi_{\rm TC}} = 246$ GeV (for two flavors). The corresponding upper bound is

$$\frac{4\pi F_{\Pi}}{\sqrt{N}} \simeq 2186 \text{ GeV}. \tag{50}$$

We conjecture that the $1/\sqrt{N_{\rm TC}}$ scaling becomes effective only for $N_{\rm TC} > 3$, so that for $N_{\rm TC} = 3$ the $\rho_{\rm TC}$ mass already saturates the bound in Eq. (50). In this case the dynamics

follow the solid-curve scenario, with $N_{\rm TC} = 3$ placing the theory close to regions A or B, while still consistent with the S-parameter constraint of Eq. (17). This picture is further supported by recent lattice computations.

Specifically, Ref. [38] finds that for $N_c = 3$ the ratio M_ρ/F_π in the chiral limit is essentially independent of N_f:

$$\left.\frac{M_\rho}{F_\pi}\right|_{N_c=3}^{N_f=2-6} = 7.95(15). \tag{51}$$

At large N_c, quenched lattice studies instead obtain [39]

$$\left.\sqrt{\frac{N_c}{3}}\,\frac{M_\rho}{F_\pi}\right|_{N_c\to\infty} = 7.08(10). \tag{52}$$

For $N_{\rm TC} = 3$, Ref. [39] further reports

$$\frac{M_{\rho_{\rm TC}}}{\sqrt{\sigma}} = 1.749(26), \tag{53}$$

with the string tension related to the decay constant by

$$\sqrt{\frac{3}{N_{\rm TC}}}\,\frac{F_{\Pi_{\rm TC}}}{\sqrt{\sigma}} = 0.2174(30). \tag{54}$$

Applying these relations with $F_{\Pi_{\rm TC}} = 246$ GeV yields

$$M_{\rho_{\rm TC}} = 1980 \text{ GeV}, \tag{55}$$

which is consistent with the bound in Eq. (17). A simple scaling relation provides an independent check [40]:

$$M_{\rho_{\rm TC}} = \frac{F_{\Pi_{\rm TC}}}{f_\pi}\sqrt{\frac{3}{N_{\rm TC}}}\,m_\rho = 2007 \text{ GeV}, \tag{56}$$

again in good agreement with Eq. (55).

F. Dark-matter

The DTC paradigm gives rise to novel classes of dark matter in its low-energy effective limits. At lower energies, the SHVM limit allows for *neutrinic dark matter* [17], while the FN mechanism gives rise to *flavonic dark matter* [23].

IV. SUMMARY

The DTC paradigm extends conventional TC dynamics to address both electroweak symmetry breaking and the problem of the SM flavour structure. It operates via an EMAC framework, predicting a hierarchy of chiral multifermion condensates. At low energies, DTC reduces effectively to either the FN mechanism or the SHVM, depending on the residual discrete symmetry. The paradigm introduces new classes of dark matter candidates and offers collider testable signatures [25]. The hierarchical mass structure of SM fermions emerges from the interplay of TC, dark TC, and DQCD dynamics, all embedded in an extended unification scheme through ETC and EDTC interactions.

For decades, theorists have pursued SUBI models to elegantly address the hierarchy problem, typically predicting new physics near the electroweak scale. Yet, despite extensive LHC searches reaching several TeV, no such particles have been found. Perhaps, as illustrated in Figure 9, nature prefers a SWEETI to an imposing SUBI.

Acknowledgement

Figures 1 and 9 were generated with the assistance of ChatGPT. This work was supported by the Council of Science and Technology, Government of Uttar Pradesh, India, under the project *"A New Paradigm for the flavour Problem"* (Project No. CST/D-1301), and by the Anusandhan National Research Foundation (formerly SERB), Department of Science and Technology, Government of India, through the project *"Higgs Physics Within and Beyond the Standard Model"* (Project No. CRG/2022/003237).

---

[1] G. Abbas, R. Adhikari, E. J. Chun and N. Singh, Eur. Phys. J. Plus **140** (2025) no.1, 73 doi:10.1140/epjp/s13360-025-06008-6 [arXiv:2308.14811 [hep-ph]].

[2] G. Abbas, doi:10.31526/ACP.BSM-2023.3 [arXiv:2404.03232 [hep-ph]].

[3] S. Weinberg, Phys. Rev. D **13**, 974-996 (1976) doi:10.1103/PhysRevD.19.1277

[4] L. Susskind, Phys. Rev. D **20**, 2619-2625 (1979) doi:10.1103/PhysRevD.20.2619

[5] T. P. Cheng and L. F. Li, "Gauge Theory of Elementary Particle Physics," Oxford University Press, 1984, ISBN 978-0-19-851961-4, 978-0-19-851961-4

[6] C. T. Hill and E. H. Simmons, Phys. Rept. **381**, 235-402 (2003) [erratum: Phys. Rept. **390**, 553-554 (2004)] doi:10.1016/S0370-1573(03)00140-6 [arXiv:hep-ph/0203079 [hep-ph]].

[7] R. Delbourgo and M. D. Scadron, *Phys. Rev. Lett.* **48**, 379 (1982).

[8] S. Navas et al. (Particle Data Group), Phys. Rev. D 110, 030001 (2024)

[9] V. Elias and M. D. Scadron, Phys. Rev. Lett. **53**, 1129 (1984) doi:10.1103/PhysRevLett.53.1129

[10] ATLAS Collaboration, Phys. Lett. B **716**, 1 (2012).

[11] CMS Collaboration, Phys. Lett. B **716**, 30 (2012).

[12] M. E. Peskin and T. Takeuchi, Phys. Rev. Lett. **65**, 964-967 (1990) doi:10.1103/PhysRevLett.65.964

[13] M. E. Peskin and T. Takeuchi, Phys. Rev. D **46**, 381-409 (1992) doi:10.1103/PhysRevD.46.381

[14] A. Pich, I. Rosell and J. J. Sanz-Cillero, [arXiv:2503.05917 [hep-ph]].

[15] A. Pich, I. Rosell and J. J. Sanz-Cillero, JHEP **01**, 157 (2014) doi:10.1007/JHEP01(2014)157 [arXiv:1310.3121 [hep-ph]].

[16] G. Abbas, Int. J. Mod. Phys. A **37**, no.11n12, 2250056 (2022) doi:10.1142/S0217751X22500567 [arXiv:2012.11283 [hep-ph]].

[17] G. Abbas and N. Singh, [arXiv:2412.08523 [hep-ph]].

[18] G. Abbas, Mod. Phys. Lett. A **40**, no.17n18, 2550056 (2025) doi:10.1142/S0217732325500567 [arXiv:2310.12915 [hep-ph]].

[19] G. Abbas, Int. J. Mod. Phys. A **34** (2019) no.20, 1950104 doi:10.1142/S0217751X19501045 [arXiv:1712.08052 [hep-ph]].

[20] C. D. Froggatt and H. B. Nielsen, Nucl. Phys. B **147**, 277 (1979). doi:10.1016/0550-3213(79)90316-X

[21] G. Abbas, Int. J. Mod. Phys. A **36**, 2150090 (2021) doi:10.1142/S0217751X21500901 [arXiv:1807.05683 [hep-ph]].

[22] G. Abbas, V. Singh, N. Singh and R. Sain, Eur. Phys. J. C **83**, no.4, 305 (2023) doi:10.1140/epjc/s10052-023-11471-5 [arXiv:2208.03733 [hep-ph]].

[23] G. Abbas, R. Adhikari and E. J. Chun, Phys. Rev. D **108**, no.11, 115035 (2023) doi:10.1103/PhysRevD.108.115035 [arXiv:2303.10125 [hep-ph]].

[24] G. Abbas, A. K. Alok, N. R. S. Chundawat, N. Khan and N. Singh, Phys. Rev. D **110** (2024) no.11, 115015 doi:10.1103/PhysRevD.110.115015 [arXiv:2407.09255 [hep-ph]].

[25] G. Abbas, V. Singh and N. Singh, [arXiv:2504.21593 [hep-ph]].

[26] H. Harari and N. Seiberg, Phys. Lett. B **102**, 263-266 (1981) doi:10.1016/0370-2693(81)90871-6

[27] K. I. Aoki and M. Bando, Phys. Lett. B **126**, 101-105 (1983) doi:10.1016/0370-2693(83)90027-8

[28] K. I. Aoki and M. Bando, Prog. Theor. Phys. **70**, 259 (1983) doi:10.1143/PTP.70.259

[29] K. I. Aoki and M. Bando, Prog. Theor. Phys. **70**, 272 (1983) doi:10.1143/PTP.70.272

[30] S. Raby, S. Dimopoulos and L. Susskind, Nucl. Phys. B **169**, 373-383 (1980) doi:10.1016/0550-3213(80)90093-0

[31] V. A. Miransky, "Dynamical symmetry breaking in quantum field theories," https://doi.org/10.1142/2170 — February 1994, World Scientific Singapore

[32] P. Huber, K. Scholberg, E. Worcester, J. Asaadi, A. B. Balantekin, N. Bowden, P. Coloma, P. B. Denton, A. de Gouvêa and L. Fields, *et al.* [arXiv:2211.08641 [hep-ex]].

[33] R. Foadi, M. T. Frandsen and F. Sannino, Phys. Rev. D **87**, no.9, 095001 (2013) doi:10.1103/PhysRevD.87.095001 [arXiv:1211.1083 [hep-ph]].

[34] G. 't Hooft, Nucl. Phys. B **72**, 461 (1974) doi:10.1016/0550-3213(74)90154-0

[35] E. Witten, Nucl. Phys. B **160**, 57-115 (1979) doi:10.1016/0550-3213(79)90232-3

[36] B. Lucini and M. Panero, Phys. Rept. **526**, 93-163 (2013) doi:10.1016/j.physrep.2013.01.001 [arXiv:1210.4997 [hep-th]].

[37] R. S. Chivukula, M. J. Dugan and M. Golden, Phys. Lett. B **292**, 435-441 (1992) doi:10.1016/0370-2693(92)91200-S [arXiv:hep-ph/9207249 [hep-ph]].

[38] D. Nogradi, D. Nogradi, L. Szikszai and L. Szikszai, JHEP **05**, 197 (2019) [erratum: JHEP **06**, 031 (2022)] doi:10.1007/JHEP05(2019)197 [arXiv:1905.01909 [hep-lat]].

[39] G. S. Bali, F. Bursa, L. Castagnini, S. Collins, L. Del Debbio, B. Lucini and M. Panero, JHEP **06**, 071 (2013) doi:10.1007/JHEP06(2013)071 [arXiv:1304.4437 [hep-lat]].

[40] J. Tandean, Phys. Rev. D **52** (1995), 1398-1403 doi:10.1103/PhysRevD.52.1398 [arXiv:hep-ph/9505256 [hep-ph]].

FIG. 1: Approximate symmetries in nature

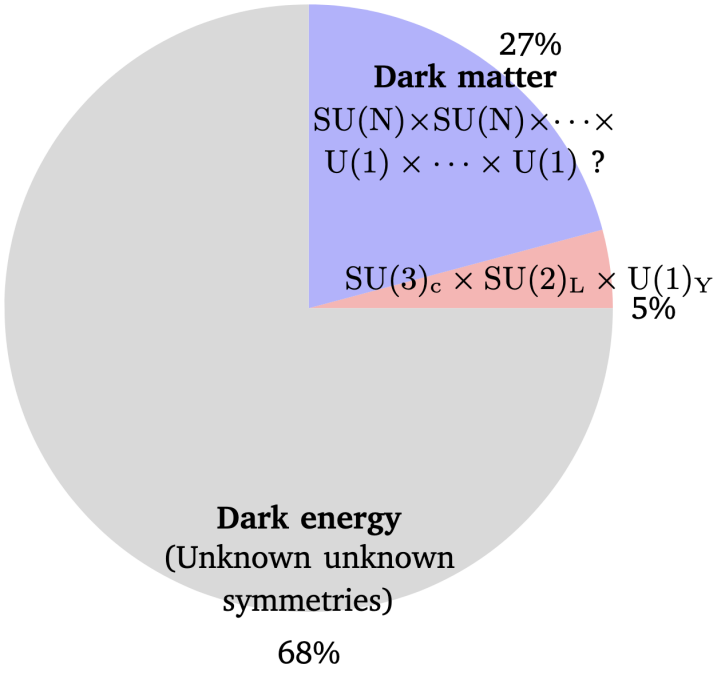

FIG. 2: The matter problem

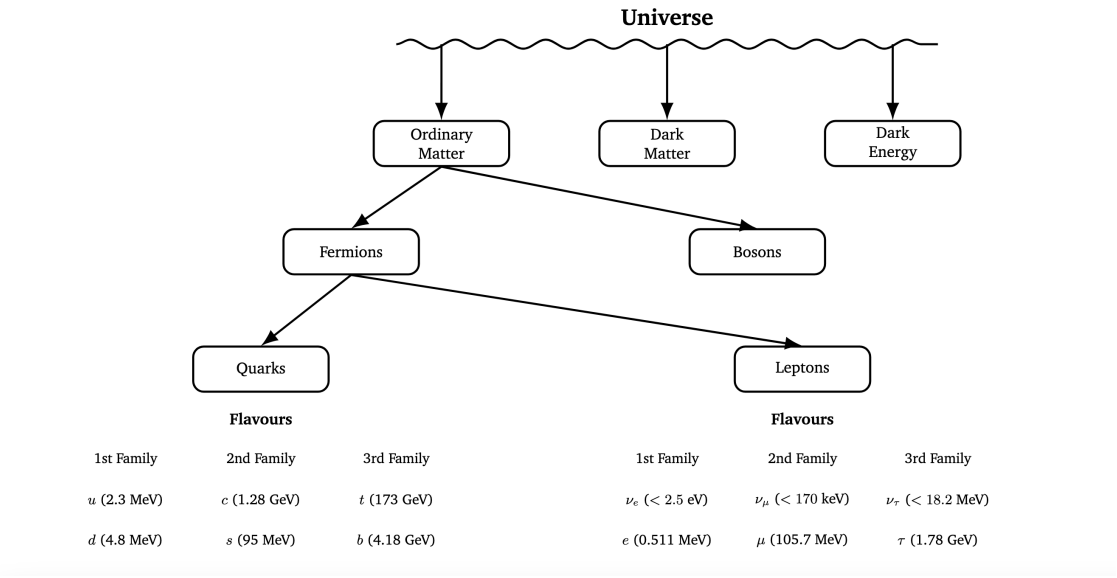

FIG. 3: The flavour problem

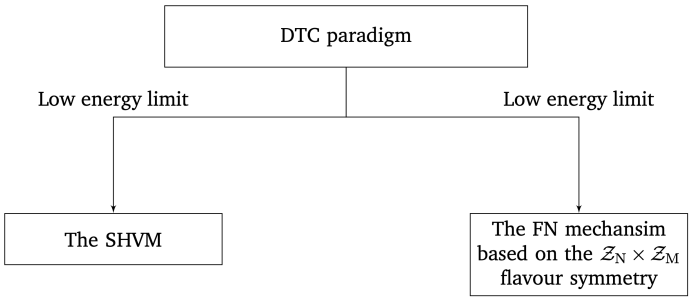

FIG. 4: At low energies, the DTC paradigm may effectively reduce to either the SHVM or the Froggatt–Nielsen mechanism, depending on the prevailing symmetry-breaking pattern.

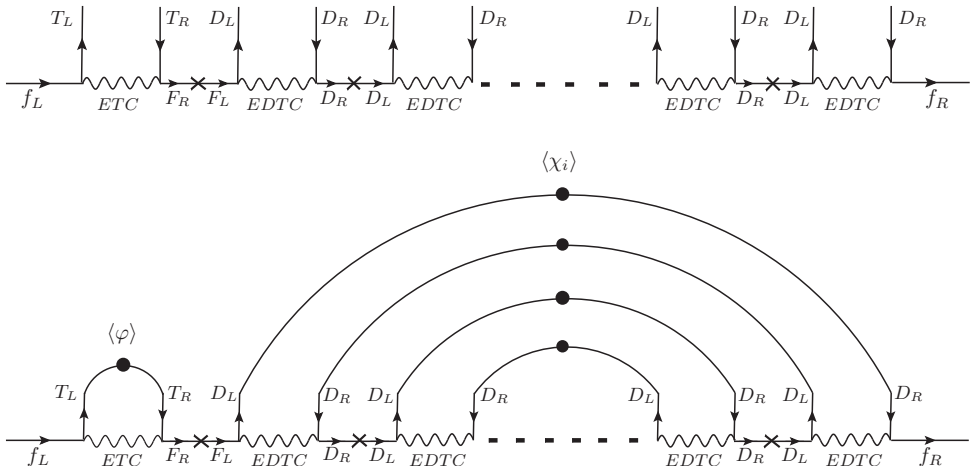

FIG. 5: The Feynman diagrams for the masses of charged fermions in the DTC paradigm. The top part shows the generic interactions of the SM, TC, DQCD and DTC fermions. In the lower part of figure, the formations of the TC chiral condensates, $\langle\varphi\rangle$ (circular blob), a generic multifermion chiral condensates $\langle\chi_r\rangle$ (collection of circular blobs), and the resulting mass of the SM charged fermion is depicted.

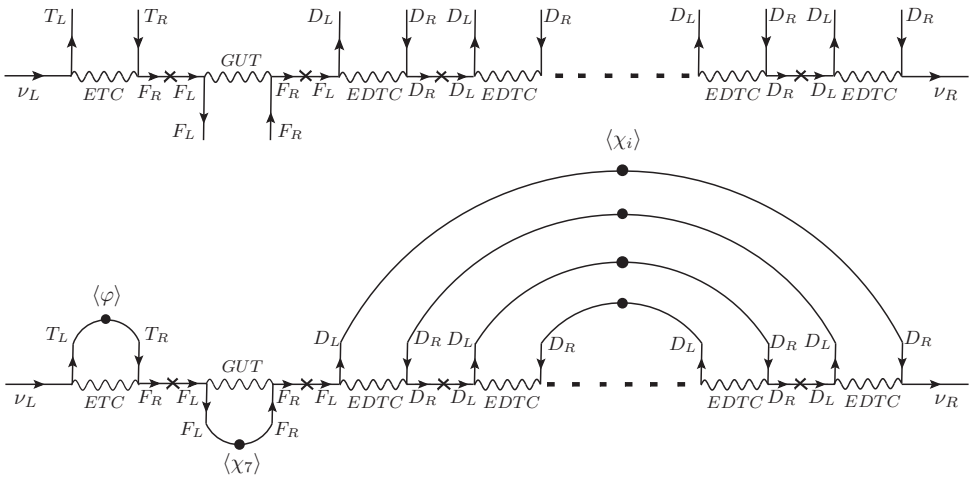

FIG. 6: Feynman diagrams for neutrino mass generation in the DTC paradigm. The top panel shows interactions among SM, TC, DQCD, and DTC sectors via ETC, EDTC, and GUT bosons. The bottom panel illustrates the effective diagram after condensate formation.

[]0.266

23

FIG. 7: SUBI

114

[]0.4

Thermodynamics of black hole in Bumblebee gravity coupled with nonlinear electrodynamics

Vartika Singh,[1,*] Shobhit Sachan,[1,†] and Dharm Veer Singh[1,‡]

[1]*Department Physics, Institute of Applied Science and Humanities, GLA University, Mathura 281406 Uttar Pradesh, India*

Abstract

In this study, We find an exact black hole (BH) solution in Bumblebee gravity coupled with nonlinear electrodynamics. The obtained BH solution introduce with the Bumblebee BH in the absence of nonlinear parameter and Bardeen BH in the absence of Bumblebee parameter. We also study the thermodynamic properties (Temperature, entropy) including local and global stability associated with the Bardeen-Bumblebee BH. The thermodynamic properties associate with the black hole is changed in the existence of nonlinear and Bumblebee parameters. The Hawking temperature of the BH reaches maximum at the point where the heat capacity diverges, indicating the occurrence of phase transition.

*Electronic address: vartikasinghvbn50@gmail.com
†Electronic address: shobhitsachan@gmail.com
‡Electronic address: veerdsingh@gmail.com

I. INTRODUCTION

The interest of the regular black hole comes from the Bardeen black hole model [3], which is based on the Sakharov [1] and Gliner proposal [2]. Such types of black holes have a horizon, but the central singularity is absent. This type of exact black hole solution was obtained when Einstein gravity coupled with NLED and was first studied after 30 years of Bardeen model [4–7]. Currently, numerous regular black hole solutions exist, although the majority of these are predicated on the Bardeen proposal. [8–22]. The generalisation of the regular black hole in EGB gravity [23–27], 4D EGB gravity [28–30], massive gravity [31], and rotating black holes are presented in ref. [32–36]. After Bekenstein proposed the concepts of entropy and temperature, black holes behaves like thermodynamic objects. [37, 38] and Hawking [39], and black holes can show phase transition by presuming that the cosmological constant (Λ) is treated as a thermodynamic pressure (P) [40–42].

The Bumblebee model introduces a dynamic vector field, B_μ, coupled non-minimally to the metric tensor $g_{\mu\nu}$. The key mechanism involves the potential $V(B_\mu B^\mu \pm b^2)$, which forces the bumblebee field to acquire a non-zero vacuum expectation value (VEV), denoted b, thereby selecting a preferred direction in spacetime and breaking the symmetry. Recent investigations into static, spherically symmetric solutions coupled to standard Maxwell electrodynamics have shown that the resulting spacetimes are modified regular charged black holes. The bumblebee theory posits that the vector field B_μ, referred to as the bumblebee field, is nonminimally related to the Ricci tensor in a quadratic manner and possesses a nonzero background value, resulting in spontaneous Lorentz symmetry violation through the minimization of its potential term V. From this perspective, many solutions involving vector fields, including spherical black holes, wormholes, and solitons [43–48]. The studies of spontaneous Lorentz symmetry violation typically assume a continuous background configuration of the Bumblebee field in asymptotically flat regions, this model is an example of such a theory. [49–52].

In this paper, we explore black hole solution in Bumblebee gravity coupled with nonlinear electrodynamics (NLED). This black hole interpolates with the Schwarzschild-Tangherlini black hole in the limit of the NLED and Bumblebee parameter. Moreover, we investigate the thermodynamic properties of this black hole solution. The thermodynamics of the black hole have changed in the presence of a nonlinear matter field. So, the physics of Bumblebee black

holes could give us a new way to look into Lorentz symmetry breaking in the strong field region. Besides that, the thermal stability of bumblebee black holes is another interesting subject. It is generally described by heat capacity and Gibbs free energy, which is how well a thermodynamic system can handle changes that come from exchanging a small amount of heat with its surroundings.

The paper is organised as follows: we obtain an black hole solution in Sec. II, and also give the consistent equations of gravity coupled with NLED and Bumblebee gravity, and study the location of the horizon structure. The study of the thermodynamical properties of obtained black hole solutions in the Sec. III. Finally, the concluding remarks and results are presented in Sec. V. We use the signature of the metric is $(-,+,+,+,+)$ with natural units $8G = c = 1$.

II. ACTION, EQUATION OF MOTION

The bumblebee theory is a vector-tensor theory is an extension of the Einstein-Maxwell electrodynamics theory. The action associated with the bumblebee theory coupled with the NLED is

$$\mathcal{L} = \int d^4x\sqrt{-g}\Big[R + \frac{\xi}{2K}B^\mu B^\nu R_{\mu\nu} - \frac{1}{4}B_{\mu\nu}B^{\mu\nu} - V(B^\mu B_\mu \pm b^2) + \mathcal{L}_M\Big] \tag{1}$$

where R is Ricci scalar, $B_{\mu\nu}$ the bumblebee field is given by $B_{\mu\nu} \equiv \partial_\mu B_\nu - \partial_\nu B_\mu$. $\mathcal{L}_M$ describes the matter field of NLED. The gravitational field equations are modified by effective energy-momentum tensor $T^B_{\mu\nu}$ derived from the Bumblebee field can be obtained by varying the action (1) w.r.t. the metric tensor $g_{\mu\nu}$, by keeping bumblebee field B_μ steady. This gives

$$\begin{aligned} G_{\mu\nu} + \Lambda g_{\mu\nu} = \quad & K(T^B_{\mu\nu} + T^M_{\mu\nu}) \equiv K\Big[2V' B_\mu B_\nu - B^\alpha_\mu B_{\nu\alpha} - \Big(V + \frac{1}{4}B_{\alpha\beta}B^{\alpha\beta}\Big)g_{\mu\nu}\Big] + \\ & \xi\Big[\frac{1}{2}B^\alpha B^\beta R_{\alpha\beta}g_{\mu\nu} - B_\mu B^\alpha R_{\alpha\nu} - B_\nu B^\alpha R_{\alpha\mu} + \frac{1}{2}\nabla_\alpha\nabla_\mu(B^\alpha B_\nu) + \frac{1}{2}\nabla_\alpha\nabla_\nu(B^\alpha B_\mu) \\ & -\frac{1}{2}\nabla^2(B_\mu B_\nu) - \frac{1}{2}g_{\mu\nu}\nabla_\alpha\nabla_\beta(B^\alpha B^\beta)\Big] + 2K\left[\frac{\partial\mathcal{L}(F)}{\partial F}F_{\mu\rho}F^\rho_\nu - g_{\mu\nu}\mathcal{L}(F)\right], \end{aligned} \tag{2}$$

The equation of motion for B^μ can also be obtained from the action (1). By varying the action with respect to the bumblebee field gives

$$\nabla_\mu B^{\mu\nu} = 2\Big(V' B^\nu - \frac{\xi}{2K}B_\nu R^{\mu\nu}\Big) \tag{3}$$

The radial bumblebee field is $B_\mu = b_\mu = (0, b_r(r), 0, 0)$, to find the black hole solution in the NLED, the static spherically symmetric line element investigation is given by

$$ds^2 = -f(r)dt^2 + \frac{1}{f(r)}dr^2 + r^2 d\Omega^2 \tag{4}$$

where $d\Omega^2$ is the line element of $2D$ sphere. Using the condition $b_\mu b^\mu = b^2 = \text{constant}$,one can have the radial component of the bumblebee field when it assumes the vacuum expectation value as

$$b_r(r) = |b|/e^{\rho(r)} \tag{5}$$

Assuming $V = V' = 0$, we find the following equation

$$ds^2 = \left(\frac{1}{1-\lambda} - \frac{2Mr^2}{(r^2+g^2)^{3/2}}\right)dt^2 + \left(\frac{1}{(1-\lambda)} - \frac{2Mr^2}{(r^2+g^2)^{3/2}}\right)^{-1} dr^2 + r^2 d\Omega^2 \tag{6}$$

This is an exact black hole solution in the presence of a Lorentz-violating factor (λ). The black hole solution obtained intersects with the Bumblebee BH in the absence of magnetic monopole charge (g) and Bardeen BH, when $\lambda = 0$. The solution (6) coincides with the Schwarzschild BH solution for $\lambda = g = 0$. Now, we study the horizon structure of the obtained black hole solution (6) $f(r) = 0$ by varying the λ and g:

$$\frac{1}{1-\lambda} - \frac{2Mr^2}{(r^2+g^2)^{3/2}} = 0 \tag{7}$$

Fig. (1) shows the horizon structure of the obtained Bumblebee Bardeen black hole (6). The

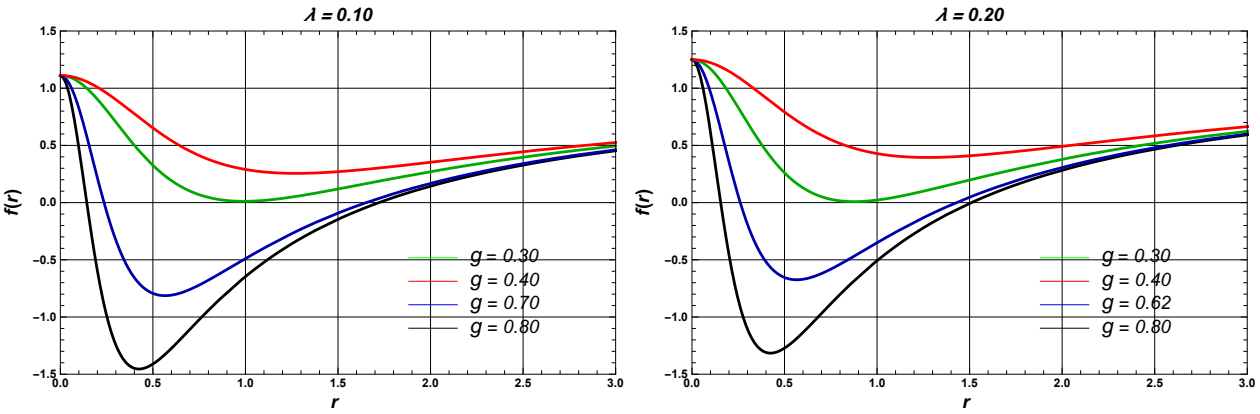

FIG. 1: The metric function $f(r)$ vs r with different value of g for fixed values $\lambda = 0.1$ and $\lambda = 0.2$

derived black hole solution (6) features two horizons (Cauchy and event) associated with the constant values of the magnetic monople charge (g) and Lorentz violating parameter (λ), as well as the mass (M). The Cauchy and event horizons coincide at the critical magnetic

monopole charge ($g = 0.30$) with a fixed value of $\lambda(= 0.1)$ and the critical magnetic monopole charge ($g = 0.42$) with fixed values of $\lambda = 0.2$. The horizon size increases as the magnetic monopole charge ((g)) and Lorentz violating parameter (λ).

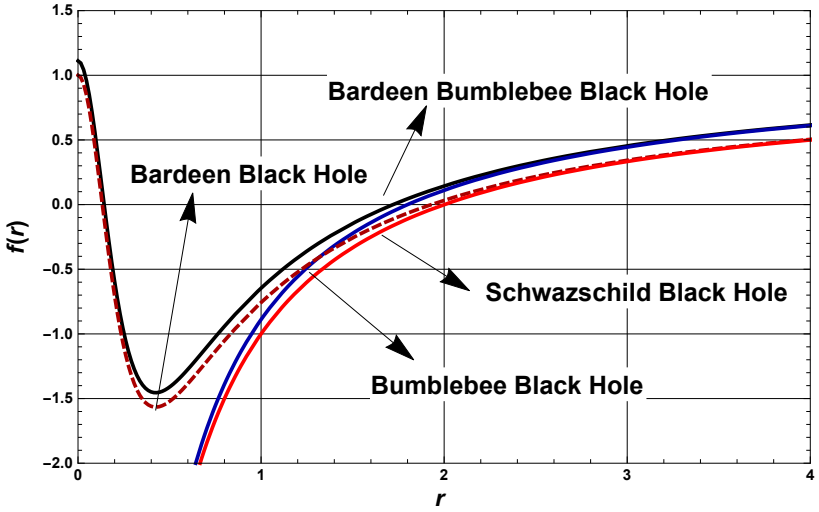

FIG. 2: The metric function ($f(r)$) vs r with limiting value of g and λ.

Fig. 2 shows the horizon structure of the obtained Bumblebee Bardeen black hole (6) in the limiting values of g and λ. The horizon of the Bumblebee Bardeen black hole coincide with the Bardeen black hole at $r_+ =$ Bumblebee black hole at $r_+ =$ and Schwarzschild black hole at $r_+ =$.

III. THERMODYNAMICS OF BARDEEN BUMBLEBEE BLACK HOLE

Now, we calculated the thermodynamic quantities associated with the black hole solution (6). The mass of the obtained black hole solution $f(r) = 0$ is

$$M_+ = \frac{r_+(r_+^2 - 2g^2)}{4(1-\lambda)(r_+^2 + g^2)}, \tag{8}$$

The mass of the Bumblebee Bardeen black hole interpolates with the Bumblebee black hole in the absence of magnetic monopole charge (g) and Bardeen BH, when $\lambda = 0$. The mass of the Bumblebee Bardeen black hole coincides with the mass of Schwarzschild BH solution for $\lambda = g = 0$. The temperature of the BH is known as Hawking temperature $T = \kappa/2\pi$, where κ is the surface gravity. The temperature of the obtained black hole solution is

$$T_+ = \frac{(r_+^2 - 2g^2)^{3/2}}{4\pi r_+(1-\lambda)} \tag{9}$$

The temperature of the Bumblebee Bardeen black hole interpolates with the Bumblebee

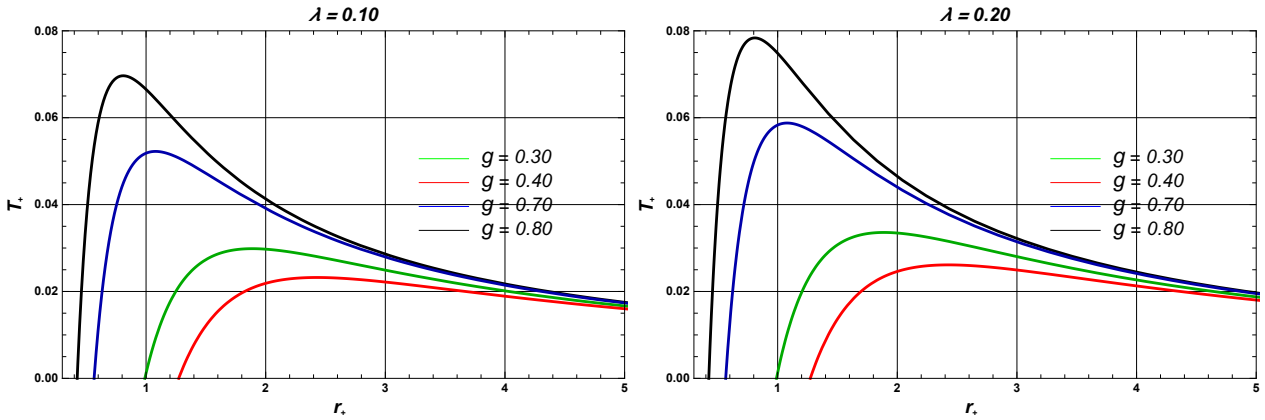

FIG. 3: The temperature (T_+) vs r_+ with different value of g for $\lambda = 0.1$ and $\lambda = 0.2$

black hole in the absence of magnetic monopole charge (g) and the temperature of the Bumblebee Bardeen BH coincides with the temperature of Schwarzschild BH solution for $\lambda = g = 0$. The temperature of the Bardeen black hole, when $\lambda = 0$

$$T_+ = \frac{(r_+^2 - 2g^2)^{3/2}}{4\pi r_+} \tag{10}$$

The graph of temperature for the different value of g for fixed values $\lambda = 0.1$ and $\lambda = 0.2$ is dipcted in Fig. 4. In these figures, we can see that the temperature first grows to a maximum value of T and then it drops to a minimum value.

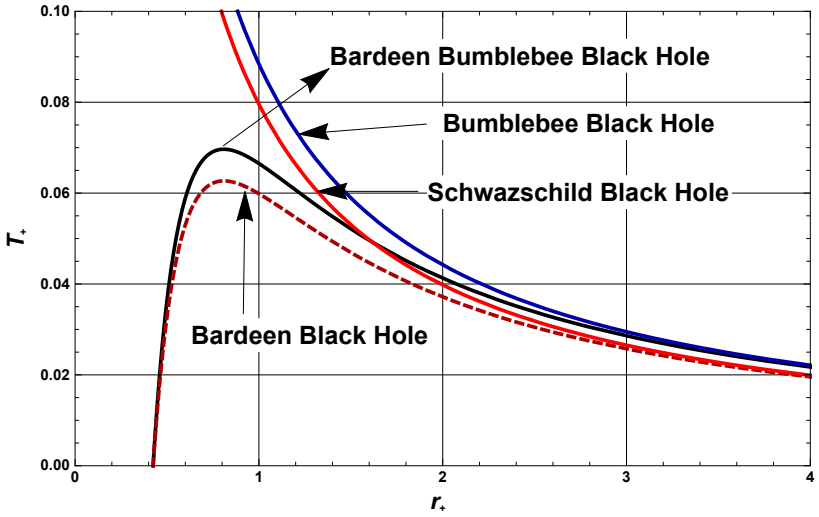

FIG. 4: The temperture (T_+) vs r_+ with limiting value of g and λ

Fig. 4 shows the temperature of the obtained Bumblebee Bardeen black hole (6) in the limiting values of g and λ. The temperature of the Bumblebee Bardeen black hole coincide

with the Bardeen black hole at $r_+ =$ Bumblebee black hole at $r_+ =$ and Schwarzschild black hole at $r_+ =$.

The entropy of the black hole is calculated by using the first law of thermodynamics ($C_+ dM_+ = T_+ dS_+$) [53, 54]. The entropy of the black hole becomes

$$S_+ = \int \frac{1}{T_+}\frac{dM_+}{dS_+}dr_+ = \pi r_+^2 = \frac{A}{4}, \tag{11}$$

IV. LOCAL AND GLOBAL STABILITY OF BARDEEN BUMBLEBEE BLACK HOLE

The heat capacity (C_+) and Gibbs free energy (G_+) are used to study how stable a black hole is. It's stable for black holes when $C_+ > 0$ and $G_+ < 0$. It's not stable for black holes when $C_+ < 0$ and $G_+ > 0$. The heat capacity is calculated using the following equation

$$C_+ = \frac{dM_+}{dT_+} = \frac{dM_+}{dr_+}\frac{dr_+}{dT_+} \tag{12}$$

Using the Eq. (8), (9) and (12), the heat capacity of the Bardeen Bumblebee black hole is

$$C_+ = \frac{\pi r_+^2 (r_+^4 + 5g^2 r_+^2 - 2g^4)}{2g^4 + 7g^2 r_+^2 - r_+^4} \tag{13}$$

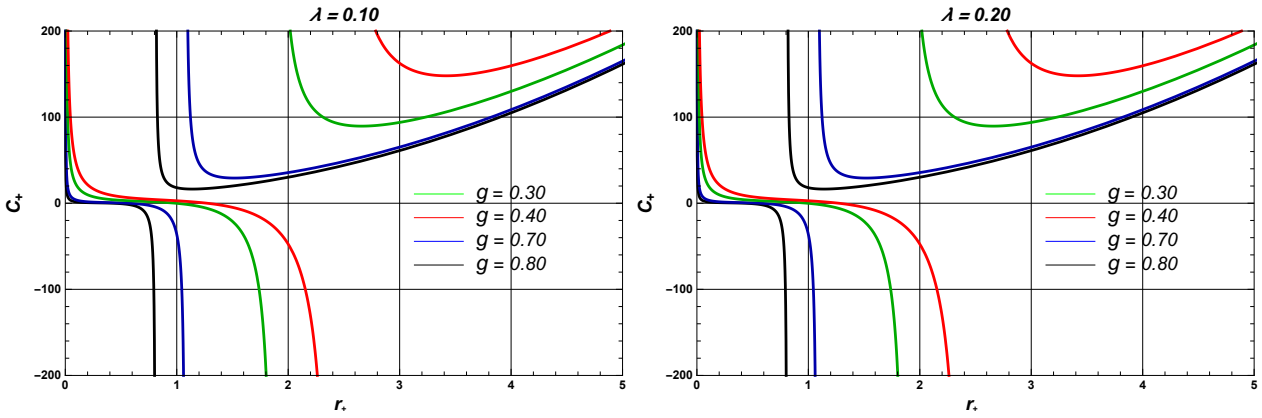

FIG. 5: The heat capacity (C_+) vs r_+ with different value of g for $\lambda = 0.1$ and $\lambda = 0.2$.

In the plot Fig. 5, we can see that the heat capacity diverges $r_+ =$ for $\lambda = 0.10$ and $r_+ =$ for $\lambda = 0.20$ respectively. For this analysis, we noticed that the the heat capacity diverges, where the temperature is maximum (See Fig. 3)

The Gibss free energy is calculated by using the relation ($G_+ = M_+ - T_+S_+$) and substituting the value of mass, temperature, and entropy from Eq. (8), (9) and (11) into the relation, the heat capacity of the obtained black hole solution is

$$G_+ = \frac{r_+(r_+^2 - 2g^2)}{4(1-\lambda)(r_+^2+g^2)} + \frac{(r_+^2 - 2g^2)^{3/2}}{2r_+^2(1-\lambda)} \tag{14}$$

In order to investigate the nature of Gibbs free energy, we plotted it in Fig. 6 for fixed values

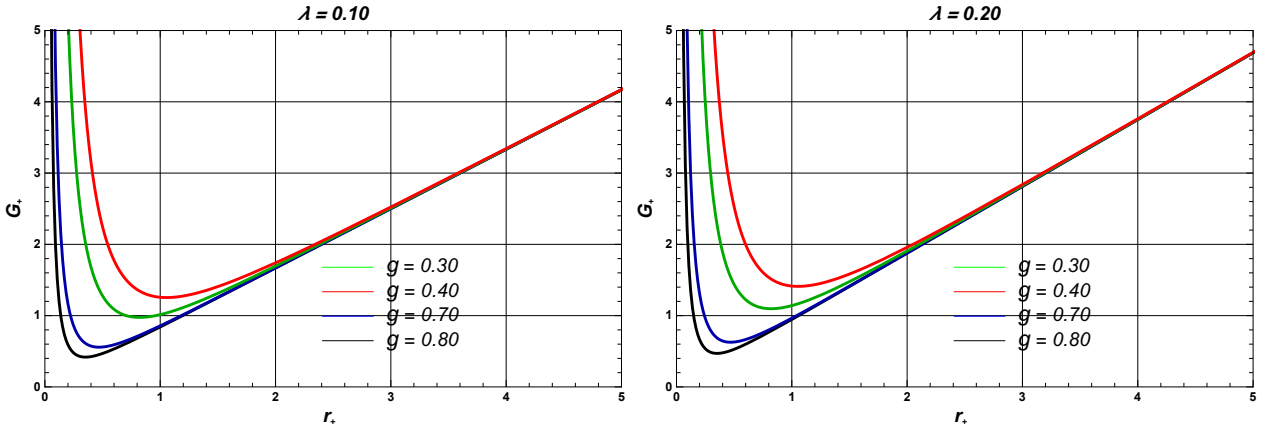

FIG. 6: The Gibbs free energy (G_+) vs r_+ with different value of g for $\lambda = 0.1$ and $\lambda = 0.2$

of the Lorentz violating parameter for $\lambda = 0.10$ and $\lambda = 0.20$, respectively, and for varying values of magnetic monopole charge (g). The figure shows that the Gibbs free energy has horizon radii $r_+ = 0.$ for $\lambda = 0.20$ and local minima $r_+ = 0$ for $\lambda = 0.10$, respectively. The temperature reaches its maximum values (see Fig. 3) and the heat capacity diverges (see Fig. 5). We observed that the black hole is unstable in the resulting black hole solution.

V. CONCLUSIONS

This work presents an accurate Bumblebee black hole within the context of NLED. The derived black hole solution interpolates between the Bumblebee black hole, absence of magnetic monopole charge, and the Bardeen black hole in the limit of the Lorentz-violating parameter (λ). A critical mass parameter $r = r_c$ exists, corresponding to an extremal black hole when the Cauchy and event horizons overlap at ($r_+ = r_- = 0.30$) for $\lambda = 0.1$. For $r > r_c$, it characterizes a nonextremal black hole possessing two horizons, whereas for $r < r_c$, no black hole exists. The thermodynamic quantities associated with the black hole solution are altered. The Hawking temperature of the black hole reaches its maximum at

the point where the heat capacity diverges and alters its sign, indicating the occurrence of a second-order phase transition.

Acknowledgments

V.S. and D.V.S. would like to thanks to Anusandhan National Research Foundation (ANRF) project grant no. EEQ/2022/00824.

---

[1] A. D. Sakharov, Sov. Phys. JETP **22**, 241 (1966).

[2] E. B. Gliner, Sov. Phys. JETP **22**, 378 (1966).

[3] J. Bardeen, in *Proceedings of GR5* (Tiflis, U.S.S.R., 1968).

[4] E. Ayon-Beato, A. Garcia, Phys. Lett. B **493**, 149 (2000).

[5] E. Ayon-Beato and A. Garcia, Gen. Relativ. Gravit. **31**, 629 (1999).

[6] E. Ayon-Beato and A. Garcia, Gen. Relativ. Gravit.**37**, 635 (2005).

[7] E. Ayon-Beato and A. Garcia, Phys. Rev. Lett. **80**, 5056 (1998).

[8] L. Xiang, Y. Ling and Y. G. Shen, Int. J. Mod. Phys. D **22**, 1342016 (2013).

[9] H. Culetu, Int. J. Theor. Phys. **54**, 2855 (2015).

[10] L. Balart and E. C. Vagenas, Phys. Lett. B **730**, 14 (2014).

[11] M. S. Ma, R. Zhao and Y. Q. Ma, Gen. Rel. Grav. **49** (2017) no.6, 79.

[12] I. G. Dymnikova, Int. J. of Mod. Phys. D, **5** 529 (1996); Phys. Lett. B **685**, 12 (2010);Gen. Rel. Grav. **24**, 235 (1992).

[13] S. H. Hendi, S. Panahiyan and B. Eslam Panah, J. High Energy Phys. **01**, 129 (2016).

[14] S. Ansoldi, arXiv:0802.0330 [gr-qc].

[15] Md. Sabir Ali and S. G. Ghosh, Phys. Rev. D **98**, 084025 (2018).

[16] A. Kumar, D. V. Singh and S. Upadhyay, JHAP **4** (2024) no.4, 85-99.

[17] A. Kumar, D. V. Singh and S. Upadhyay, Int. J. Mod. Phys. A **39** (2024) no.31, 2450136.

[18] H. K. Sudhanshu, D. V. Singh, S. Upadhyay, Y. Myrzakulov and K. Myrzakulov, Phys. Dark Univ. **46** (2024), 101648.

[19] B. Singh, D. Veer Singh and B. Kumar Singh, Phys. Scripta **99** (2024) no.2, 025305.

[20] P. Paul, S. Upadhyay, Y. Myrzakulov, D. V. Singh and K. Myrzakulov, Nucl. Phys. B **993** (2023), 116259.

[21] D. V. Singh, A. Shukla and S. Upadhyay, Annals Phys. **447** (2022), 169157.

[22] D. V. Singh, S. G. Ghosh and S. D. Maharaj, Nucl. Phys. B **981** (2022), 115854.

[23] A. Kumar, D. V. Singh, Y. Myrzakulov, G. Yergaliyeva and S. Upadhyay, Eur. Phys. J. Plus **138** (2023) no.12, 1071.

[24] P. Paul, S. Upadhyay and D. V. Singh, Eur. Phys. J. Plus **138** (2023) no.6, 566.

[25] B. Singh, B. K. Singh and D. V. Singh, Int. J. Geom. Meth. Mod. Phys. **20** (2023) no.08, 2350125.

[26] Y. Myrzakulov, K. Myrzakulov, S. Upadhyay and D. V. Singh, Int. J. Geom. Meth. Mod. Phys. **20** (2023) no.07, 2350121.

[27] D. V. Singh, V. K. Bhardwaj and S. Upadhyay, Eur. Phys. J. Plus **137** (2022) no.8, 969.

[28] C. S. Varsha, V. Venkatesha, N. S. Kavya and D. V. Singh, Annals Phys. **477** (2025), 170002.

[29] B. Pourhassan, M. Dehghani, S. Upadhyay, I. Sakalli and D. V. Singh, Mod. Phys. Lett. A **37** (2022) no.33n34, 2250230.

[30] S. Upadhyay and D. V. Singh, Eur. Phys. J. Plus **137** (2022) no.3, 383.

[31] B. K. Singh, R. P. Singh and D. V. Singh, Eur. Phys. J. Plus **135** (2020) no.10, 862

[32] S. G. Ghosh, Eur. Phys. J. C **75**, no. 11, 532 (2015).

[33] B. K. Vishvakarma, D. V. Singh and S. Siwach, Phys. Scripta **99** (2024) no.2, 025022.

[34] D. V. Singh, S. Upadhyay and M. S. Ali, Int. J. Mod. Phys. A **37** (2022) no.09, 2250049.

[35] F. Ahmed, D. V. Singh and S. G. Ghosh, Gen. Rel. Grav. **54** (2022) no.2, 21.

[36] D. V. Singh, M. S. Ali and S. G. Ghosh, Int. J. Mod. Phys. D **27** (2018) no.12, 1850108.

[37] J. D. Bekenstein, Lett. Nuovo Cim. 4, 737 (1972).

[38] J. D. Bekenstein, Phys. Rev. D 7, 2333 (1973).

[39] S. W. Hawking, Phys. Rev. D 13, 191 (1976).

[40] A. Chamblin, R. Emparan, C.V. Johnson, and R.C. Myers, Phys. Rev. D **60** (1999) 064018.

[41] A. Chamblin, R. Emparan, C.V. Johnson, and R.C. Myers, Phys. Rev. D 60 (1999) 104026.

[42] B.P. Dolan, Class. Quant. Grav. 28 (2011) 125020.

[43] O. Bertolami and J. Paramos, Phys. Rev. D **72**, 044001 (2005).

[44] R. Oliveira, D. M. Dantas, and C. A. S. Almeida, EPL **135**, 10003 (2021).

[45] I. Güllü and A. Övgün, Annals Phys. **436**, 168721 (2022).

[46] R. V. Maluf and J. C. S. Neves, Phys. Rev. D **103**, 044002 (2021).

[47] R. N. Izmailov and K. K. Nandi, Class. Quant. Grav. **39**, 215006 (2022).

[48] W. Liu, X. Fang, J. Jing, and J. Wang, Eur. Phys. J. C **83**, 83 (2023).

[49] V. A. Kostelecky, 2004, Phys. Rev. D, **69**, (2004) 105009.

[50] V. A. Kostelecky, Z. Li, Z. , Phys. Rev. D, **99**, (2019) 056016.

[51] V. A. Kostelecky, M. Mewes, Phys. Rev. D, **80**, (2009) 015020.

[52] V. A. Kostelecky, N. Russell, Rev. Mod. Phys, **83** (2011) 11.

[53] Mang-Sen Ma and Ren Zhao, Class. Quantun Grav. **31** 245014 (2014).

[54] R. V. Maluf and J. C. S. Neves, Phys. Rev. D **97**, 104015 (2018).

Shadow of regular rotating traversable wormhole

Dharm Veer Singh,[1,*] Sudhaker Upadhyay,[†],[2,‡] and Pramod Kumar Singh[3,§]

[1]*Department of Physics, Institute of Applied Sciences and Humanities, GLA Univesity, mathura*

[2]*Department of Physics, K.L.S. College, Magadh University, Nawada 805110, India*

[3]*Shri Sadguru Saibaba Science and Commerce College Ashti Tah. Chamorshi, Gadchiroli, Maharashtra -442707, India*

Abstract

We find an exact $4D$ rotating wormhole (WH) solution in the presence of non-linear electrodynamics. This solution is a variation of the Kerr black hole (BH) which reduces to a wormhole configuration for non-zero values of the deviation parameter (k). For regular rotating (Kerr-like) WH, we derive the shadow shapes and talk about how the spin (a), and the deviation parameter (k) affect the shadow's size and composition. We observe that both the spin (a) and the deviation parameter (k) distort the shadow, and the shadow radius is inversely proportional to the deviation parameter.

[†] Visiting Associate: Inter-University Center of Astronomy and Astrophysics (IUCAA), Pune
[*]Electronic address: veerdsingh@gmail.com
[‡]Electronic address: sudhakerupadhyay@gmail.com
[§]Electronic address: pramod0002000@yahoo.com

I. INTRODUCTION

General relativity admit a spacetime with nontrivial topology such as a wormhole (WH). A WH is a tunnel-like structure hat connect distinct areas of spacetime. This phenomenon requires solving Einstein's equations in a reverse manner to derive solutions that permit WH. The original wormhole solution, which is called the Einstein Rosen bridge, was discovered by Einstein and Rosen [1]. This phenomenon requires solving Einstein's equations in a reverse manner to derive solutions that permit WH. There are two main types of studies on this topic: those that look at Euclidean WH [2–5] and Lorentzian WH. In 1916, Flamm [6] worked further on Schwarzschild solution, and the idea of WH was formed. To remove coordinate singularities, Rosen and Einstein [7] introduced the Einstein-Rosen bridge, which connects two identical sheets as a bridge-like structure. Although this model was unsuccessful, but it formed the base for WH now used in gravitational physics. Later, in 1950s Wheeler[7–9] used Kruskal-Szekers coordinates for explaining Schwarzschild WH, though they exist at quantum scales. The concept of WH introduced by Wheeler was subsequently adapted into Euclidean WH by Hawking and others.

This paper primarily aims to examine the shadow characteristics for Kerr-like WH derived [10], wherein Kerr BH is identified as solution for WH that Kerr-like spacetime coupled with the nonlinear electrodynamics (NLED) based on the Bardeen Proposal. From this point of view, various solutions, such as spherical black holes, wormholes We perform an analysis of the shadow associated with Kerr-like WH. Furthermore, the shadow of Kerr-like WH is anticipated to facilitate the investigation of the fundamental characteristics of WH. A recent study explored association of shadow boundary with outer spherical orbits [11, 12], which was subsequently expanded upon by [13]. Ellis WH have been examined through the analysis of images depicting WH encircled by optically thin dust as presented in [14]. A possible method for probing wormholes, gravitational lensing of Ellis wormholes has been intensively studied in the literature. Basic properties of their gravitational lensing were investigated theoretically [2–6].

This paper is structured as follows, we examine Kerr-like WH solution in Section II. Further in Section III and IV, we analyze geodesic equations and photon trajectories, as well as the construction of shadow images, associated with Kerr-like wormholes. The conclusion and results are in Section. V.

II. REGULAR ROTATING WORMHOLES

The action of Einstein gravity coupled to NLED in four-dimensional spacetime is written as

$$S = \frac{1}{16\pi G}\int d^4x\sqrt{-g}\left[R - 4\pi\mathcal{L}(F)\right], \tag{1}$$

where R is Ricci Scalar, and $\mathcal{L}(F)$ is Lagrangian density of NLED, defined as the function of electromagnetic field tensor $F = F_{\mu\nu}F^{\mu\nu}/4$. Using the Legendre transformation ($\mathcal{H} = 2F\partial\mathcal{L}/\partial F - \mathcal{L}$), the Lagrangian can be formulated as

$$\mathcal{L} = 2P\mathcal{H}_P - \mathcal{H} \qquad \text{and} \qquad \mathcal{H}_P = \frac{\partial\mathcal{H}}{\partial P}, \tag{2}$$

where $P = P_{\mu\nu}P^{\mu\nu}$ and the relation between $F_{\mu\nu}$ and auxilary field $P_{\mu\nu}$ is given vial $F_{\mu\nu} = \mathcal{H}_P P_{\mu\nu}$, where $\mathcal{H}(P)$ is the structure function is relate with the electromagnetic field tensor $F_{\mu\nu} = \partial_\mu A_\nu - \partial_\nu A_\mu$, where A_μ as the electromagnetic potential.

When the action is varied (1) with respect to the metric tensor ($g_{\mu\nu}$) and the electromagnetic potential (A_μ), Einstein field equations coupled to NLED becomes

$$\begin{aligned} R_{\mu\nu} + \frac{1}{2}g_{\mu\nu}R &= 2\left(\mathcal{H}_P P_{\mu\lambda}P^{\lambda}_{\nu} - 2P\mathcal{H}_P + \mathcal{H}(P)\right), \\ \text{and} \quad \nabla_\mu P^{\mu\nu} &= 0. \end{aligned} \tag{3}$$

The line element of a spherically symmetric space-time is given by

$$ds^2 = -f(r)dt^2 + \frac{1}{f(r)}dr^2 + r^2d\Omega^2, \tag{4}$$

We employ the subsequent ansatz for the electromagnetic field

$$P_{\mu\nu} = 2\delta^r_{[\mu}\delta^t_{\nu]}D(r) \qquad \text{and} \qquad P = -\frac{D^2}{2} = \frac{g^2}{2r^4}. \tag{5}$$

The structure function of the NLED is represented by $\mathcal{H}(P)$

$$\mathcal{H}(P) = Pe^{-k(-2g^2P)^{1/4}} \tag{6}$$

The variation of action (1) with respect to $g_{\mu\nu}$ and A_μ is give by

$$R_{ab} - \frac{1}{2}g_{ab}R = T_{ab} \equiv 2\left[\frac{\partial\mathcal{L}(F)}{\partial F}F_{ac}F^c_b - g_{ab}\mathcal{L}(F)\right], \tag{7}$$

$$\nabla_a\left(\frac{\partial\mathcal{L}(F)}{\partial F}F^{ab}\right) = 0 \qquad \text{and} \qquad \nabla_a(*F^{ab}) = 0, \tag{8}$$

The Einstein field equation (7) admits the following solution

$$f(r) = 1 - \frac{2Me^{-k/r}}{r} \tag{9}$$

The Newman-Janis algorithm effectively constructs a metric for rotating black holes based on static spherically symmetric solutions. Utilizing the Newman–Janis algorithm, the four-dimensional rotating regular Kerr-like BH metric is obtained in Boyer–Lindquist coordinates expressed as

$$\begin{aligned} ds^2 \;=\; & -\Big[1 - \frac{2Mr^4e^{-k/r}}{\Sigma}\Big]dt^2 - \frac{4aMr^4e^{-k/r}\sin^2\theta}{\Sigma}dtd\phi + \frac{\Sigma}{\Delta}dr^2 + \Sigma d\theta^2 \\ & + \Big[r^2 + a^2 + \frac{2Ma^2r^4e^{-k/r}\sin^2\theta}{\Sigma}\Big]\sin^2\theta d\phi^2, \end{aligned} \tag{10}$$

whereas

$$\Sigma = r^2 + a^2\cos^2\theta, \qquad \text{and} \qquad \Delta = r^2 + a^2 - Mr^4e^{-k/r} \tag{11}$$

Here, $k = \frac{g^2}{2M}$, with the parameters M, a, and k assumed to be positive. The metric (10) encompasses the $4D$ Kerr solution as a specific instance when $k = 0$ and the Schwarzschild solution when both a and k are equal to zero. To visualize the geometry of the Kerr-like WH, we construct embedding diagrams and analyze an equatorial slice $\theta = \pi/2$, at a fixed time, $t = a$ constant. The metric in this case takes the form

$$ds^2 = \frac{dr^2}{1 - b(r)/r} + R^2d\phi^2, \tag{12}$$

where

$$R^2 = r^2 + a^2 + \frac{2Ma^2e^{-k/r}}{r^2}, \qquad \text{and} \qquad b(r) = \frac{a^2}{r^4} - Me^{-k/r} \tag{13}$$

To visualize this slice, the metric (4) is embedded into 3D Euclidean space and the spacetime can be expressed in cylindrical coordinates as

$$ds^2 = dz^2 + dR^2 + R^2d\phi^2 = \left(\left(\frac{dz}{dr}\right)^2 + \left(\frac{dR}{dr}\right)^2\right)dr^2 + R^2d\phi^2, \tag{14}$$

The integration of (4) and (6) yields the equation for the embedding surface, expressed as

$$\frac{dz}{dr} = \pm\sqrt{\frac{r}{r - b(r)} - \left(\frac{dR}{dr}\right)^2} \tag{15}$$

In the absence of the deviation parameter (k) and the spin parameter (a), we obtain

$$z = \sqrt{8Mr - 2M} \tag{16}$$

The geodesic equations for a test particle with rest mass m_0 can be derived utilizing conserved quantities alongside the Hamilton-Jacobi equation. The geodesic equations for the coordinates t and ϕ can be derived using the conserved quantities, $E = -p_t$ and $L_z = p_\phi$, resulting in the following expressions.

$$\Sigma \frac{dt}{d\sigma} = -a(aE\sin^2\theta - L_z) - \frac{(r^2 + a^2)\mathcal{P}}{r^2 + a^2 - 2Mre^{-k/r}} \tag{17}$$

$$\Sigma \frac{d\phi}{d\sigma} = (aE - L_z \csc^2\theta) - \frac{a\mathcal{P}}{r^2 + a^2 - 2Mre^{-k/r}} \tag{18}$$

where $\mathcal{P} = (r^2 + a^2)E - aL_z$. The remaining geodesic equations, specifically for the r and θ coordinates, can be derived utilizing the Hamilton-Jacobi method. The geodesics of a test particle in the context of Kerr-like WH spacetime (4) adhere to the Hamilton-Jacobi equation [18]. This equation allows for the separation of the radial and angular components of the equation of motion [18]. The general form of the Hamilton-Jacobi equation is expressed as

$$-\frac{\partial S}{\partial \lambda} = \frac{1}{2} g^{ab} \frac{\partial S}{\partial x^a} \frac{\partial S}{\partial x^b} \tag{19}$$

where λ represents an affine parameter and S denotes the Jacobi action, which in the context of four dimensions is expressed as

$$S = \frac{1}{2} m^2 \lambda - Et + L_\phi \phi + L_\psi \psi + S_\theta(\theta) + S_r(r), \tag{20}$$

where m is mass, E is energy, and L is angular momentum, respectively. The Eqs.(19) and Eq. (20) can be expressed in the following form

$$\frac{\partial S_\theta}{\partial \theta} = \pm\sqrt{\Theta} \quad \text{and} \quad \frac{\partial S_r}{\partial r} = \pm\sqrt{\mathcal{R}}, \tag{21}$$

Where,

$$\mathcal{R} = ((r^2 + a^2)E - aL_z)^2 - \Delta(\mathcal{K} - (L_z - aE)^2) \tag{22}$$

$$\Theta = \mathcal{K} \tag{23}$$

III. SPHERICAL PHOTON ORBITS AROUND KERR-LIKE WORMHOLES

The radial geodesic equation for the massless particle can be expressed in the following form to determine the boundary of the WH shadow:

$$\left(\Sigma\frac{dr}{d\sigma}\right)^2 + V_{eff}(r) = 0, \tag{24}$$

Here, $V_{eff}(r)$ denotes the effective potential that characterizes the trajectories of photons in the vicinity of the WH. We express the effective potential of photons using two independent impact parameters: $\xi = L_z/E$ and $\eta = \mathcal{K}/E^2$. The effective potential exhibits a dependency on the deviation parameter (k), which influences the trajectories of photons. The effective potential for circular null geodesics must satisfy the following conditions:

$$V_{eff} = \frac{\partial V_{eff}}{\partial r} = 0. \tag{25}$$

where prime ($\prime$) denotes derivatives with respect to r. The conditions for unstable photon orbits in relation to $\mathcal{R}$ are transformed as follows:

$$\mathcal{R} = \frac{d\mathcal{R}}{dr} = 0 \tag{26}$$

Utilizing Eqs. (23) and (27), we can directly derive the expressions for the impact parameters

$$\begin{aligned}\xi &= \frac{M\left(a^2(k+r)+r^2(k-3r)\right)+r^2\left(a^2+r^2\right)e^{k/r}}{aM(k+r)-ar^2e^{k/r}},\\ \eta &= -\frac{r^4\left(4a^2Me^{k/r}(k-r)+\left(r\left(re^{k/r}-3M\right)+kM\right)^2\right)}{a^2\left(r\left(M-re^{k/r}\right)+kM\right)^2}\end{aligned} \tag{27}$$

where r denotes unstable spherical photon orbit radius. Eq. (27) defines the critical locus of the impact parameters, representing the set of unstable photon orbits. Equation (27) demonstrates that the impact parameters depend on the spin a and the mass M. The computed expressions of the impact parameters, when compared with those of the Kerr spacetime, are found to be indistinguishable. The deviation parameter (k) is related to the impact parameters through the ADM mass, as expressed by the relation $M = Me^{-k/r}$.For the case of $a = 0$ (non rotating), the computation of the impact parameters yields the following relation:

$$\eta = 27M^2 - \xi^2, \qquad \text{with} \qquad r = 3M \tag{28}$$

We proceed to construct and characterize the shadow of Kerr-like WH. To prepare for the shadow investigation, consider a plane that intersects the centre of the WH, with its normal extending from the WH's centre to the observer's line of sight. We present new coordinates (α, β)[17], commonly referred to as celestial coordinates, which define a two-dimensional plane known as the celestial plane. This construction yields the projection of the WH's throat onto the observer's sky. The celestial coordinates are expressed as

$$\begin{aligned} \alpha &= -\frac{\xi(r, a, M, k)}{\sin(\theta)}, \\ \beta &= \sqrt{\eta - \cot^2(\theta)\xi^2 + a^2\cos^2(\theta)} \end{aligned} \tag{29}$$

where,

$$\begin{aligned} \xi &= \frac{M\left(a^2(k+r) + r^2(k-3r)\right) + r^2\left(a^2+r^2\right)e^{k/r}}{aM(k+r) - ar^2e^{k/r}}, \\ \eta &= -\frac{r^4\left(4a^2Me^{k/r}(k-r) + \left(r\left(re^{k/r} - 3M\right) + kM\right)^2\right)}{a^2\left(r\left(M - re^{k/r}\right) + kM\right)^2} \end{aligned} \tag{30}$$

The Eq. (31), is effected by both its spin (a) and its inclination angle (θ_0). When the observer is situated in the equatorial plane $(\theta_0 = \pi/2)$ of the WH, the equations in Eq. (30) simplify to

$$\begin{aligned} \alpha &= \xi, \\ \beta &= \pm\sqrt{\eta} \end{aligned} \tag{31}$$

We present the shadow images of Kerr-like WH for various values of deviation parameter (k), spin (a), and inclination angle (θ_0) (see Figs. 2). It is observed that the shadow exhibits an oblate shape rather than a circular one when compared to the non rotating case. The oblateness, or distortion in shape, results from the nonzero values of the spin (a). Figure 2 illustrates the variation of the spin (a), while it also depicts the influence of the deviation parameter (k) on the shape of the shadow. The deviation parameter (k) significantly affects the radius of the shadow

IV. CONCLUSIONS

This paper focuses on the construction of the shadow casted by Kerr-like WH. The geodesics of test particles have been evaluated, leading to the determination of photon trajectories around the Kerr-like WH. Photons with adequate angular momentum approaching

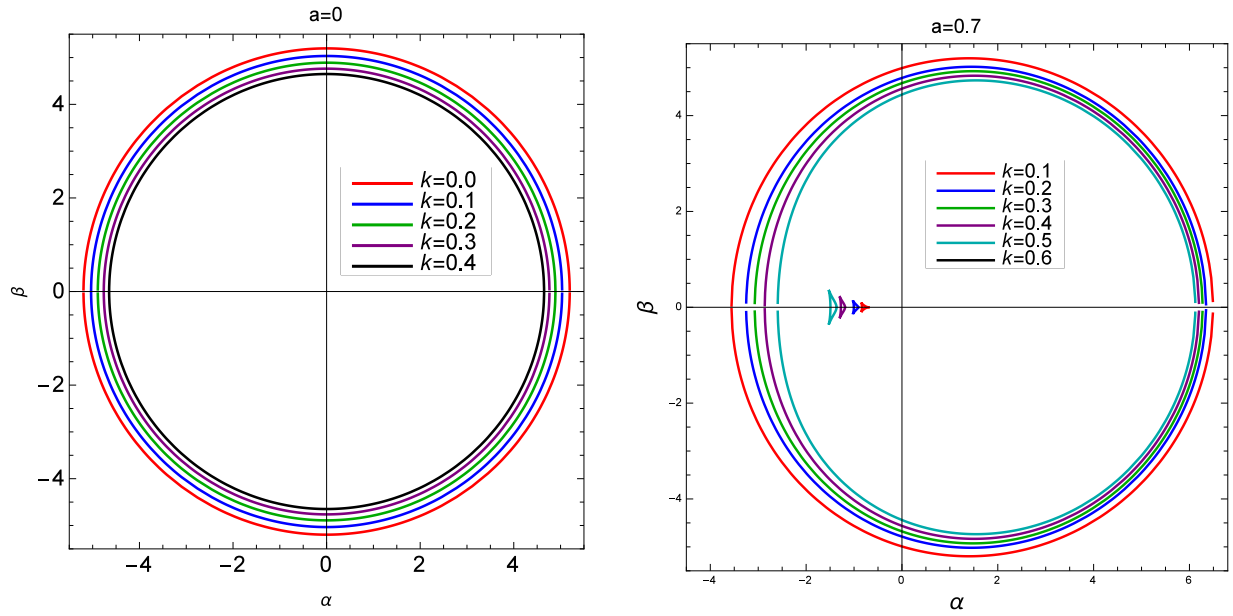

FIG. 1: he shadow of kerr like wormhole different values of k with fixed values of $a = 0.1$ and $a = 0.7$.

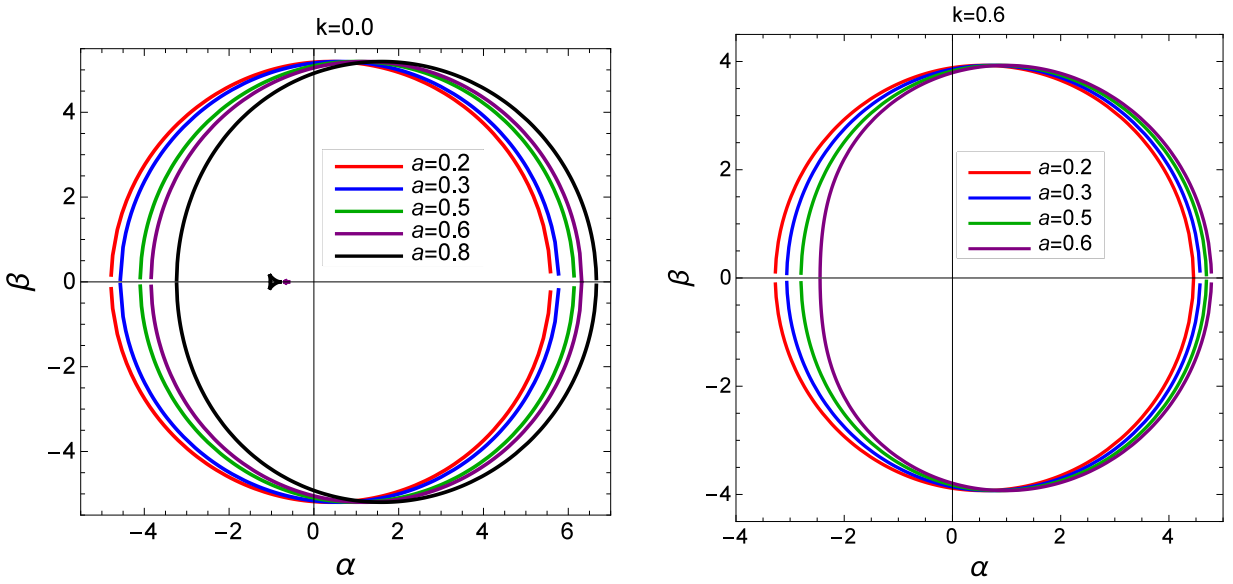

FIG. 2: The shadow of kerr like wormhole different values of a with fixed values of $k = 0.1$ and $k = 0.6$.

the WH exhibit unstable spherical orbits around it. In subsequent analysis, we incorporated the impact parameters that delineate the boundary of the shadow in relation to the illuminated background. The celestial coordinates are evaluated to visualize the optical images of the shadow of the Kerr-like WH. The coordinates were plotted onto the celestial plane to

obtain the shadow images, followed by a discussion of the non rotating and rotating cases of the WH's shadows. Our findings indicate that the radii of the shadows of non rotating WH are smaller than those of Schwarzschild black holes. Different shapes of the shadow for Kerr-like WH have been obtained by varying the parameters. The shapes of the Kerr-like WH's shadow are observed to be oblate or distorted. This distortion primarily arises from the magnitude of the spin parameter a and the inclination angle θ_0. The shapes exhibit greater distortion at the extreme value of the spin parameter a, particularly when the observer is positioned in the equatorial plane. Furthermore, the radius of the shadow images exhibits sensitivity to the deviation parameter (k); a minor alteration in (k) significantly reduces the radius of the shadow. The radius generally decreases with the deviation parameter (k).

Acknowledgments

D.V.S. would like to thank the Council of Science and Technology for grant no. CST/D-828.

---

[1] A. Einstein and N. Rosen, Phys. Rev. 48, 73 (1935).

[2] S. Ruz, S. Debnath, A. K. Sanyal and B. Modak, Euclidean wormholes with minimally coupled scalar fields, Class. Quant. Grav. 30, 175013 (2013).

[3] N. Arkani-Hamed, J. Orgera and J. Polchinski, Euclidean wormholes in string theory, J. High Energy Phys. 0712, 018 (2007).

[4] S.W. Hawking, Quantum Coherence Down the Wormhole, Phys. Lett. B 195, 337 (1987).

[5] S.W. Hawking, Wormholes in Space-Time, Phys. Rev. D 37, 904 (1988).

[6] L. Flamm, Beitrage zur Einsteinschen Gravitationstheorie Phys. Z. 17, 448 (1916).

[7] A. Einstein and N. Rosen, The Particle Problem in the General Theory of Relativity, Phys. Rev. 48, 73 (1935).

[8] J. A. Wheeler, Geons, Phys. Rev. 97, 511 (1955).

[9] J. A. Wheeler, Geometrodynamics, (Academic Press, New York, 1962).

[10] P. Bueno, P.A. Cano, F. Goelen, T. Hertog and B. Vercnocke, Echoes of Kerr-like wormholes, Phys. Rev. D 97, 024040 (2018).

[11] T. Damour and S. N. Solodukhin, Wormholes as black hole foils, Phys. Rev. D 76, 024016 (2007).

[12] P.G. Nedkova, V.K. Tinchev, and S.S. Yazadjiev, Shadow of a rotating traversable wormhole, Phys. Rev. D 88, 124019 (2013).

[13] R. Shaikh, Shadows of rotating wormholes, Phys. Rev. D 98, 024044 (2018).

[14] T. Ohgami and N. Sakai, Wormhole shadows, Phys. Rev. D 91, 124020 (2015).

[15] A. Abdujabbarov, B. Juraev, B. Ahmedov and Z. Stuchl´ık, Shadow of rotating wormhole in plasma environment, Astrophys. Space Sci. 361, 226 (2016).

[16] M. Amir, A. Banerjee and S. D. Maharaj, Shadow of charged wormholes in Einstein-Maxwelldilaton theory, Annals Phys. 400, 198 (2019).

[17] J.M. Bardeen, Black holes, in Proceeding of the Les Houches Summer School, Session 215239, edited by C. De Witt and B.S. De Witt and B.S. De Witt (Gordon and Breach, New York, 1973).

[18] S. Chandrasekhar, The Mathematical Theory of Black Holes (Oxford University Press, New York, 1992).

[19] L. Chetouani and G. Clement, Gen. Relativ. Gravit. 16, 111 (1984).

[20] G. Clement, Int. J. Theor. Phys. 23, 335 (1984).

[21] V. Perlick, Phys. Rev. D 69, 064017 (2004).

[22] K. K. Nandi, Y.-Z. Zhang, and A. V. Zakharov, Phys. Rev. D 74, 024020 (2006)

[23] T. K. Dey and S. Sen, Mod. Phys. Lett. A 23, 953 (2008).

Photon radius and quasinormal modes of regular black holes influenced by dark matter field

Nitin Kumar,[1,*] Indra Sen Ram,[2,†] and Manish Pandey[3,‡]

[1]*Department of Physics, Rajdhani College, University of Delhi, New Delhi, 110015 India*

[2]*Department of Physics, Dyal singh College, University of Delhi, New Delhi 110003, India*

[3]*Department of Civil Engineering, Faculty of Engineering, Marwadi University, Rajkot, Gujrat 360003, India*

Abstract

This study examines the correlation between geometrical parameters, the photon sphere, and quasinormal modes in the eikonal limit of black holes associated with nonlinear electrodynamics (NLED) and perfect fluid dark matter (PFDM). We investigate the photon sphere and quasinormal modes employing the WKB approach, and our findings suggest that the real component of the eikonal quasinormal mode frequencies of test fields is associated with the unstable circular null geodesics.

*Electronic address: nitinksmp@gmail.com

†Electronic address: indra77dsc@gmail.com

‡Electronic address: manish07sep@gmail.com

I. INTRODUCTION

Einstein's general theory of relativity says that black holes(BH) exist, which is one of the most interesting things it says. Black holes have been studied by physicists for decades, but they have also been a source of debate for a long time. In current black hole physics, conventional black holes have become a major area of study [5–21, 23]. The 'Regular' black holes don't have any center curvature singularities. People usually say that the lack of a singularity is because normal black holes have a core in the middle that goes against the strong energy condition. This core gets around the Penrose singularity theorem and gets rid of the singularity.

Black holes exhibit Quasinormal Modes (QNMs), which are a distinctive characteristic that delineates their damped oscillations in spacetime resulting from external perturbations [22–32]. The frequencies of these QNMs of black holes are complex,where the real part denotes the oscillation frequency and the imaginary part represents the rate at which the oscillation amplitude decays. Quasinormal modes (QNMs) have various important applications in black hole research, including the investigation of surface gravity (κ) and horizon area (A), stability assessment, gravitational wave detection, and evaluation of geometrical characteristics such as mass, spin, and charge. These oscillations occur at the eikonal limit, when the real part of the QNM frequency is intricately linked to the unstable circular null geodesics of the black hole. This equation clarifies the relationship between QNMs and the geometric properties of the black hole. Eikonal QNMs denote a specific class of oscillations that are particularly beneficial for analyzing high-frequency QNMs and their applications.

This study examines the influence of perfect fluid dark matter (PFDM) on thermodynamics properties and QNMs around a specific category of regular black holes. The distribution is asymmetric, exhibiting a larger density of dark matter in proximity to conventional black holes, while demonstrating a lower density at greater distances. This research aims to investigate the impact of PFDM fluid on scalar field perturbation. To achieve this objective, we will employ the black hole solution enveloped by PFDM fluid [33, 34] using the WKB approach. Cardoso [35] demonstrated that the real component of the QNMs correlates with the angular velocity of the final circular null geodesic, whereas Stefanov [36] established a relationship between black hole QNMs in the eikonal limit and lensing in the strong deflection limit. The investigation of eikonal quasi-normal modes in black hole solutions of

general relativity and their association with the photon sphere has been thoroughly examined in prior studies [37]. The research has been broadened to encompass modified theories of gravity, including Scalar Gauss-Bonnet gravity [38], Einstein-dilaton-Gauss-Bonnet black holes [39], dynamical Chern-Simons gravity [40], Rotating Loop Quantum black holes [41], string-corrected D-dimensional black holes [42], and deformed Schwarzschild black holes [43].

The study is structured as follows: in Section II, we derive a (AdS) regular black hole solution in conjunction with PFDM fluid and NLED, provide the coherent equations of gravity coupled to NLED, and delineate the configuration of the horizon structure. Section III addresses the examination of the thermodynamic properties of the regular (AdS) black hole solution. Section IV is dedicated to examining the local and global stability of the derived black hole solution. Section V examines the QNM of the derived black hole solutions. Ultimately, the final observations and findings are delineated in Section VI.

II. SOLUTION OF REGULAR BLACK HOLE

The Einstein-Hilbert action, incorporating a negative cosmological constant together with NLED and PFDM, is expressed as

$$\mathcal{S} = \frac{1}{2}\int d^D x\sqrt{-g}\,[\mathcal{R} - 2\Lambda - 2(\nabla_a\phi\nabla^a\phi - 2V(\phi)) - 4(L_{DM} + L(F))] \tag{1}$$

where $\mathcal{R}$ denotes the curvature scalar, Λ represents the cosmological constant associated with the AdS length by $\Lambda = -3/l^2$, and $\mathcal{L}(F)$ is the Lagrangian density of the nonlinear matter field, which is a function of the electromagnetic field tensor $F_{\mu\nu}$, defined as $F_{ab} = \partial_\mu A_\nu - \partial_\nu A_\mu$, where A_μ is the electromagnetic potential. The equation of motion (EOM) is derived by altering the action (1) concerning $g_{\mu\nu}$. The equation of motion is expressed as

$$R_{\mu\nu} - \frac{1}{2}g_{\mu\nu}R = T^{DM}_{\mu\nu} + T^{NED}_{\mu\nu} \tag{2}$$

The Lagrangian $L(F)$ is the function of $F = -\frac{1}{4}F_{ab}F^{ab}$. In Eq.(1) the action with fuction of g_{ab} and the potential A_a, has the equations of motion as given below:

$$R_{ab} - \frac{1}{2}\tilde{g}_{ab}R + \Lambda g_{ab} = T_{ab} \equiv 2\left[\frac{\partial L(F)}{\partial F}F_{ac}F^c_b - \tilde{g}_{ab}L(F)\right], \tag{3}$$

$$\nabla_a\left(\frac{\partial L(F)}{\partial F}F^{ab}\right) = 0 \qquad \text{and} \qquad \nabla_a(*F^{ab}) = 0, \tag{4}$$

In this context, $L(F)$ is an arbitrary continuous function of F such that $\partial L/\partial F \to \infty$ as $F \to \infty$ and $L(F) = 1$ as $F \to 0$. The solution of interest can be deduced from the Lagrangian $L(F)$, which assumes the following form

$$L(F) = Fe^{-\frac{s}{e}(2e^2F)^{\frac{1}{4}}} \tag{5}$$

where $s = g/2M$, where M and e are the free parameters associated with magnetic monopole charge and black hole mass. using

$$0 = d\mathbf{F} = e'(r)\sin\theta dr \wedge d\theta \wedge d\phi, \tag{6}$$

his results in $e(r) = e$, with the integration constant selected as e. These equations of motion present the following spherically symmetric black hole solution.

$$ds^2 = -\left(1 - \frac{2Me^{-k/r}}{r} + \frac{\lambda}{r}\log\left(\frac{r}{\lambda}\right) + \frac{r^2}{l^2}\right)dt^2 + \frac{dr^2}{\left(1 - \frac{2Me^{-k/r}}{r} + \frac{\lambda}{r}\log\left(\frac{r}{\lambda}\right) + \frac{r^2}{l^2}\right)} + r^2 d\Omega_2^2, \tag{7}$$

This is black hole solution, which is characterised by the mass (M), deviation parameter (k), anistropic fluid parameter (λ) and AdS length (l). This black hole solution interpolates wit the regular black hole in the absence of λ and AdS Schwarzschild black hole in the limit of λ and k.

III. PHOTON SPHERE AND BLACK HOLE SHADOW

The photon sphere is the determinant of the shadow of the black hole. To ascertain the photon radius and shadow, we initially formulate the Lagrangian for photon motion constrained to the equatorial plane. $(\theta = \frac{\pi}{2})$ as

$$L = -g_{tt}\dot{t}^2 + g_{rr}\dot{r}^2 + g_{\theta\theta}\dot{\theta}^2 + g_{\phi\phi}\dot{\phi}^2, \tag{8}$$

and the corresponding Hamiltonian is articulated as

$$\mathcal{H} = p_t\dot{t} + p_r\dot{r} + p_\phi\dot{\phi} - L, \tag{9}$$

where the overdot signifies the derivative with respect to the affine parameter. The generalised momenta are given by

$$p_t = \frac{\partial \mathcal{H}}{\partial \dot{t}} \equiv E = \text{constant}, \tag{10}$$

$$P_\phi = \frac{\partial \mathcal{H}}{\partial \dot{\phi}} \equiv -J = \text{constant}, \tag{11}$$

$$p_r = \frac{\partial \mathcal{H}}{\partial \dot{r}} = g_{rr}\dot{r}. \tag{12}$$

The equation of motion about the photon can be determined via the Hamiltonian formalism, which is derivable as follows

$$\dot{t} = \frac{\partial \mathcal{H}}{\partial p_t} = -\frac{p_t}{g_{tt}}, \qquad \dot{\phi} = \frac{\partial \mathcal{H}}{\partial p_\phi} = \frac{p_\phi}{r^2}, \qquad \text{and} \qquad \dot{r} = \frac{\partial \mathcal{H}}{\partial p_r} = -\frac{p_r}{g_{rr}}. \tag{13}$$

The Hamiltonian is invariant with respect to time (t) and the azimuthal coordinate (ϕ) and, therefore, leads to the following null geodesics equation:

$$\dot{r}^2 + V_{eff}(r) = 0, \quad \text{with} \quad V_{eff} = f(r)\left(\frac{J^2}{r^2} - \frac{E^2}{f(r)}\right). \tag{14}$$

The effective potential for circular null geodesics, which delineates the radius of the photon sphere, must adhere to the following conditions:

$$V_{eff} = \frac{\partial V_{eff}}{\partial r} = 0. \tag{15}$$

The formula for the photon radius (r_p) is determined as

$$3kM - r(6M - e^{k/r}(2r - \lambda)) + 3e^{k/r} r\lambda \log\left[\frac{r}{\lambda}\right] = 0. \tag{16}$$

Since there is no analytical way to solve this equation, we use numerical methods instead. The numerical values of the photon radius with different values of k and λ are presented in the Tab I. The tables indicate that the photon radius increases with the deviation parameter and PFDM fluid parameter (λ).

IV. QNMS IN EIKLON LIMIT

It is quite clear that QNMs of black holes can be described as test fields scattered in the background of the holes. Henceforth, the eikonal modes can be elucidated as wave packets

	r_p		
k	$\lambda = 0.1$	$\lambda = 0.2$	$\lambda = 0.3$
0.1	0.005	0.0125	...
0.2	0.009	0.0200	0.0358
0.3	0.0121	0.0255	0.0416
0.4	0.0149	0.0297	0.0470
0.5	0.0161	0.0331	0.0516
0.6	0.0176	0.0354	0.0555

TABLE I: The numerical values of photon radius (r_p) corresponding to the deviation parameter (k) with fixed values of $\lambda = 0.1$, 0.2 and $\lambda = 0.3$. The dots represent values are imaginery.

localised around the photon spheres according to the geometric optics approximation. So, we first consider a scalar (test) field in the background of a black hole (7). The equation of these perturbations takes the following form [24, 25]:

$$\frac{1}{\sqrt{-g}}\partial_\mu\left(\sqrt{-g}g^{\mu\nu}\partial_\nu\right)\Psi = 0, \tag{17}$$

where $g^{\mu\nu}$ denotes the components of the metric described in equation (7). The mode decomposition of the scalar perturbation into the relevant harmonics is given as

$$\Psi = \frac{1}{r}\sum_{lm} e^{i\omega t}\phi_{lm}Y_l^m(\theta,\phi). \tag{18}$$

At this point, l, m, Y_l^m, and ω stand for the angular quantum number, magnetic quantum numbers, spherical harmonics, and angular frequency of the scalar field, respectively. The reason for employing the WKB approximation for QNMs lies in the resemblance between the equations governing black hole perturbations and the one-dimensional Schrödinger equation describing a potential barrier. Equation (17) can be transformed into a Schrodinger-like equation by replacing the value of Ψ with the tortoise coordinate $dr^* = dr/f(r)$ as

$$\left(\frac{d^2}{dr^{*2}} + \omega^2 - V(r^*)\right)\Psi = 0, \tag{19}$$

where $V(r^*)$ is the effective potential and has the form

$$V(r^*) = f(f)\left(\frac{f'(r)}{f(r)} + \frac{l(l+1)}{r^2}\right). \tag{20}$$

To find the QNF, boundary constraints must be imposed at the event horizon. The boundary conditions on the solution in the limits $r_* \to \pm\infty$ are fixed by requiring consistency with the radiation flux measured by physical observers at spatial infinity and just outside the event horizon. As $r_* \to +\infty$, observers at infinity register both ingoing and outgoing waves, whereas as $r_* \to -\infty$ (i.e. at the horizon) only ingoing radiation is admissible. These physical requirements thereby translate directly into precise boundary conditions on the radial functions $\Psi(r_*)$ in the asymptotic regions. The boundary conditions can be written as

$$\Psi(r_\star) \to e^{i\omega r_\star}, \qquad r_\star \to -\infty, \tag{21}$$

$$\Psi(r_\star) \to e^{-i\omega r_\star}, \qquad r_\star \to +\infty. \tag{22}$$

Here, the + sign denotes the inflowing waves on the horizon, whereas the − sign signifies the outflowing waves at infinity. The frequencies associated with the QNM are expressed as $\omega = \omega_R + i\omega_I$, where ω_R and ω_I represent the oscillatory and damping components of the frequency, respectively. To determine QNM frequencies, the WKB method can be employed, initially formulated by Schutz and Will [24], subsequently expanded to third order by Iyer and Will [25], and further extended to sixth order by Konoplya [26]. The WKB formula is expressed as follows [24]:

$$\frac{\omega^2 - V_0}{\sqrt{-2V_0''}} - L_2 - L_3 - L_4 - L_5 - L_6 = n + \frac{1}{2}, \tag{23}$$

where V_0 is the height of the barrier, V_0'' is the second derivative of the potential with respect to the tortoise coordinate, and L_2, L_3, L_4, L_5 and L_6 are the constants. We will examine the acquired QNM categorised by harmonic index l for this black hole solution.

The QNFs are complex numbers represented as $\omega = \omega_R + i\omega_I$. We employ the WKB formula in the large l limit [24–26] to derive the QNFs as

$$\omega = l\Omega - i\left(n + \frac{1}{2}\right)|\Lambda|, \tag{24}$$

with

$$\Omega = \frac{\sqrt{f(r_p)}}{r_p} = \frac{1}{L_p} \text{ and } \Lambda = \frac{\sqrt{2f(r_p) - r_p^2 f''(r_p)}}{\sqrt{2}L_p}, \tag{25}$$

where L_p and r_p are the Lyapunov exponent and photon radius, respectively. There is a presentation of the numerical values of the real and imaginary parts of QNFs in table II,

and these values are plotted in Tab. II for various values of the black hole parameters. A confirmation that the modes of the acquired black hole are unstable is provided by the fact that the imaginary part of the QNMs has positive values.

	$\omega_R - i\omega_I$		
k	$\lambda = 0.1$	$\lambda = 0.2$	$\lambda = 0.3$
0.1	$1.66 \times 10^7 - 53817.1i$	$3.84 \times 10^5 + 5062.83i$	...
0.2	$6.39 \times 10^6 - 24884.0i$	$2.42 \times 10^5 + 3202.36i$	$2.12 \times 10^4 + 693.73i$
0.3	$4.43 \times 10^6 - 17892.3i$	$2.11 \times 10^5 + 2655.24i$	$2.76 \times 10^4 + 743.69i$
0.4	$3.44 \times 10^6 - 14221.2i$	$2.07 \times 10^5 + 2443.84i$	$3.10 \times 10^4 + 743.69i$
0.5	$3.97 \times 10^6 - 14720.8i$	$2.12 \times 10^5 + 2348.26i$	$3.40 \times 10^4 + 746.27i$
0.6	$4.02 \times 10^6 - 14178.7i$	$2.35 \times 10^5 + 2399.29i$	$3.72 \times 10^4 + 754.19i$

TABLE II: The numerical values of real and imaginary parts of QNMs corresponding to the deviation parameter (k) with fixed values of $\lambda = 0.1$, 0.2 and $\lambda = 0.3$. The dots represent values without real parts.

The effects of parameters k and λ on the behaviour of QNMs and QNFs are depicted in Tab. II. We now examine the characteristics of QNF for massless scalar fields in the case of $l > 0$ modes. We note that for all computed ω, the imaginary part $Im\,\omega$ is negative, concluding that the black hole is stable against scalar perturbations for $l > 0$. Now, QNFs calculated by varying the deviation parameter (k) (upper panel) and anisotropic fluid parameter λ (lower panel) are plotted in Tab. II. When the anisotropic fluid parameter λ and the deviation parameter (k)increase, $Im\,\omega$ gradually decreases, and the real part of the QNM decreases with k and the anisotropic fluid parameter λ. From Tab. II, we can see that the real part of the QNFs decreases with the deviation parameter and the anisotropic fluid parameter. This means that the roles of deviation parameter and anisotropic fluid parameters mimic each other. The imaginary part of the QNFs increases with the deviation parameter and first decreases, then increases anisotropic fluid parameters. The obtained black hole solution is more stable at the small deviation parameter and anisotropic fluid parameter value.

We calculate the radius of the black hole horizon r_+ and illustrate $Re\,\omega$ as a function of r_+ in Tab. II. Here, we observe that r_+ diminishes as λ increases. Consequently, it is not

unexpected that $Re\,\omega$ diminishes as r_+ escalates. Conversely, the behaviour of $Im\,\omega$ about r_+ parallels that of $Im\,\omega$ about λ; there exists a particular value of r_+ at which $Im\,\omega$ attains its maximum, representing the unstable radius of the horizon in terms of stability.

V. CONCLUSIONS

In this work, we have found a regular black hole solution in the presence of PFDM. We have also studied the QNMs of the obtained black hole solution. The obtained black hole interpolates with regular black hole in the absence of the PFDM fluid parameter, as well as a Schwarzschild black hole in the limit of the PFDM parameter and the deviation parameter. The real part of the QNFs is found to decrease with the deviation parameter and the PFDM parameter. In contrast, the imaginary part of the QNFs increases with the deviation parameter and simultaneously lowers and subsequently raises the parameters. The deviation parameter and the anisotropic fluid factor contribute to an increase in the size of the photon radius. This conclusion can be drawn from the findings presented here. In the case of the QNMs and crucial thermodynamic quantities connected with the black hole, the impacts of the λ and q are inversely proportional.

Data Availability Statement

Data sharing not applicable to this article as no datasets were generated or analysed during the current study.

[1] E. Ayon-Beato and A. Garcia, Gen. Rel. Grav. 31, 629 (1999).

[2] E. Ayon-Beato, A. Garcia, Phys. Lett. B 493 (2000) 149.

[3] T. G. Rizzo JHEP **09**, 021 (2006).

[4] D. V. Singh, S. G. Ghosh and S. D. Maharaj, Nucl. Phys. B **981** (2022), 115854.

[5] K. A. Bronnikov, Phys. Rev. D **96** (2017) no.12, 128501.

[6] K. A. Bronnikov, Phys. Rev. D **63** (2001), 044005.

[7] D. V. Singh and S. Siwach, Phys. Lett. B. 408 135658 (2020).

[8] S. G. Ghosh, D. V. Singh, R. Kumar and S. D. Maharaj, Annals Phys. **424** (2021) 168347.

[9] A.G. Tzikas, Phys. Lett. B 788 (2019) 219.

[10] F. Ahmed, D. V. Singh and S. G. Ghosh, Gen. Rel. Grav. **54** (2022) 21.

[11] D. V. Singh, B. K. Singh and S. Upadhyay, Annals Phys. **434** (2021) 168642.

[12] S. Upadhyay and D. V. Singh, Eur. Phys. J. Plus **137** (2022) 383.

[13] A. Ovğun, Phys. Lett. B 820 (2021) 136517.

[14] W. Javed, J. Abbas and A. Ovğun, Eur. Phys. J. C 79 (2019) 694.

[15] Md Sabir Ali, S.G. Ghosh, Phys. Rev. D 98, 084025 (2018).

[16] D. V. Singh, S. G. Ghosh and S. D. Maharaj, Annals Phys. 412, 168025 (2019).

[17] A. Kumar, D. V. Singh and S. G. Ghosh, Eur. Phys. J. C 79, 275 (2019).

[18] J. M. Bardeen, Conference Proceedings of GR5, Tbilisi, USSR, 1968, p. 174.

[19] A. Kumar, D. V. Singh and S. Upadhyay, JHAP **4** (2024) no.4, 85-99

[20] D. V. Singh, S. G. Ghosh and S. D. Maharaj, Annals Phys. **412**, 168025 (2020).

[21] Mang-Sen Ma and Ren Zhao, Class. Quantun Grav. **31** 245014 (2014).

[22] B. K. Vishvakarma, D. V. Singh and S. Siwach, Eur. Phys. J. Plus 138 (2023) 536.

[23] D. V. Singh, S. G. Ghosh and S. D. Maharaj, Nucl. Phys. B 981 (2022) 115854.

[24] B. F. Schutz and C. M. Will, Astrophys J. 291, L33 (1985).

[25] S. Iyer and C. M. Will, Phys. Rev. D 35, 3621(1987).

[26] R. A. Konoplya, Phys. Rev. D 68, 024018 (2003).

[27] K. W. Ford, and J. A. Wheeler, Ann. Phys. 7(3), (1959) 259.

[28] K. Jusuf, Phys. Rev. D 101, (2020) 084055.

[29] R. A. Konoplya, and Z. Stuchlík, Phys. Lett. B 771 (2017) 597.

[30] A. Kumar, D. V. Singh and S. Upadhyay, Int. J. Mod. Phys. A **39** (2024) no.31, 2450136.

[31] Y. Myrzakulov, K. Myrzakulov, S. Upadhyay and D. V. Singh, Int. J. Geom. Meth. Mod. Phys. **20** (2023) no.07, 2350.

[32] D. V. Singh, A. Shukla and S. Upadhyay, Annals Phys. **447** (2022), 169157.

[33] M. H. Li and K. C. Yang, Phys. Rev. D 86, 123015 (2012).

[34] V.V. Kiselev (2003) arXiv:gr-qc/0303031

[35] V. Cardoso, A. S. Miranda, E. Berti, H. Witek, and V. T. Zanchin, Phys. Rev. D 79, 064016 (2009).

[36] I. Z. Stefanov, S. S. Yazadjiev and G. G. Gyulchev, Phys. Rev. Lett. 104 (2010) 251103.

[37] Li, P.C., Lee, T.C., Guo, M., Chen, B. Phys. Rev. D 104, 084044 (2021).

[38] Bryant, A., Silva, H.O., Yagi, K., Glampedakis, K. Phys. Rev. D 104, 044051 (2021).

[39] Konoplya, R.A., Zinhailo, A.F., Stuchlík, Z. Phys. Rev. D 99, 124042 (2019).

[40] Glampedakis, K., Silva, H.O. Phys. Rev. D 100, 044040 (2019).

[41] Liu, C., Zhu, T., Wu, Q., Jusufi, K., Jamil, M., Azreg-Aïnou, M., Wang, A. Phys. Rev. D 101, 084001 (2020).

[42] Moura, F., Rodrigues, J. Phys. Lett. B 819, 136407 (2021).

[43] Chen, C.Y., Chiang, H.W., Tsao, J.S. Phys. Rev. D 106,(2022).

International Conference on Astroparticle Physics, Gravitation and Cosmology (APGC-2025)
26-28 June 2025, GLA University, Mathura, India

Using CMG Model to Investigate the Emission Feature of the Projectile and Target Fragments

N. Maitry[1] and M. K. Singh[1,*]

[1]*Department of Physics, Institute of Sciences and Humanities, GLA University, Mathura - 281406, India*

Abstract

In this study, the Coulomb Modified Glauber (CMG) model is used to assess the total nuclear reaction Cross-Section (CS) for target participants [P_{targ}] and projectile participants [P_{proj}] in interactions of $^{84}Kr_{36}$ at 1 A GeV with Nuclear Emulsion Detector (NED). We observed that there is a good match between the experimental results and the average reaction CS with nuclear medium effect. The distinct target groups of the nuclear emulsion nuclei are associated with these predicted [P_{proj}] and [P_{targ}].

*Electronic address: singhmanoj59@gmail.com

I. INTRODUCTION

Since the discovery of QGP, physicists from all over the globe have been interested in nucleus-nucleus (A-A) and nucleon-nucleus (h-A) interactions because they provide a precise explanation of nuclear matter properties including quarks, gluons and nuclear matter density. Because of its great spatial persistence, the NED, a composite target detector, can detect short-lived particles like charm mesons and similar particles.

According to the participant spectator model, three distinct regions can arise from the collision of two nuclei: the target spectator region which produces grey and black particles, the participant region which produces shower particles and the projectile spectator regions, which produce projectile fragments [1]. We have measured target participants (P_{targ}) and projectile participants (P_{proj}) considering each case with and without medium effect by using the CMG model for interactions of $^{84}Kr_{36}$-Em at 1 A GeV.

II. EXPERIMENTAL DETAIL

We used NIKFI-BR2 nuclear emulsion plate (NEP) in this observation, which were exposed at GSI in Darmstadt, Germany, having dimensions of $9.8 \times 9.8 \times 0.06$ cm^3. The NED consists of H, O, C, N, Ag, Br, and small amounts of S and I [1].

The Olympus binocular transmitted light microscope BH-2 was used to identify physics events from NED plates using line and volume scanning methods. Events were categorized into shower, black and grey particles. For this analysis, 550 events were used out of 700.

III. RESULT AND DISCUSSION

Using the CMG model, it is possible to compute the total nuclear reaction cross-section (σ_R) for the proton and for each projectile's interactions with the different targets, or the NED's elemental components. The average number of P_{targ} and P_{proj} may be determined as:

$$\langle P_{\text{proj}} \rangle = \frac{A_P \sigma_{PAT}}{\sigma_{A_P A_T}}, \quad \langle P_{\text{targ}} \rangle = \frac{A_P \sigma_{PAP}}{\sigma_{A_P A_T}} \tag{1}$$

Here, σ_{PAT} and σ_{PAP} are the total nuclear reaction cross-sections of the proton with

the target and projectile respectively, A_P is the projectile mass, and $\sigma_{A_P A_T}$ is the total projectile's nuclear reaction cross-section.

We compute and compare P_{targ} and P_{proj} for interactions within the framework of the CMG model for various nuclei at relativistic energy. Figures 1 and 2 show the relationships for projectiles ^{56}Fe, ^{84}Kr, ^{132}Xe, ^{197}Au, and ^{238}U.

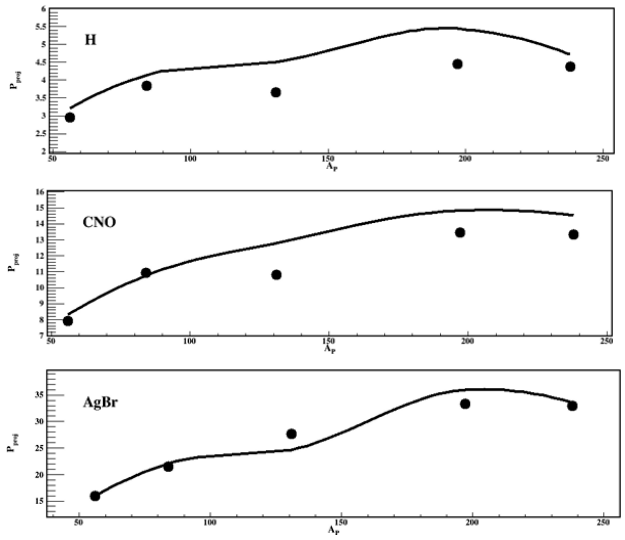

FIG. 1: The correlation of P_{proj} with A_P using the CMG model. The curved line represents the CMG model prediction.

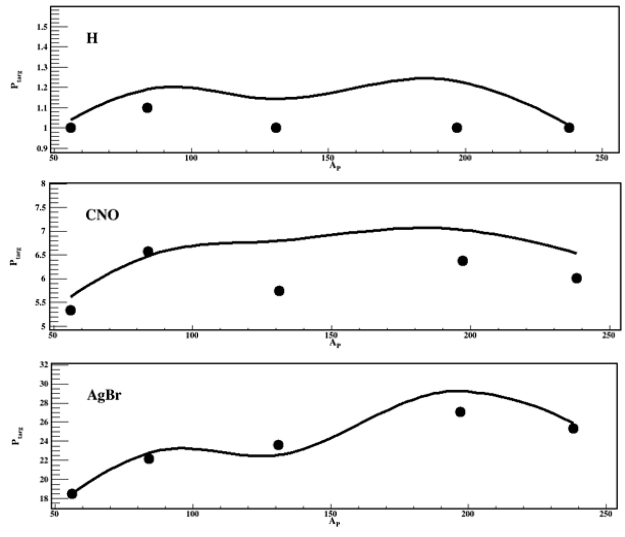

FIG. 2: The correlation of P_{targ} with A_P using the CMG model. The curved line represents the CMG model prediction.

The nuclear medium effect is an essential component of the CMG model, as evidenced by comparative results. Reaction cross-sections accounting for medium effects predict lower values than those without it.

IV. CONCLUSION

In this work, the nucleus-emulsion interactions inside the CMG model for various nuclei at relativistic energy are estimated and compared for P_{targ} and P_{proj}. The results show that the CMG model cannot clearly describe heavy-ion interactions without nuclear medium effect [7]. It was found that including the medium effect results in lower predicted cross-sections. Emulsion technology, more especially, nuclear emulsion detector, offers special capabilities for tracking particles, detection rare interaction, and researching basic physics process, making it an effective tool for rare events searches in particle physics and beyond. The detection and analysis of rare interaction and decays are made possible by the exceptional precision with which these detectors, which are made of fine grain silver halide crystals, can follow particles. Currently, this detector technology is employed for the search for rare events in a number of experiments throughout the world, including CHORUS, OPERA, and CERN.

Acknowledgments

We are grateful to the scientific team at GSI, Germany, for their support in exposing the NED to the $^{84}Kr_{36}$ beam at 1 A GeV.

---

[1] M. K. Singh et al., Int. J. Mod. Phys. E, 28, 1950063 (2019).

[2] P. J. Karol et al., Phys. Rev. C, 46(5), 1988 (1992).

[3] M. S. M. Nour El-Din et al., Can. J. Phys., 86, (2008).

[4] M. A. Jilany et al., Int. J. Mod. Phys. E, 4, 815 (1995).

[5] P. L. Jain et al., Phys. Rev. Lett., 45(20), 1763 (1984).

[6] M. A. Jilany et al., Nucl. Phys. A, 705, 477 (2002).

[7] U. Rawat et al., Iran. J. Sci., 705, 477 (2024).

International Conference on Astroparticle Physics, Gravitation and Cosmology (APGC-2025)
26-28 June 2025, GLA University, Mathura, India

Accretion disk around a black hole coupled with nonlinear electrodynamics and dRGT massive gravity

Bablu[1,*] and Dharm Veer Singh [†1,2,‡]

[1]*Department of Physics, Institute of Applied Science and Humanities, GLA University, Mathura 281406, India*

[2] *School of Physics, Damghan University, P.O. Box 3671641167, Damghan, Iran*

Abstract

In this paper, we explore a thin accretion disk around a black hole with nonlinear electrodynamics in dRGT massive gravity, and the black hole we use which is static and spherically symmetric. We take non-zero graviton mass for analysis of accretion disk. We have done calculations for event horizons, equation of motion, and effective potential of black hole. From the calculations, we obtain different types of results like specific energy, specific angular momentum, and angular velocity of the particle that moves in circular orbits. We also plot these results and calculate the stable orbits. We obtain a relation of the flux radiant energy over the disk.

[†] Visiting Associate: Inter-University centre of Astronomy and Astrophysics (IUCAA) Pune, India
[*]Electronic address: babluchaudhary0003@gmail.com
[‡]Electronic address: veerdsingh@gmail.com

I. INTRODUCTION

Observational data derived from cosmological investigations, including Type Ia supernovae (SNe Ia), fluctuations in the cosmic microwave background (CMB), and baryon acoustic oscillations (BAO), have substantiated the conclusion that the Universe is undergoing accelerated expansion in its later phases. Nonetheless, within the established framework of general relativity (GR), this acceleration presents a challenge, as it cannot be reconciled without the introduction of an enigmatic form of energy referred to as dark energy. The theory of massive gravity has been introduced as a modification to General Relativity (GR), model that addresses cosmic acceleration without depending on the concept of dark energy. This theoretical framework includes a mass term for the graviton, by changing the Einstein-Hilbert action, and result in modified gravity

The initial concept of massive gravity was put forth by Fierz and Pauli in 1939, who devised a distinct, ghost-free, and Lorentz-invariant linear theory by integrating interaction terms related to the mass of the graviton.Subsequent investigations conducted by van Dam, Veltman, and Zakharov revealed that the initial formulation of the theory exhibited a discontinuity in its behavior as the mass of the graviton approached zero, a phenomenon that has come to be known as the van Dam-Veltman-Zakharov (vDVZ) discontinuity. Vainshtein proposed that non-linear interactions of massive gravity resolve the discontinuity with general relativity at large distances. However, Boulware and Dieser identified that these non-linear modifications gave rise to an instability referred to as the Boulware-Dieser ghost, a independent research conducted by Arkani-Hamed and Creminelli. In 2010, de Rham, Gabadadze, and Tolley advanced the field by developing a non-linear massive gravity theory that effectively circumvented these ghost instabilities through a careful design of the interaction potential, thereby avoiding inconsistencies linked to higher-order derivatives.

It is important to note that black holes serve as optimal subjects for the examination of modifications to the theories of general relativity. The significance of this matter arises from the discrepancies that exist between the predictions made by general relativity and those proposed by alternative theoretical frameworks. Most of studies have been conducted to identify spherically symmetric black holes within various massive gravity theories. Solutions for spherically symmetric black holes in the dRGT massive gravity have been successfully derived. Furthermore, research has also produced solutions for charged black holes within

the dRGT framework. Recently, investigations into the gravitational wave drived from black holes in the context of massive gravity have also been undertaken.

At this stage, it is noteworthy that the investigation of accretion disks surrounding compact objects represents one of the viable methodologies for distinguishing between general relativity and alternative theoretical frameworks. It is established that the mass of black holes can increase due to the accretion disks that envelop them, which implies the existence of gas clouds functioning as an accretion disk. It is important to acknowledge that studies related to accretion disks of black holes have been conducted over the years. This particular study focused to the mass of the accretion disk of rotating black holes. Furthermore, the radiation characteristics of thin accretion disks, as well as the general relativistic attributes of such disks, have been explored in the references[]. Concurrently, the physical properties and characteristics of the matter constituting thin accretion disks within static and spherically symmetric wormhole spacetimes have also been investigated. In this research, the properties of the electromagnetic radiation emitted from Kerr black holes have been reviewed. Additionally, the optical characteristics of a thin accretion disk in the vicinity of compact objects have been analyzed within the framework of Einstein–Gauss–Bonnet gravity. Further studies on this topic can be found in references [].

The objective of this paper is to detailed analysis of the accretion disk around a black hole within the framework of dRGT massive gravity theory. We will identify the various parameters associated with the accretion disk of the black holes. In Section 2, we will present and review the non-linear dRGT massive gravity theory, of a static and spherically symmetric black hole solution derived from this theoretical framework. Furthermore, we will analyze the properties of the horizon of this black hole. Subsequently, we will derive the equations of motion and the effective potential associated with the system. In Section 3, we will compute all relevant parameters pertaining to the accretion disk of the black hole within the context of dRGT massive gravity. Additionally, we will provide a numerical analysis that includes the determination of stable circular orbit locations under two distinct systems. We have taken all constsnt values to fix units i.e. $(8\pi G = c^4 = 1)$.

II. ACTION, BLACK HOLE SOLUTION AND EQUATION OF MOTION

In this section we review the nonlinear dRGT massive gravity theory, which is free from BD ghost at non-linear. This theory consists of Einstein-Hilbert action and non-linear interaction terms as follows:

$$S = \int d^4x\sqrt{-g}\frac{1}{2k^2}[R + m_g^2 U(g,\phi^a)], \tag{1}$$

This action can be described by a metric $g_{\mu\nu}$ and four scalar fields, $\phi^a(a = 0, 1, 2, 3)$. The action includes the Ricci scalar R, a dynamical metric $g_{\mu\nu}$ and its determinant $\sqrt{-g}$, where the potential $U(g,\phi^a)$ is the part of the action that provides the mass to the graviton and consists of three parts

$$U(g,\phi^a) = U_2 + \alpha_3 U3 + \alpha_4 U4 \tag{2}$$

here α_3 and α_4 are dimensionless free parameters of the theory. $U_i(i = 2, 3, 4)$ is given by,

$$\begin{aligned} U_2 &= [k]^2 - [\kappa]^2 - [\kappa^2], \\ U_3 &= [\kappa]^3 - 3[\kappa][\kappa^2] + 2[\kappa^3], \\ U_4 &= [\kappa]^4 - 6[\kappa]^2[\kappa^2] + 8[\kappa][\kappa^3] + 3[\kappa^2]^2 - 6[\kappa^4]. \end{aligned} \tag{3}$$

we know that the building block tensor κ is defined as

$$\kappa^\mu_\nu = \delta^\mu_\nu - \sqrt{g^{\mu\sigma} f_{ab}\partial_\sigma\phi^a\partial_\nu\phi^b} \tag{4}$$

where the square brackets denote a trace of the block tensor and f_{ab} is the fiducial metric.

As mentioned in [20], new parameters of α and β introduced by dimensionless free parameters of the theoryα_3 and α_4.

$$\alpha_3 = \frac{\alpha - 1}{3}, \qquad \alpha_4 = \frac{\beta}{4} + \frac{1-\alpha}{12} \tag{5}$$

In dRGT massive gravity there are two types of black hole solutions. The first one is encountered with strongly coupled and the second one is dynamical and fiducial metrics are simultaneously diagonal. These solutions exhibit singularities at the horizon that are invariant under coordinate transformations [50].

In order to mitigate these issues, we adopt an alternative approach. Specifically, we can identify a suitable formulation that facilitates the simplification of the calculations involved. In this paper, we follow [19-23] by considering the fiducial metric as follows.

$$f_{\mu\nu} = diag(0, 0, c^2, c^2 sin^2\theta), \tag{6}$$

here c is a constant.

We consider a static and spherically symmetric black hole solution in dRGT massive gravity theory.

$$ds^2 = -f(r)dt^2 + \frac{dr^2}{f(r)} + r^2(d\theta^2 + sin^2\theta d\varphi^2), \tag{7}$$

Solution for the metric funcation $f(r)$,

where

$$f(r) = 1 - \frac{2Mr^2}{(r^2+g^2)^{\frac{3}{2}}} + \frac{\Lambda}{3}r^2 + \gamma r + \varsigma \tag{8}$$

with

$$\Lambda = 3m_g^2(1+\alpha+\beta), \tag{9}$$

$$\gamma = -cm_g^2(1+2\alpha+3\beta), \tag{10}$$

$$\varsigma = c^2m_g^2(\alpha+3\beta), \tag{11}$$

In this we find that Eq. 7 reduces to a Bardeen black hole solution if we put $m_g = 0$ and it can be reduced to a Schwarzschild black hole if both $m_g = 0$ and the magnetic charge, $g = 0$.

To find the horizons of this black hole by $g^{rr} = 0$ i.e. $f(r) = 0$, this will give three real roots which corresponds to Cauchy horizon, event horizon, and cosmological horizon. This third root or horizon is related to the graviton mass. The roots or zeros of each curve which means that curve cross over the r axis, and the number of crossing shows the number of zeros. Fig.1 has four horizon plots in which we use variation of magnetic charge (g) with fixed parameters α, β, and $c = 1$ for different values of graviton mass m_g. It is clear from Fig. , that the seize of the black hole decreases with an increase in magnetic charge. In above two plots have three horizons for left side plot when $g < 0.792$ and right side plot when $g < 0.86$ but in below two plots have two horizons in left side plot when $g < 0.772$ and in right side plot when $g < 0.76$.In this we find if $(1+\alpha+\beta) < 0$ then we have three horizons and if $(1+\alpha+\beta) > 0$ then we have two horizons for small and large values of graviton mass.

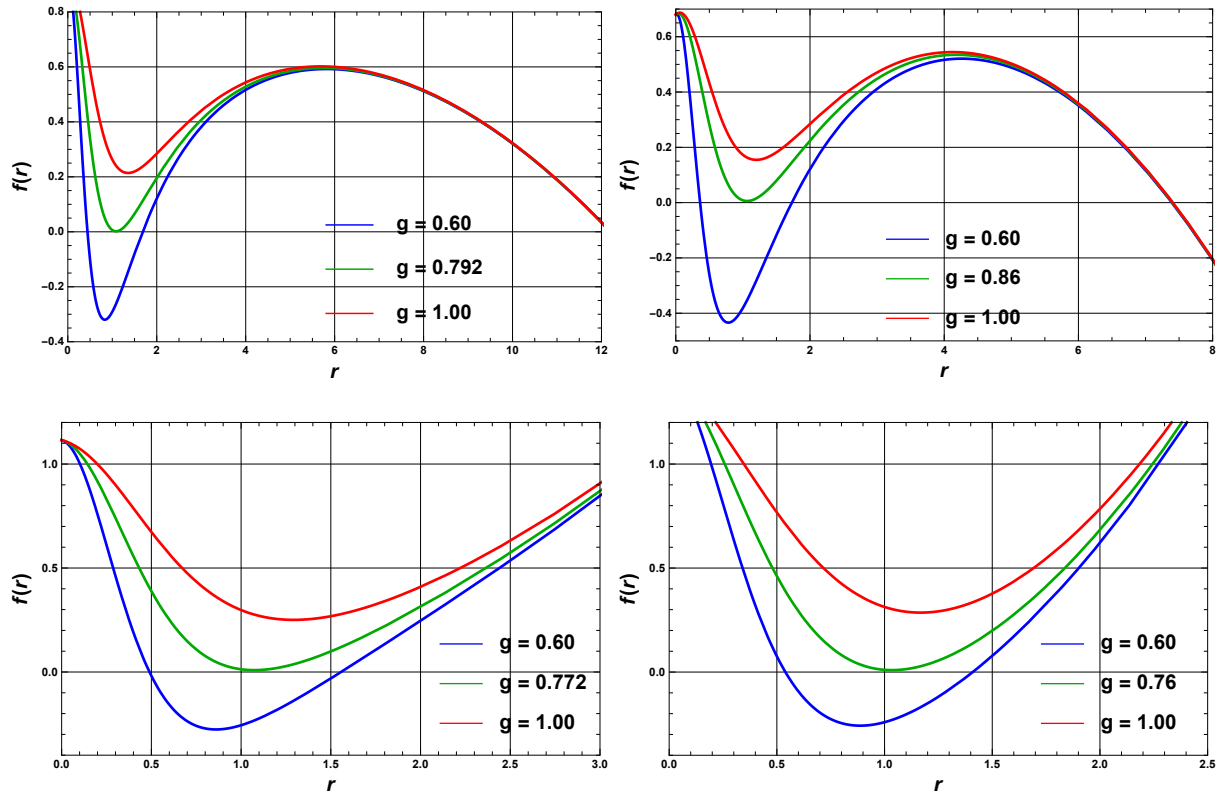

FIG. 1: Plots of $f(r)$ vs r for different values of magnetic charge g with fixed values of α, β, and m_g. In above left side plot $\alpha = 1$, $\beta = -3$, and $m_g = 0.1$. and in right side we change $m_g = 0.2$. In bottom left side plot $\alpha = 10$, $\beta = 0.5$, and $m_g = 0.1$. and in right side we change $m_g = 0.2$

1. *Geodesic or equation of motion*

In this section we calculate equation of motion and effective potential for this black hole solution. We have a spherically symmetric spacetime for these there time-like and space-like Killing vectors $(\partial/\partial t)^\mu$ and $(\partial/\partial\phi)^\mu$ for time translations and spatial rotations, respectively, and consider an equatorial approximation $(\theta = \pi/2)$.

The Lagrangian density of the scalar field in the background of BH is

$$\mathcal{L} = \frac{1}{2} g_{\mu\nu} \dot{x}^\mu \dot{x}^\nu \tag{12}$$

where the dot denotes the derivative with respect to an affine parameter. The motion should satisfy the constraint $g_{\mu\nu}\dot{x}^\mu\dot{x}^\nu = -k$, in which $k = 1$ is for massive particles and $k = 0$ for massless particles.The spherical symmetry of the spacetime allows us to assume that the movement takes place on the equatorial surface $\theta = \frac{\pi}{2}$. Since the metric is independent of t and ϕ, their conjugates give two constants of motion, the energy and angular momentum of

the particle can be calculated as follows.

$$E = g_{tt}\dot{t} = f(r)\dot{t} = \left(1 - \frac{2Mr^2}{(r^2+g^2)^{\frac{3}{2}}} + \frac{\Lambda}{3}r^2 + \gamma r + \varsigma\right)\dot{t} \tag{13}$$

$$L = g_{\phi\phi}\dot{\phi} = r^2\dot{\phi} \tag{14}$$

Geodesic equations of a massive particle can be calculated as follows.

$$\left(\frac{dr}{d\tau}\right)^2 = E^2 - f(r)\left(1 + \frac{L^2}{r^2}\right) \tag{15}$$

$$\left(\frac{dr}{d\phi}\right)^2 = \frac{r^4}{L^2}\left(E^2 - f(r)\left(1 + \frac{L^2}{r^2}\right)\right) \tag{16}$$

$$\left(\frac{dr}{dt}\right)^2 = \frac{1}{E^2}(f(r))^2\left(E^2 - f(r)\left(1 + \frac{L^2}{r^2}\right)\right) \tag{17}$$

Then, the equation of motion can be written in terms of the effective potential.

$$\dot{r}^2 + V(r) = E^2, \quad V(r) = f(r)\left(1 + \frac{L^2}{r^2}\right) \tag{18}$$

we consider the motion of massive partcle and the effective potential can be found by Eq. 15 as shown below

$$V(r) = \left(1 - \frac{2Mr^2}{(r^2+g^2)^{\frac{3}{2}}} + \frac{\Lambda}{3}r^2 + \gamma r + \varsigma\right)\left(1 + \frac{L^2}{r^2}\right) \tag{19}$$

Here we use dimensionless quantities such as

$\bar{r} = \frac{r}{M}$, $\bar{\Lambda} = \frac{\Lambda}{3M^2}$, $\bar{g} = \frac{g}{2M}$ $\bar{\gamma} = \gamma M$, $\bar{L} = \frac{L}{M}$

So Eq.19 can be written in terms of dimensionless quantities.

$$V(\bar{r}) = \left(1 - \frac{2\bar{r}^2}{(\bar{r}^2+\bar{g}^2)^{\frac{3}{2}}} + \bar{\Lambda}\bar{r}^2 + \bar{\gamma}\bar{r} + \varsigma\right)\left(1 + \frac{\bar{L}^2}{\bar{r}^2}\right) \tag{20}$$

The effective potential provides the condition under which the particles go through circular orbital motion. It is defined by conditions $V(r) = 0$ and $\frac{dV(r)}{dr} = 0$ and the innermost circular orbit takes place at local minima of the effective potential, i.e. $\frac{d^2V(r)}{dr^2} = 0$. These conditions show the specific energy $\bar{E}$ and the specific angular momentum $\bar{L}$ as functions of the angular velocity Ω of the particle. All these kinematic quantities depend on the radius of orbit.

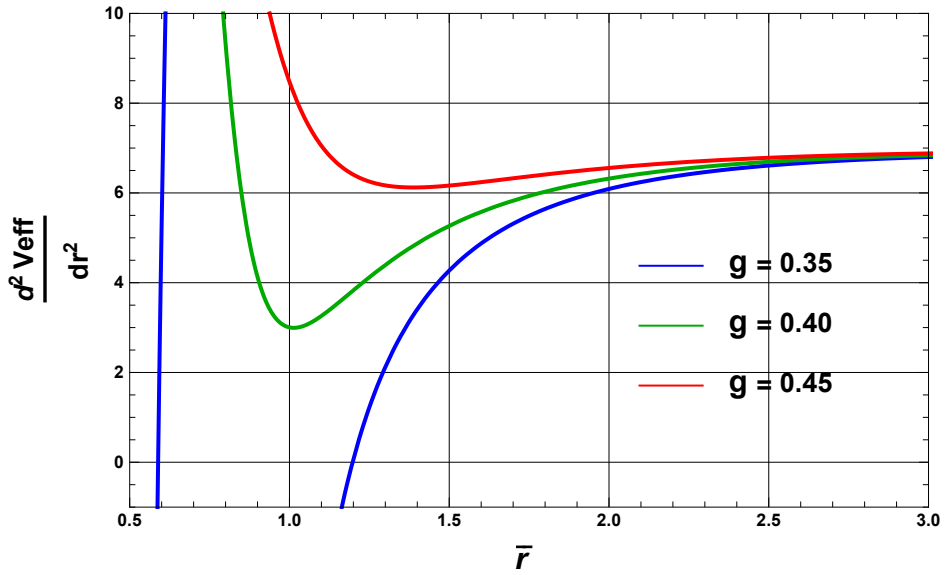

FIG. 2: In this plot second derivative of the potential vs $\bar{r}$ increases with magnetic charge,g with fixed values of $\bar{\Lambda}$, $\bar{\gamma}$ and ς equals to 1

III. THIN ACCRETION DISK IN DRGT MASSIVE GRAVITY

The thin accretion disk that surrounded by a black hole around the gravitational singularity, where astronomical matter orbits in a disk-like formation. These accretion disks are shaped by a variety of complex factors including gravitational forces, magnetic fields, and the viscosity of the material. Generally composed of distinct rings, these disks rotate at high velocities due to the gravitational pull of the black hole, producing significant radiation, which emitt X-rays and gamma rays. The temperature gradient within the accretion disk increases with distance from the center of the balck hole. In this section we study the properties of thin accretion disks surrounding black holes is important insights into the processes of accretion, the mechanisms behind jet formation. Note that the physical properties of the accretion disk follow from certain structure equations which are related to the conservation of the mass, the energy, and the angular momentum.

In this we also calculate all parameters of the accretion of the black hole. they can be obtained using the general expression which are introduced by Novikov-Throne and Shakura-Sunyaev models, which are as follows.

$$\Omega = \sqrt{-\frac{g_{tt,r}}{g_{\phi\phi,r}}} = \sqrt{\frac{\bar{r}^2 - 2\bar{g}^2}{(\bar{g}^2 + \bar{r}^2)^{5/2}} + \bar{\Lambda} + \frac{\bar{\gamma}}{2\bar{r}}}, \tag{21}$$

$$\bar{E} = -\frac{g_{tt}}{\sqrt{-g_{tt} - g_{\phi\phi}\Omega^2}} = \frac{\bar{r}\left(\bar{\gamma} + \bar{r}\left(\bar{\Lambda} - \frac{2}{(\bar{g}^2+\bar{r}^2)^{3/2}}\right)\right) + \varsigma + 1}{\sqrt{-\frac{3\bar{r}^4}{(\bar{g}^2+\bar{r}^2)^{5/2}} + \frac{\bar{\gamma}\bar{r}}{2} + \varsigma + 1}}, \tag{22}$$

$$\bar{L} = \frac{g_{\phi\phi}\Omega}{\sqrt{-g_{tt} - g_{\phi\phi}\Omega^2}} = \frac{\sqrt{2}\bar{r}^2\sqrt{\frac{\bar{r}^2-2\bar{g}^2}{(\bar{g}^2+\bar{r}^2)^{5/2}} + \bar{\Lambda} + \frac{\bar{\gamma}}{2\bar{r}}}}{\sqrt{-\frac{6\bar{r}^4}{(\bar{g}^2+\bar{r}^2)^{5/2}} + \bar{\gamma}\bar{r} + 2\varsigma + 2}}, \tag{23}$$

According to Fig 3 the angular velocity and $\bar{r}$ of the dRGT massive gravity black hole we

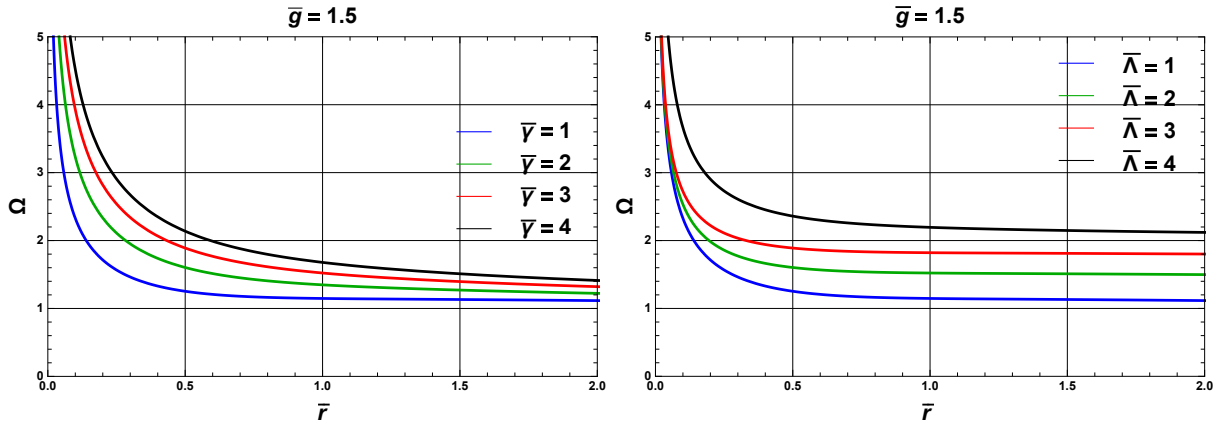

FIG. 3: The above two plots of angular velocity Ω vs r, in this angular velocity increases with different values of $\bar{\gamma}$ and $\bar{\Lambda}$. In left side we have fixed $\bar{\Lambda} = 1$ and in right side plot $\bar{\gamma} = 1$ is fixed

have two plots shows that angular velocity moderately increase with variation of $\bar{\gamma}$ and $\bar{\Lambda}$ for $\bar{g} = 1.5$ and it is seen that angular velocity sharply high for small value of $\bar{r}$ as the distance $\bar{r}$ increases then angular velocity decreases.

However, In Fig4 the specific energy $\bar{E}$ to $\bar{r}$ demonstrated three plots for different values

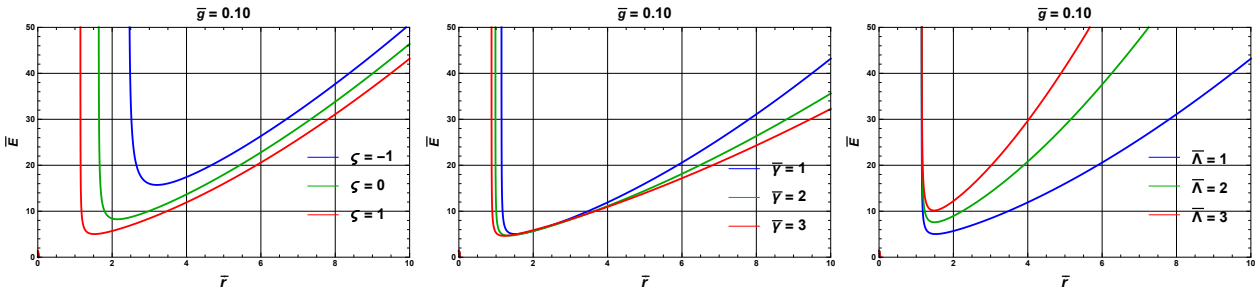

FIG. 4: These are the plots of specific energy $\bar{E}$ and r. In first two plots specific energy is decreases with different values of ς and $\bar{\gamma}$ with $\bar{g} = 0.10$ and $\bar{\Lambda} = 1$ respectively, but in third one specific energy increases with increase in parameters values with fixed $g = 0.10$, $\varsigma = 1$ and $\bar{\gamma} = 1$

of ς, $\bar{\gamma}$ and $\bar{\Lambda}$ for fixed value of magnetic charge $\bar{g} = 0.10$. It seen that behavior of plots

are similar in these plots,, we see the specific energy firstly at peak or higher and after that it goes to low level and then it sharply to higher level for different distance range values $\bar{r}$.. In the top two graphs as ς and $\bar{\gamma}$ increase then the specific energy decreases, but in the bottom graph of Fig. 4 the specific energy increases with increasing value of $\bar{\Lambda}$. Fig4 shows

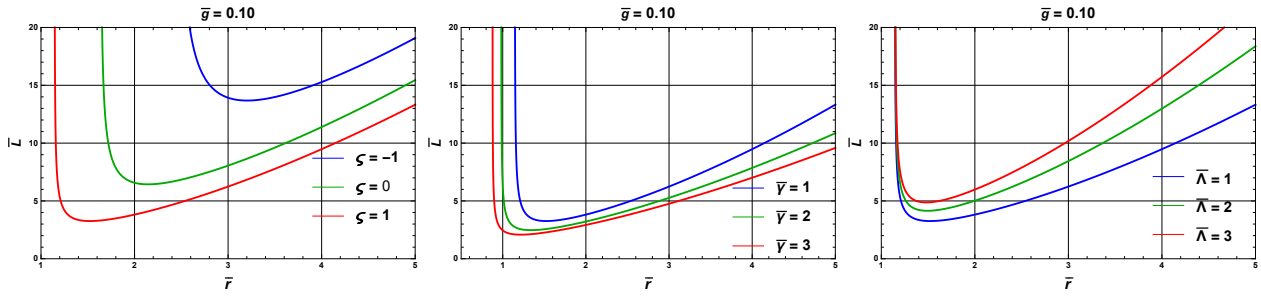

FIG. 5: Graphs of specific angular momentum $\bar{L}$ vs r. They shows similar results like specific energy $\bar{E}$, In first two plots specific angular momentum is decreases with different values of ς and $\bar{\gamma}$ with $\bar{g} = 0.10$ and $\bar{\Lambda} = 1$ respectively, but last plot specific angular momentum increases by increasing $\bar{\Lambda}$ values with fixed $g = 0.10$, $\varsigma = 1$ and $\bar{\gamma} = 1$

graphs of specific angular momentum $\bar{L}$ vs $\bar{r}$ that exhibit a decreasing trend followed by an increasing trend, respectively. The behavior of plots is similar to that of specific energy, the specific angular momentum decreases with an increase in ς and $\bar{\gamma}$ but increases with $\bar{\Lambda}$.

The accretion disk is geometrically thin, orbiting particles the central compact object travel between the outer edge and inner edge, the equatorial circular orbits are stable which we called inner most stable circular orbits r_{ISCO} we are for inner boundary of the disk. The accretion disk is perpendicular to the compact object, i.e. black hole's spin axis and due to thermodynamic equilibrium within the disk, the electromagnetic radiation emitted from surface of disk which is assumed to a black hole spectrum, mass of the accretion disk, M_0 remains constant.

From conservation of rest mass, energy, and the angular momentum of the disk particles, the radiant energy flux over the disk surface can be calculated as follows

$$F(r) = -\frac{c^2\dot{M}_0}{4\pi\sqrt{-g}}\frac{\Omega_{,r}}{(\bar{E}-\Omega\bar{L})^2}\int_{r_{ISCO}}^{r}(\bar{E}-\Omega\bar{L})\bar{L}_{,r}\,dr \tag{24}$$

Here, c represents the speed of light and $\dot{M}_0$ is the mass accretion rate.

Fig. 6 demonstrate the energy flux $F(r)$ emitted from the disk surface with different values of magnetic charge, g. The graph pattern represents that the radiation flux decreases with

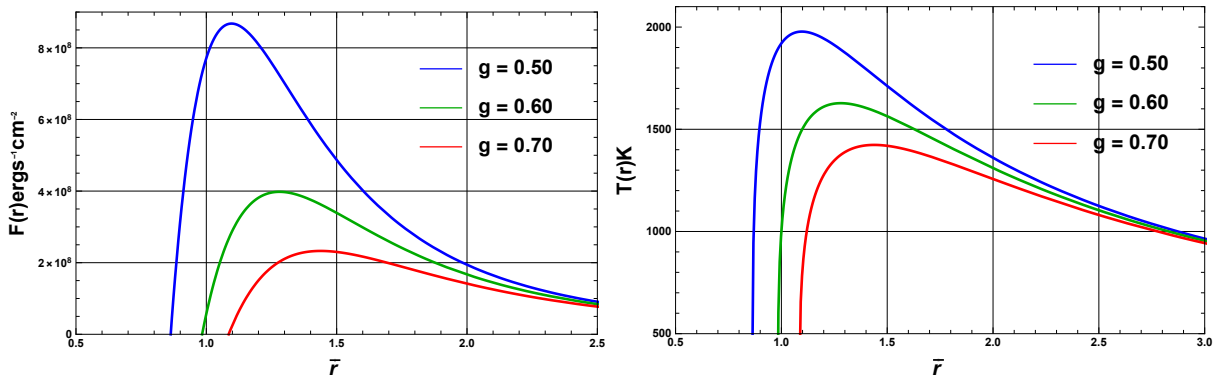

FIG. 6: Left side plot is of the energy flux $F(r)$ around the black hole for different values of g and right is for radiation temperature $T(r)$ vs $\bar{r}$. Here we use $\sigma_{SB} = 5.67 * 10^{-5} ergs^{-1} cm^{-2} K^{-4}$

increase of the parameter g, which shows that the magnetic charge has a direct impact on the contour of the radiation flux. As we know that it will attains a thermal equilibrium state. the radiation temperature $T(r)$ is connected to energy flux of the disk via Stefan-Boltzmann law as $F(r) = \sigma_{SB} T^4(r)$, where σ_{SB} denotes the Stefan-Boltzmann constant. The plot of the radiation temperature $T(r)$ in Fig.6, it can be inferred that as the magnetic charge increase then $T(r)$ initially increasing and then decreasing.

IV. CONCLUSIONS

In our research, we have explore the thin accretion disk around the a black hole coupled with non linear electrodynamics in dRGT massive gravity. We have analyzed the event horizons of the black hole with massive gravity parameters, in which we found two different behavior of roots or zeros. After that we write geodesics an equation of motion of black hole solution, using equation of motions we calculate the effective potential and its derivatives and follow the conditions $V(r) = 0$ and $\frac{dV(r)}{dr} = 0$ to calculate innermost stable orbits for moving particle in disk. Furthermore we have plotted the $\frac{d^2V(r)}{dr^2}$ We examine essential physical dynamic quantities like angular velocityΩ, specific angular momentum $\bar{L}$,and specific energy $\bar{E}$. The graphical representation of angular velocity shows it increases with $\bar{\gamma}$ and $\bar{\Lambda}$, specific energy $\bar{E}$ and specific angular momentum $\bar{L}$ have similar pattern ,initially both decrease sharply to low and then goes to high. Finally we discussed about the emitted energy flux from the surface of the disk and we plotted this flux from this we observed that radiation

flux decreases with increase in magnetic charge g. It can be concluded that massive gravity parameters have some effects on this type of black hole solution coupled with non linear electrodynamics in dRGT massive gravity.

Acknowledgments

I want to acknowledge the financial support from CSIR. DST SERB project to use their systems.

---

[1] M. H. Dehghani and S. H. Hendi, Int. J. Mod. Phys. D **16**, 1829 (2007).

[2] D. J. Gross and J. H Sloan, Nucl. Phys. B **291**, 41 (1987).

[3] M. C. Bento and O. Bertolami, Phys. Lett. B **368**, 198 (1996).

[4] S. G. Ghosh, U. Papnoi, and S. D. Maharaj, Phys. Rev. D **90**, 044068 (2014).

[5] R.G. Cai, Phys. Rev. D **65**, 084014 (2002).

[6] S. H. Hendi, S. Panahiyan and B. Eslam Panah, J. High Energy Phys. **01**, 129 (2016).

[7] Md. Sabir Ali and S. G. Ghosh, Phys. Rev. D **98**, 084025 (2018).

[8] S. G. Ghosh, U. Papnoi, and S. D. Maharaj, Phys. Rev. D **90**, 044068 (2014).

[9] J. L. Synge, *Relativity: The General Theory*, (North Holland, Amsterdam, 1966), p. 175.

[10] P. Letelier, Phys. Rev. D **20**, 1294 (1979).

[11] M. Barriola, A. Vilenkin, Phys. Rev. Lett. **63**, 341 (1989).

[12] S. G. Ghosh, Eur. Phys. J. C **75**, no. 11, 532 (2015).

[13] R. C. Myers and J. Z. Simon, Phys. Rev. D **38**, 2434.

[14] Y. Zhang, Y. Zhu, L. Modesto and C. Bambi, Eur. Phys. J. C **75**, 96 (2015).

[15] A. Borde, Phys. Rev. D **50**, 3692 (1994).

[16] A. Borde, Phys. Rev. D **55**, 7615 (1997).

[17] J. Bardeen, in *Proceedings of GR5* (Tiflis, U.S.S.R., 1968).

[18] E. Ayon-Beato, A. Garcia, Phys. Lett. B **493**, 149 (2000).

[19] E. Ayon-Beato and A. Garcia, Gen. Relativ. Gravit. **31**, 629 (1999).

[20] E. Ayon-Beato and A. Garcia, Gen. Relativ. Gravit.**37**, 635 (2005).

[21] E. Ayon-Beato and A. Garcia, Phys. Rev. Lett. **80**, 5056 (1998).

[22] S. Ansoldi, arXiv:0802.0330 [gr-qc].

[23] J. P. S. Lemos and V.T. Zanchin, Phys. Rev. D **83**, 124005 (2011) .

[24] O.B. Zaslavskii, Phys. Rev. D **80**, 064034 (2009).

[25] S. G. Ghosh, Eur. Phys. J. C **75**, no. 11, 532 (2015).

[26] L. Xiang, Y. Ling and Y. G. Shen, Int. J. Mod. Phys. D **22**, 1342016 (2013).

[27] H. Culetu, Int. J. Theor. Phys. **54**, 2855 (2015).

[28] L. Balart and E. C. Vagenas, Phys. Lett. B **730**, 14 (2014).

[29] S. G. Ghosh and D. W. Deshkar Phys. Rev. D **77**, 04750.

[30] J. M. Bardeen, B. Carter and S. W. Hawking, Commun. Math. Phys. **31** 161 (1973).

[31] S. Hawking and D. Page, Commun. Math. Phys. **87**, 577 (1983).

[32] P. Davis, Proc. R. Soc.A **353**, 499 (1977).

[33] M. S. Ma, R. Zhao and Y. Q. Ma, Gen. Rel. Grav. **49** (2017) no.6, 79.

[34] J.H. MacGibbon, Nature **329** 308 (1987).

[35] I. G. Dymnikova, Int. J. of Mod. Phys. D, **5** 529 (1996); Phys. Lett. B **685**, 12 (2010);Gen. Rel. Grav. **24**, 235 (1992).

[36] R. M. Wald, Phys. Rev. **D 43**, R3427 (1993).

[37] Mang-Sen Ma and Ren Zhao, Class. Quantun Grav. **31** 245014 (2014).

[38] R. V. Maluf and J. C. S. Neves, Phys. Rev. D **97**, 104015 (2018).

[39] K. Z. Amin, N. ul Islam, D. V. Singh and P. A. Ganai, Int. J. Mod. Phys. A **40** (2025) no.19, 2550057.

[40] V. K. Srivastava, S. Upadhyay, A. K. Verma, D. V. Singh, Y. Myrzakulov and K. Myrzakulov, Phys. Dark Univ. **48** (2025), 101915.

[41] B. Pourhassan, H. Farahani, F. Kazemian, İ. Sakallı, S. Upadhyay and D. V. Singh, Phys. Dark Univ. **44** (2024), 101444.

[42] A. Kumar, D. V. Singh and S. Upadhyay, JHAP **4** (2024) no.4, 85-99.

[43] A. Kumar, D. V. Singh and S. Upadhyay, Int. J. Mod. Phys. A **39** (2024) no.31, 2450136.

[44] H. K. Sudhanshu, D. V. Singh, S. Upadhyay, Y. Myrzakulov and K. Myrzakulov, Phys. Dark Univ. **46** (2024), 101648.

[45] B. Singh, D. Veer Singh and B. Kumar Singh, Phys. Scripta **99** (2024) no.2, 025305.

[46] P. Paul, S. Upadhyay, Y. Myrzakulov, D. V. Singh and K. Myrzakulov, Nucl. Phys. B **993** (2023), 116259.

[47] D. V. Singh, A. Shukla and S. Upadhyay, Annals Phys. **447** (2022), 169157.

[48] D. V. Singh, S. G. Ghosh and S. D. Maharaj, Nucl. Phys. B **981** (2022), 115854.

[49] A. Kumar, D. V. Singh, Y. Myrzakulov, G. Yergaliyeva and S. Upadhyay, Eur. Phys. J. Plus **138** (2023) no.12, 1071.

[50] P. Paul, S. Upadhyay and D. V. Singh, Eur. Phys. J. Plus **138** (2023) no.6, 566.

[51] B. Singh, B. K. Singh and D. V. Singh, Int. J. Geom. Meth. Mod. Phys. **20** (2023) no.08, 2350125.

[52] Y. Myrzakulov, K. Myrzakulov, S. Upadhyay and D. V. Singh, Int. J. Geom. Meth. Mod. Phys. **20** (2023) no.07, 2350121.

[53] D. V. Singh, V. K. Bhardwaj and S. Upadhyay, Eur. Phys. J. Plus **137** (2022) no.8, 969.

[54] C. S. Varsha, V. Venkatesha, N. S. Kavya and D. V. Singh, Annals Phys. **477** (2025), 170002.

[55] B. Pourhassan, M. Dehghani, S. Upadhyay, I. Sakalli and D. V. Singh, Mod. Phys. Lett. A **37** (2022) no.33n34, 2250230.

[56] S. Upadhyay and D. V. Singh, Eur. Phys. J. Plus **137** (2022) no.3, 383.

[57] B. K. Vishvakarma, D. V. Singh and S. Siwach, Phys. Scripta **99** (2024) no.2, 025022.

[58] B. K. Vishvakarma, D. V. Singh and S. Siwach, Eur. Phys. J. Plus **138** (2023) no.6, 536 doi:10.1140/epjp/s13360-023-04174-z.

[59] D. V. Singh, S. Upadhyay, Y. Myrzakulov, K. Myrzakulov, B. Singh and M. Kumar, Nucl. Phys. B **1016** (2025), 116915.

[60] H. K. Sudhanshu, S. Upadhyay, D. Veer Singh, Y. Myrzakulov and K. Myrzakulov, Mod. Phys. Lett. A **38** (2023) no.34n35, 2350153

[61] H. K. Sudhanshu, D. V. Singh, S. Bekov, K. Myrzakulov and S. Upadhyay, Int. J. Mod. Phys. A **38** (2023) no.29n30, 2350165.

[62] H. K. Sudhanshu, S. Upadhyay, D. V. Singh and S. Kumar, Int. J. Theor. Phys. **61** (2022) no.10, 248.

Phase transition and thermodynamic behavior of AdS black hole coupled with Nonlinear Electrodynamics

Shobhit Sachan[1] and Vartika Singh[2]

[1]*Department of Physics, Institute of Applied Sciences and Humanities, GLA University, Mathura 281406, Uttar Pradesh, India;*
E-mail: shobhitsachan@gmail.com

[2]*Department of Physics, Institute of Applied Sciences and Humanities, GLA University, Mathura 281406, Uttar Pradesh, India;*
E-mail: vartikasinghvbn50@gmail.com

Abstract

In this article, we analyze an exact d-dimensional AdS black hole solution coupled with nonlinear electrodynamics (NLED) and investigate the thermodynamic properties of the solution. It is found that the thermodynamic quantities get modified due to the presence of non linear terms. In our extended analysis, we broadened the scope of our findings by treating the cosmological constant (Λ) as a dynamic thermodynamic variable, specifically relating it to pressure via the relation ($P = -\Lambda/8\pi$). This approach allowed us to derive the critical values for key parameters, including the critical pressure, critical temperature, and horizon radius, which mark the boundaries of distinct thermodynamic regimes in the black hole system. Furthermore, we conducted a study on the global thermodynamic parameter $P_c v_c/T_c$. In addition, we explored the nature of the phase transition occurring between small and large black holes, revealing striking analogies to the liquid-gas phase transition observed in the Van der Waals fluid model.

I. INTRODUCTION

Black holes, one of the most fascinating and mysterious objects in our universe, behave like a thermodynamic object. Their behavior like a thermodynamic object was studied extensively by Bekenstein [1–4] and Hawking [5] and they proposed laws of black hole thermodynamics which has the same analogy as that of laws of thermodynamics. Black holes have shown phase transitions and their equation of state can be studied by presuming that the cosmological constant (Λ) behaves as a thermodynamic variable ($P = -\Lambda/8\pi$). This phase structure is present for both asymptotically de-Sitter and flat black holes in addition to asymptotically AdS. Bardeen, Brown, Whiting and York were the first persons to study the phase structure of the asymptotically flat charged black hole [6]. In this article they have considered the spherical charged black hole in thermal equilibrium in a grand canonical ensemble and studied the eigenvalue and thermodynamic behavior of the said system.

The interest in the study of the regular black hole comes from the Bardeen black hole model [7] which has its roots in the proposal made by Sakharov [8] and Gliner [9]. Such types of black hole have a horizon, but the central singularity is missing. This exact black hole solution is obtained when gravity couples to non-linear matter field. These solutions were studied by Ayno, Beato and Garcia [10–12] after 30 years of Bardeen's proposal. In present, we have a large class of regular black hole solutions; however, the majority of them are based on the proposal made by Bardeen [13–26]. The generalizations of the regular black hole in Einstein-Gauss-Bonnet (EGB) gravity are studied in [27–32], $4D$ EGB gravity in [33–38], and massive gravity in [39]. The details of the rotating counterpart of previously mentioned solution are presented in [40, 41]. The authors had used Newman Janis algorithm to find the solutions. The black hole solutions which incorporated rotating parameter are presented in [42–50].

In this paper, we study the higher dimensional regular (AdS) black hole solution which is obtained when gravity couples to nonlinear electrodynamics (NLED). This black hole interpolates with the Schwarzschild-Tangherlini black hole in the limit of nonlinear parameter. Moreover, we investigate the thermodynamic properties of this black hole. The thermodynamics of the black hole has changed in the presence of nonlinear matter field. In addition we also study the phase transition of the black hole by considering cosmological constant (Λ) as a thermodynamics variable [**?**].

The paper is organized as follows, we obtain a higher dimensional regular (AdS) black hole solution present in Sec. II and also give the consistent equations of gravity coupled to NLED and show the location of the horizon structure. The study of the thermodynamical properties of higher dimensional regular (AdS) black hole solution is the subject of Sec. III. Finally, the concluding remarks and results are presented in Sec. V. The signature of the metric is (-, +,+,+,+) with natural units $8\pi G = c = 1$.

II. SOLUTION OF HIGHER DIMENSIONAL REGULAR BLACK HOLE

The d dimensional Einstein-Hilbert action, incorporating a negative cosmological constant along with non-linear electrodynamics (NLED), can be expressed as,

$$\mathcal{S} = \frac{1}{2}\int d^D x\sqrt{-g}\,[\mathcal{R} - 2\Lambda] + \int d^D x\sqrt{-g}\;\mathcal{L}(F), \tag{1}$$

where $\mathcal{R}$ is Ricci curvature, Λ is cosmological constant associated with the length of AdS by relation $\Lambda = -(D-1)(D-2)/2l^2$, and $\mathcal{L}(F)$ is the Lagrangian density of nonlinear matter field. $\mathcal{L}(F)$ is the function of electromagnetic field tensor F_{ab} which is defined as $F_{ab} = \partial_a A_b - \partial_b A_b$, with A_a representing the electromagnetic potential. The equation of motion (EoM) of the action (1) is obtained by varying g_{ab} and A_a [21]. The EoM is given by,

$$R_{ab} - \frac{1}{2}g_{ab}R = \mathcal{T}^a_b \equiv \delta^a_b\mathcal{L} - 4\frac{\partial\mathcal{L}}{\partial F}F^{ab}_{ab}, \tag{2}$$

and the Lagrangian density by relation,

$$\mathcal{L}(F) = \frac{\beta\,\exp[-k(2F)^\gamma]}{q^{\frac{D-3}{D-2}}} \qquad \text{with} \qquad k = \frac{q^2}{\mu} \tag{3}$$

where

$$\beta = \frac{(D-2)(D-3)}{2} \qquad \text{and} \qquad \frac{D-3}{2D-4}. \tag{4}$$

TO proceed for our analysis, we assume the following *anstaz* for the Maxwell field [47]

$$\begin{aligned} F_{ab} &= 2\delta^{\theta_1}_{[a}\delta^{\theta_2}_{b]}q(r)\sin\theta_1; && D = 4, \\ F_{ab} &= 2\delta^{\theta_{D-3}}_{[a}\delta^{\theta_{D-2}}_{b]}\frac{q(r)}{r^{D-4}}\sin\theta_{D-3}\left[\prod_{j=1}^{D-4}\sin^2\theta_j\right]; && D \geq 5. \end{aligned} \tag{5}$$

Eq. (5) implies that $dF = 0$, thereby we obtain,

$$2\delta^{\theta_{D-3}}_{[a}\delta^{\theta_{D-2}}_{b]}\frac{q(r)}{r^{D-4}}\sin\theta_{D-3}\left[\prod_{j=1}^{D-4}\sin^2\theta_j\right]d\theta\wedge d\phi\wedge\ldots\wedge d\psi_{(D-2)}. \tag{6}$$

Hence the field strength tensor $F_{\theta\phi}$, F and $\mathcal{L}(F)$ are simplified as

$$F_{\theta\phi} = \frac{q(r)}{r^{D-4}}\sin\theta_{D-3}\left[\prod_{j=1}^{D-4}\sin^2\theta_j\right], \qquad F = \frac{q^2}{2r^{2(D-2)}} \tag{7}$$

$$\mathcal{L}(F) = \frac{(D-2)(D-3)q^2}{4r^{2(D-2)}}\exp\left[-\frac{k}{r^{D-3}}\right]. \tag{8}$$

Our aim is to obtain static spherically symmetric regular black hole in d dimensional space-time for the action given by relation (1). We consider the following form of line element

$$ds^2 = -f(r)dt^2 + \frac{1}{f(r)}dr^2 + r^2 d\Omega_{D-2}, \tag{9}$$

where $d\Omega_{D-2}$ is the metric of a $(D-2)$-dimensional sphere and T_{ab} is the energy momentum tensor of nonlinear field. The (r,r) component of the Eq. (2) is

$$\frac{D-2}{2r^2}\left[r^2(f^2)' + (D-3)(f^2-1) - (D-1)\Lambda r^2\right] = \frac{(D-2)(D-3)q^2}{2r^{2(D-2)}}\exp\left[-\frac{k}{r^{D-3}}\right]. \tag{10}$$

The solution of this black hole is obtained by integrated the differential equation

$$f(r) = 1 - \frac{M}{r^{D-3}}e^{k/r^{D-3}} + \frac{r^2}{l^2}, \tag{11}$$

where M is the integrating constant identified as the mass of the regular black hole. The Eq. (11) is an exact solution of the black hole which is characterized by the mass parameter (M), Cosmological constant (Λ) and the deviation parameter (k). In the absence of the deviation parameter (k), the solution 11 reduces to AdS Schwarzschild-Tangherlini black hole solution, and for $r >> k$ the d dimensional AdS charged black hole is

$$f(r) = 1 - \frac{M}{r^{D-3}} + \frac{Q^2}{r^{D-2}} + \frac{r^2}{l^2}. \tag{12}$$

Now, we look for the event horizon for $5D$ regular black hole, which we can be obtain by $f(r) = 0$ and substitute $D = 5$ in Eq. (11. This is transdential equation and cannot be solved analytically. Therefore, we plot the $f(r)$ with $D = 5$ which is plotted in Fig. (1).

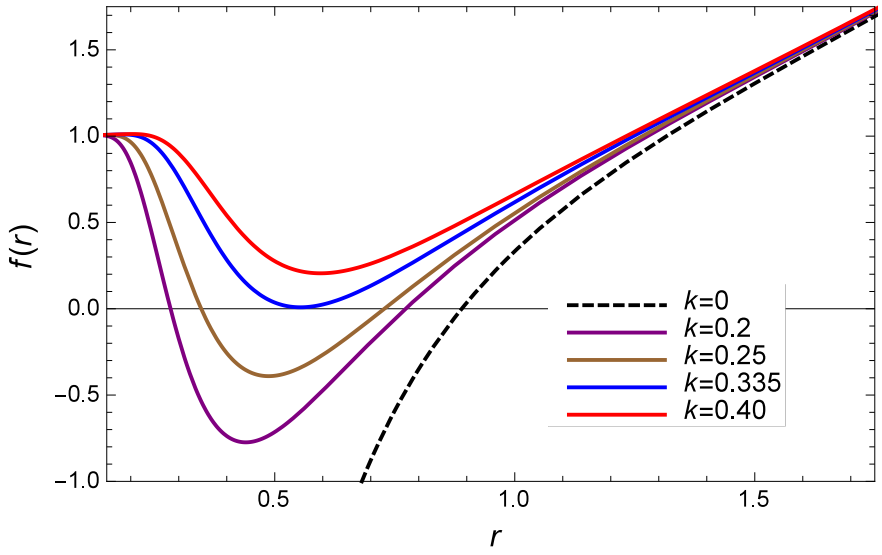

FIG. 1: The behavior of the metric function $f(r)$ with respect to the radius r for different values of the deviation parameter k with a fixed mass value $M = 1$.

The plot of horizon of $5D$ regular AdS black hole is depicted in Fig. (1). The figure shows that the black hole has two horizon in contrast with the Schwarzschild solution which is due to the exponential factor $e^{-k/r}$ present in the Eq. (11) that modifies the black hole solution. The size of the black hole horizon decreases with increases the value of deviation parameter k and coincides the horizon of the Schwarzschild-Tangherlini black hole at $r \approx 1.65$.

III. THERMODYNAMICS AND PHASE TRANSISTION

Now we will analyse the thermodynamical behavior of the quantities associated with the $5D$ regular AdS black hole solution 11 in terms of the horizon radius r_+. The mass parameter of the black hole can be calculated by equating $f(r) = 0$ at the horizon of solution 11 [51–54],

$$M_+ = r_+^2 e^{k/r_+^2} \left(1 + \frac{r^2}{l^2}\right) \tag{13}$$

In the vanishing limit of deviation parameter k, we can recover the mass of the Schwarzschild Tangherlini black hole. The temperature of the black hole [51–54] is known as Hawking temperature which is given by

$$T_+ = \frac{f'(r)}{4\pi} = \frac{1}{2\pi r_+}\left[1 + \frac{r_+^2}{l^2} - \frac{k}{r_+^2}\left(1 + \frac{r_+^2}{l^2}\right)\right]. \tag{14}$$

The modification in the temperature of regular AdS black hole is due the the presence of deviation parameter k. If this deviation parameter is absent, we can recover the usual result $T_+ = 1/2\pi r_+$. Using the modified Hawking temperature and first law of black hole thermodynamics $dM_+ = T_+\, dS_+ + PdV$ [51–54], the expression of the black hole entropy can be obtained and given by the relation,

$$S_+ = \int \frac{1}{T_+}\frac{\partial M_+}{\partial r_+}dr_+ = \frac{4r_+^3}{3\pi}\left[\frac{2k + r_+^2}{r_+^2}e^{k/r_+^2} - \frac{8k\sqrt{\pi k}}{r_+^3}\text{erf}\left(\frac{\sqrt{k}}{r_+}\right)\right], \tag{15}$$

If we substitute $k = 0$, the above relation reduces to $S_+ = 4\pi r_+^3/3$, which is the well-known entropy of $5D$ the Schwarzschild-Tangherlini black hole. This relation is in accordance with the Bekenstein Hawking area law.

The first law of thermodynamics include pressure and volume, when cosmological constant considered as a pressure. The cosmological constant corresponds to pressure as

$$P = -\frac{\Lambda}{8\pi} = \frac{(d-1)(d-2)}{16\pi l^2} \tag{16}$$

and the equation of state $P = P(V, T)$ for $5D$ regular black hole

$$P = \frac{3(k - r_+^2 - 2\pi r_+^3 T)}{4\pi(2r_+^2 - k)} \tag{17}$$

and the critical points obtained from

$$\frac{\partial P}{\partial r_+} = 0, \qquad \frac{\partial^2 P}{\partial r_+^2} = 0 \tag{18}$$

which leads to

$$r_c = \sqrt{\frac{6k + \sqrt{42}k}{2}} \tag{19}$$

$$T_c = \frac{8\sqrt{2}}{\pi\sqrt{k}(6 + \sqrt{42})^{3/2}} \tag{20}$$

$$P_c = \frac{36 - 3\sqrt{42}}{\pi k(288 + 44\sqrt{42})} \tag{21}$$

In order to ensure phase transition, we are plotting the Gibbs free energy G_+ as the function of temperature T_+.

The characteristic swallowtail which appears in the $G_+ - T_+$ curve present in the figure 2, we obtain the critical values for which phase transition takes place.

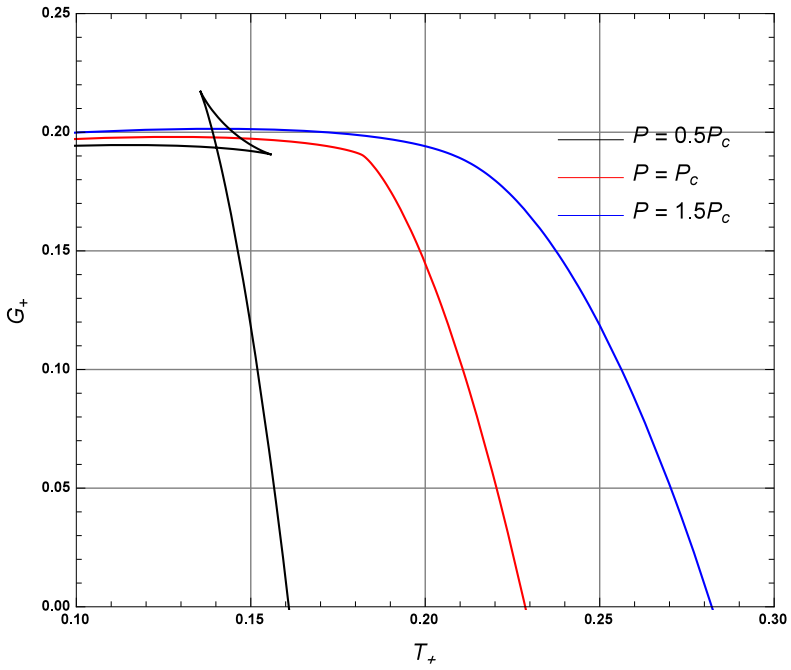

FIG. 2: Plots showing the behavior of Gibbs free energy G_+ w.r.t. temperature T_+ for the different values of pressure parameter $P < P_c, P = P_c$ and $P > P_c$ with fixed value of $k = 0.20$. where $P_c = 0.459$ and corresponding temperature $T_c = 0.182$.

IV. CONCLUSIONS

We have studied the $d-$ dimensional regular black hole with negative cosmological constant and calculated the thermodynamic quantities with the black hole solution in term of horizon radius r_+. The black hole thermodynamics has modified in the presence of the exponential factor $e^{-k/r}$ which is present in the Eq. (11). black hole has two horizon in contrast with the Schwarzschild-Tangherlini black hole coincides with the $5D$ regular AdS black hole at $r \approx 1.65$. We also extend our results by presuming that the cosmological constant (Λ) as a thermodynamics pressure ($P = -\Lambda/8\pi$). The phase transition between small and large black hole is very much like the phase transition of Van der Walls fluids.

Acknowledgment

SS would like to thank CST UP grant no CST/D-828 for financial support and VS would like to thank ANRF grant no EEQ/2022/000824 for financial support.

---

[1] J.D. Bekenstein, "Black Holes and Entropy," Phy. Rev. D 7, 2333 (1973).

[2] J.D. Bekenstein, "Black holes and the second law," Lett. al Nuovo Ciemnto 4 (1972) 15.

[3] J.D. Bekenstein, Phy. Rev. D 9, 3292 (1974).

[4] J.D. Bekenstein, Phy. Rev. D 12, 3077 (1975).

[5] S. W. Hawking, Phy. Rev. D 13, 191 (1976).

[6] H. W. Bardeen J. D. Brown B. F. Whiting and J. W. York, Phys. Rev. D **42** (1990).

[7] J. Bardeen, in *Proceedings of GR5* (Tiflis, U.S.S.R., 1968).

[8] A.D. Sakharov, Sov. Phys. JETP, **22**, 241 (1966).

[9] E.B. Gliner, Sov. Phys. JETP, **22**, 378 (1966).

[10] E. Ayon-Beato and A. Garcia, Gen. Rel. Grav. **31**, 629 (1999).

[11] E. Ayon-Beato and A. Garcia, Gen. Rel. Grav.**37**, 635 (2005).

[12] E. Ayon-Beato, A. Garcia, 'Phys. Lett. B **493**, 149 (2000).

[13] S. Ansoldi, arXiv:0802.0330 [gr-qc].

[14] K.A. Bronnikov, Phys. Rev. D **63**, 044005 (2001)

[15] O.B. Zaslavskii, Phys. Rev. D **80**, 064034 (2009)

[16] J.P.S. Lemos and V.T. Zanchin, Phys. Rev. D **83**, 124005 (2011) .

[17] H. Culetu, Int. J. Theor. Phys. **54**, no.8, 2855-2863 (2015).

[18] L. Balart and E. C. Vagenas, Phys. Rev. D **90**, no.12, 124045 (2014).

[19] L. Balart and E. C. Vagenas, Phys. Lett. B **730**, 14-17 (2014).

[20] L. Xiang, Y. Ling and Y. G. Shen, Int. J. Mod. Phys. D **22**, 1342016 (2013).

[21] D. V. Singh and N. K. Singh, Annals Phys. **383**, 600 (2017).

[22] D. V. Singh, M. S. Ali and S. G. Ghosh, Int. J. Mod. Phys. D **27** (2018) no.12, 1850108.

[23] S. Fernando, Int. Journal of Mod. Phys. D **26**, 1750071 (2017).

[24] D. V. Singh, A. Shukla and S. Upadhyay, Annals Phys. **447** (2022), 169157.

[25] D. V. Singh, S. G. Ghosh and S. D. Maharaj, Nucl. Phys. B **981** (2022), 115854.

[26] B. K. Singh, R. P. Singh and D. V. Singh, Eur. Phys. J. Plus **136** (2021) no.5, 575.

[27] A. Kumar, D. V. Singh and S. G. Ghosh, Annals Phys. **419**, 168214 (2020).

[28] D. V. Singh, S. G. Ghosh and S. D. Maharaj, Annals Phys. **412**, 168025 (2020).

[29] A. Kumar, D. Veer Singh and S. G. Ghosh, Eur. Phys. J. C **79**, no.3, 275 (2019).

[30] S. G. Ghosh, D. V. Singh and S. D. Maharaj, Phys. Rev. D **97**, no.10, 104050 (2018)

[31] S. G. Ghosh, A. Kumar and D. V. Singh, Phys. Dark Univ. **30**, 100660 (2020).

[32] D. V. Singh, V. K. Bhardwaj and S. Upadhyay, Eur. Phys. J. Plus **137** (2022) no.8, 969.

[33] S. G. Ghosh, D. V. Singh, R. Kumar and S. D. Maharaj, Annals Phys. **424** (2021), 168347.

[34] D. V. Singh, S. G. Ghosh and S. D. Maharaj, Phys. Dark Univ. **30** (2020), 100730.

[35] D. V. Singh and S. Siwach, Phys. Lett. B. **408** 135658 (2020).

[36] S. Upadhyay and D. V. Singh, Eur. Phys. J. Plus **137** (2022) no.3, 383.

[37] Yarlin Myrzakulov, Sudhaker Upadhyay, Dharm Veer Singh, International Journal of Geometric Methods in Modern Physics (2023).

[38] Bhupendra Singh, Benoy Kumar Singh, Dharm Veer Singh International Journal of Geometric Methods in Modern Physics (2023).

[39] B. Pourhassan,M. Dehghani, Sudhaker Upadhyay, I. Sakallı, Dharm Veer Singh, Modern Physics Letters A Vol. 37, No. 33n34, 2250230 (2022).

[40] C. Bambi and L. Modesto, Phys. Lett. B **721**, 329 (2013).

[41] S. G. Ghosh, ' Eur. Phys. J. C **75**, 532 (2015).

[42] B. Toshmatov, B. Ahmedov, A. Abdujabbarov and Z. Stuchlik, Phys. Rev. D **89**, 104017 (2014).

[43] S. G. Ghosh and S. D. Maharaj,
Eur. Phys. J. C **75**, 7 (2015).

[44] J. C. S. Neves and A. Saa,
Phys. Lett. B **734**, 44-48 (2014).

[45] F. Ahmed, D. V. Singh and S. G. Ghosh, Gen. Rel. Grav. **54** (2022) no.2, 21.

[46] D. V. Singh, S. Upadhyay and M. S. Ali, Int. J. Mod. Phys. A **37** (2022) no.09, 2250049.

[47] F. Ahmed, D. V. Singh and S. G. Ghosh, "5D rotating regular Myers-Perry black holes and their shadow," [arXiv:2008.10241 [gr-qc]].

[48] H. K. Sudhanshu, S. Upadhyay, D. V. Singh and S. Kumar, Int. J. Theor. Phys. **61** (2022) no.10, 248

[49] N. Godani, D. V. Singh and G. C. Samanta, Phys. Dark Univ. **35** (2022), 100952.

[50] B. K. Vishvakarma, D. V. Singh and S. Siwach, Eur. Phys. J. Plus **138** (2023) no.6, 536.

[51] P. Chaturvedi, N. K. Singh and D. V. Singh, Int. J. Mod. Phys. D **26**, no.08, 1750082 (2017).

[52] D. V. Singh, S. Upadhyay and M. S. Ali, K. Z. Amin, N. ul Islam, D. V. Singh and P. A. Ganai, Int. J. Mod. Phys. A **40** (2025) no.19, 2550057

[53] S. Upadhyay and D. V. Singh,
Eur. Phys. J. Plus **137** (2022) no.3, 383.

[54] D. V. Singh, B. K. Singh and S. Upadhyay, Annals Phys. **434** (2021), 168642.

International Conference on Astroparticle Physics, Gravitation and Cosmology (APGC-2025)
26-28 June 2025, GLA University, Mathura, India

Application of Emulsion Technology in the search of rare event

U. Rawat[1,*] and M. K. Singh[1]

[1]*Department of Physics, Institute of Sciences and Humanities, GLA University, Mathura - 281406, INDIA*

Abstract

According to cosmological observations, Dark Matter makes up the majority of the universe's matter. Because of the elastic scattering off target nuclei, Weakly Interacting Massive Particles (WIMPs) are a clear indicator of Dark Matter. Located in the Gran Sasso subterranean laboratory in Italy, NEWSdm seeks to be the first directed dark matter search experiment with a solid target. Its goal is to offer a unique signal of the finding of Galactic dark matter and to expand dark matter investigations beyond the neutrino floor. The detector is based on nuclear emulsion and serves as both a target and a tracking device. A new general-purpose fixed target facility called SHiP (Search for Hidden Particles) has been suggested for the CERN SPS accelerator. Neutrinos are abundant in the beam dump, and tau neutrinos—the less well-known particle in the Standard Model—are especially well-found there. The paper describes the emulsion technology in the search of dark matter, neutrino studies, CERN and double beta decay.

*Electronic address: upasnarawat999@gmail.com

1. Introduction

Emulsion(EM) technology in the search of rare events typically refers to the use of nuclear emulsion detectors in experimental particle physics, particularly for detecting rare phenomena such as neutrino interactions, dark matter(DM) or short-lived particles (e.g. tau leptons). These detectors combine with the microscopic resolution of photographic film with the ability to record particle tracks in 3D, making them ideal for observing rare, short-range events that other detectors might miss. Numerous astrophysical and cosmological observations, involving various physical processes at different scales, demonstrate the presence of non-baryonic DM throughout the cosmos, namely in our Galaxy's halo, which accounts for 27% of the total mass-energy density of the universe. These findings imply that the foundation of DM is at least one quasi-stable particle that differs from the Standard Model (SM) of particle physics. The WIMP, a massive, stable, and neutral particle, is currently the favoured DM candidate [1]. Multiple techniques for detecting WIMPs have been suggested and are currently in development. Efforts to find laboratory-generated WIMPs continue at the Large Hadron Collider, along with endeavors to view SM particles produced in our galaxy and extragalactic DM halos as a result of WIMP annihilation.

Several investigations attempt to find neutrinoless double beta decays in order to quantify the effective neutrino mass and prove the Majorana particle is classified as neutrinos (neutrinos and anti-neutrinos are the identical). The permitted form of double beta decay has previously been observed, but the forbidden type, which violates the leptonic number by two units, has not yet been observed [3].

The finding at CERN on the Large Hadron Collider of the Higgs boson in the ATLAS and CMS experiments marked the successful ending of the SM. Nonetheless, certain experimental data including non-zero neutrino masses suggests the model is still incomplete, the Universe's baryon asymmetry, DM and dark energy. To test these theories, suitable experimental settings must be designed and theoretical models must be developed to explain the occurrences under question. Among these kinds of projects is the SHiP experiment at CERN SPS (Super Proton Synchrotron). The SHiP is a new general-purpose fixed target experiment in the largely unexplored field of Beyond Standard Model (BSM) physics for studying tau-neutrino physics and very weakly interacting particles (heavy neutral leptons, dark photons, light scalars, supersymmetric particles, axions, etc). Because they may si-

multaneously explain the necessary effects, the search for the correct SM neutrino partners is of special interest and is driven by the theory. In order to find new physical objects, the main objective of the experiment preparation phase is to offer integrated detector solutions with extremely weak interactions with conventional matter and low weight [4].
Nuclear EM technology plays an important role in the search of rare event from the birth of experimental physics. This technology has achieved mildstone achievement in nuclear and particle physics due to its unique feature.

2. Application of Emulsion Technology

A. Application in Dark matter:

Some DM experiments (e.g., NEWSdm project) explore using nuclear EMs to detect nuclear recoils from WIMP interactins. EMs can detect low-energy nuclear recoils with directional sensitivity which is crucial for confirming a galactic origin of DM. The strategy suggested by the NEWSdm Collaboration involves utilizing a nuclear EM-based detector that functions as both the target and the tracking device. The initiative plans to implement an innovative EM technology known as Nano Imaging Trackers (NIT), which has a position resolution significantly superior to that of the EM used in the OPERA experiment. To reduce the effect of outside background radiation, the detector's design includes a mass of NIT protected by a shield. Additionally, to take into consideration the Earth's rotation, the detector is mounted on an equatorial telescope, thereby maintaining a fixed orientation concerning the incoming apparent WIMP flux.
It is predicted that the distribution of nuclei scattered by WIMPs will be highly anisotropic in the forward direction. Crystals of silver halide immersed in a gelatinous matrix to form nuclear EMs. As ionizing particles traverse this medium, some of the halide crystals undergo changes that convert them into silver grains during the developing process. By linking all the silver grains together andusing an optical microscope, the 3-D path of the particles can be reconstructed. NIT represent a new category of EM films characterized by grain sizes reaching as small as a few tens of nanometers, which is one order of magnitude smaller than traditional films. These films exhibit a linear density of approximately 11 crystals per micrometer. They consist of the following nuclei with mass fractions in different

percentage: H, C, N, O, S, Br, Ag and I. The overall density measures 3.2 grams per cubic centimeter. When viewed with high-resolution microscopes, they make it possible to recreate paths with lengths shorter than 100 nm. An essential component of the NEWSdm research is the addition of lighter nuclei, such as C, O and N to the EM gel in addition to the heavier ones, such as Ag and Br. Effective sensitivity to WIMPs with both light and heavy masses is therefore made possible[2].

B. Application in Double beta decay:

Numerous investigations attempt to find neutrinoless double beta decays in order to determine the effective neutrino mass and demonstrate that neutrinos are Majorana particles. The proposed Super-NEMO experiment and the ongoing NEM03 experiment will serve as references for this proposal to use nuclear electromagnetic fields to detect neutrinoless double beta decays. The two electrons from each processes are found in double-beta tests. While the energy for the forbidden process is clearly defined and mostly distributed by the detector energy resolution, the electron energy distribution for the first instance is rather large because of the missing neutrino energy. These tests have taken two approaches: one that just measures the energy with high precision, and another that measures the energy and detects the two electrons. While the second one has higher background rejection but poorer energy resolution, the first one is impacted by numerous different processes that deposit energy in the detector. This second group includes NEMO3 and the projected Super-NEMO trials. NEMO3 uses double-beta decaying isotopes of double-beta decay in a foil shape is enclosed by scintillator and gaseous detectors to identify the two electron tracks and estimate their energy.

The NEM03 experiment uses 7 Kg isotopes to achieve the order of 0.3 eV of neutrino effective mass limit, with a target foil thickness of about 60 pm and surface of 20 m^2 . The Super-NEMO project for electrons at 1 MeV will raise the energy resolution from 15% to less than 7% and use ten times more isotope mass in order to obtain 50 meV effective neutrino mass. Super-NEMO would employ a modular detector to accomplish these objectives; for a total of 1500m^3 each module would be roughly 1×5×4m^3. Nuclear EMs might be employed to achieve comparable results. This method is widely used in the

OPERA experiment, and significant work has been done to automate and speed up the EM scanning process.

In the basic unit of this double-beta EM detector, an isotope foil with an EM sheet thick enough to block electrons at energies of around 4 MeV on either side acts as a calorimeter and a tracker. To tag external tracks, a thin EM layer ($\sim$50μm like OPERA EMs) might be put to the outside of the EMs' plastic base. The final $\sim$50μm of the inner EM, which detects electrons from double-beta decays, may likewise be used to reject external tracks. It would be possible to make and store isotope/EM envelopes in boxes in a temperature-controlled, low-radiation setting. The EMs may be taken out, developed, and scanned after a specific amount of exposure time to look for electrons coming from the same location on the isotope foils. The electron energy may be determined by the number of grains in the EM. New EM sheets could be used with the extracted isotope sheets. Electrons with kinetic energies as low as 1 MeV and even lower must be detectable by this experimental method [3].

C. Application in CERN:

To measure the invariant mass of the long-lived particles and to fully reconstruct their unique decays, the SHiP facility is designed . Over the course of five years of operation, 2 $\times$ 10^{20} protons will be accumulated using the 400 GeV/c proton beam with high density Mo/W target that was removed from the SPS, which is tentatively scheduled to begin in 2026. Access to a broad range of light, long-lived exotic particles is made possible by the SPS's high intensity and charm meson production. Decay modes involving electrons, neutral, and charged π-mesons, muons, and other particles will be identified using the final state. Furthermore, the SHiP facility is perfect for researching tau-neutrino interactions. It will be the first to investigate the physics of ν_τ and anti-ν_τ, the only missing element in the SM. The τ lepton generation and decay will be detected in order to identify the ν_τ and anti-ν_τ interactions. The facility will have a tiny tau-neutrino detector and a detector to look for hidden particles. The detector for hidden particles consists of a long evacuated decay chamber with muon detectors at the far end, calorimeters, and a magnetic spectrometer. A separate timing detector and background taggers ensure robustness against

different kinds of background. A muon spectrometer is placed after an EM target that has tracking in a magnetic field as part of the tau-neutrino detector.
The tau-neutrino detector's primary goal is to investigate the characteristics and cross section of ν_τ and anti-ν_τ and to observe the anti-ν_τ for the first time directly. Finding the neutrino interaction and the decay τ vertices is a prerequisite for identifying the ν_τ and anti-ν_τ interactions. There are two processes used: the decay search and the event location. Reconstructing the neutrino interaction vertex and defining its 3-D position with micrometric accuracy comprise the event location. The goal of the decay search process is to find the τ decay vertex. To determine the decay channel by classifying the tracks created in the τ decay, lepton identification is used. By analysing the flavour of the primary charged lepton production in neutrino charged-current interactions, one can determine the neutrino flavour . A small neutrino detector, muon spectrometer and 5 m long EM serve as the foundation for the study of ν_τ physics in SHiP which is situated upstream of the SHiP decay region and directly downstream on the beam axis of the muon filter. In the Emulsion Cloud Chamber (ECC) technology, which is based on a sequence of passive material plates interspersed with nuclear electromagnetic films, a Muon Magnetic Spectrometer (MMS) is positioned behind the Neutrino Emulsion Target (NET) in a magnetic field. Enhancing muon momentum measurement in the magnetised target and efficiently detecting muons generated in τ decays and neutrino interactions are the goals of the MMS.
The two components are the Compact Emulsion Spectrometer (CES) and the ECC brick that make up the modular EM target. Measuring the electric charge of the τ daughters is one of the most crucial components of the ν_τ and anti-ν_τ identification. High performance for hadrons produced in the τ decay in charge measurement is achieved by optimising the detector's layout.

The detector can also be used to analyse the decay and production of charmed hadrons because it is optimised for the τ lepton identification. The odd quark content measurement of the nucleons will be much improved by the investigation of the charm production cross section. Light Dark Matter (LDM) production in the EM target, the experiment may have important implications. In theory, DM particles can be found by observing their interactions with SM particles, such as electrons and nuclei. The detection of DM particle scattering off electrons is the foundation for the research on the SHiP neutrino detector. Signals from

the sub-GeV DM will be regarded as the recoil electrons generated by the scattered LDM particles in the detector. The low cross section area in the phase space could be explored by using a nuclear EM detector that serves as both a target and a tracking device. The research will cover entire parameter space of minimum theoretical models of 1 MeV to 1 GeV mass range. The beam-induced neutrinos in the background is the main challenge for detecting LDM scattering at SHiP using electron recoils. A nuclear EM facility is being constructed to measure the energy and direction of impact electrons as well as the multiplicity of secondary particles to track the dominant neutrino scattering background.

Following exposure, the target's EM films will be prepared, and measuring devices will be used to analyse the entire detector volume. Similar to the OPERA experiment, the analysis, search, identification of primary and secondary vertices created by neutrinos in the EM target will be carried out. The designation data from the CS is used to find the upstream direction in the ECC films for the neutrino interaction vertex. Up to three consecutive films from the most recent detected segment are followed for each track. Either the decay of short-lived particles or the principal vertex may be linked to the track rupture. The full area of potential interactions close to the searched event vertex is covered by track reconstruction in the 1 cm ^{2} region in 10–15 EM films around the track stopping point. When scanning the defined area, the majority of the track segments are not contacted in long tracks and are not considered for further inquiry. Moreover, if cosmic muon tracks pass straight across the examined volume, they are not considered for the precise mutual alignment of ECC films. New tracks orientated downstream towards the primary vertex are looked for, while the tracks found have been kept for future analysis. It is feasible to obtain an accurate 3D reconstruction of the event due to nuclear EMs excellent spatial resolution [4].

3. Conclusion

EM technology has proven to be a powerful tool in advancing frontier research in particle physics, particularly in the areas of DM detection, experiments at CERN, and double beta decay studies. Its unparalleled spatial resolution allows for the precise tracking of particle interactions, enabling the identification of rare events that are central to these fields. In DM research, nuclear EMs are instrumental in directional detection, offering a promising method to distinguish potential DM interactions from background noise based on track orientation.

This enhances sensitivity and strengthens the case for WIMP searches.

At CERN, EM detectors have contributed significantly to neutrino physics (e.g., in the OPERA experiment), validating the feasibility of using EM technology in large-scale, high-energy particle environments. Their compactness, resolution, and passive operation make them ideal for detecting short-lived particles and rare decays.

In double beta decay experiments, EMs can help in precise vertex reconstruction and energy estimation, aiding the search for neutrinoless double beta decay—a key to understanding the nature of neutrinos and the matter-antimatter asymmetry in the universe.

Overall, the integration of EM technology continues to enhance experimental sensitivity and resolution in fundamental physics, offering a unique and complementary method to traditional electronic detectors in the ongoing search for answers to some of the universe's most profound mysteries.

---

[1] J. B. R. Battat, et al.,Physics Reports **662**, 1-46 (2016).

[2] A. Umemoto et al., J. of Cos. and Astro. Phys., **2**, 12, (2025).

[3] M. Dracos, J. Soc. Photogr. Sci. Technol. Japan, **71(5)**, 335-337, (2008).

[4] N. Konovalova, Perspectives in Sci., **12**, 100401 (2019).

Cosmic dynamics in the holographic dark energy models with a parameterized deceleration parameter

S. Kotambkar[1] and R. Kelkar[2]

[1]*Laxminarayan Innovation Technological University,*
Nagpur, Maharashtra 440033, India;
Corresponding Author E-mail:shubha.kotambkar@gmail.com
[2]*S. B. Jain Institute of Technology, Management and Research,*
Nagpur, Maharashtra 441501, India;
E-mail:rupalikelkar@sbjit.edu.in

Abstract

In the present work we explore a new form of dark energy called Holographic dark energy (HDE), within the framework of general relativity for spatially FRW model of the universe. To understand evolution of the universe we used parametrization of deceleration parameter q. We use Cosmic Chronometer (CC) data also Pantheon+SHOES data to obtain constraints on model parameters. We investigate cosmological parameters like energy density, equation of state parameter, stability parameter, jerk parameter and snap parameter in terms of z with different IR cut-offs.

One of the most astonishing findings in modern cosmology is that the universe is not only expanding but also accelerating, due to some kind of negative pressure form of matter known as "dark energy", which makes up nearly 70% of the universe's present-day energy budget. This finding is supported by independent observational sources [1–4]. Gravitational wave detection and black hole shadow imaging have reaffirmed the accuracy of general relativity. Any extra source term such as Einstein's cosmological "Constant" could be added into energy momentum tensor and serve as a candidate of dark energy. To match with the recent observational data many dark energy models have been proposed [5, 6] . The Λ -CDM model is the most fundamental and straightforward option in this series. but it is associated with problems like "fine tuning problem" [7], "coincidence problem" [8] and the "age problem" [5]. To address these issues different dark energy models were examined such as Quintessence, K-essence, Phantom, Tachyon, Chaplygin gas and so on (refer [9] and references therein).

Another possible approach to solving the dark energy problem drawn on accepts of quantum gravity theory, specifically the Holographic principle [10–14].The HDE model is the theoretical model of dark energy inspired from Holographic principle. According to the Holographic principle, the entropy of a system scales not with its volume but with its surface area. In recent decades, in order to develop and examine cosmological models, various entropy formulations have been applied. This led to many innovative HDE models such as Tsallis HDE [15, 16], Sharma-Mittal HDE [16, 17] and Renyi HDE model [18].

A new infrared cut off for HDE density demonstrating that it represents accelerated universe is consistent with current observations data has been proposed by Granola and Oliveros [19, 20]. Numerous researchers have investigated HDE model to explain late time accelerating phase of the universe [21–25].

The modeling of cosmos supported by different parametrization of cosmological parameters like pressure, equation of state parameter, deceleration parameter, Hubble parameter, jerk parameter also the scale factor have been significantly investigated for identifying physically reasonable cases [26–45]. The ansatzs of the physical and geometrical quantities may be used and these cases must be consistent with observations. In this work we explore deceleration parameter's observational compatibility anstazs with cosmological dynamics of the model within the framework of general relativity theory.

In section 2 we write motivation and basic equation of model along with behaviour of var-

ious parameters like energy density, cosmic pressure and equation of state parameter.Also we parameterize deceleration parameter q in terms of z and study the Hubble parameter by use of observational data. The model's parameters were constrained using observations from CC data and Pantheon+SHOES data in section 3 In section 4 we investigate HDE model with different cut-offs and the section 5 includes results with the conclusion on agreement of assumed anstazs with observations.

I. FIELD EQUATIONS AND SOLUTIONS:

A. Field equations in general relativity

The isotropic and spatially flat universe may be modeled with Friedman-Robertson-Walker metric given by

$$ds^2 = dt^2 - a^2(t)\left(dx^2 + dy^2 + dz^2\right), \tag{1}$$

Here we set c = 1 due to the homogeneity property and scale factor "a" is a function of t . We adopt the framework of general relativity, with the matter content of the universe is represented by a fluid describe through its energy momentum tensor

$$T^{\mu}_{\nu} = d_{iag}\left(\rho, -p, -p, -p\right), \tag{2}$$

where ρ is energy density and p is cosmic pressure. The Einstein's field equations for FRW metric (1) yields

$$\rho = 3H^2, \quad -p = 2\dot{H} + 3H^2, \tag{3}$$

$H = \frac{\dot{a}}{a}$, in general relativity the equation of conservation of energy can be expressed as

$$\dot{\rho} = 3H\left(\rho + p\right) \tag{4}$$

B. Deceleration parameter in general relativity and observational constraints:

The deceleration parameter $q = \frac{-\ddot{a}}{aH^2}$ can be used to explain the rate of the universe's expansion, which can also be expressed as $q = q_0 + \frac{d}{dt}\left(\frac{1}{H}\right)$. To reconstruct the model deceleration parameter may be the basis, as it is based on the derivative of scale factor and the Hubble parameter. The parametrization of deceleration parameter may have reasonably

good impact on universe expanding rate. Adopting a parametric approach to estimate the universe transition from a decelerating to an accelerating phase is reasonable, as it offers a promising means to enhance the efficiency of future cosmological studies. Motivated by these reality, in present paper we have considered special form of q(z). We proceed with the form [46]

$$q(z) = q_0 + \frac{q_1 z}{1+z} \tag{5}$$

Where q_0 and q_1 are dimensionless parameters can be constrained by observational data set. The relation between red shift z scale factor is defined by $\frac{a_0}{a} = 1 + z$, where $a_0 = 1$ is for present day universe which is in fair agreement with observations. For past a lies in the range $0 < a < 1$ and $a > 1$ for later universe. In terms of red-shift the range $0 < z < \infty$, corresponds to past whereas $-1 < z < 0$ for later universe. For present day universe z is almost zero [47].

For this model the Hubble parameter can be obtained in form of red-shift (z) as

$$H(z) = H_0(z+1)^{(1+q_0+q_1)} \left(e^{\frac{-q_1 z}{1+z}}\right) \tag{6}$$

H_0 is present value of Hubble parameter, Using relation $\frac{a_0}{a} = 1 + z$ for $a_0 = 1$ one can have $\dot{H} = -(1+z)\,H(z)\frac{dH}{dz}$, then equation (6) takes the form

$$H'(z) = H_0(1+q_0+q_1)(1+z)^{(q_0+q_1)} e^{\frac{-q_1 z}{1+z}} - H_0(1+z)^{(1+q_0+q_1)} \left(e^{\frac{-q_1 z}{1+z}}\right)\left(\frac{-q_1}{(1+z)^2}\right) \tag{7}$$

From equation (3), we get

$$\rho = 3H_0^2\,(1+z)^{2(1+q_0+q_1)}\, e^{\left(\frac{-2q_1 z}{1+z}\right)} \tag{8}$$

and

$$-p = 2\left[(1+z)\,H\,(z)\,\frac{dH}{dz}\right] + 3H^2$$

By using equations (6) and (7) above equation takes the form

$$p = H_0^2\,(1+z)^{2(1+q_0+q_1)}\, e^{\left(\frac{-2q_1 z}{1+z}\right)} \left(2\,(1+q_0+q_1) - \frac{2q_1}{1+z} - 3\right) \tag{9}$$

We consider the equation of state

$$p = \gamma\rho, \tag{10}$$

By use of equations (8) and (9) in equation (10), we can get

$$\gamma = \frac{1}{3}\left[2\left(1 + q_0 + q_1\right) - \frac{2q_1}{1+z} - 3\right] \tag{11}$$

II. OBSERVATIONAL CONSTRAINT:

This section is dedicated to study the closeness of results obtained in this work by using CC data and Pantheon+SHOES [48, 49] which are pertinent for the observed universe in recent times. This data set also used in [50]

The important cosmic variable which directly explore cosmic expansion history is Hubble parameter. The Hubble parameter rate can be inferred either from the baryon acoustic oscillations in the redial direction because of clustering of galaxies [51] or from the method of differential age. The latter consists of expressing the Hubble parameter as a rate of change of red-shift.

$$H(z) = -\frac{1}{(1+z)}\frac{dz}{dt}$$

We use the CC data. By minimizing the χ^2 function, the observational constraints on the model parameters q_0, q_1 and H_0 can be evaluated and is given by

$$\chi^2 = \delta V_i {C_{ij}}^{-1} \delta V_j$$

where ${C_{ij}}^{-1}$ is inverse of total covariance matrix and $\delta V_i = m_{b_{obs}} - m_b(z_i)$.

We have obtained the best fit values for present model as given below

$q_0 = -0.464 \pm 0.059, q_1 = 0.99 \pm 0.26, H_0 = 72.00 \pm 0.91$.

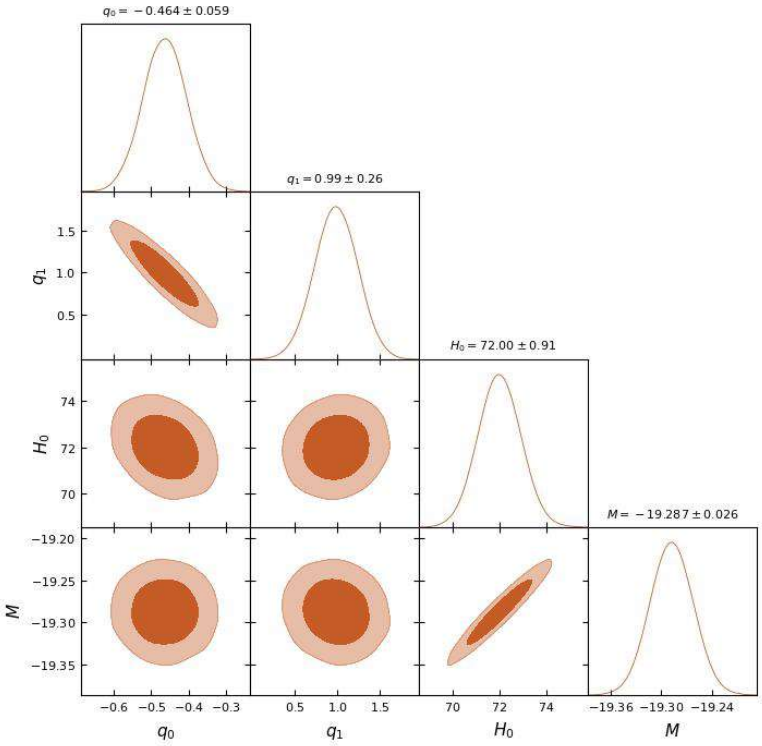

1.pdf

FIG. 1: The 1 σ and 2 σ contour plots for q_0, q_1, H_0 and M using CC and Pantheon data

.

III. HDE MODELS IN GENERAL RELATIVITY:

We study HDE models with different cut-offs in general relativity for the deceleration parameter q given by equation (5)

A. HDE model with Granda-Oliveros(GO) cut-off

The event horizon is a global property of space-time, and its existence depends on the future evolution of the universe. An event horizon is present only in a universe that undergoes eternal accelerated expansion [52]. Motivated by this, Granda and Oliveros [19] proposed a new infrared cut-off for HDE, involving a term proportional to the square of the Hubble parameter along with the time-dependent derivative of the Hubble parameter. Thus, the IR cutoff was introduced by Granda and Oliveros in terms of $\dot{H}$ and H^2 [19].

$$L_g = \left(\alpha_2 \dot{H} + \beta_2 H^2\right)^{-\frac{1}{2}} \tag{12}$$

Here α_2, β_2 are arbitrary constants.

The energy density ρ_g of HDE in GO cut-off model is expressed as

$$\rho_g(t) = 3\left[\alpha_2 \dot{H}(t) + \beta_2 H^2(t)\right] \tag{13}$$

which for present model in terms of red-shift z takes the form

$$\rho_g(z) = 3\left[-\alpha_2(z+1)H'(z)H(z) + \beta_2 H^2(z)\right] \tag{14}$$

By use of equations (6) and (7), equation (14) can be expressed as

$$\rho_g(z) = 3H_0^2\,(1+z)^{2(1+q_0+q_1)}\, e^{\left(\frac{-2q_1 z}{1+z}\right)} \left(-\alpha_2\,(1+q_0+q_1) - \frac{\alpha_2 q_1}{1+z} + \beta_2\right) \tag{15}$$

Using (9) and (15), EoS parameter is given by,

$$\gamma = \frac{(1+z)\,[2(1+q_0+q_1)-3] - 2q_1}{(1+z)\,[3\beta_2 - 3\alpha_2(1+q_0+q_1)] - 3\alpha_2 q_1} \tag{16}$$

On differentiating equation (9) with respect to z, we get

$$\frac{dp}{dz} = H_0^2(1+z)^{2m-2} e^{\frac{-2q_1 z}{(1+z)}} \left[(2m(1+z)-2q_1)(2m - \frac{2q_1}{1+z} - 3) + 2q_1\right] \tag{17}$$

where $m = 1 + q_0 + q_1$

On differentiating (15) with respect to z, we get

$$\frac{d\rho}{dz} = H_0^2(1+z)^{2m-2} e^{\frac{-2q_1 z}{1+z}} \left[(2m(1+z)-2q_1)(-3\alpha_2 m - \frac{3\alpha_2 q_1}{1+z} + 3\beta_2) + 3\alpha_2 q_1\right] \tag{18}$$

The stability parameter for present model can be calculated by use of equations (17) and (18) as

$$C_{sg}^2 = \frac{3\gamma\,(2m\,(1+z) - 2q_1) + 2q_1}{3\,(2m\,(1+z) - 2q_1)\left(-\alpha_2 m - \frac{\alpha_2 q_1}{1+z} + \beta_2\right) + 3\alpha_2 q_1} \tag{19}$$

The evolution of $C_{sg}^2(z)$ have been shown in Fig. 2. For this, we take the values $H_0 = 72.00, q_1 = 0.99, q_0 = -0.464, \alpha_2 = -0.001, \beta_2 = 10.0, m = 1.526$. The present choice of α_2 and β_2 gives $\frac{\dot{H}}{H^2} \geq 0$ for late time expansion it yields $q < 0$. At late times z approaches to -1 .

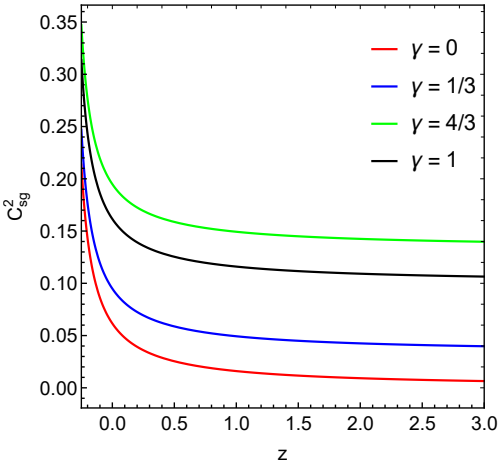

1 case.pdf

FIG. 2: Shows the evolution of stability parameter $C_s^2(z)$ for HDE of GO cut-off model for the values $H_0 = 72.00, q_0 = -0.464, q_1 = 0.99, \alpha_2 = -0.001, \beta_2 = 10, m = 1.526$

.

B. Modified holographic Ricci dark energy (MHRDE) model

The MHRDE model is modified type of original Ricci model of dark energy. In this section we discuss HDE model along with IR cut-off as reported by Modified Ricci radius. The energy density for MHRDE model is given by

$$\rho_m(t) = \frac{2}{\alpha_3 - \beta_3}\left(\dot{H}(t) + \frac{3\alpha_3}{2}H^2(t)\right), \tag{20}$$

where α_3 and β_3 are constants.We use the Holographic principle [49] associating the infrared cut off L with modified Ricci radius. We take L^{-2} as a linear combination of $\dot{H}$ and H^2, with this MHRDE $\rho_m = 3C^2M_p^2L^{-2}$ [20, 50, 51] and it lead to the form

$$\rho_m(z) = \frac{2}{\alpha_3 - \beta_3}\left(\frac{3\alpha_3}{2}H^2(z) - (1+z)H(z)H'(z)\right), \tag{21}$$

where the Hubble parameter $H = \frac{\dot{a}}{a}$, a is scale factor and α_3, β_3 are constants.

$$\rho_m(z) = \frac{2}{\alpha_3 - \beta_3}H_0^2\,(1+z)^{2(1+q_0+q_1)}\,e^{\left(\frac{-2q_1z}{1+z}\right)}\left(1.5\alpha_3 - (1+q_0+q_1) + \frac{q_1}{1+z}\right) \tag{22}$$

The EoS parameter for MHRDE model is expressed as

$$\gamma = \frac{(\alpha_3 - \beta_3)\left[(2(1+q_0+q_1)-3)(1+z)-2q_1\right]}{2\left[\left(\frac{3}{2}\alpha_3 - (1+q_0+q_1)\right)(1+z)-q_1\right]} \tag{23}$$

By differentiating eq (22) with respect to z, we get

$$\frac{d\rho_m}{dz} = \frac{2H_0^2}{\alpha_3-\beta_3}(1+z)^{2m-2}e^{-\frac{2q_1 z}{1+z}}\left[\left(\frac{3}{2}\alpha_3 - m + \frac{q_1}{(1+z)}\right)(2(1+z)m-2q_1)-q_1\right] \tag{24}$$

For MHRDE model C_s^2 can be expressed by use of equations (17) and (24)

$$C_s^2(z) = \frac{(\alpha_3-\beta_3)\left[(2m(1+z)-2q_1)3\gamma+2q_1\right]}{2\left[(2m(1+z)-2q_1)\left(1.5\alpha_3 - m + \frac{q_1}{1+z}\right)-q_1\right]} \tag{25}$$

Graphs of $\rho_m(z)$ and C_s^2 are given in Fig. 5 and Fig. 3 respectively for the values of $H_0 = 72.00, q_0 = -0.464, q_1 = 0.99, \alpha_3 = -0.1, \beta_3 = 0.0001, m = 1.526$. In this model, for the accelerating evolution of universe we need $\rho_m \geq 0$. Under these conditions, the $\rho_m(z)$ is always positive and tends to constant value.

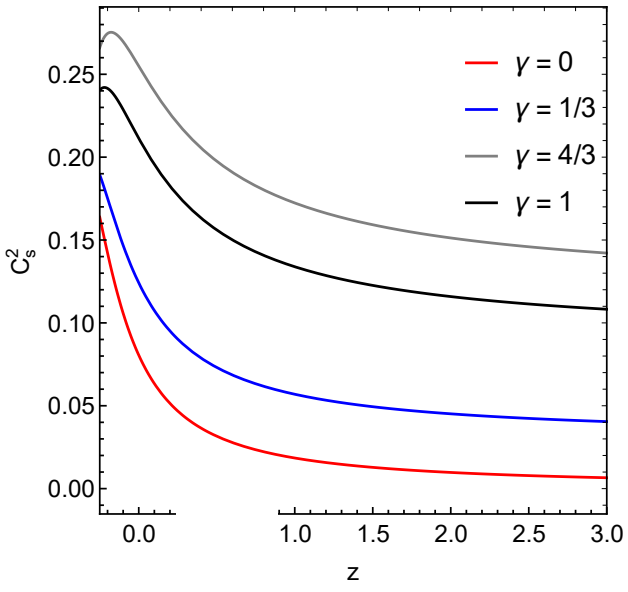

2 case.pdf

FIG. 3: Presents the graph of the stability parameter $C_s^2(z)$ Vs. z for MHRDE model for the values $H_0 = 72.00, q_0 = -0.464, q_1 = 0.99, \alpha_3 = -0.1, \beta_3 = 0.0001, m = 1.526$

.

C. RÃ©nyi holographic dark energy (RHDE) model

Few new models are evolved in recent years like RHDE [17], Sharma-Mittal [16] and Tsalis [15]. Among these models more stable model is RHDE. Renyi and Tsallis entropies

are widely recognized measures of generalized entropy and are defined as

$$S_R = \frac{1}{\delta} ln \sum_{i=1}^{m} P_i^{1-\delta}, \quad S_T = \frac{1}{\delta} \sum_{i=1}^{m} (P_i^{(1-\delta)} - P_i), \tag{26}$$

where $\delta \equiv 1 - U$ and U is a real parameter. By combining equation (26), we may write the relation given as

$$S_R = \frac{1}{\delta} ln(1 + \delta S_T). \tag{27}$$

where δ is constant and S_T is Tasllis entropy.For homogeneous systems, S_R represents one of the most general forms of entropy. It has been argued that the Bekenstein entropy ($S = \frac{A}{4}$) can be viewed as a special case of Tsallis entropy, leading to [54, 55]

$$S_R = \frac{1}{\delta} ln \left(1 + \delta \frac{A}{4}\right) \tag{28}$$

If δ approaches to 0, then the Renyi entropy reduces into

$$\rho_{de} = \frac{3d^2}{8\pi L^2} \left(1 + \pi\delta L^2\right)^{-1}, \tag{29}$$

where d^2 is constant. In order to evaluate equation (29), we have used $T = \frac{1}{2\pi L}, V = \frac{4\pi}{3} L^3$ and $A = 4\pi L^2$ relation, valid for a flat FRW space-time. We consider RHDE model along with GO cut-off to explore various properties. By using equations (17) and (29), for RHDE model with GO cut-off energy density in present model obtained as

$$\rho_{Rg}(t) = \frac{3d^2}{8\pi} \left\{ \frac{\left(\alpha_2 \dot{H}(t) + \beta_2 H^2(t)\right)^2}{\pi\delta + \left(\alpha_2 \dot{H}(t) + \beta_2 H^2(t)\right)} \right\}. \tag{30}$$

Equation (30) in form of z is given by

$$\rho_{Rg}(z) = \frac{3}{8\pi} \frac{d^2}{} \frac{\left(H_0^4 (1+z)^{4m} \left(e^{\frac{-4q_1 z}{1+z}}\right) \left(m_1 + \frac{\alpha_2 q_1}{1+z}\right)^2\right)}{(\pi\delta + H_0^2(1+z))^{2m} \left(e^{\frac{-2q_1 z}{1+z}}\right) \left(m_1 + \frac{\alpha_2 q_1}{1+z}\right)} \tag{31}$$

The EoS parameter for RHDE model in form of red-shift (z) is expressed as

$$\gamma = \frac{8\pi}{3d^2} (2m - \beta - \frac{2q_1}{1+z}) \frac{\left[\pi\delta + H_0^2(1+z)^{2m} e^{\frac{-2q_1 z}{1+z}} \left(m_1 + \frac{\alpha_2 q_1}{1+z}\right)\right]}{H_0^2 (1+z)^{2m} e^{\frac{-2q_1 z}{1+z}} \left(m_1 + \frac{\alpha_2 q_1}{1+z}\right)^2} \tag{32}$$

The stability parameter C_{sg}^2 in this case in terms of z is given by

$$C_{sg}^2(z) = \frac{8\pi \left[\pi\delta + H_0^2(1+z)^{2m} e^{\frac{-2q_1 z}{1+z}} \left(m + \frac{\alpha_2 q_1}{1+z}\right)\right]^2 \left[(2m(1+z) - 2q_1)3\gamma + 2q_1\right]}{3d^2 H_0^2 (1+z)^{2m} e^{\frac{-2q_1 z}{1+z}} M \left[2m(1+m-2q_1)M - \alpha_2 q_1\right] \left[2\pi\delta + H_0^2(1+z)^{2m} e^{\frac{-2q_1 z}{1+z}} M\right]} \tag{33}$$

where $M = \left(m_1 + \frac{\alpha_2 q_1}{(1+z)}\right)$

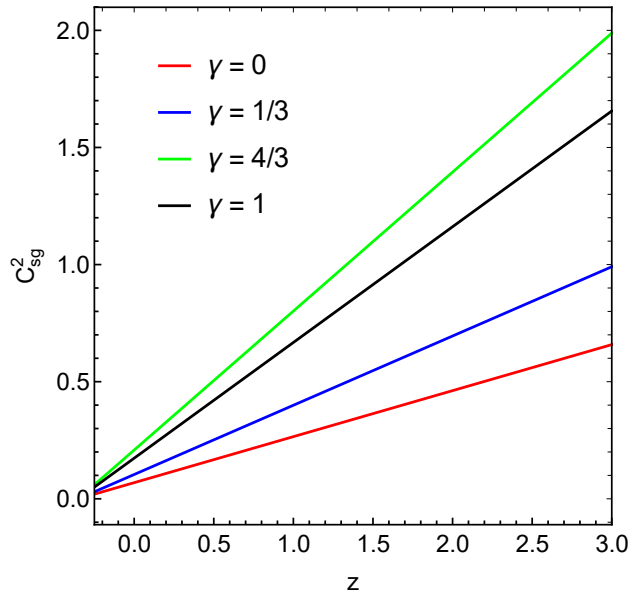

3 case.pdf

FIG. 4: Indicate stability parameter $C_s^2(z)$ versus z for RHDE model for the values $H_0 = 72.00, q_0 = -0.464, q_1 = 0.99, \alpha_2 = -0.001, \beta_2 = 10, m = 1.526, d = 3.5, \delta = 0.5, m1 = 10.001526$

.

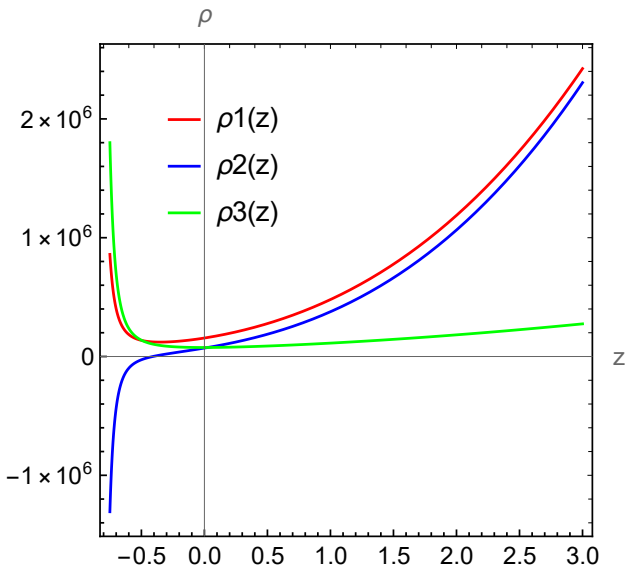

FIG. 5: Represents the energy density ρ versus z for the values $H_0 = 72.00, q_0 = -0.464, q_1 = 0.99, \alpha_2 = -0.001, \beta_2 = 10, \alpha_3 = -0.1, \beta_3 = 0.0001, m = 1.526, d = 3.5, \delta = 0.5, m1 = 10.001526$ for all three models

.

The cosmic evolution can also be studied by use of jerk parameter defined by $j = \frac{\dddot{a}}{aH^3}$ in terms of z takes the form

$$j(z) = (z+1)\frac{dq}{dz} + q(z) + 2q^2(z) \tag{34}$$

For present model, it takes the form

$$j = \left(q_1 + q_0 + 2q_0^2\right) + \frac{2q_1 z}{1+z}\left(2q_0 + \frac{q_1 z}{1+z}\right) \tag{35}$$

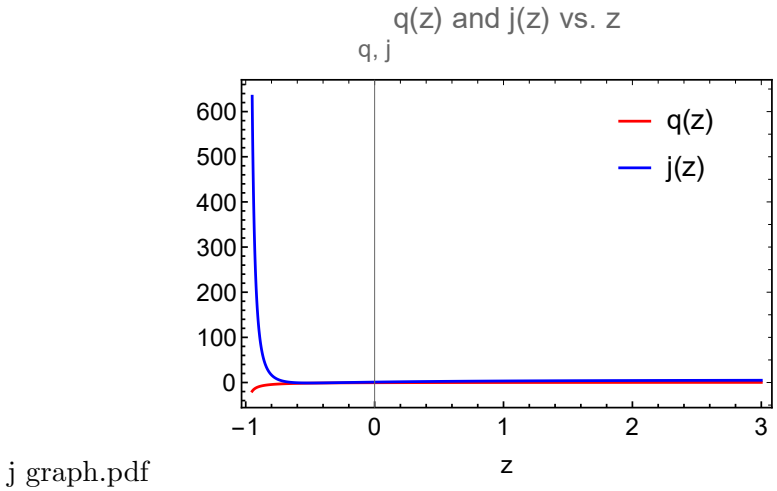

j graph.pdf

FIG. 6: Depicts the deceleration parameter and jerk parameter $q(z), j(z)$ versus z for the values $H_0 = 72.00, q_0 = -0.464, q_1 = 0.99$

.

The snap parameter is defined as $s = \frac{d^4a}{dt^4}\frac{1}{aH^4}$. Alternatively, one may have $s = -(z+1)j' - (3q+2)j$. In the de Sitter phase of ΛCDM model, $s = 1$ [54]

$$s(z) = -(z+1)\frac{dj}{dz} - j(z)(2+3q(z)), \tag{36}$$

which for this model takes the form

$$s = \frac{-4q_0q_1}{1+z} - \frac{4q_1^2 z}{(1+z)^2} - \left(2 + 3q_0 + \frac{3q_1 z}{1+z}\right)\left[\left(q_0 + q_1 + q_0^2\right) + \frac{2q_1 z}{1+z}\left(2q_0 + \frac{q_1 z}{1+z}\right)\right] \tag{37}$$

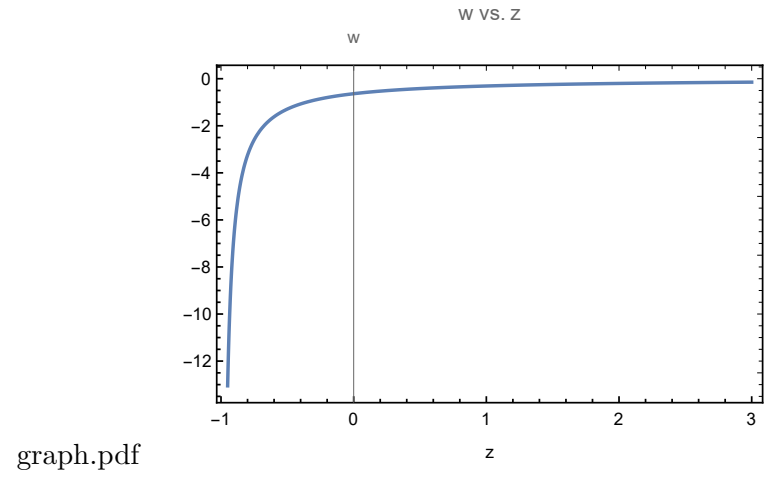

graph.pdf

FIG. 7: Shows $\omega(z)$ versus z for the values $q_0 = -0.464, q_1 = 0.99$

.

IV. CONCLUSION:

In this study, cosmological parameters have been derived for a remodeled universe using a parametric form of the deceleration parameter within the framework of general relativity. Cosmic Chronometer and Pantheon data are utilized to constrain model parameters and uncover insights into Cosmic dynamics.The most suitable value of the model parameters for the CC data are resulted in $H_0 = 72.00 \pm 0.99 \quad KM/S/MPC, q_0 = -0.464 \pm 0.059, q_1 = 0.99 \pm 0.26$.

We investigated three HDE models with different IR cut off (1) HDE model with GO cut off (2) MHRDE model and (3) RHDE model. By parametrizing deceleration parameter, we obtained exact solution of energy density, equation of state parameter. To understand evolution of cosmic parameter we sketched graphs of energy density, stability parameter, jerk parameter and EoS parameter for all three formulated HDE models.

The important insights of the present work we summaries as follow:

1. The HDE model with GO cut-off has consistently demonstrated classical stability throughout its past, present and future projections. In this model energy density is positive during evolution of universe for different values of red shift.
2. The MHRDE model is classically stable at past, present and future also.
3. For the RHDE model classical stability vs. red-shift z is a straight line, it means the parameter evolves linearly with red shift. This implies a predictable and smooth evolution perturbative stability in cosmic fluid.
4. The energy density is positive for all the three cases.
5. For this model $j_0 = 0.956592$ and $s_0 = 1.386733$.

Authors' Contributions

All authors have the same contribution.

Data Availability

The manuscript has no associated data or the data will not be deposited.

Conflicts of Interest

The authors declare that there is no conflict of interest.

Ethical Considerations

The authors have diligently addressed ethical concerns, such as informed consent, plagiarism, data fabrication, misconduct, falsification, double publication, redundancy, submission, and other related matters.

Funding

This research did not receive any grant from funding agencies in the public, commercial, or non-profit sectors.

Acknowledgment

Authors would like to thank Iran Science Elites Federation, Tehran, Iran.

---

[1] A. G. Riess, A.V. Filippenko, P. Challis, A. Clocchiatti, A. Diercks, P. M. Garnavich, R. L. Gilliland, C. J. Hogan, S. Jha, R. P. Kirshner, B.R.U.N.O. Leibundgut, "Observational evidence from supernovae for an accelerating universe and a cosmological constant", Astron. J. **116**, 3, 1009, (1998). DOI:10.1086/300499

[2] S. Perlmutter, G. Aldering, G. Goldhaber, R. A. Knop, P. Nugent, P. G. Castro, S. Deustua, S. Fabbro, A. Goobar, D.E. Groom, I. M. Hook,"Measu rements of Ω and Λ from 42 high-redshift supernovae", Astrophys. J.,**517**,565, (1999). DOI:10.1086/307221

[3] N. Aghanim, M.A. Miville-Deschênes, V. Pettorino, M. Bucher, J. Delabrouille, K. Ganga, M. Le Jeune, G. Patanchon, C. Rosset, G. Roudier, Y. Fantaye, M. Kunz, "Planck 2018 results: VI. Cosmological parameters", Astron. Astrophys. **641**, A6 (2020). DOI:10.1051/0004-6361/201833910

[4] A. Dev, D. Jain, S. Jhingan, S. Nojiri, M. Sami, I. Thongkool, "Delicate $f(R)$ gravity models with a disappearing cosmological constant and observational constraints on the model parameters", Phys. Rev. D, **78**, 083515, (2008). DOI:10.1103/PhysRevD.78.083515

[5] E. J. Copeland, M. Sami, S. Tsujikawa, 2006. "Dynamics of dark energy", Int. Mod. Phys. D, **15**, 1753, (2006). DOI:10.1142/S021827180600942X

[6] J. A. Frieman, M. S. Turner, D. Huterer. "Dark energy and the accelerating universe." Annu. Rev. Astron. Astrophys. **46**, 385, (2008). DOI:10.1146/annurev.astro.46.060407.145243

[7] S. Weinberg, "The cosmological constant problem", Rev. Mod. Phys. **61**, 1 (1989). DOI:10.1103/RevModPhys.61.1

[8] P. J. Steinhardt, L. Wang,I. Zlatev, "Cosmological tracking solutions", Phys. Rev. D, **59**, 12, 123504, (1999). DOI:10.1103/PhysRevD.59.123504

[9] L. Amendola, S. Tsujikawa, "Dark energy: theory and observations. Cambridge University Press", (2010)

[10] J. D. Bekenstein, "Black holes and entropy.", Phys. Rev. D, **7**, 2333, (1973). DOI:10.1103/PhysRevD.7.2333

[11] G 't Hooft, "Dimensional reduction in quantum gravity", arXiv preprint gr-qc/9310026 (1993).

[12] L. Susskind, "The world as a hologram" J. Math. Phys.,**36**, 11, 6377, (1995). DOI:10.1063/1.531249

[13] R. Bousso, "A covariant entropy conjecture", JHEP, **1999**, 7,004, (1999). DOI:10.1088/1126-6708/1999/07/004

[14] A. Cohen, D. Kaplan, A. Nelson. "Effective field theory, black holes, and the cosmological constant." Phys. Rev. Lett., **82**, 25, 4971 (1999). DOI:10.1103/PhysRevLett.82.4971

[15] C. Tsallis, "Possible generalization of Boltzmann-Gibbs statistics", J. Stat. Phys. **52**, 479 (1988). DOI:10.1007/BF01016429

[16] A. S. Jahromi, S. A. Moosavi, H. Moradpour, J. M. GraÃ§a, I. P. Lobo, I. G. Salako, A. Jawad, "Generalized entropy formalism and a new holographic dark energy model", Phys. Lett. B **780**, 21 (2018). DOI:10.1016/j.physletb.2018.02.052

[17] H. Moradpour, S. A. Moosavi, I. P. Lobo, J. M. GraÃ§a, A. Jawad, I. G. Salako, "Thermodynamic approach to holographic dark energy and the RÃ©nyi entropy", Eur. Phys. J. C **78**, 829 (2018). DOI:10.1140/epjc/s10052-018-6310-6

[18] A. Rényi, "Probability Theory", North-Holland, Amsterdam (1970).

[19] L. N. Granda, A. Oliveros, "Infrared cut-off proposal for the holographic density", Phys. Lett. B **669**, 275 (2008). DOI:10.1016/j.physletb.2008.10.017

[20] L. N. Granda, A. Oliveros, "New infrared cut-off for the holographic scalar fields models of dark energy", Phys. Lett. B **671**, 199 (2009). DOI:10.1016/j.physletb.2008.12.025

[21] M. Li, X.-D. Li, Y.-Z. Ma, X. Zhang, Z. Zhang, "Planck constraints on holographic dark energy", J. Cosmol. Astropart. Phys. **1309**, 021 (2013). DOI:10.1088/1475-7516/2013/09/021

[22] A. Pasqua, R. da Rocha, S. Chattopadhyay, "Holographic dark energy models and higher order generalizations in dynamical Chern-Simons modified gravity", Eur. Phys. J. C **75**, 44 (2015). DOI:10.1140/epjc/s10052-014-3256-x

[23] R. Chaubey, A. K. Shukla, "Holographic dark energy model with quintessence in general class of Bianchi cosmological models", Can. J. Phys., **93**, 68-79 (2015). DOI:10.1139/cjp-2014-0225

[24] S. Mandal, A. Singh, R. Chaubey, "Cosmic evolution of holographic dark energy in $f(Q,T)$ gravity", Int. J. Geom. Methods Mod. Phys., **20**, 2350084 (2023). DOI:10.1142/S0219887823500846

[25] G. Varshney, U. K. Sharma, A. Pradhan, N. Kumar, "Reconstruction of Tachyon, Dirac-Born-Infeld-essence and Phantom model for Tsallis holographic dark energy in f (R, T) gravity", Chin. J. Phys., **73**, 56 (2021). DOI:10.1016/j.cjph.2021.04.014

[26] A. R. Lalke, G. P. Singh, A. Singh, "Late-time acceleration from ekpyrotic bounce in f (Q, T) gravity", Int. J. Geom. Methods Mod. Phys., **20**, 2350131 (2023). DOI:10.1142/S0219887823501311

[27] S. Mandal, A. Singh, R. Chaubey, "Cosmic evolution of holographic dark energy in $f(Q,T)$ gravity", Int. J. Geom. Methods Mod. Phys., **20**, 2350084 (2023). DOI:10.1142/S0219887823500846

[28] R.R. Sahoo, K.L. Mahanta, S. Ray, "Nonsingular phantom cosmology in five-dimensional f (R, T) gravity.", Universe, **8**, 573 (2022). DOI:10.3390/universe8110573

[29] N. Ahmed, A. Pradhan, "Probing cosmic acceleration in K(R,T) gravity", Indian J. Phys., **96**, 301, (2022). DOI:10.1007/s12648-020-01948-4

[30] S. Capozziello, V.F. Cardone, E. Elizalde, S. Nojiri, S.D. Odintsov, "Observational constraints on dark energy with generalized equations of state.", Phys. Rev. D-Particles, Fields, Gravita-

tion and Cosmology, **73**, 043512 (2006). DOI:10.1103/PhysRevD.73.043512

[31] S. Nojiri, S.D. Odintsov, "Inhomogeneous equation of state of the universe: Phantom era, future singularity and crossing the phantom barrier", Phys. Rev. DâParticles, Fields, Gravitation, and Cosmology,**72**, 023003 (2005). DOI:10.1103/PhysRevD.72.023003

[32] S. Nojiri, S.D. Odintsov, "Is the future universe singular: Dark matter versus modified gravity?", Phys. Lett. B, **686**, 44, (2010). DOI:10.1016/j.physletb.2010.02.017

[33] A.V. Astashenok, S. Nojiri, S.D. Odintsov, R.J. Scherrer, "Scalar dark energy models mimicking ΛCDM with arbitrary future evolution." Phys. Lett. B,**713**, 145, (2012). DOI:10.1016/j.physletb.2012.06.017

[34] A. Singh, R. Raushan, R. Chaubey, S. Mandal, K.C. Mishra, "Lagrangian formulation and implications of barotropic fluid cosmologies." Int. J. Geom. Methods Mod. Phys., **19**, 2250107, (2022). DOI:10.1142/S0219887822501079

[35] N. Hulke, G.P. Singh, B.K. Bishi, A. Singh, "Variable Chaplygin gas cosmologies in f (R, T) gravity with particle creation.", New Astron., **77**, 101357 (2020). DOI:10.1016/j.newast.2020.101357

[36] A. Singh, A.K. Shukla, S. Krishnannair, "Cosmic dynamics of isotropic models with inhomogeneous EoS: a dynamical system perspective.", Int. J. Mod. Phys. A, **38**, 2350169,(2023). DOI:10.1142/S0217751X23501695

[37] A. Singh, "A complete cosmological scenario with particle creation", Astrophys. Space Sci.,**365**, 54 (2020). DOI:10.1007/s10509-020-03768-8

[38] G.P. Singh, N. Hulke, A. Singh,"Cosmological study of particle creation in higher derivative theory.", Indian J. Phys.,**94**, 127, (2020). DOI:10.1007/s12648-019-01426-6

[39] G.P. Singh, A.R. Lalke, N. Hulke, "Study of particle creation with quadratic equation of state in higher derivative theory.", Braz. J. Phys.,**50**, 725, (2020). DOI:10.1007/s13538-020-00788-1

[40] A. Singh, "Thermodynamic implications of BransâDicke cosmologies.", Eur. Phys. J. Plus,**136**, 522, (2021). DOI:10.1140/epjp/s13360-021-01519-4

[41] A.A. Mamon, S. Das, "A parametric reconstruction of the deceleration parameter.", Eur. Phys. J. C ,**77**, 495, (2017). DOI:10.1140/epjc/s10052-017-5066-4

[42] J.-Z. Ma, X. Zhang, "Probing the dynamics of dark energy with novel parametrizations.", Phys. Lett. B,**699**, 233, (2011). DOI:10.1016/j.physletb.2011.04.013

[43] J.C. Wang, X.H. Meng, "Exploring the deviation of cosmological constant by a generalized pressure dark energy model.", Eur. Phys. J. C,**79**, 848, (2019). DOI:10.1140/epjc/s10052-019-7343-x

[44] G.P. Singh, A. Lalke, "Cosmological study with hyperbolic solution in modified f (Q, T) gravity theory.", Indian J. Phys.,**96**, 4361, (2022). DOI:10.1007/s12648-022-02341-z

[45] A. Singh, "Qualitative study of Lyra cosmologies with spatial curvature.", Chin. J. Phys., **79**, 481, (2022). DOI:10.1016/j.cjph.2022.09.009

[46] B. Santos, J. C. Carvalho, J. S. Alcaniz, "Current constraints on the epoch of cosmic acceleration.", Astroparti. Phys., **35**, 17, (2011). DOI:10.1016/j.astropartphys.2011.04.002

[47] A. Singh, "Homogeneous and anisotropy cosmologies affine EoS; a dynamical system perspectiveâ Eur. Phys. J. C., **83**, 8, 896 (2023) DOI:10.1140/epoc/5100052-023-11879-2

[48] D. Brout, et al., Astrophys. J. 938 (2022) 110, http://dx.doi.org/10.3847/1538 4357/ac8e04.

[49] D. Scolnic, et al., Astrophys. J. 938 (2022) 113, http://dx.doi.org/10.3847/ 1538-4357/ac8b7a.

[50] H. Akaike, "A new look at the statistical model identification.", IEEE, Trans. Autom. Control, **19**, 6, 716, (2003). DOI:10.1109/TAC.1974.1100705

[51] K. Karami, J. Fehri. "Holographic dark energy in a non-flat universe with Granda-Oliveros cut-off." International Journal of Theoretical Physics **49**,5, 1118,(2010). DOI:10.1007/s10773-010-0291-8

[52] S. D. Hsu, "Entropy bounds and dark energy", Phys. Lett. B **594**, 1 (2004). DOI:10.1016/j.physletb.2004.05.020

[53] I. Durán, D. Pavón, "Model of interacting holographic dark energy at the Ricci scale", Physical Review DâParticles, Fields, Gravitation, and Cosmology **83**, 023504 (2011). DOI:10.1103/PhysRevD.83.023504

[54] L. P. Chimento, M. G. Richarte, "Interacting dark matter and modified holographic Ricci dark energy induce a relaxed Chaplygin gas", Phys. Rev. D **84**, 123507 (2011). DOI:10.1103/PhysRevD.84.123507

[55] N. Komatsu, "Cosmological model from the holographic equipartition law with a modified Rényi entropy", Eur. Phys. J. C **77**, 229 (2017). DOI:10.1140/epjc/s10052-017-4790-6

[56] H. Moradpour, A. Bonilla, E. M. C. Abreu, J. A. Neto, "Accelerated cosmos in a nonextensive setup", Phys. Rev. D **96**, 123504 (2017). DOI:10.1103/PhysRevD.96.123504

[57] A. Singh, "Dynamical systems of modified GaussâBonnet gravity: cosmological implications."

Eur. Phys. J. C, **85**, 24, (2025). DOI:10.1140/epjc/s10052-024-13732-3

International Conference on Astroparticle Physics, Gravitation and Cosmology (APGC-2025)
26-28 June 2025, GLA University, Mathura, India

Thermodynamic Properties and Stability of a New Class of Regular Black Holes

Aradhya Shukla[1,*] and Bhupendra Singh[2,†]

[1]*Department of Physics, Institute of Applied Sciences and Humanities, GLA University, Mathura 281406, Uttar Pradesh, India*

[2]*Department of Physics, Atma Ram Sanatan Dharma College, University of Delhi, Delhi, India.*

Abstract

A new class of exact, regular black hole solutions characterized by two parameters: the mass M and a positive deviation parameter $k > 0$ has been obtained. These solutions reduce to the Schwarzschild black hole in the limit $k > 0$, thereby smoothly interpolating between the modified and classical cases. Unlike the Schwarzschild black hole, which possesses a single event horizon, the solutions discussed here exhibit two horizons, reflecting richer causal structure. The thermodynamic properties of the black hole are modified due to the presence of an exponential factor in the mass function. In particular, we analyze the local thermodynamic stability of the black hole through the heat capacity at the outer horizon, C_+. he black hole is found to be thermodynamically stable when $C_+ > 0$ and unstable when $C_+ < 0$.

*Electronic address: ashukla038@gmail.com

†Electronic address: rajbhupendra81@gmail.com

I. INTRODUCTION

The concept of regular black holes, which possess event horizons but are free from central curvature singularities, has attracted significant interest as a possible resolution to the singularity problem in general relativity. The first model of a regular black hole was proposed by Bardeen [1], motivated by the early insights of Sakharov [2] and Gand Gliner [3]. who suggested that quantum effects or a vacuum-like equation of state might prevent the formation of singularities at the core of collapsing matter. Unlike the standard Schwarzschild or Reissner–Nordström black holes, which are geodesically incomplete due to central singularities, regular black holes are geodesically complete and often exhibit a de Sitter-like core at the origin.

Bardeen's model initially lacked an underlying physical mechanism; however, it was later reinterpreted by Ayón-Beato and García [4–6] as an exact solution to the Einstein equations coupled to non-linear electrodynamics (NED). This approach provided a self-consistent theoretical framework for constructing regular black hole spacetimes by modifying the matter sector. Their pioneering work reopened a line of inquiry into the interplay between classical gravity and non-linear fields, leading to a large body of literature focused on generalizing and extending Bardeen-type solutions.

Since then, numerous regular black hole solutions have been developed based on similar principles, many of which maintain the Bardeen-like structure while introducing different types of non-linear sources[7–17]. hese include magnetically and electrically charged configurations, anisotropic fluids, and even effective geometries inspired by quantum corrections. Such models have proven useful not only in addressing the singularity problem but also in studying black hole thermodynamics, horizon structure, and evaporation dynamics under modified conditions. The idea of regular black holes has also been extended to higher-curvature theories of gravity, particularly in the context of Einstein–Gauss–Bonnet (EGB) gravity[18–22], which arises naturally as a low-energy limit of string theory. In four-dimensional EGB gravity, made well-defined through dimensional regularization or other reformulations [44–46], new classes of regular black hole solutions have been reported [37–43]. Similarly, the framework has been adapted within massive gravity theories [], offering further avenues to modify the infrared behavior of gravitational interactions and avoid singularities.

Beyond static and spherically symmetric cases, efforts have been made to construct rotating regular black holes. The Newman–Janis algorithm (NJA) has played a crucial role in generating rotating counterparts from static seed metrics[23, 24] and This method, although originally developed for Kerr-like spacetimes, has been widely applied to regular black holes to obtain rotating extensions. More sophisticated techniques and further families of rotating regular black holes have been presented in recent works [25–28] , some of which explore astrophysically realistic configurations and address observational signatures such as gravitational lensing and shadow properties. The ongoing development of regular black hole models across various gravitational theories continues to provide valuable insights into the nature of spacetime under extreme conditions, bridging classical and quantum gravity. These solutions not only offer a potential resolution to the long-standing singularity problem but also serve as fertile ground for testing the robustness of black hole thermodynamics, quantum field theory in curved spacetime, and holographic principles in modified gravity contexts.

II. REGULAR BLACK HOLE: A NEW CLASS OF SOLUTION

We investigate a novel family of singularity-free black hole solutions to Einstein's field equations that generalize the Schwarzschild metric while incorporating quantum-gravitational inspired regularization effects through two key parameters: a deviation parameter k that controls the departure from classical black hole geometry and an exponent b that determines the asymptotic behavior of the metric correction. The spacetime geometry is described by a static, spherically symmetric metric of the form

$$ds^2 = -f(r)dt^2 + \frac{1}{f(r)}dr^2 + r^2 d\Omega^2, \tag{1}$$

with

$$f(r) = 1 - \frac{2M}{r}\left(\frac{2}{1+e^{k/r}}\right)^b, \tag{2}$$

where, the metric function $d\Omega^2 = d\theta^2 + sin^2\theta\, d\phi^2$ is the metric element of the $2D$ sphere, introduces a smooth, exponentially decaying modification to the Schwarzschild potential that becomes significant at small radii while preserving asymptotic flatness. The solution's behavior is governed by three parameters: the ADM mass M setting the large-scale gravitational field, the length scale k determining where quantum-gravity effects become dominant, and the dimensionless exponent b influencing how rapidly the solution approaches its clas-

sical limit. In the limit where $k \to 0$ with $b = 1$, we recover exactly the Schwarzschild solution, while for finite $k > 0$ the exponential correction term acts to smear out the central singularity, producing a regular de Sitter-like core with finite curvature invariants at $r = 0$. The event horizon of the largest root of the of the $f(r)$, and the zeros of $f(r_+)$=0. The variation of $f(r)$ w.r.t horizon radius r is depicted in Fig 1. In Fig. 1, one can see clearly that for values of the deviation parameter below a critical threshold $k < k_c$(where $k_c \approx 1.119M$ represents a phase transition point in the solution space), the spacetime possesses both an outer event horizon and an inner Cauchy horizon analogous to the Reissner-Nordstrom solution; when k precisely equals k_c these horizons merge into a single extremal horizon indicating the minimum mass configuration where a black hole can form; while for supercritical values $k > k_c$ the horizon disappears entirely leaving behind what may be interpreted as a self-gravitating, non-singular gravitational condensate or dark matter remnant.

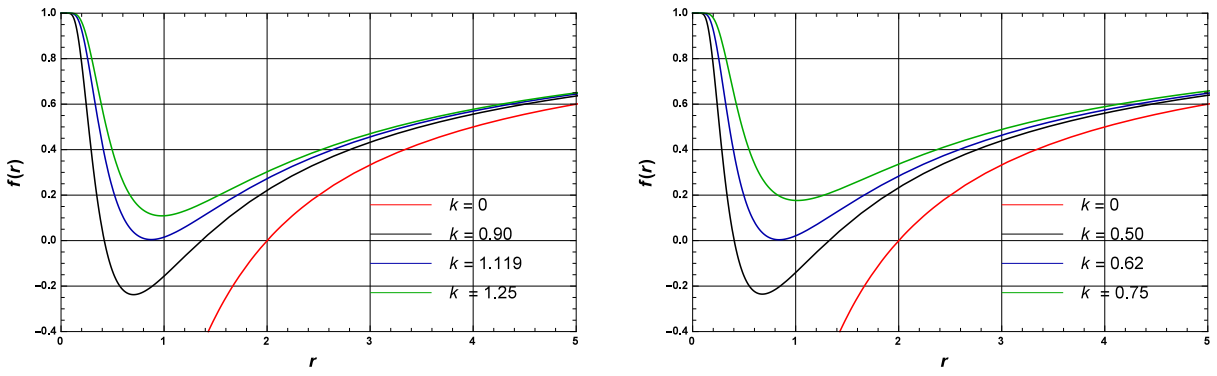

FIG. 1: The plot of $f(r)$ vs radius with the different value of deviation parameter k with fixed value of mass $M = 1$ for $b = 1$ (left) and $b = 2$ (right).

The dependence of the horizon radius r_+ on the parameters reveals that increasing either k or b leads to a systematic reduction in horizon size, with the black hole phase eventually giving way to a horizonless object when the quantum-gravitational correction becomes sufficiently strong. Furthermore, the existence of a critical parameter value k_c separating black holes from horizonless objects suggests a possible thermodynamic phase transition in the final stages of black hole evaporation, while the horizonless configurations for $k > k_c$ may serve as candidate models for ultra-compact dark matter halos or other exotic compact objects that could be detectable through gravitational wave signatures.

III. ENERGY CONDITION AND STABILITY CHECK

Now, we also study the energy conditions for the regular black hole (3).The weak energy condition states that $T_{ab}t^at^b \geq 0$ for all timelike vectors t^a, i.e., the local energy density cannot be negative. The dominent energy condition (DEC) states that $T_{ab}t^at^b \geq 0$ and that $T^{ab}t_b$ must be spacelike, for any timelike vector t^a, Hence, the weak energy condition requires $\rho \geq 0$ and $\rho + P_i \geq 0$,

$$\rho + P_2 = \rho + P_3 = \frac{Mbk^2(be^{\frac{k}{r}} - 1)e^{\frac{k}{r}}}{r^5(1 + e^{\frac{k}{r}})^{b+2}} \tag{3}$$

The energy momentum tensor obeys the inequality $T_{ab}t^at^b \geq 0$ for any timelike vector,i.e $\rho \geq 0$ and $\rho + P_i \geq 0$. Thus the black hole satisfies the weak energy condition, when the parameter b is swithched off.

The black hole mass is obtained by $f(r_+) = 0$ in terms of horizon radius r_+ as

$$M_+ = \frac{r(1 + e^{\frac{k}{r}})^b}{2} \tag{4}$$

Eq.(8) reduce to the Schwarzschild black hole mass $M_+ = 2r_+$,when $k = 0$. The temperature

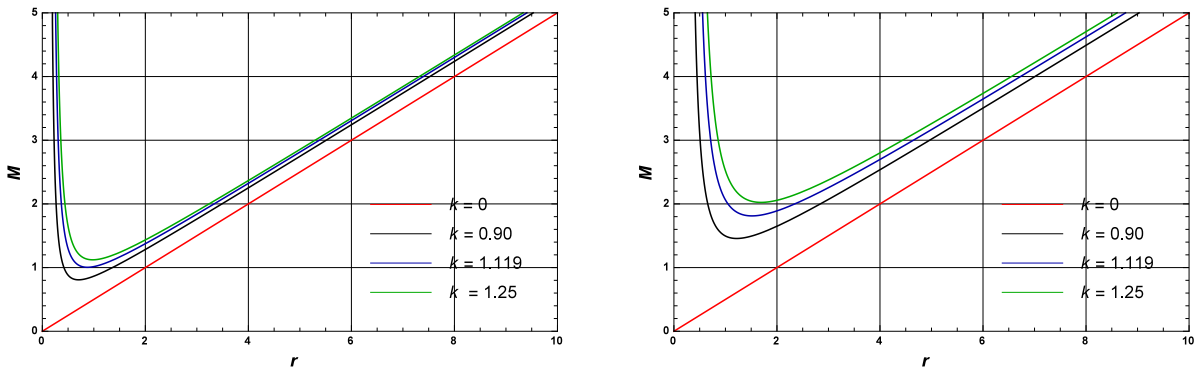

FIG. 2: The plot of mass vs horizon radius r_+ with the different value of deviation parameter a for fixed value of mass $M = 1$ for $b = 1$ (left) and $b = 2$ (right).

of the black hole is known as Hawking temperature associted with the surface gravity κ, $T = \kappa/2\pi$ The temperature of the black hole is calculated as

$$T_+ = \frac{f'(r_+)}{4\pi} = \frac{1}{4\pi r_+}\left(2 - \frac{ke^{\frac{k}{r}}}{r(1 + e^{\frac{k}{r}})}\right) \tag{5}$$

Note that the factor k modifies the temperature of the general relativity Schwarzschild black

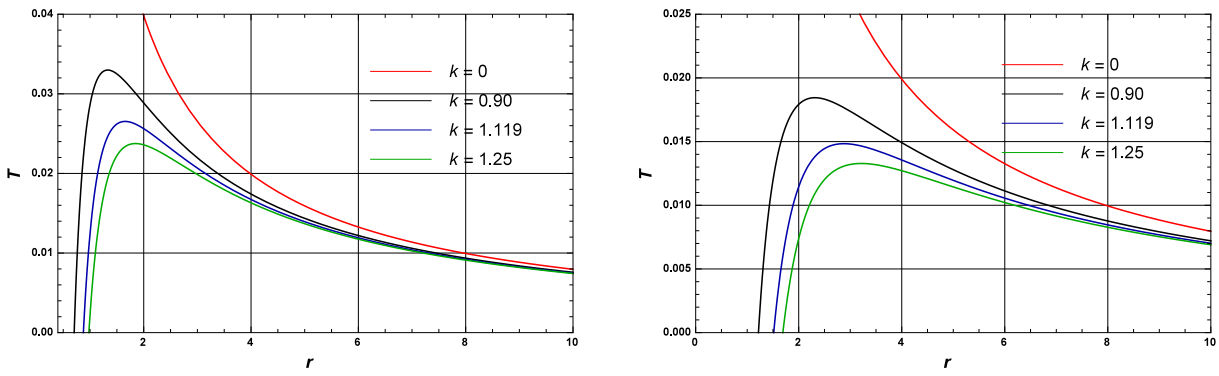

FIG. 3: The plot of temperature vs horizon radius r_+ with the different value of deviation parameter a for fixed value of mass $M = 1$ for $b = 1$ (left) and $b = 2$ (right).

hole.When the temperature vanishes the two horizones coincide,and also the temperature has a peak. The peak of the temperature increases with decreases the deviation parameter k and the temperature diverges in the absence of deviation parameter. The temperature (5) reduces to temperature of Schwarzschild black hole when $k = 0$.

$$T_+ = \frac{1}{4\pi r_+} \tag{6}$$

Next we study the stability of the black hole which is performed by studying the behaviour of its heat capacity (C_+), when $C_+ > 0$ it is stable and $C_+ < 0$ it is called unstable. The heat capacity of a black hole is defined as [53]

$$C_+ = \frac{\partial M_+}{\partial T_+} = \Big(\frac{\partial M_+}{\partial r_+}\Big)\Big(\frac{\partial r_+}{\partial T_+}\Big) \tag{7}$$

substituting (4)and (5) into (7), the heat capacity of the regular hole is

$$C_+ = \frac{(4\pi r^3)(1+e^{\frac{k}{r}})^{1+b}(bke^{\frac{k}{r}} - 2kr + 4r^2)}{(k^2+2kr-4r^2)e^{\frac{k}{r}} - 2e^{\frac{2k}{r}} - 2r^3} \tag{8}$$

In the limit $k = 0$ corresponds to the heat capacity of the Schwarzschild black hole observed two kinds of behaviour: first is the positive heat capacity $r_+ > r_c$ suggesting the thermodynamics stability of black hole and other is negative heat capacity suggests the instability of black hole.The heat capacity is discontinuous at r_+=r_c the second order phase transition occurs. Interestingly, the discontinuity of the heat capacity occurs at the value where the Hawking temperature reached maximum value, but also the heat capacity blows up. Hence phase transition occurs from the lower to higher mass corresponding to positive to heat capacity of a black hole.

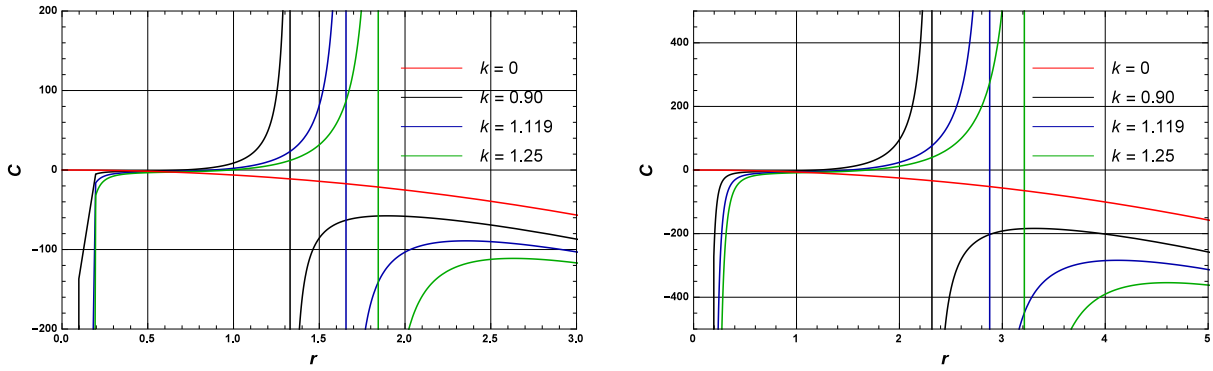

FIG. 4: The plot of heat capacity vs. horizon radius r_+ with the different value of deviation parameter a for fixed value of mass $M = 1$ for $b = 1$ (left) and $b = 2$ (right).

IV. CONLUSION

We derive an exact black hole solution that generalizes the classical Schwarzschild metric through the inclusion of an exponential correction term of the form $e^{-k/r}$, where k is a deformation parameter. This correction emerges naturally from quantum considerations and can be interpreted as a probabilistic weighting factor, potentially linked to quantum gravitational effects at short distances. The metric reduces to the standard Schwarzschild solution in the classical limit when $k = 0$, thus preserving consistency with general relativity in the appropriate regime. A key feature of this modified solution is the presence of two distinct horizons. This result is totally different from the Schwarzschild geometry, which admits only a single event horizon. The existence of multiple horizons is indicative of richer causal and thermodynamic structures, often associated with quantum-corrected or regular black hole models.

We further investigate the thermodynamic properties of the black hole, focusing on quantities such as ADM mass, Hawking temperature, and specific heat capacity . Our results reveals that the heat capacity diverges at the point where Hawking temperature reaches its maximum, suggesting the occurrence of a second-order phase transition. This behavior is consistent with thermodynamic stability analysis in quantum gravity-inspired black hole models and provides deeper insight into the microphysical processes governing black hole

evolution.

---

[1] J. Bardeen, in *Proceedings of GR5* (Tiflis, U.S.S.R., 1968).

[2] A.D. Sakharov, Sov. Phys. JETP, **22**, 241 (1966).

[3] E.B. Gliner, Sov. Phys. JETP, **22**, 378 (1966).

[4] E. Ayon-Beato and A. Garcia, Gen. Rel. Grav. **31**, 629 (1999).

[5] E. Ayon-Beato and A. Garcia, Gen. Rel. Grav.**37**, 635 (2005).

[6] E. Ayon-Beato, A. Garcia, Phys. Lett. B **493**, 149 (2000).

[7] S. Ansoldi, arXiv:0802.0330 [gr-qc].

[8] K.A. Bronnikov, Phys. Rev. D **63**, 044005 (2001)

[9] O.B. Zaslavskii, Phys. Rev. D **80**, 064034 (2009)

[10] J.P.S. Lemos and V.T. Zanchin, Phys. Rev. D **83**, 124005 (2011) .

[11] H. Culetu, arXiv:1408.3334v1 [gr-qc].

[12] L. Balart and E. C. Vagenas, Phys. Lett. B **730**, 14 (2014)

[13] L. Balart and E. C. Vagenas, Phys. Rev. D **90**, no. 12, 124045 (2014).

[14] L. Xiang, Y. Ling and Y. G. Shen, Int. J. Mod. Phys. D **22**, 1342016 (2013).

[15] D. V. Singh and N. K. Singh, Annals Phys. **383**, 600 (2017).

[16] D. V. Singh, M. S. Ali and S. G. Ghosh, arXiv:1707.07445 [gr-qc].

[17] S. Fernando, " Int. Journal of Mod. Phys. D **26**, 1750071 (2017).

[18] A. Kumar, D. V. Singh, Y. Myrzakulov, G. Yergaliyeva and S. Upadhyay, Eur. Phys. J. Plus **138** (2023) no.12, 1071.

[19] P. Paul, S. Upadhyay and D. V. Singh, Eur. Phys. J. Plus **138** (2023) no.6, 566.

[20] B. Singh, B. K. Singh and D. V. Singh, Int. J. Geom. Meth. Mod. Phys. **20** (2023) no.08, 2350125.

[21] Y. Myrzakulov, K. Myrzakulov, S. Upadhyay and D. V. Singh, Int. J. Geom. Meth. Mod. Phys. **20** (2023) no.07, 2350121.

[22] D. V. Singh, V. K. Bhardwaj and S. Upadhyay, Eur. Phys. J. Plus **137** (2022) no.8, 969.

[23] C. Bambi and L. Modesto, Phys. Lett. B **721**, 329 (2013).

[24] S. G. Ghosh, Eur. Phys. J. C **75**, 532 (2015).

[25] B. Toshmatov, B. Ahmedov, A. Abdujabbarov and Z. Stuchlik, Phys. Rev. D **89**, 104017

(2014).

[26] S. G. Ghosh and S. D. Maharaj, Eur. Phys. J. C **75**, no. 1, 7 (2015).

[27] J. C. S. Neves and A. Saa, Phys. Lett. B **734**, 44 (2014).

[28] F. Ahmed, D. V. Singh and S. G. Ghosh, [arXiv:2002.12031 [gr-qc]].

[29] D.G. Boulware and S. Deser, Phys. Rev. Lett. **55**, 2656 (1985).

[30] R. G. Cai, Y. P. Hu, Q. Y. Pan and Y. L. Zhang, Phys. Rev. D **91** (2015) no.2, 024032.

[31] R.C. Myers and J.Z. Simon, Phys. Rev. D **38**, 2434 (1988).

[32] S. H. Hendi, N. Riazi, S. Panahiyan and B. Eslam Panah, arXiv:1710.01818 [gr-qc].

[33] S. Panahiyan, S. H. Hendi and N. Riazi, arXiv:1802.00309 [gr-qc].

[34] K. Z. Amin, N. ul Islam, D. V. Singh and P. A. Ganai, Int. J. Mod. Phys. A **40** (2025) no.19, 2550057.

[35] V. K. Srivastava, S. Upadhyay, A. K. Verma, D. V. Singh, Y. Myrzakulov and K. Myrzakulov, Phys. Dark Univ. **48** (2025), 101915.

[36] B. Pourhassan, H. Farahani, F. Kazemian, İ. Sakallı, S. Upadhyay and D. V. Singh, Phys. Dark Univ. **44** (2024), 101444.

[37] A. Kumar, D. V. Singh and S. Upadhyay, JHAP **4** (2024) no.4, 85-99.

[38] A. Kumar, D. V. Singh and S. Upadhyay, Int. J. Mod. Phys. A **39** (2024) no.31, 2450136.

[39] H. K. Sudhanshu, D. V. Singh, S. Upadhyay, Y. Myrzakulov and K. Myrzakulov, Phys. Dark Univ. **46** (2024), 101648.

[40] B. Singh, D. Veer Singh and B. Kumar Singh, Phys. Scripta **99** (2024) no.2, 025305.

[41] P. Paul, S. Upadhyay, Y. Myrzakulov, D. V. Singh and K. Myrzakulov, Nucl. Phys. B **993** (2023), 116259.

[42] D. V. Singh, A. Shukla and S. Upadhyay, Annals Phys. **447** (2022), 169157.

[43] D. V. Singh, S. G. Ghosh and S. D. Maharaj, Nucl. Phys. B **981** (2022), 115854.

[44] C. S. Varsha, V. Venkatesha, N. S. Kavya and D. V. Singh, Annals Phys. **477** (2025), 170002.

[45] B. Pourhassan, M. Dehghani, S. Upadhyay, I. Sakalli and D. V. Singh, Mod. Phys. Lett. A **37** (2022) no.33n34, 2250230.

[46] S. Upadhyay and D. V. Singh, Eur. Phys. J. Plus **137** (2022) no.3, 383.

[47] B. K. Vishvakarma, D. V. Singh and S. Siwach, Phys. Scripta **99** (2024) no.2, 025022.

[48] B. K. Vishvakarma, D. V. Singh and S. Siwach, Eur. Phys. J. Plus **138** (2023) no.6, 536.

[49] D. V. Singh, S. Upadhyay, Y. Myrzakulov, K. Myrzakulov, B. Singh and M. Kumar, Nucl.

Phys. B **1016** (2025), 116915.

[50] H. K. Sudhanshu, S. Upadhyay, D. Veer Singh, Y. Myrzakulov and K. Myrzakulov, Mod. Phys. Lett. A **38** (2023) no.34n35, 2350153

[51] H. K. Sudhanshu, D. V. Singh, S. Bekov, K. Myrzakulov and S. Upadhyay, Int. J. Mod. Phys. A **38** (2023) no.29n30, 2350165.

[52] H. K. Sudhanshu, S. Upadhyay, D. V. Singh and S. Kumar, Int. J. Theor. Phys. **61** (2022) no.10, 248.

[53] P. Chaturvedi, N. K. Singh and D. V. Singh, Int. J. Mod. Phys. D **26** (2017) no.08, 1750082.

International Conference on Astroparticle Physics, Gravitation and Cosmology (APGC-2025)
26-28 June 2025, GLA University, Mathura, India

Coupled Dark Energy: A Diagnostic Study Beyond ΛCDM

Sahit Kumar[†] and S. D. Pathak[§]
Department of Physics,
Lovely Professional University, Phagwara, 144411, Punjab, India.

Abstract

Dynamic scalar field models—such as quintessence, phantom, K-essence, tachyon, Chaplygin gas, and unparticles—provide alternatives to the cosmological constant by allowing evolving equations of state. This study explores interacting dark energy within the coupled ϕCDM framework using the $O_m(z)$ diagnostic and the evolution of $h^2(z)$. Results indicate that interaction significantly alters cosmic expansion: moderate coupling ($\alpha = 0.2$) increases matter density at high redshift, while strong coupling ($\alpha = 0.89$) suppresses expansion due to energy transfer from dark energy to dark matter. These deviations from ΛCDM underscore the value of diagnostic tools in examining dark sector dynamics and highlight the need for continued theoretical and observational efforts.

Keywords: Quintessence, tachyon, scalar field potential, and Phantom field.

1 Introduction

Over the past few decades, cosmological observations have significantly reshaped our understanding of the universe's evolution. A significant breakthrough in modern cosmology emerged in the late 1990s when observations of Type Ia supernovae provided the first evidence that the universe's rate of expansion is not slowing down, but rather increasing over time [1, 2]. This remarkable observation indicated the presence of an unknown form of energy, generally known as dark energy (DE), which is estimated to account for approximately 70% of the Universe's total energy budget [3–15]. Further confirmation of DE's role in the universe has been provided by various observational probes, such as temperature fluctuations in the CMB, distribution patterns of matter on cosmic scales, and signatures of sound waves imprinted in the early universe, known as baryon acoustic oscillations. Although DE accounts for a significant fraction of the Universe's overall energy distribution, its fundamental nature remains one of the deepest and most unresolved puzzles in contemporary physics. The standard cosmological model, ΛCDM, attributes DE to a cosmological constant (Λ), which represents vacuum energy with a constant equation of state $w = -1$. Nevertheless, this interpretation encounters major theoretical difficulties, especially related to the fine-tuning issue and the coincidence problem. The vast difference of more than 100 orders of magnitude between the observational estimate of Λ and its theoretical prediction from quantum field theory presents one of the greatest challenges in contemporary physics, commonly referred to as the cosmological constant problem. Furthermore, the question of why DE has only begun to dominate cosmic evolution in the present epoch remains an open challenge.

Given these unresolved issues, alternative models of DE [16–35] have been proposed to explore scenarios beyond the cosmological constant. These models broadly fall into categories such as dynamical scalar field theories, modifications to gravity, and exotic energy components. Among scalar field models, quintessence represents a dynamically evolving field that can vary over cosmic time, unlike the fixed energy density of Λ. Some alternative approaches involve phantom fields [36–40, 42, 43], which are defined by the EoS parameter satisfying $w < -1$, potentially driving the universe towards a catastrophic future singularity often referred to as the Big Rip. Another class includes k-essence models, where the dynamics of the field are controlled by a non-standard kinetic term. In addition to scalar field models, several modifications to Einstein's general relativity have been investigated in an attempt to account for the observed cosmic acceleration. Theories such as $f(R)$ gravity [44–49] introduce modifications to the Ricci scalar in Einstein's field equations, allowing for self-accelerating solutions without requiring a DE component. Similarly, extra-dimensional theories, including braneworld cosmologies [50, 63], propose that our observable universe exists within a higher-dimensional space, affecting cosmic expansion through gravitational leakage into extra dimensions. Another intriguing avenue of research involves more exotic energy components that deviate from standard particle physics predictions. One such proposal is unparticle physics, introduced by Howard Georgi, which suggests the existence of a scale-invariant sector that does not conform to conventional particle descriptions. Unparticles exhibit continuous mass spectra and could serve as a viable candidate for DE, as they naturally allow for evolving equations of state while avoiding fine-tuning problems associated with fundamental scalar fields [52, 53].

This article aims to provide a comprehensive analysis of alternative DE models, examining their theoretical motivations, observational implications, and potential to address the shortcomings of the cosmological constant paradigm. By critically evaluating different approaches, including scalar field models, modified gravity theories, and unconventional energy components, we seek to understand whether any of these frameworks offer a more natural explanation for cosmic acceleration. As future observational data from large-scale surveys and next-generation CMB experiments become available, distinguishing between competing DE models will be crucial for advancing our understanding of the universe's late-time dynamics.

[*] sahitsharmasharma649@gmail.com
[†] ORCiD: 0000-0003-4232-0873
[‡] shankar.23439@lpu.co.in
[§] ORCiD: 0000-0001-9689-7577

2 Scalar Field DE Models

2.1 Quintessence

Scalar fields hold significant importance in particle physics and appear in several theoretical frameworks, including those based on string theory concepts and supergravity models. The concept of quintessence corresponds to a standard scalar field, represented by ϕ, characterized by a self-interacting potential $V(\phi)$, and its interaction with other cosmic components occurs solely through gravitational effects. The action corresponding to the quintessence model takes the form:

$$S = \int d^4x\sqrt{-g}\left[\frac{1}{2\kappa^2}R + \mathscr{L}\phi + S_M\right], \tag{1}$$

here, $\kappa^2 = 8\pi G$, and R denotes the Ricci scalar curvature. The Lagrangian for the scalar field is [32,54]:

$$\mathscr{L}\phi = -\frac{1}{2}g^{\mu\nu}\partial_\mu\phi\partial_\nu\phi - V(\phi), \tag{2}$$

and S_M represents the action associated with matter.

2.2 Equations of Motion

Consider a perfect fluid characterized by its density of energy, denoted by ρ_m, and pressure, represented as p_m. The ratio of these quantities defines the EoS parameter $w_M = p_M/\rho_M$. The time evolution of such a fluid follows the continuity equation:

$$\dot{\rho}_M + 3H(\rho_m + p_m) = 0. \tag{3}$$

The notation m in the subscript is employed to indicate a general perfect fluid, which may include both relativistic and non-relativistic components.

The mathematical expression for the energy-momentum tensor corresponding to the quintessence field is given by:

$$T^{ik} = \frac{\partial\mathscr{L}}{\partial(\partial_i\phi)}\partial^k\phi - g^{ik}\mathscr{L}. \tag{4}$$

Using the Lagrangian (2) within equation (4), the T_{00} and T_{11} components, corresponding to the energy density and pressure of a spatially homogeneous scalar field, are obtained as follows:

$$\rho_\phi = \frac{1}{2}\dot{\phi}^2 + V(\phi), \quad p_\phi = \frac{1}{2}\dot{\phi}^2 - V(\phi). \tag{5}$$

The EoS parameter is given by:

$$w_\phi = \frac{p_\phi}{\rho_\phi} = \frac{\dot{\phi}^2 - 2V(\phi)}{\dot{\phi}^2 + 2V(\phi)}. \tag{6}$$

2.3 Cosmic Evolution

For a universe with zero spatial curvature ($k = 0$), the set of equations describing its dynamical behaviour can be expressed as

$$H^2 = \frac{\kappa^2}{3}\left(\frac{1}{2}\dot{\phi}^2 + V(\phi) + \rho_m\right), \tag{7}$$

$$\dot{H} = -\frac{\kappa^2}{2}(\dot{\phi}^2 + \rho_m + p_m). \tag{8}$$

The evolution equation for the quintessence field can be derived by applying the variational principle to the action [33,34]:

$$\ddot{\phi} + 3H\dot{\phi} + V_{,\phi} = 0, \tag{9}$$

where $V_{,\phi}$ represents the rate of change of the potential V concerning the scalar field ϕ, i.e.,
$V_{,\phi} = \frac{dV}{d\phi}$

2.4 Quintessence Potentials

Quintessence potentials fall into two primary categories:

2.5 Freezing Models

The field initially rolls down the potential but slows as cosmic acceleration begins. Examples include:

$$V(\phi) = M^{4+n}\phi^{-n}, \quad (n > 0), \tag{10}$$

$$V(\phi) = M^{4+n}\phi^{-n}e^{\alpha\phi^2/m_{\rm pl}^2}. \tag{11}$$

The first allows indefinite rolling, appearing in models like fermion condensates. The second, motivated by supergravity, has a stable minimum where $w_\phi = -1$.

2.6 Thawing Models

Owing to the effect of Hubble damping, the scalar field stays nearly constant during the early stages of the universe and begins to evolve only when the Hubble parameter H drops below the field mass m_ϕ. Some typical choices of potentials are:

$$V(\phi) = V_0 + M^{4-n}\phi^n, \quad (n > 0), \tag{12}$$

$$V(\phi) = M^4 \cos^2(\phi/f). \tag{13}$$

The first resembles chaotic inflation, while the second, based on pseudo-Nambu–Goldstone bosons, allows the field to remain near its potential maximum until today.

3 k-Essence

In standard quintessence models, the late-time acceleration of the universe arises from the potential energy of a scalar field. Alternatively, another line of research investigates whether altering the kinetic term of the scalar field could be responsible for driving the accelerated expansion of the universe. This concept was originally introduced during the study of the early universe's rapid expansion phase, referred to as K-inflation, by Armendáriz-Picón and collaborators [55,56]. Later, Chiba [57] and others extended this concept to describe DE, leading to the formulation of K-essence [58,59].

K-essence models involve a scalar quantity whose dynamics are influenced by a non-canonical kinetic term. The general action describing the evolution of this field can be written as [60],

$$S = \int d^4x\sqrt{-g}\, p(\phi, X), \tag{14}$$

where $p(\phi, X)$ serves as the Lagrangian density and is the functional characteristics of the scalar field ϕ and the kinetic term $X \equiv -\frac{1}{2}(\nabla\phi)^2$. The framework of K-essence includes quintessence as a special case but is typically considered in a more generalized form, such as [57–59]

$$p(\phi, X) = f(\phi)\hat{p}(X). \tag{15}$$

One of the motivations for this Lagrangian structure comes from string theory, where effective field theories contain higher-order derivative corrections [55, 56]. In the low-energy limit, string theory introduces additional kinetic terms that lead naturally to non-canonical scalar dynamics. In string theory, the four-dimensional effective action generally involves the contribution of a scalar field known as the dilaton ϕ, which regulates the behavior of the string coupling parameter, expressed as $g_s^2 \sim e^{\phi}$. By applying a conformal transformation, the initial string-frame action is reformulated within the Einstein frame, resulting in an effective Lagrangian expressed as:

$$p(\phi, X) = X^2 L(\phi) + XK(\phi) \tag{16}$$

here, $K(\phi)$ and $L(\phi)$ are field-dependent functions derived from the original string-inspired action. By redefining the field appropriately, this action can be further rewritten in the form [57]

$$p(\phi, X) = f(\phi)(-X + X^2), \tag{17}$$

which explicitly demonstrates the non-canonical nature of K-essence models.

The expression for the energy density corresponding to this particular model can be written as:

$$\rho = 2X\frac{\partial p}{\partial X} - p = f(\phi)(-X + 3X^2). \tag{18}$$

Accordingly, the EoS parameter for the scalar field can be derived as:

$$w_\phi = \frac{p}{\rho} = \frac{1-X}{1-3X}. \tag{19}$$

In the scenario where the kinetic term remains constant, denoted by X, the corresponding EoS parameter does not vary. In particular, when $X = \frac{1}{2}$, the scalar field effectively behaves like a cosmological constant, yielding $w_\phi = -1$. In a more general context, the condition required for the universe to exhibit accelerated expansion is $w_\phi < -\frac{1}{3}$, which is achievable when $X < \frac{2}{3}$.

During the epochs dominated by radiation or matter, the evolution of energy density follows the continuity equation. For a background fluid described by the EoS parameter W_m the evolution of the scalar field's energy density follows the relation:

$$\dot{\rho} = -\frac{2(1+w_\phi)}{(1+w_m)(t-t_0)}\rho. \tag{20}$$

For constant X, the function $f(\phi)$ becomes:

$$f(\phi) \propto (\phi - \phi_0)^{-\alpha} \tag{21}$$

where, $\alpha = \frac{2(1+w_\phi)}{1+w_m}$. In particular, if $w_\phi = w_m$, this function scales as $f(\phi) \propto (\phi-\phi_0)^{-2}$, which corresponds to a class of scaling solutions. When $w_\phi = -1$, the function $f(\phi)$ becomes a constant, leading to a specific case known as the ghost condensate scenario.

It should be emphasized that the aforementioned findings are obtained by considering the condition where the scalar field's energy density remains negligible in comparison to the dominant background matter density. However, when DE starts

to dominate the cosmic dynamics, alternative solutions can emerge, enabling the universe to shift its expansion behaviour from a decelerating phase to an accelerating one.

Overall, K-essence models introduce a novel mechanism for cosmic acceleration by modifying the kinetic structure of the scalar field, offering an alternative to quintessence and potentially addressing the coincidence problem. Several extensions and modifications of these models have been analyzedin the literature, emphasizing their suitability in accounting for the universe's rapid expansion observed in later epochs.

4 Phantom Energy

Observations suggest that the EoS w lies around $w = -1$, with strong indications that it may be below this value [61, 62]. Conventional scalar field models generally satisfy $w \geq -1$. However, when $w < -1$, the corresponding DE component is classified as phantom (or ghost) DE. Several theoretical frameworks [63–65] can also give rise to such phantom energy.

A simple approach to modelling phantom DE involves introducing a scalar field, which is associated with a kinetic term carrying a negative sign [36]. These types of fields naturally emerge within the framework of theories involving extra spatial dimensions, for instance, in two-time physics associated with type IIA string theory [66, 67], or in the reformulation of F-theory at low energies, represented by a 12-dimensional type IIB action [67]. Historically, phantom-like fields appeared in Hoyle's steady-state cosmology, where a creation field (C-field) was introduced to maintain a homogeneous matter distribution in the expanding universe [68,69]. This idea was subsequently extended within the framework of the gravitational theory proposed by Hoyle and Narlikar, which offered a more sophisticated theoretical basis [70–72].

The action corresponding to a phantom scalar field that interacts minimally with gravity can be represented as:

$$S = \int d^4x\sqrt{-g}\left[\frac{1}{2}(\nabla\phi)^2 - V(\phi)\right], \tag{22}$$

Here, the kinetic term carries a negative sign in contrast to the standard scalar field. The respective expressions for the components of the energy-momentum tensor, specifically the energy density and pressure, can be written as,

$$\rho = -\frac{1}{2}\dot{\phi}^2 + V(\phi), \quad p = -\frac{1}{2}\dot{\phi}^2 - V(\phi). \tag{23}$$

This results in the EoS:

$$w_\phi = \frac{p}{\rho} = \frac{\dot{\phi}^2 + 2V(\phi)}{\dot{\phi}^2 - 2V(\phi)}. \tag{24}$$

For $\frac{1}{2}\dot{\phi}^2 < V(\phi)$, it follows that $w_\phi < -1$, confirming the phantom nature of the field.

An important outcome of a universe dominated by phantom energy is the occurrence of the so-called Big Rip singularity, in which the cosmic curvature increases without bound within a finite time interval. If the potential $V(\phi)$ has a maximum, the singularity can be ignored as [73]:

$$\frac{V(\phi)}{V_0} = -\left[1 - \cosh\left(\frac{\alpha\phi}{m_{\rm pl}}\right)\right], \tag{25}$$

In such cases, the field evolves toward the maxima of the potential and cross the opposite side and consequently undergoes damped oscillations around the maximum before settling into a de-Sitter-like phase with $w_\phi = -1$. This behavior has been observed in multiple models where the potential exhibits a maximum; while in above equation (25) α is a constant as provided in [40].

Despite its intriguing cosmological implications, the phantom field faces significant quantum-level challenges. A major issue associated with such models is the occurrence of significant ultraviolet (UV) instabilities, since the field's energy density does not possess a lower bound. This leads to vacuum instability, allowing spontaneous creation of ghost particles and normal energy states. Even when phantom fields are decoupled from ordinary matter, their interaction with gravitons can trigger vacuum decay processes such as [74]:

$$\text{vacuum} \rightarrow 2\ \text{ghosts} + 2\gamma. \tag{26}$$

Some studies [42] suggest that an unnatural violation of Lorentz invariance with a cutoff around the MeV scale may be necessary to suppress excessive cosmic gamma-ray production. As a result, the fundamental origin of phantom fields remains an open question, presenting a challenge for theoretical physics. Numerous studies have explored the cosmological implications of phantom energy, highlighting both its potential significance and unresolved theoretical issues.

5 Tachyon Field

In recent times, rolling tachyon condensates emerging from string theory have attracted significant interest due to their potential relevance in cosmology. Sen [75, 76] demonstrated that when D-branes undergo decay, the resulting configuration behaves like a pressureless fluid possessing a finite energy density, similar to that of classical dust [77–82]. The EoS parameter corresponding to the tachyon field varies gradually from -1 to 0 [83], which has motivated extensive research on its potential role as an inflaton during the early high-energy phases of the universe. [84–88]. However, tachyon-driven inflation in open string models often encounters difficulties [89], particularly in relation to density perturbations and the reheating process.

Apart from its significance in driving inflation, the tachyon field has also attracted considerable attention as a potential candidate for DE, depending on the form of its potential [54, 90–92]. Below, we analyze how the tachyon field can lead to viable DE models.

The effective action for a tachyon field on a non-BPS D3-brane is given by:

$$S = -\int d^4x V(\phi)\sqrt{-\det(g_{ab} + \partial_a\phi\partial_b\phi)}, \tag{27}$$

here, $V(\Phi)$represents the tachyonic potential corresponding to the scalar field. Within the framework of open string theory, a particular form of this potential has been proposed in [93]:

$$\frac{V(\phi)}{V_0} = \cosh^{-1}(\phi/\phi_0), \tag{28}$$

where
for the non-BPS D-brane in superstring theory

$$\phi_0 = \sqrt{2} \tag{29}$$

and for bosonic string theory

$$\phi_0 = 2 \tag{30}$$

As $\phi \to \infty$, the field reaches its ground/stable state. For another case, the potential associated with massive scalar field excitations on anti-D-branes [94–96], takes the form:

$$V(\phi) = V_0 e^{\frac{1}{2}m^2\phi^2}, \tag{31}$$

which has a minimum at $\phi = 0$.

The corresponding energy-momentum tensor obtained from the above action is given by:

$$T_{\mu\nu} = V(\phi)\frac{\partial_\mu\phi\partial_\nu\phi}{\sqrt{1+g^{\alpha\beta}\partial_\alpha\phi\partial_\beta\phi}} - g_{\mu\nu}V(\phi)\sqrt{1+g^{\alpha\beta}\partial_\alpha\phi\partial_\beta\phi}. \tag{32}$$

For a spatially homogeneous and isotropic FLRW universe, the energy density and pressure can be written as:

$$\rho = \frac{V(\phi)}{\sqrt{1-\dot{\phi}^2}}, \quad p = -V(\phi)\sqrt{1-\dot{\phi}^2}. \tag{33}$$

From the Friedmann equations:

$$H^2 = \frac{8\pi G}{3}V(\phi)\frac{1}{\sqrt{1-\dot{\phi}^2}}, \tag{34}$$

$$\frac{\ddot{\phi}}{1-\dot{\phi}^2} + 3H\dot{\phi} + \frac{1}{V}\frac{dV}{d\phi} = 0. \tag{35}$$

Combining these equations, we obtain:

$$\frac{\ddot{a}}{a} = \frac{8\pi G}{3}V(\phi)\frac{(1-\frac{3}{2}\dot{\phi}^2)}{\sqrt{1-\dot{\phi}^2}}, \tag{36}$$

$\dot{\phi}^2 < 2/3$ implies the cosmic acceleration and EoS parameter can be expressed as:

$$w_\phi = \frac{p}{\rho} = \dot{\phi}^2 - 1. \tag{37}$$

This implies that, regardless of the potential's steepness, the EoS remains between -1 and 0, leading to an energy density evolution of $\rho \propto a^{-m}$ with $0 \le m \le 3$.

To express the tachyon potential and field evolution in terms of H and $\dot{H}$, as done in quintessence models, we use:

$$\frac{H}{\dot{H}^2} = -\frac{3}{2}\dot{\phi}^2. \tag{38}$$

Combining this with the Friedmann equation, we obtain [90]:

$$V = \frac{3H^2}{8\pi G}\left(1+\frac{2\dot{H}}{3H^2}\right)^{1/2}, \tag{39}$$

$$\phi = \int dt\left(-\frac{2\dot{H}}{3H^2}\right)^{1/2}. \tag{40}$$

For a power-law expansion of the form $a \propto t^p$, the corresponding tachyon potential is:

$$V(\phi) = \frac{2p}{4\pi G}\left(1-\frac{2}{3p}\right)^{1/2}\phi^{-2}. \tag{41}$$

This inverse-square potential aligns with those found in scaling solutions [91]. Numerous studies have investigated the role of tachyons in cosmology, particularly in the context of inflation and late-time acceleration.

6 Chaplygin gas

Beyond scalar field approaches to DE, another intriguing model involves a fluid known as the Chaplygin gas [97]. This model exhibits properties that lead to cosmic acceleration at late times. The Chaplygin gas framework is characterized through the following EoS,

$$p = -\frac{A}{\rho}, \tag{42}$$

this equation bears similarity to the EoS of a tachyonic field, $p = -V^2(\phi)/\rho$, indicating that the Chaplygin gas may be viewed as a particular scenario of a tachyonic field possessing a constant potential.

6.1 Energy Density Evolution

Nambu–Goto type action can lead to EoS of Chaplygin gas, which describes the dynamics of a D-brane moving within a space having extra spatial dimensions. By solving the continuity equation, the evolution of the energy density is found to be [98]:

$$\rho = \sqrt{A + \frac{B}{a^6}}, \tag{43}$$

here, B appears as an integration constant. The asymptotic analysis of the solution highlights two distinct phases:

- In the initial stages of the Universe's evolution ($a \ll 1$), the energy density exhibits a behavior similar to that of non-relativistic matter, following $\rho \propto a^{-3}$.
- In the far future limit ($a \gg 1$), the energy density tends towards a constant value, $\rho \approx \sqrt{A}$, effectively imitating the role of a cosmological constant and leading to the late-time accelerated expansion of the Universe.

This transition makes the Chaplygin gas an intriguing candidate for unifying DM and DE.

7 Scalar Field Representation of Chaplygin Gas

The Chaplygin gas model can also be formulated in terms of a scalar field ϕ characterized by an associated potential function $V(\phi)$. Within this framework, the quantities representing energy density and pressure are determined through the conventional expressions:

$$\rho = \frac{1}{2}\dot{\phi}^2 + V(\phi), \quad p = \frac{1}{2}\dot{\phi}^2 - V(\phi). \tag{44}$$

Solving for $\dot{\phi}^2$ and $V(\phi)$, we obtain:

$$\dot{\phi}^2 = \frac{B}{a^6}\sqrt{A + \frac{B}{a^6}}, \tag{45}$$

$$V(\phi) = \frac{1}{2}\left(\sqrt{A + \frac{B}{a^6}} + \frac{A}{\sqrt{A + \frac{B}{a^6}}}\right). \tag{46}$$

Rewriting in terms of the field evolution, we express the relationship between ϕ and a as:

$$\kappa\sqrt{3}\frac{d\phi}{da} = \frac{\sqrt{B}}{a\sqrt{Aa^6 + B}}. \tag{47}$$

Upon integration, this leads to:

$$a^6 = \frac{4Be^{2\sqrt{3}\kappa\phi}}{A(1 - e^{2\sqrt{3}\kappa\phi})^2}. \tag{48}$$

Substituting into the potential expression gives:

$$V(\phi) = \frac{\sqrt{A}}{2}\left(\cosh(\sqrt{3}\kappa\phi) + \frac{1}{\cosh(\sqrt{3}\kappa\phi)}\right). \tag{49}$$

Hence, a scalar field, when minimally interacting with gravity and associated with this potential, can successfully mimic the evolution pattern of the Chaplygin gas.

7.1 Observational Constraints

Despite its theoretical appeal, the Chaplygin gas model faces significant observational challenges. Studies of CMB anisotropies reveal that perturbed Chaplygin gas behave similarly to CDM fluctuations at early epoch but are strongly suppressed during the acceleration phase. This suppression produces a significant (ISW) effect, reducing power in the CMB spectrum.

To address these issues, a generalized Chaplygin gas model was introduced with the EoS:

$$p = -\frac{A}{\rho^\alpha}, \quad 0 < \alpha < 1. \tag{50}$$

However, even this extension remains under stringent observational constraints, with the parameter bound as $0 \leq \alpha < 0.2$ at the 95% confidence level. Ongoing investigations aim to examine whether possible modifications of the model could enhance its consistency with the available observational evidence.

The Chaplygin gas model offers a fascinating approach towards describing both DM and DE simultaneously through a unified theoretical framework. Its ability to shift from a dust-like phase to a cosmological constant-like phase makes it an attractive model. However, its difficulties in reproducing large-scale structure observations and CMB anisotropies pose serious challenges. While the generalized Chaplygin gas mitigates some of these issues, observational constraints remain tight, necessitating further investigations into its viability as a DE model.

8 Unparticle DE

The concept of unparticles, introduced by Georgi [53], extends the standard field-theoretic description of particles by incorporating a scale-invariant sector with non-integral scaling dimensions. Unlike conventional particles, which have well-defined masses, unparticles exhibit a continuous mass spectrum and can interact with standard model fields via suppressed couplings. This intriguing property has led to the exploration of unparticles in various cosmological contexts, including their potential role in explaining DE.

Dai, Dutta, and Stojkovic [52] proposed an unparticle-based DE model where a scalar unparticle field, denoted by ϕ, plays the role of quintessence. The dynamics of the unparticle field are controlled by a conventional kinetic component along with a basic mass potential, which can be expressed as:

$$\mathscr{L} = \frac{1}{2}(\partial_\mu \phi)(\partial^\mu \phi) - V(\phi), \tag{51}$$

where the effective potential takes the form:

$$V(\phi) = B\sqrt{\rho_u}\phi^2. \tag{52}$$

Here, B is a parameter dependent on the unparticle scaling dimension d_u, and ρ_u represents the energy density of the unparticle field. The mass of the unparticle field is derived by integrating over its continuous mass distribution:

$$M^2 = \frac{(d_u - 1)}{d_u}\Lambda_u^2. \tag{53}$$

As the field evolves over time, the corresponding expressions describing its energy density and pressure take the form:

$$\rho_u = \frac{1}{2}\dot{\phi}^2 + B\sqrt{\rho_u}\phi^2, \tag{54}$$

$$P_u = \frac{1}{2}\dot{\phi}^2 - B\sqrt{\rho_u}\phi^2. \tag{55}$$

The EoS parameter for unparticle DE, defined as $w = P_u/\rho_u$, evolves over time and is determined by the parameters B, d_u, and the initial field value ϕ_i. Numerical analyses show that w starts near -1, similar to a cosmological constant, but evolves slightly depending on the choice of model parameters.

Observational constraints from Type Ia supernovae, BAO and CMB data indicate that unparticle DE models remain viable within current empirical limits. Unlike traditional quintessence models, which often suffer from severe fine-tuning issues due to radiative corrections, unparticle models benefit from the protection provided by their underlying fermionic structure, making them more stable against quantum corrections.

From a phenomenological perspective, unparticle DE offers an alternative mechanism for cosmic acceleration by introducing a scale-invariant sector into cosmology. The fractional scaling dimension d_u modifies the field dynamics, leading to distinct signatures that can be tested with future observational data. Given its theoretical robustness and ability to evade many of the challenges faced by standard scalar field models, unparticle DE represents an intriguing possibility in the quest to understand the nature of DE.

9 $O_m(x)$ Diagnostic for coupled ϕCDM model

The $Om(x)$ diagnostic, originally introduced in earlier studies [99], has been further extended to incorporate the influence of interaction effects.

$$O_m(x) = \frac{E^2(x) - 1}{x^3 - 1} \tag{56}$$

Here $x = 1 + z = \frac{a_0}{a}$ and $E^2(x) = \frac{H^2(x)}{H_0^2}$

Now by using Friedmann equation,

$$\left(\frac{\dot{a}}{a}\right)^2 = \frac{8\pi G}{3}\left(\rho_m + \rho_\phi\right) \tag{57}$$

For interaction term $Q = 3\alpha\dot{\rho}_m$,

$$E^2(x) = \Omega_m^0 x^{\frac{3}{1-3\alpha}} + \frac{3\alpha\Omega_m^0}{(1-3\alpha)(1+w_{\phi)-1}}\left(x^{\frac{3}{1-3\alpha}} - x^{3(1+w_\phi)}\right) + \Omega_\phi^0 x^{3(1+w_\phi)} \tag{58}$$

Now on substituting the value of (58) in equation (56) we have

$$O_m(x) = \frac{\Omega_m^0 x^{\frac{3}{1-3\alpha}} + \frac{3\alpha\Omega_m^0}{(1-3\alpha)(1+w_\phi)-1}\left(x^{\frac{3}{1-3\alpha}} - x^{3(1+w_\phi}\right)\Omega_\phi^0 + x^{3(1+w_\phi)} - 1}{x^3 - 1} \tag{59}$$

Now using $\Omega_\phi^0 = 1 - \Omega_m^0$, one obtain,

$$O_m(x) = \frac{\Omega_m^0\left(\left(x^{\frac{3}{1-3\alpha}} - x^{3(1+w_\phi)}\right)\left(1 + \frac{3\alpha}{(1-3\alpha)(1+w_\phi)-1}\right)\right) + x^{3(1+w_\phi)} - 1}{x^3 - 1} \tag{60}$$

On further solving one obtain,

$$O_m(x) = \frac{\Omega_m^0\left(1 + \frac{3\alpha}{(1-3\alpha)(1+W_\phi)-1}\right)\left(x^{\frac{3}{1-3\alpha}} - x^{3(1+w_\phi}\right) + x^{3(1+w_\phi)} - 1}{x^3 - 1} \tag{61}$$

In the limiting case where interaction vanishes ($\alpha = 0$), the expression for $O_m(x)$ simplifies directly to the current matter density parameter Ω_m^0.

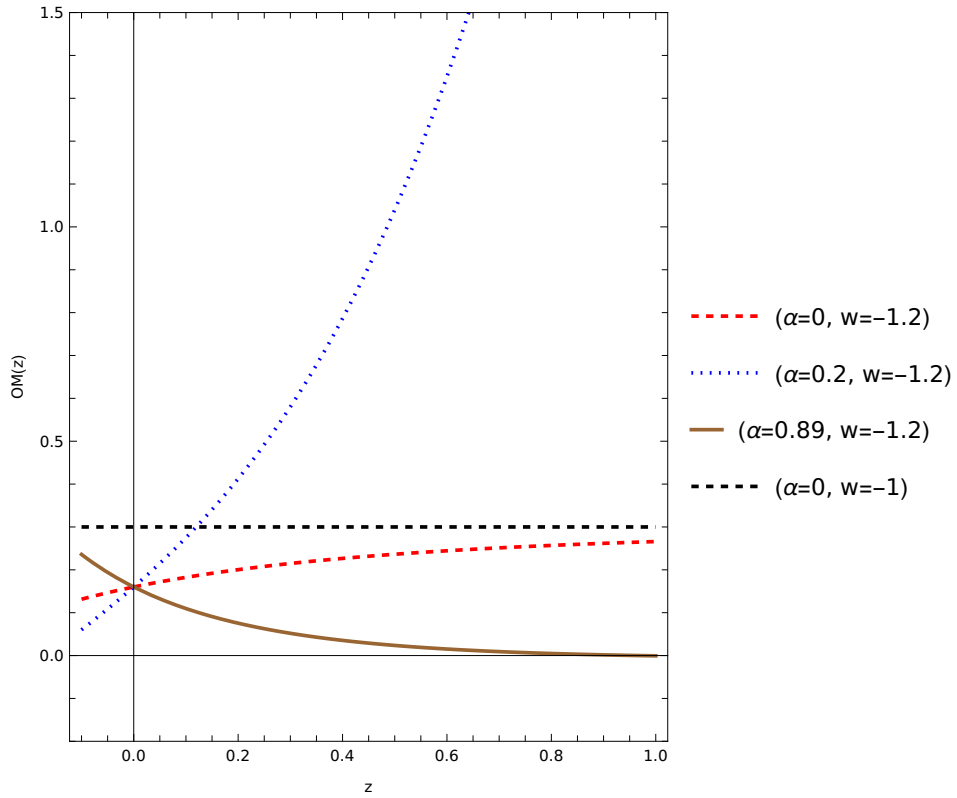

Figure 1: Variation of $O_m(x)$ with redshift z for different DE models.

Figure (1) depicts how the $O_m(z)$ diagnostic varies with redshift for different values of the interaction parameter α, assuming a fixed dark energy EoS $w = -1.2$, alongside the reference non-interacting ΛCDM model where $w = -1$. This diagnostic proves to be an effective method for differentiating between various dark energy models, especially when examining interacting frameworks.

The conventional ΛCDM framework (black dashed line) yields a constant $O_m(z)$, reflecting the absence of interaction between the dark sectors and acting as a reference model for comparative analysis. The non-interacting phantom scenario ($\alpha = 0$, $w = -1.2$, red dashed line) exhibits a gentle rise in $O_m(z)$ with increasing redshift, highlighting deviations from ΛCDM due to the phantom nature of dark energy but without any coupling. When interaction is present ($\alpha = 0.2$, blue dotted line), $O_m(z)$ rises more noticeably with redshift, pointing to a substantial energy influx into the dark matter component. In the case of a stronger coupling ($\alpha = 0.89$, brown solid line), $O_m(z)$ declines steeply as redshift increases, indicating a dominant directional flow of energy from dark energy to dark matter, which effectively reduces the matter density at earlier cosmic times.

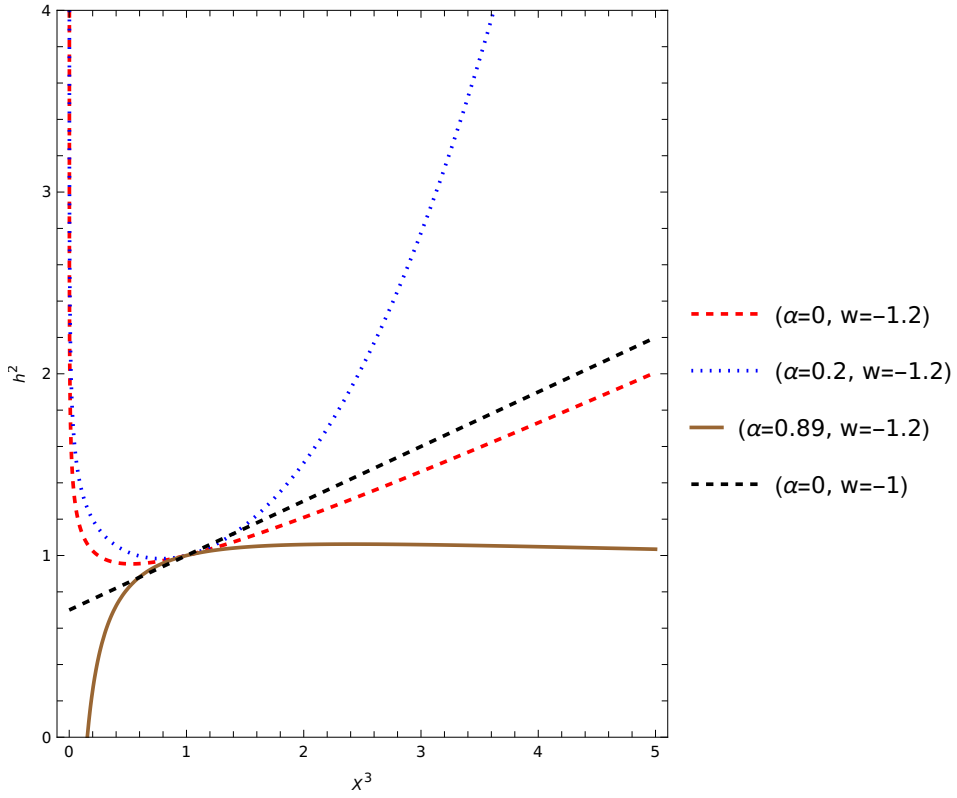

Figure 2: Evolution h^2 verses X^3 for different value of coupling parameter α and EoS w

Figure (2), illustrates the variation of the dimensionless Hubble parameter squared, h^2, as a function of x^3, where $x = 1+z$ and z denotes the redshift. Different curves correspond to various choices of the interaction parameter α and the equation of state parameter w, characterizing interacting phantom DE models.

- **Red dashed curve**: Represents the non-interacting phantom scenario with $\alpha = 0$ and $w = -1.2$. Here, the expansion rate grows steadily with redshift, as expected in a standard phantom cosmology.
- **Blue dotted curve**: Corresponds to a moderate interaction strength with $\alpha = 0.2$ and the same phantom EoS $w = -1.2$. The plot shows a much steeper rise in h^2 at higher redshifts, indicating enhanced energy transfer into the DM sector, which boosts the expansion rate.
- **Brown solid curve**: Depicts a strongly interacting case with $\alpha = 0.89$ and $w = -1.2$. Unlike the previous cases, this curve initially increases but then flattens out and eventually declines, highlighting a significant energy transfer from DE to DM. As a result, the effective DE density gets diluted at higher redshifts, suppressing the expansion rate.
- **Black dashed curve**: Shows the standard ΛCDM model with $\alpha = 0$ and $w = -1$, where DE behaves like a cosmological constant. The evolution is linear in x^3, reflecting the standard expansion history.

10 Conclusion

Scalar field DE models—such as quintessence, phantom fields, K-essence, tachyons, Chaplygin gas, and unparticles—offer dynamic alternatives to the cosmological constant, characterized by evolving equations of state. While these models provide greater flexibility in fitting observational data, they face ongoing challenges, including fine-tuning, theoretical instabilities, and tensions with large-scale structure observations. To evaluate interacting DE scenarios, we employed the $O_m(z)$ diagnostic and examined the evolution of the dimensionless Hubble parameter squared, h^2, as functions of redshift. The results reveal that interactions significantly modify the cosmic expansion history. Moderate interaction ($\alpha = 0.2$) enhances the matter density at high redshift, while strong interaction ($\alpha = 0.89$) leads to suppressed expansion due to energy transfer from DE to DM. These deviations from ΛCDM highlight the utility of diagnostics like $O_m(z)$ in probing the dark sector. Overall, such tools, combined with future observational and theoretical advancements, are essential to assess whether scalar field models can fundamentally explain DE or if new paradigms are needed.

References

[1] A.G et al., *Astron. J.* , **116**, 1009(1998).

[2] S. Perlmutter et al., *ApJ*, **517**, 565(1999).

[3] P. A. R. Ade *et al.*, *Astron. Astrophys.* **596**, A100 (2016).

[4] N. Aghanim et al., *Astron. Astrophys.*, **641** , A6(2020).

[5] N. Aghanim et al., *Astron. Astrophys.*, **641** , A1(2020).
[6] S. D Pathak and M. M Verma, *IJTP* , **51** , 2370(2012).
[7] S. Unnikrishnan and V. Sahni, *JCAP*, **2013** , 063(2013).
[8] S.Bahamonde et al., *Phys. Rep*, **775** 1(2018).
[9] V. Faroni, *Phys. Rev. D.* **69** , 123520(2004).
[10] S. Kumar, S. D Pathak and M. Khlopov *IJTP*, **63**, 238(2024).
[11] T. Padmanabhan, *Phys. Rept*, **380**, 235 (2003).
[12] M. Sami, *Curr. Sci.*, 887(2009).
[13] T. Patil and S. Panda, *Eur. Phys. J. Plus.*, **138**, 1(2003).
[14] A. Singh, H.K Jassal and M. Sharma,*JCAP* , **2020**, 008(2008).
[15] W. Yang et al., *JHEAP*, **40**, 19(2023).
[16] Y. Fujii, *Phys. Rev. D*, **26**, 2580(1982).
[17] R.D Peccei, J. Sola and W. Wetterich *Phys. Lett. B.* , 195 (1987).
[18] L. H Ford, *Phys. Rev. D* , **35**, 2339(2019).
[19] C. Wetterich *Nucl. Phys. B.* , **302** , 668(1988).
[20] B.Ratra and P.J.E. Peebles, *Phys. Rev. D* , **37**, 3406 (1988).
[21] Y. Fujii and T. Nishioka, *Phys. Rev. D*, **42** , 361(1990).
[22] T.Chiba, N. Sugiyama*MNRAS*, **289**, L5(1997).
[23] P.G. Ferreira and M. Joyce, *PRL*, **79**, 4740(1997).
[24] P.G. Ferreira and M. Joyce, *Phys. Rev. D* **58**, 023503(1998).
[25] R. R. Caldwell, R. Dave and P.J. Steinhardt *PRL*, **80**, 1582(1998).
[26] S.M. Carroll, *AIP Conf. Proc.*, **478**, 291(1999).
[27] E.J. Copeland, A. R. Liddle and D. Wands, *Phys. Rev. D.* , **57**, 4686(1998).
[28] I. Zlatev, L. Wang and P.J. Steinhardt *PRL*, **82**, 896(1999).
[29] P.J. Steinhardt, L. Wang and I. Zlatev, *Phys. Rev. D.*, **59**, 123504(1999).
[30] A. Hebecker and C. Wetterich, *PRL*, **85**, 3339(2000).
[31] A. Hebecker and C. Wetterich, *Phys. Lett. B.* , **497**, 3(2001).
[32] E.V. Linder, *GRG*, **40**, 329(2008).
[33] C. Rubano and P. Scudellaro, *GRG*, **34** 307 (2002).
[34] S. Capozziello, S. Carloni and A. Troisi *arXiv preprint astro-ph/0303041*, (2003) .
[35] L.A. Urena Lopez,*JCAP* ,**2009** , 014(2019) .
[36] R. R Caldwell *Phys. Lett. B.* , **545** , 23(2002) .
[37] R. R Caldwell, M. Kamionkowski and N. N Weinberg *PRL* ,**91** , 071301(2003) .
[38] S. M. Carroll, M. Hoffman and M. Trodden *Phys. Rev. D.* , **68** , 023509, (2003) .
[39] S. Nojiri and S.D . Odintsov *Phys. Lett. B.*, **562** , 147(2003) .
[40] P. Singh, M. Sami and N. Dadhich *Phys. Rev. D.* , **68** , 075013 (2021) .
[41] T. Karakasis, E. Papantonopoulos and C. Vlachos, *Phys. Rev. D* , **105** , 023522 (2003) .
[42] M . Sami and A. Toporensky, *Modern Physics Letters A* , **19** , 1509 (2004) .
[43] M. Ballardini, A. Ferrari and F. Finelli, *Phys. Rev. D.*, **70** , 043543 (2004) .
[44] V. K. Sharma and M. M. Verma, *EPJ C*, **82** 400 (2022) .
[45] V. K. Sharma, B.K. Yadoo and M.M. Verma, *EPJ C*, **81** ,1 (2021).
[46] V. K. Sharma, B.K. Yadoo and M.M. Verma, *EPJ C* **80** , 619(2020).
[47] V.K. Sharma et al. , *Phys. Lett. B.* , **859** , 139093 (2024).
[48] S. Capozziello and M. Francaviglia ,*GRG*, **40** , 357 (2008).
[49] S. Capozziello and V. Faraoni, **170** (2010) .
[50] G. R. Dvali, G. Gabadadze and M. Porrati, *Phys. Lett. B*,**485** , 208 (200O) .
[51] V. Sahni and Y. Shtanov ,*JCAP* ,**2003** , 014 (2003) .
[52] D. C. Dai, S. Dutta and D. Stojkovic, *Phys. Rev. D.*,**80**, 063522(2009) .
[53] H. Georgi,*PRL* ,**98** , 221601(2007) .
[54] J. S. Bagla, H. K. Jassal and T. Padmanabhan *Phys. Rev. D.* , **67**, 063504 (2003).
[55] C. Armendariz-Picon, T. Damour and V. Mukhanov *Phys. Lett. B* , **458** 209 (1999) .

[56] G. Garriga and V. Mukhanov, *Phys. Lett. B* **458**, 219(1999) .

[57] T. Chiba, T. Okabe and M. Yamaguchi *Phys. Rev. D*, **62** 023511 (2000) .

[58] C. Armendariz-Picon, V. Mukhanov and P. Steinhardt, *PRL*, **85** 4438(2000) .

[59] C. Armendariz-Picon, V. Mukhanov and P. Steinhardt, *Phys. Rev. D.* ,**63** 103510 (2001) .

[60] E. J. Copeland, M. Sami and S. Tsujikawa *Int. J. Mod. Phys. D.* ,**15** 1753 (2006) .

[61] P. S.Corasaniti et al. *Phys. Rev. D* **70**, 083006 (2004) .

[62] U. Alam et al.*MNRAS*,**354** , 275 (2004) .

[63] V. Sahni and Y. Shtanov, *JCAP*, **11** , 014(2003) .

[64] Z. G. Huang, X.H. Li and Q.Q. Sun, *Ap&SS*,**310** , 53 (2007) .

[65] V. Sahni and Y. Shtanov, *Int. J. Mod. Phys. D*, **11** , 1515(2002) .

[66] E.Elizalde, S. Nojiri and S. D. Odintsov, *Phys. Rev. D*, **70** , 043539 (2004) .

[67] I. Bars, C. Deliduman and D. Minic, *Phys. Lett. B*, **457** , 275 (1999) .

[68] S. Roy, *Phys. Lett. B*, **567** , 322 (2003).

[69] F. Hoyle, *MNRAS*, **108** , 372 (1948).

[70] F. Hoyle, *MNRAS*, **109** , 365 (1949).

[71] F. Hoyle and J.V . Narlikar, *Proceedings of the Royal Society of London. Series A. Mathematical and Physical Sciences*, **282** , 191 (1964).

[72] F. Hoyle and J.V . Narlikar, *MNRAS*, **155** , 323 (1972).

[73] P. Singh, M. Sami and N. Dadhich, *Phys. Rev. D*, **68**, 023522 (2003).

[74] J.M. Cine, S. Jeon, and G. D. Moore, *Phys. Rev. D*, **70**, 043543 (2004).

[75] A. Sen, *JHEP*, **04**, 048 (2002).

[76] A. Sen, *JHEP*, **07**, 065 (2002).

[77] A. Sen, *JHEP*, **1999**, 008 (1999).

[78] M. R. Garousi, *Nucl. Phys. B*, **584**, 284 (2000).

[79] M. R. Garousi, *Nucl. Phys. B*, **647**, 117 (2002).

[80] M. R. Garousi, *JHEP*, **2000**, 058 (2003).

[81] E. A. Bergshoeff et. al. *JHEP*, **2003**, 009 (2000).

[82] J. Kluson *Phys. Rev. D*, **62**,126003 (2000).

[83] G. W. Gibbons *Phys. Lett. B*, **537**,1 (2002).

[84] A. Feinstein *Phys. Rev. D*, **66**,063511 (2002).

[85] A. Mazumdar, S. Panda and A. Perez-Lorenzana,*Nucl. Phys. B*, **614**,101 (2001).

[86] M. Fairbairn and M. H. G Tytgat,*Phys. Lett. B*, **546**,1 (2002).

[87] M. Sami, P. Chingangbam and T. Qureshi,*Phys. Rev. D*, **66**,043530 (2002).

[88] M. Sami,*Mod Phys Lett A*, **18**,691 (2003).

[89] L. Kofman and L. Linde,*JHEP*, **2002**,004 (2002).

[90] J. S. Bagla, H. K . Jassal and T. Padmanabhan, *Phys. Rev. D*, **67**,063504 (2003).

[91] J. M. Aguirregabiriaand R. Lazkoz,*Phys. Rev. D*, **69**,123502 (2004).

[92] E. J. Copeland, *Phys. Rev. D*, **71**,043003 (2005).

[93] D. Kutasov and V. Kutasov, *Nucl. Phys. B*, **666**,56 (2003).

[94] M. R. Garousi, M. Sami and S. Tsujikawa, *Phys. Rev. D*, **70**,043536 (2004).

[95] M. R. Garousi, M. Sami and S. Tsujikawa, *Phys. Lett. B*, **606**,1 (2005).

[96] P. Chingangbam and T. Qureshi, *Int. J. Mod. Phys. A*, **26**,6083 (2005).

[97] A. Kamenschchick, U. Moschella and U. Pasquier, *Phys. Lett. B*, **511**,265 (2001).

[98] N. Bilic, G. B Tupper and R. D. Viollier, *Dark Matter in Astro-and Particle Physics: Proceedings of the International Conference DARK 2002, Cape Town, South Africa,*, 306 (2002).

[99] V. Sahni, A. Shafieloo and A. Starobinsky, *Phys. Rev. D*, **78**,103502 (2008).